Yu. V. NIKITYUK, A. A. SEREDA, A. N. SERDYUKOV

LASER CLEAVING OF BRITTLE NON-METALLIC MATERIALS

Nikityuk, Yu. V.
    Laser cleaving of brittle non-metallic materials / Yu. V. Nikityuk, A. A. Sereda, A. N. Serdyukov ; Francisk Skorina Gomel State University. – Gomel : Francisk Skorina Gomel State University, 2025. – 217 p.
    ISBN 978-985-32-0081-2

This monograph analyses the findings from studies on the controlled laser thermal cleaving of brittle non-metallic materials. It presents newly developed laser techniques for high-precision separation of products from various silicate glasses, alumina ceramics, and anisotropic crystals, as well as enhancements to existing technologies.

It is designed for researchers, postgraduates, master's degree students, undergraduates, and professionals in mechanical engineering, instrument making, and the electronics industry, as well as individuals interested in the processing and manufacturing of products from fragile non-metallic materials.

Tables 29. Figures 135. References 240 sources.

Recommended for publication by the science and technology council
of Francisk Skorina Gomel State University

Reviewers:

V. N. Belyi,
Academician of the National Academy of Sciences of Belarus,
Dr. Sci. in Physics and Mathematics;
V. A. Yemelyanov,
Corresponding Member of the National Academy of Sciences of Belarus,
Professor, Dr. Sci. in Engineering;
I. A. Khorsun,
PhD in Philology, Associate Professor

CONTENTS

INTRODUCTION

The miniaturization of modern equipment, in conjunction with the continuous rise in the quality of precision processing of products from brittle non-metallic materials, necessitates the development of new laser methods for the high-precision separation of products from a variety of silicate glasses, alumina ceramics, and anisotropic crystals, as well as the enhancement of the efficiency of existing technologies.

At present, various methods for precision laser processing of brittle non-metallic materials have been developed, including through-the-thickness laser thermal cleaving, controlled laser thermocleaving (CLT), parallel thermocleaving, and thermal cleaving of tubular-shaped products.

Controlled laser thermocleaving is recognized as a highly effective method for the high-precision separation of brittle nonmetallic materials. This technique is characterized by the separation of the material into specifically shaped parts, which occurs through the formation of a microcrack. This microcrack is generated as a result of surface heating of the material via laser radiation, followed by the cooling of the heating zone using a refrigerant. The primary benefits of controlled laser thermocleaving are its precision in separation, rapid processing capabilities, and waste-free operation.

However, the technological processes for the separation of brittle non-metallic materials utilizing controlled laser thermocleaving exhibit several characteristics that hinder their broad industrial application.

One feature of laser thermocleavage technology is the low stability of the microcrack development process, which is significantly influenced by the refrigerant that penetrates into the laser impact zone, affecting the thermophysical conditions within that area. This situation is a primary factor contributing to the undesirable failures in the development process of the splitting microcrack.

Another notable disadvantage of the controlled laser thermocleavage technology relates to the significant limitation on the maximum depth of microcrack penetration into the material, which is attributed to the reliance on surface laser heating.

Moreover, the application of controlled laser thermocleavage technology for cutting brittle nonmetallic materials along closed curvilinear contours presents several noticeable drawbacks that result in reduced processing accuracy and inferior quality of the final products. The methods to address these drawbacks remain insufficiently clarified, necessitating further investigation.

It is important to highlight that the established mathematical models for laser thermocleaving processes are formulated as analytical solutions to ther-

moelastic equations. The analysis of the solutions derived from the two-dimensional formulation of the problem has led to the establishment of the dynamics involved in the formation of thermoelastic fields, revealing several regularities in the processes of thermal cleaving. Nevertheless, the current models derived from the linear differential equation of thermal conductivity, which do not consider the temperature dependence of thermophysical coefficients, fail to provide reliable predictions for the technological parameters of processing modes.

The existing models of laser thermocleaving processes present a notable limitation, as the determination of stress tensor components in bulk samples is conducted within a two-dimensional framework. This approach not only reduces the accuracy of calculations but also complicates the analysis of the actual spatial distribution of stresses significantly.

In light of this, the advancement of novel and effective methodologies for the high-precision separation of brittle nonmetallic materials through thermal laser cleaving, grounded in numerical three-dimensional modelling, is a pressing issue that holds both scientific and practical significance for enhancing technological characteristics.

CHAPTER 1. TECHNIQUES FOR LASER DIMENSIONAL PROCESSING OF BRITTLE NON-METALLIC MATERIALS

A significant area of application for lasers in technology involves the separation processes of nonmetallic materials. As noted in [1, p. 6], "non-metals encompass extensive categories of materials (dielectrics, semiconductors, plastics, rocks, textiles, etc.) that vary considerably in terms of chemical composition, properties, manufacturing techniques, purposes, applications, and, inherently, processing methods. However, the introduction of lasers has established practical conditions for the implementation of thermal processes aimed at the separation of nonmetals across all classifications". Additionally, it is stated that "a specific laser separation operation can be classified as one of three types of processing: cutting, drilling, or thermal cleaving" in relation to non-metallic materials. It is observed that "an intermediate position between cutting and thermal cleaving is occupied by the scribing method employed to separate semiconductor, ceramic, and sitall substrates into distinct elements" [1 p. 11].

A more complete classification is provided in [2, p. 4], which identifies the following methods for processing glass and other brittle non-metallic materials:

− laser cutting through the vaporization of material along the designated cutting line;

− gas-laser cutting utilizing a jet of compressed gas (typically air) to expel the molten material;

− gas-laser cutting that initiates a thermal reaction using an active gas;

− scribing technique;

− through-the-thickness laser thermocleaving method;

− controlled laser thermocleaving (CLT).

A substantial number of sources detail the fundamental methods of laser processing of materials (e.g., in [3–6]), with specific emphasis on the processing of brittle nonmetallic materials through laser thermocleavage methods as outlined in [2, 7–23].

Analysis of the features associated with various methods of laser separation for nonmetallic materials, specifically silicate glasses and alumina ceramics, as detailed in the aforementioned sources (Table 1.1 [2, p. 11]), reveals the following observations:

− laser and gas-laser cutting via the evaporation of material along the cutting line is energy-intensive and lacks high processing accuracy, which makes inefficient the applicability of these methods for obtaining precision products from brittle nonmetallic materials [2, p. 9];

– laser scribing is noted for producing edges of products that exhibit low quality. Furthermore, the application of this method is linked to the contamination of the material surface due to the byproducts of evaporation. Therefore, the application of scribing for precision machining may, in certain instances, be deemed unsuitable [2, p. 9].

Table 1.1 – Common modes of various techniques for laser dimensional cutting of glass

Laser dimensional cutting technique	Laser power, W	Cutting speed, mm/s	Thickness of glass, mm	Energy intensity, J/mm^2
Laser	200	0.42	3.5	143
Gas-laser	200	6.35	1.57	20.1
Scribing	50	58	6	0.144
Through-the-thickness thermal cleaving	9	5.1	1.6	1.1
Controlled thermal cleaving	25	39	3	0.21

The drawbacks observed are not inherent to the method of through-the-thickness laser thermal cleaving [7]. The initial findings on this topic were presented by R. Lamley. They originate from the late 1970s of the 20th century [24, 25]. The lack of the previously noted drawbacks, along with waste-free separation and the sufficiently high quality of the resulting edges of products, led to a comprehensive investigation and widespread adoption of the method of through-the-thickness laser separation of brittle nonmetallic materials in the Soviet Union during the 1980s, as evidenced in the works of G. A. Machulka [7, 26].

The fundamental principle of through-the-thickness laser thermal cleavage involves the creation of a through-the-thickness microcrack and its subsequent propagation within a brittle nonmetallic material. This occurs under the influence of thermoelastic stresses generated by the surface laser heating along the processing line, which is a result of the relative motion between the laser beam and the material surface [7, 27–31]. The temperature in the processing area is constrained from above to values that prevent the relaxation of thermoelastic stresses resulting from plastic deformation [7, 31].

However, the examination of through-the-thickness laser thermocleaving revealed serious drawbacks, and addressing these issues proved to be quite challenging. Thus, through-the-thickness laser cleaving is characterized by a low cutting speed [2, 31] and a dependence of the thermocleavage modes on the dimensions of the initial workpiece. Due to these factors, con-

ducting thermocleaving on samples of considerable size is unfeasible. Furthermore, the drawbacks of through-the-thickness thermal cleaving include low separation accuracy, which is attributed to the inherent distribution of tensile and compressive stress zones within the work material, resulting from surface laser heating (a detailed analysis of thermoelastic fields is conducted in the third chapter). The identified drawbacks of through-the-thickness laser thermocleaving have resulted in its classification as an unpromising method [31].

Currently, the most efficient technique for separating brittle nonmetallic materials is controlled laser thermocleaving [2, 8–10, 31]. This method is characterized by the creation of a microcrack, which results from the surface heating of the material through laser radiation, followed by the cooling of the heating area using a refrigerant. The primary benefits of CLT are its precision in operations, elimination of waste during separation, and rapid processing capabilities.

As previously mentioned, the development and research of this method were carried out in the second half of the 1970s in the USSR, associated with the efforts of a group of scientists led by V. S. Kondratenko [2, 8, 31–52]. This topic has been the subject of research in various countries, including Belarus [53–95], Russia [96–107], Germany [108–111], the USA [112–114], China [115–120], among others.

Research has led to the development of several methods for precision laser-beam processing of brittle nonmetallic materials. These methods, alongside CLT, encompass parallel and asymmetric laser thermocleaving.

Parallel laser thermal cleaving occurs when the material is subjected to an elliptical laser beam aligned with its minor axis in the direction of movement, resulting in the thermal separation of the sample [9, 10, 59]. The technique of rounding sharp edges, involving the detachment of a narrow strip of glass, as proposed in [42], can be regarded as a limiting form of this processing procedure.

The fundamental principle of asymmetric laser thermal cleaving is that when a material is heated with a laser beam of elliptical cross-section, positioned at an angle to the direction of relative displacement, an oblique crack with rounded edges is generated [10, 31, 69]. An option of the asymmetric thermal cleavage method is proposed in [121], utilized for producing glass wafers with a complex edge profile, resulting from both the beam's rotation at an angle of $5 - 26°$ to the separation line and the refrigerant's movement relative to the laser beam and the separation line.

The integration of parallel thermal cleaving and CLT within a singular processing cycle is employed in combined laser thermocleaving to produce mutually perpendicular cracks in the sample [9, 10].

The high cost of laser technological equipment resulted in a decline in the intensity of research related to the laser separation of brittle nonmetallic materials in the early 1990s within the CIS [98].

The growing demands for the quality of precision products composed of brittle nonmetallic materials, primarily driven by the miniaturization of contemporary electronic devices, necessitated the development of innovative laser techniques and the enhancement of existing technologies for the high-precision separation of products made from this specific class of materials.

At present, CLT technology has evolved into an industrial technology. The German company "JENOPTIC Automatisierungstechnik GmbH" manufactures glass and ceramic cutting machines known as "VOTAN-G". Concurrently, the abbreviation TLS, which stands for Thermal Laser Separation, is utilized to refer to the CLT technology [122].

American companies PTG Industries and Fonon Technology International provide technology for industrial applications involving controlled laser thermocleaving, referred to in the U.S. as Zero Width Cutting Technology – ZWCT™ [123, 124]. EsseTech Co., a South Korean manufacturer, specializes in the production of GCM200L glass cutting units designed for LCD flat panels.

In the Russian Federation, analogous services are offered by JSC Moskovskij zavod "SAPPHIR", Nano Lab company, and VOTSS LTD (Moscow) [125–127].

Alongside the previously mentioned companies and enterprises that offer services for processing brittle non-metallic materials through laser thermal cutting methods, several major corporations, including Corning Incorporated, Seagate Technology, Hitachi Ltd, and Samsung Electronics, possess pertinent patents and employ laser thermal cleavage technologies.

Thus, CLT represents the most efficient technique for the separation of brittle nonmetallic materials implemented in industry. Despite its advantages, this technology shows several drawbacks that impede its broader industrial adoption and require further research to enhance the processes involved in high-precision separation of brittle nonmetallic materials through laser thermal cleaving.

The feasibility of employing CLT for the separation of brittle nonmetallic materials along closed curvilinear trajectories has been established in references [31, 35, 50, 110]. The examination of these works and the outcomes of our own research [68] identified several issues that arise during the implementation of this technology.

When employing CLT, notable deviations of the generated microcrack from the laser impact line occur during machining along a curvilinear contour with small radii of curvature. The reason for this is that, during straight-

line cutting, the thermoelastic stress fields maintain symmetry in relation to the trajectory of the laser beam. However, when cutting along a curvilinear contour, the symmetry of thermoelastic stresses is disrupted. The smaller the radius of curvature of the curvilinear contour, the more asymmetric the distribution of thermoelastic stresses becomes. The deviation of the crack from the processing line is the cause of this circumstance. This results in a reduction in the accuracy of product manufacturing.

The introduction of supplementary heating in the processing circuit through laser radiation, utilizing a wavelength that facilitates surface heating of the material being treated as proposed in [31], does not effectively address the aforementioned issue.

The concept presented in references [50, 110] is noteworthy. It involves the process of cutting along a closed curvilinear contour, where heating is applied using a beam that has a sickle shape with a specific radius of curvature on the material surface. The application of these beams is expected to facilitate a symmetrical distribution of thermoelastic stresses during the cutting process along curvilinear contours. The primary drawback of this processing method lies in the technical challenges encountered during its implementation, which are linked to the necessity of substantially complicating the optical systems employed in the relevant setups.

In the application of CLT, notable deviations occur in the microcrack generated from the laser impact line during the cutting process along a closed curvilinear contour, particularly at the junction where the machining contour closes. The reason for this is that at the closure of the machining contour, the propagation of the deposited microcrack is significantly influenced by its own "tail." The tip of this tail, along with the tip of the microcrack itself, serves as a location of significant stress concentration. The implementation of preliminary notching along the processing line, with a gradually increasing depth as proposed in [31], does not effectively mitigate this disadvantage.

Furthermore, substantial challenges exist in the final cleaving of the deposited laser microcracks to achieve a final product constrained by a closed curvilinear contour. The process of straight-line cutting involves the final separation of material into blanks, which is achieved by manually breaking the cut material or utilizing specialized mechanisms and devices. However, due to the high percentage of rejects associated with this method, it is generally deemed unacceptable for separating blanks into sections defined by a closed curvilinear contour. The application of repeated laser heating on the machining contour, as proposed in [31], frequently proves inadequate in addressing this issue, as the depth of microcracks attained through this method remains insufficient for achieving a definitive qualitative separation.

In [57], it is observed that an important disadvantage of the current CLT technology is the considerable restriction on the allowable thickness of work samples. This limitation is linked to the application of laser radiation, which results in surface heating of the material. The authors [43, 57] propose employing controlled final cleaving as a solution to this issue. The proposed solution involves applying additional impact on the material's surface in the notching zone through elastic waves. The amplitude and frequency of these waves are determined based on the requirement to deepen the notch to a specified depth or to achieve through-cutting.

Reference [49] proposes the utilization of pulsed laser radiation as a source of elastic waves. In [57], many implementations of this technology are presented, with the Nd-laser approach for generating sound waves in liquid being deemed the most effective. Simultaneously, it is observed that employing lasers for the direct excitation of shock acoustic waves to regulate the movement of microcracks yielded unsatisfactory results. It is important to note that, aside from the aforementioned two methods of generating elastic waves in the material, the alternative methods suggested by the authors involve mechanical impact on the surface, frequently resulting in damage, which is generally unacceptable in most cases.

A variation of CLT proposed in [48] is noteworthy, since its implementation enhances the depth of microcrack penetration by multistage controlled cooling. In [52], it is suggested that a refrigerant be employed to enhance microcrack depth, utilizing "a two-level dispersed system comprising a dispersed air medium and a two-phase composition of the dispersed phase, which includes water droplets as the first dispersed phase and a colloidal composition or solid micro-particles as the second dispersed phase".

The authors [55, 98–100] indicate that the controlled propagation of a microcrack when using CO_2 laser radiation is feasible only with a material thickness that is relatively small. They proposed employing the radiation of a solid-state laser at a wavelength of 1.06 μm as a technological tool.

Attention must be given to the observation that nearly all the studies referenced regarding the separation of brittle nonmetallic materials through thermal cleaving employed laser radiation, specifically CO_2 laser radiation, to achieve surface heating of the material. The selection of this specific type of laser as a technological instrument is based on several factors.

Specifically, [7, p. 10] states that "industrial CO_2 lasers provide maximum power in continuous mode compared to other lasers, maximum performance, are quite simple in design and durable". Simultaneously, [7] highlights the potential applications of radiation emitted from CO_2 lasers, while also addressing the inefficiencies associated with radiation from solid-state lasers functioning at a wavelength of 1.06 μm.

It is also concluded that "glass undergoes a heating process when exposed to radiation of sufficient intensity (tens of watts), which can be employed for thermal cleaving. However, the potential applications of this type of laser radiation are constrained. Initially, the losses in glass at the operational wavelengths of solid-state lasers are minimal, and a considerable portion of the radiation power is dissipated during the processing phase. Secondly, the efficiency of solid-state lasers is limited to 2 %, raising concerns regarding the economic viability of using this heating source extensively in glass processing technology" [7, p. 10].

The study in publication [128] outlines the application of the technological unit "Kvant-20" for the heat treatment of glass. However, work [10] raises concerns about its viability, citing the low rate of thermal cleaving as a significant issue.

However, the studies [98–100, 129] provide results demonstrating the feasibility of using radiation from solid-state lasers at a wavelength of 1.06 µm for the processing of thick glasses.

In [129, p. 787], a method for cutting glass wafers using radiation from a pulsed neodymium laser with passive mode synchronization is proposed. The method involves the formation of microcrack channels, followed by the subsequent (self)splitting of the material along these channels.

The authors of [98, 99] demonstrated the possibility of separating packages of glass wafers with a thickness of up to 24 mm using solid-state laser radiation. Reference [100] indicates that the benefits of using solid-state laser radiation encompass the capability of cutting multiple sheets simultaneously, specifically up to 4 to 6 sheets. The authors of these works cite the challenges associated with processing thick samples using alternative methods as a key argument in support of utilizing the radiation from solid-state lasers at a wavelength of 1.06 µm as a technological tool.

Nonetheless, following the examination of these studies and the findings from our experimental investigations [67], we must concur with the conclusion that the autonomous application of radiation at a wavelength of 1.06 µm for the separation of brittle nonmetallic materials proves ineffective in all circumstances, with the exception of the previously mentioned specific instances.

One more drawback of CLT is the limited reliability of the separation process in modes where there is a minimal distance from the edge of the laser spot on the surface of the material being processed to the front of the cooling zone, particularly when a fine mixture is employed as a refrigerant.

The analysis of the CLT process revealed multiple factors contributing to its instability [73]. The presence of the refrigerant substance in the laser impact zone significantly influences the thermophysical conditions, leading to frequent failures in the development of the splitting microcrack.

It is important to highlight that the refrigerant plays a crucial role in the process of laser-controlled thermocleaving, which enables the achievement of a qualitatively new result, i.e., a controlled microcrack penetrating into the glass at a specified depth [2, p. 35].

Research conducted by the author of [8] indicates (see Table 1.2) that the most effective application as a refrigerant is a fine air-water mixture delivered under pressure to the processing area. The higher specific heat capacity of water, when compared to other substances used in the experiments, accounts for this observation. The chemical composition of the refrigerant impacts the cracking process in silicate glasses and alumina ceramics, highlighting the potential for chemical reactions that may expedite the fracture process [130, p. 140].

Table 1.2 – Comparative analysis of parameters involved in the laser-controlled thermocleaving process of 6 mm thick sheet glass using various refrigerants

Refrigerant name	CLT rate, mm/s	Microcrack depth, mm	Refrigerant flow rate, ml/sec
Air current	7	0.72	–
Water	25	0.35	0.04
Propyl alcohol	20	0.35	0.08
Ethylic alcohol	25	0.35	0.1
Glycerin	10	0.45	0.1

Research findings indicate that the cooled surface exhibits not only a zone characterized by stable intensive cooling but also the formation of a film resulting from the spreading of liquid over the surface [73]. The primary cooling of material areas heated by laser radiation typically occurs beneath this film and is marked by considerable instability in heat exchange.

The aforementioned drawbacks can be addressed by employing a gas stream as a refrigerant [97], although this method is inefficient. Alternatively, a specialized vacuum device can be utilized to extract the refrigerant substance, though this presents significant technical challenges.

In [57], challenges encountered during the material cutting process using the CLT method in perpendicular directions were observed. The authors of this work proposed a method for non-contact microdefect creation to address these issues, achievable through exposure to radiation from various types of pulsed lasers. In this scenario, it is posited that erbium and TEA CO_2 lasers represent the most suitable tools for defect formation. The authors

of [131] propose utilizing mutually perpendicular cuts on opposite sides of the workpiece for this purpose.

Paper [108] proposes a method for laser cutting via thermal cleaving. The primary characteristic of this method is that the cross section of the CO_2 laser beam, at a wavelength of 10.6 μm, is shaped on the working surface as a V- or U-shaped spot. A proposal was given in [50, 132] to provide optimal conditions along the cutting line by employing a laser beam that delivers a radiation power density distribution on the material surface, which decreases from the periphery towards the center of the beam. It is expected that employing such laser beams will prevent material warming along the cutting line. Nonetheless, the application of laser beams in the suggested structures, while potentially enhancing the quality of thermal cleaving, is not advantageous due to the considerable complexity it introduces to the optical systems of the respective setups.

A novel variation of the method for microcrack formation in brittle nonmetallic materials is presented in [112]. The laser beam is pointed at the material, ensuring that the focal spot is positioned between the front and back surfaces of the material. Simultaneously, a coolant jet is directed onto the surface area above the focal spot, leading to the formation of an internal crack within the material, which does not reach any of the material's surfaces.

Several effective technical solutions outlined in [113] deserve individual recognition. In this study, the authors propose the introduction of a cooling source within the laser beam impact zone on the material surface. This approach aims to achieve a notable reduction in the deviation of the splitting microcrack from the processing line. The invention proposes the use of an additional laser beam to preheat the material, thereby enhancing the processing speed. To mitigate edge effects, it is suggested to modify the processing speed at various stages of the treatment procedure. Besides, the setup in this invention includes a novel final cleavage device designed as tubes situated in technological recesses, which expand in volume as the pressure of the fluid flowing through them increases.

Research paper [44] provides a double-beam method of through-the-thickness laser thermocleaving, using radiation from two CO_2 lasers. When the surface of a brittle nonmetallic material wafer is subjected to heating via two laser beams that strike the material surface at a specified distance apart and are offset from the separation line in a direction perpendicular to the relative displacement of the laser beams and the material, compression stresses develop in the heating zones. Concurrently, substantial tensile stresses emerge in the region situated between these heating zones. This is a prerequisite for the development of a splitting microcrack. Unlike controlled

thermal cleaving, where separation occurs through the heating of the material surface with a laser beam and subsequent local cooling using a refrigerant, the application of heating via two laser beams to create a controlled microcrack allows for the elimination of refrigerant in the cutting process. In many circumstances, it is of paramount significance. This cutting procedure is largely inappropriate for producing small-sized products due to the expansion of the heat-affected zone. This explains the constraints on the effective implementation of this strategy in contemporary industry.

It was previously observed that in the process of producing glass products through laser thermal cleaving, the temperature within the laser processing area must remain below the glass transition temperature specific to the type of glass being used [7, 31]. It is important to clarify that, in certain instances, heating the processing zone to a temperature above the glass transition temperature can be beneficial.

In [104], a method for cutting thin glass is introduced, involving the heating of the glass to a temperature exceeding the softening point during the initial exposure to a focused CO_2 laser beam. This process results in the formation of a band of material, either concave or convex relative to the product's surfaces, characterized by residual tensile stresses in the near-surface layers. The width of this band approximates the diameter of the laser beam. With continued exposure to the defocused beam, further tensile stresses develop, ultimately surpassing the glass's strength and leading to crack formation.

A method for creating through-holes in glass is proposed in [102]. This invention fundamentally involves the process of heating a localized area of material using YAG-laser radiation, followed by the cooling of the irradiated zone. The glass is subjected to heating at a temperature exceeding the softening point across its entire thickness. The process of crack formation in [102, p. 2] is outlined as follows: "As the glass volume expands and "freezes" in the irradiation zone, residual thermoelastic stresses are generated, compressing within the local zone and stretching beyond it, leading to a crack along the line of maximum tensile stresses, encircling the local heating zone".

It is essential to focus specifically on the techniques of laser thermal cleaving that employ the interplay of laser radiation effects across various wavelengths. In an early contribution to this field, Lambert introduced a technique for double-beam laser cutting of glass in 1976 [133].

In the Soviet Union, the application of double-beam material processing technology was carried out to enhance the efficiency of laser cutting for dielectric materials featuring a metallized surface [134].

The concept proposed by Lambert was expanded upon in the studies conducted by C. Tsai [115, 119, 120]. The statement indicates that a system of microcracks develops on the surface of ceramics when subjected to focused YAG laser radiation, which subsequently evolve due to thermal stresses caused by the defocused beam of CO_2 laser radiation. The analysis of the aforementioned works leads to the conclusion that the processing methods that integrate laser scribing and through thermal cleaving exhibit the drawbacks associated with each of these techniques.

The double-beam method for segmenting a sheet of brittle material into fragments of desired geometry, as proposed in the invention [135], is noteworthy. This procedure unfolds in two distinct phases: first, the laser processing of the sheet is executed to create a scribing line, followed by a secondary laser processing that results in the formation of a fracture. The scribing process involves the localized effect of the pulsed laser beam on distinct segments of the scribing line, facilitating their heating followed by the cooling of these segments. The final cleaving is simultaneously conducted under the influence of CO_2 laser radiation functioning in continuous mode. The authors [135] employ supplementary cooling of the heated surface, integrating the techniques outlined in Tsai's works. Nonetheless, the edges produced by this cutting technique are marked by a quality that is not sufficiently high, attributed to the preliminary scribing process employed.

CHAPTER 2. NUMERICAL SIMULATION TECHNIQUES AND EXPERIMENTAL EQUIPMENT

2.1. Numerical simulation techniques

Considerable challenges encountered with analytical approaches to address thermoelasticity issues have led to the adoption of numerical techniques for simulating laser thermal cleaving processes. The finite element method (FEM) is particularly well-suited for these applications [136]. "The fundamental concept of the FEM is that any continuous quantity, like temperature or displacement, can be represented by a discrete model constructed from a collection of piecewise-continuous functions defined over a finite number of subregions" [136, c 10].

A variety of works, such as [136–139], outline the fundamentals of the FEM and its practical applications.

The application of the algorithm typically involves four steps [140]:

1) extraction of finite elements;
2) identification of the approximating function for each element;
3) integration of the finite elements into a cohesive ensemble;
4) calculation of the vector of nodal function values.

The key benefits of employing the FEM for calculating laser thermo-cleavage modes of brittle non-metallic materials within the framework of the phenomenological model described above include the following:

− consideration of the dependence of material properties on temperature during numerical simulation;

− simplification of the problem when using mixed boundary conditions;

− applicability of the method for composite materials;

− utilization of the FEM for solving problems involving bodies of arbitrary geometric shapes.

ANSYS software is one of the most renowned packages for finite element analysis, used for dealing with a diverse array of problems related to deformable solid mechanics, heat exchange and transfer, hydro aerodynamics, acoustics, and electrodynamics. This program serves as a toolkit designed for mathematical modelling and computational experimentation, incorporating efficient numerical methods for the execution of user-developed models [141, 142].

ANSYS software functions as an open system for programming, using the integrated APDL language alongside various high-level programming languages. The user can embed procedures and elements, modify and add menus, and connect message files to create custom programs.

Developing universal computer technologies internally is generally unfeasible and often impractical in many instances.

The exceptional quality of this software product is demonstrated by the inclusion of ANSYS software for finite element analysis in the roster of applications certified by the Software Certification Board of Gosatomnadzor (Federal Nuclear and Radiation Safety Authority) of Russia [143]. Calculations of the static stress-strain state of core elements and reactor equipment constructed from metals and alloys are advised to be conducted within the linear-elastic region, while also considering deformations such as plasticity and creep.

It is important to acknowledge the substantial volume of publications that showcase successful finite-element simulations of various laser technologies for materials processing, using the ANSYS software package. The outcomes of the simulation regarding laser thermohardening processes are detailed in [144]. It is important to emphasize the studies [115, 118–120], where ANSYS software was effectively implemented to compute the thermoelastic fields generated in brittle nonmetallic materials during the process of laser thermal cleaving.

The simulation of laser thermocleavage processes in ANSYS employs thermal-strength analysis tools that are relevant for strength analysis derived from the results of the thermal conductivity problem [145]. In ANSYS software, thermal and strength analyses are conducted in a sequential manner, aligning with the approach used to address the uncoupled thermoelasticity problem within a quasi-static framework.

In the application of the FEM within ANSYS for determining temperature fields, the matrix equation representing the heat transfer process can be expressed as follows [145]:

$$[C] \{T'\} + [K] \{T\} = \{Q\}, \tag{2.1}$$

where [C] is the specific heat capacity matrix;
      $\{T'\}$ is the time derivative of the temperature at the node;
      [K] is the effective thermal conductivity matrix;
      $\{T\}$ is the nodal temperature vector;
      $\{Q\}$ is the vector of effective heat flow at the node.

In this scenario, matrices [C] and [K] incorporate the temperature dependence of thermal conductivity and heat capacity of the material. Additionally, vector $\{Q\}$ accounts for the characteristics of the laser beam impact and the cooling effects on the material surface due to the refrigerant influence.

The determination of the temperature field represents the initial phase in the simulation of the laser thermal cleavage process. The subsequent step

of significant importance involves the assessment of thermoelastic stresses within the work material.

In [136], it is observed that the standard formulation of the FEM presumes the definition of the displacement field. Consequently, solving the problem requires the minimization of the system's potential energy. The resolvent equation for handling this problem in ANSYS software is expressed as follows:

$$[K]\{u\} = \{F\}, \qquad (2.2)$$

where [K] is the stiffness matrix;
$\qquad$ {F} is the nodal force vector;
$\qquad$ {u} is the nodal displacement vector.

When simulating laser thermal cleavage processes, the formation of the vector {F} is executed by considering the effects of deformation linked to the thermal expansion of the material during laser heating, as well as its compression in the area subjected to the refrigerant. Subsequently, the identified values of nodal displacements are used to ascertain the components of the stress tensor [136].

The main disadvantage of the FEM, along with any variational method, was highlighted in [138] as the challenge of acquiring a-priori estimates. The reliability can solely be assessed through testing for precise solutions.

In [146], a summary of three primary sources of error in the numerical solution of problems using the finite element method is presented:

− discretization error resulting from the approximation using basis functions;

− round-off error associated with the finite representation accuracy of numbers in computational devices;

− error in the mathematical model, stemming from its misalignment with physical reality.

Furthermore, it was observed in [147] that the origin of error is linked to the initial data, which is typically derived from experimental procedures; however, overall, the precision of the results obtained does not surpass the precision of the initial data [139].

Reference [141] indicates that round-off errors occurring during arithmetic operations on computers are less significant compared to the other types of errors mentioned previously; consequently, this source of errors will not be addressed further.

A primary issue in employing the FEM is the validation of the selected finite element size, as any numerical approach exhibits a dependence of the

findings on the nature of discretization [148]. The main reason for the FEM error that requires thorough examination is discretization error [146]. According to [149], employing coarse network models results in an underestimation of outcomes by 20 –40 % relative to the actual values.

A common practice of substantiating the convergence of the FEM to an exact solution involves comparing the numerical solution, performed with a large number of domain partition intervals, with the previous lower-order approximation. The proximity of the derived solutions acts as an indicator of the method's convergence [146]. As stated by [149], reducing the element size to a specific extent enhances the detail of the computational model and yields reliable results.

However, it is important to emphasize that the most effective method for verifying the accuracy of numerical simulation results is through comparison with precise analytical solutions [138].

To evaluate the error arising from the implementation of the chosen finite element model, the precise analytical solution [9] of the inhomogeneous linear heat conduction equation was used

$$\nabla^2 \cdot T(\vec{r},t) - \frac{1}{a} \cdot \frac{\partial T(\vec{r},t)}{\partial t} = \frac{-Q(\vec{r},t)}{\lambda} \qquad (2.3)$$

with a source

$$Q(\vec{r},t) = \gamma \cdot P_0 \cdot \exp\left[\frac{-(x-vt)^2 - (y)^2}{A^2} - \gamma z\right], \qquad (2.4)$$

which models the uniform motion of the laser beam along a straight line. In the above equations:

λ is the thermal conductivity of the material;

a is the thermal diffusivity of the material;

P_0 is the laser power density at the beam's center;

γ is the absorption constant of the medium;

v is the linear velocity of the laser beam;

R is the laser beam radius.

The Green's function for the thermal conductivity equation in a semi-infinite medium, considering heat transfer from the surface, is represented as follows [150]:

$$G(\vec{r},\vec{r}',\tau) = \frac{a}{8 \times \lambda (\pi \times a \times \tau)^{3/2}} \times \exp\left[\frac{-(y-y')^2 - (x-x')^2}{4 \times a \times \tau}\right] \times$$

$$\times \left\{ \exp\left[-\frac{(z-z')^2}{4 \times a \times \tau}\right] + \exp\left[-\frac{(z+z')^2}{4 \times a \times \tau}\right] - 2 \times h_0 \times \sqrt{\pi \times a \times \tau} \times \right. \qquad (2.5)$$

$$\left. \times erfc\left(\frac{(z+z')}{\sqrt{4 \times a \times \tau}} + h_{0\times}\sqrt{a \times \tau}\right) \times \exp\left[h_0 \times (z+z') + a \times h_0^2 \times \tau\right] \right\}.$$

Here, $h_0 = h/\lambda$ represents the relative heat-transfer coefficient (h is the heat-transfer coefficient), $\tau = t - t'$.

It is widely acknowledged [150, 151] that

$$T(\vec{r},t) = \int d^3\vec{r}' \int dt' G(\vec{r},\vec{r}',t-t') \cdot Q(\vec{r}',t'). \qquad (2.6)$$

The integration of equation (2.6) generates the subsequent expression for the temperature field:

$$T(\vec{r},t) = \frac{P_0 \cdot \gamma \cdot a \cdot R^2}{2 \cdot \lambda} \int_0^t dt' f(\vec{r},\tau), \qquad (2.7)$$

where

R is laser beam radius

$$f(\vec{r},t) = \frac{\exp\left\{\dfrac{-(x-v\cdot\tau)^2 - (y)^2)}{4\cdot a\cdot\tau + R^2}\right\}}{4\cdot a\cdot\tau + R^2} \times$$

$$\times \left\{ \exp(\gamma^2 \cdot a \cdot \tau - \gamma \cdot z) \cdot erfc(\gamma \cdot \sqrt{a\cdot\tau} - z/\sqrt{4\cdot a\cdot\tau}) + \right.$$

$$+ \frac{\gamma + h_0}{\gamma - h_0} \exp(\gamma^2 \cdot a \cdot \tau + \gamma \cdot z) \cdot erfc(\gamma \cdot \sqrt{a\cdot\tau} + z/\sqrt{4\cdot a\cdot\tau}) - \qquad (2.8)$$

$$\left. - \frac{2 \cdot h_0}{\gamma - h_0} \exp(h_0^2 \cdot a \cdot \tau + h_0 \cdot z) \cdot erfc(h_0 \cdot \sqrt{a\cdot\tau} + z/\sqrt{4\cdot a\cdot\tau}) \right\}.$$

As the absorption coefficient approaches infinity, the solution represented by equations (2.7) – (2.8) can be expressed as [9]:

$$T(\vec{r},t) = \frac{P_0 \cdot a \cdot R^2}{\lambda \cdot \pi^{1/2}} \int_0^t dt' f(\vec{r},\tau), \qquad (2.9)$$

where

$$f(\vec{r},t) = \frac{\exp\left\{\dfrac{-(x-v\cdot t')^2 - (y)^2}{4\cdot a\cdot \tau + R^2}\right\}}{(4\cdot a\cdot \tau + R^2)\cdot \sqrt{a\cdot \tau}} \times$$

$$\times \left\{ \begin{array}{l} \exp(\dfrac{-z^2}{4\cdot a\cdot \tau}) - h_0\cdot \pi\cdot \sqrt{a\cdot \tau}\cdot \\[2mm] \cdot erfc(\dfrac{z}{2\cdot \sqrt{a\cdot \tau}} + h_0\cdot \pi\cdot \sqrt{a\cdot \tau}) \\[2mm] \cdot \exp(h_0\cdot z + h_0^2\cdot a\cdot \tau) \end{array} \right\}. \qquad (2.10)$$

The derived exact analytical solution (2.9) was eventually employed to assess the validity of the finite-element simulation findings. The sufficiency of the acquired results was assessed by juxtaposing the maximum temperature values derived from the FEM with those based on the analytical solution (2.9).

The calculations were performed with the following parameters in mind: $P_0 = 2.238\cdot 10^6$ W/m^2, $R = 1.5\cdot 10^{-3}$ m, $v = 25\cdot 10^{-3}$ m/s. The characteristics of silicate sheet glass and alumina ceramics used for calculations are presented in Table 2.1. The calculations derived from expression (2.9) yielded a maximum temperature of 769.7 ˚K for sheet glass and 347.1 ˚K for polycore.

The verification results of the numerical simulation presented in Table 2.2 indicate that the finite element model demonstrates convergence to the exact solution as the element sizes are decreased. The discretization error is approximately 2 – 3.5 %.

Table 2.1 – Characteristics of various types of silicate glasses and alumina ceramics

Material properties	Sheet glass	Fused quartz	S52-1	Polycore (VK 100-1)	22XC (VK 94-1)
Density, kg/m^3	2450	2200	2390	3960	3860
Specific heat capacity, J/kg ·K	860	880	837	760	760
Thermal conductivity, W/m ·K	0.88	1.34	0.96	32.50	10.45
Thermal linear expansion coefficient, deg$^{-1}\cdot 10^{-7}$	89	5	52	75	80
Young's modulus, GPa	70	78	66	380	247
Poisson ratio	0.22	0.17	0.21	0.22	0.22

Table 2.2 –Parameters of finite element models and the results of the investigation into the accuracy of solutions

Material	Sheet glass	Sheet glass	Sheet glass	Polycore
Material type	Solid70	Solid70	Solid90	Solid90
Sample spacing, s	0.01	0.005	0.005	0.005
Element edge length in cutting plane, 10^{-3} m	0.25	0.125	0.125	0.125
Temperature peak, K	720.7	731.4	744.3	340.6
Percentage error, %	6.4	5.0	3.3	1.9

We will now focus on an additional source of error, namely, the error that is present in the mathematical model employed.

The thermal conductivity and heat capacity of silicate glass and alumina ceramics exhibit a notable dependence on the temperature of the material. Considering this dependence, the maximum temperature in the silicate glass sheet was determined to be 731.4 °K, which is lower than the previously calculated temperature of 637.7 °K that did not account for this dependence. Consequently, the previously used models for the laser thermocleavage process of silicate glass produced significantly overestimated temperature values in the laser irradiation zone. The error in the calculation of temperature fields was around 10 – 15 %.

The calculations conducted in [99] suggest that the energy flux density from the glass surface resulting from radiation at the glass transition temperature is approximately $3 \cdot 10^4$ W/m^2, while the flux density attributed to convective heat transfer remains below 25 W/m^2. In [31], power densities enclosed in the range of $0.3 \cdot 10^6$ W/m^2 to $20 \cdot 10^6$ W/m^2 were used for thermal cleaving. Thus, when determining the temperature fields generated during laser thermal cleaving, energy losses from the material surface due to radiation and convection can be neglected, with the exception of the region exposed to the refrigerant.

Furthermore, aside from the previously identified sources of error in the employed model, it is important to highlight that the uncoupled quasi-static formulation of the thermoelasticity problem is utilized for determining stress fields. The distinctive feature of this model for laser thermocleavage processes is the neglect of the interdependence between the strain field and the temperature field (the coupling effect), along with the disregard for dynamic effects resulting from the motion of solid particles during thermal expansion [152]. However, reference [9] presents a statement regarding the relatively small magnitude of the coupling effect and the dynamic effects observed during laser thermal cleaving.

The material fracture criterion employed in this study to elucidate the physical regularities of laser thermal cleaving of silicate glasses and alumina ceramics calls for particular attention. As previously noted, it is appropriate to use the tensile strength of specific types of silicate glass and alumina ceramics as a criterion for material fracture when simulating the relevant processes.

Thus, the criterion of maximum tensile stresses, first introduced by E. Ioffe [153, p. 193], is chosen as the main criterion for determining the direction of crack development in this study. As per this criterion, the laser micro-crack propagates in the direction perpendicular to the action of maximum tensile stresses. The propagation of a crack in the tensile zone is noted to halt its growth and may exhibit a tendency to "reflect" from the compression zone [154, p. 188].

Further enhancement of the accuracy in engineering calculations related to the laser thermocleavage process can be achieved through the application of fracture mechanics, specifically using the Griffiths-Irwin theory of crack formation. By examining laser thermal cleaving through this methodology, one can gain a clearer understanding of the temperature and stress values present in the processing area. This possibility arises from the disturbance in heat exchange between the material parts separated by a crack, with the tip of the moving crack serving as a source of heat [155, p.178]. In this scenario, as previously mentioned, there exists a concentration of stresses at the crack tip.

By employing the previously mentioned approach for simulating laser thermocleavage processes in this study, it was feasible to address the identified challenges and, primarily, to effectively ascertain the physical principles and characteristics associated with various forms of laser thermal cleaving of brittle materials. Simultaneously, to uncover the unique characteristics of microcrack formation under various laser thermal cleaving schemes, we utilized the spatial distributions of thermoelastic fields calculated for the processing modes. These modes are either detailed in existing literature [31] or have provided satisfactory results in our experiments.

2.2. Experimental test procedure

This work focuses on the processes involved in the laser separation of brittle nonmetallic materials, specifically those resulting from microcrack formation due to thermoelastic stresses. Therefore, the experimental study program encompassed measurements of the technological parameters associated with laser thermal cleaving and an analysis of the geometric characteristics of the resulting microcracks.

The primary factors impacting the process of laser thermal cleaving are the energy parameters of laser beams, including radiation power for continuous mode lasers, and radiation energy and pulse duration for pulsed mode lasers. Additionally, the size and shape of the beams on the surface of the material being processed play a significant role.

The average power and energy of laser radiation were measured with the IMO-2H meter consisting of a sensing head, a measurement unit, and a power attenuator (Figure 2.1). The specifications of the IMO-2H meter for average power and energy of laser radiation are given in Table 2.3, referenced from [156, p.64].

Figure 2.1 – Meter for average power and energy pulses of laser radiation IMO – 2H

Table 2.3 – IMO – 2H specifications

Operating wavelength, μm	1.06; 10.6
Power measurement range, W	$10^{-3} \div 10^2$
Energy measurement range, J	$10^{-2} \div 10^1$
Maximum beam diameter, mm	12
Basic error, %	7

The relative instability of the average power was calculated as a percentage using the following formula:

$$S_p = \frac{P_{max} - P_{min}}{P_{max} + P_{min}} \cdot 100,$$ (2.11)

26

where P_{max} and P_{min} are the maximum and minimum values of the average power obtained throughout the measurement process. The average power of the ILGN 802 laser exhibited a relative instability of 8 %.

The extinction coefficient [157] was determined by measuring the transmission of YAG laser radiation by wafers composed of alumina ceramics and silicate glasses of different thicknesses, using the IMO-2H meter as outlined in [158].

The intensity of laser radiation was initially measured following the method described in [158]. Afterwards, along the trajectory of the laser beam, which is orientated perpendicular to its direction, wafers composed of silicate glass or alumina ceramics with different thicknesses were positioned. The intensity of the transmitted radiation was subsequently measured.

The extinction coefficients were calculated by measuring the transmittance of the wafers in relation to their thickness, applying a formula that incorporates the radiation losses due to reflection from both surfaces:

$$I = I_0 \cdot (1 - R^2) \exp(-kl), \qquad (2.12)$$

where I_0 is the radiation intensity incident on the wafer surface;

I is the radiation intensity after the wafer transit;

R is the reflectance;

l is the wafer thickness.

The determined extinction coefficients for the YAG laser in sheet glass and polycore are 72 m^{-1} and 1560 m^{-1}, respectively, aligning well with the data presented in [158].

The velocity of the laser beam's relative motion and the material being processed was established in a programmatic manner. The refrigerant supply was controlled using a reducer equipped with a manometer.

The depth of laser cracks, along with the quality and accuracy of material separation into fragments, was assessed using a toolroom microscope BMI–1C (Figure 2.2).

The toolroom microscope's performance specifications are presented in Table 2.4.

Table 2.4 – BMI–1C performance specifications

Longitudinal measuring range, mm	$0 \div 150$
Traverse measuring range, mm	$0 \div 50$
Microscope magnification, diameters	10; 15; 30; 50
Basic error, μm	± 3

Figure 2.2 – Toolroom microscope BMI–1C

Figures 2.3 and 2.4 illustrate a standard end view of glass products produced through conventional processing and laser thermal cleaving methods.

The accuracy attained in the application of the splitting microcrack during the experimental studies was approximately 0.05 mm. This measurement was primarily influenced by the error associated with linear displacement and the positioning of the coordinate table.

The quality of the optical elements and the variability in the power of the generated laser radiation, attributed to the technical characteristics of the equipment, influenced the cutting accuracy.

Glass samples underwent strength testing via transverse bending and centrally-symmetric bending using an INSTRON 5567 testing machine. In the transverse bending tests, a total of 30 to 40 glass samples were used, each measuring 90x20x5 mm. The spacing between the supports for the bending tests was established at 60 mm. The indenter radius was set to 5 mm, and the displacement speed of the indenter was maintained at 0.05 mm/s. A total of 30 to 40 glass samples, each measuring 100x100x5 mm, were used for the centrally-symmetric bending strength tests. The ground ring had a radius of 20 mm, while the shaping ring had a radius of 10 mm. The displacement speed of the indenter was set at 0.05 mm/sec. The strength of the samples acquired through the controlled laser thermocleavage method was measured at 68.3 ± 4.8 MPa for transverse bending and 195.2 ± 4.0 MPa for centrally-symmetric bending.

The outcomes of the strength tests performed align well with the findings reported in [38], supporting the conclusion that using laser thermal cleaving enhances the strength of glass product edges when compared to the strength obtained through conventional cutting methods.
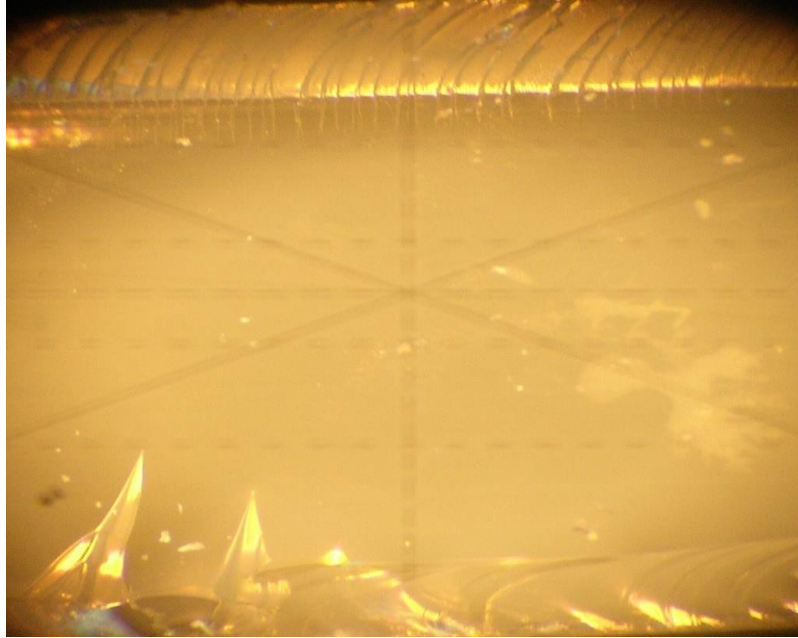

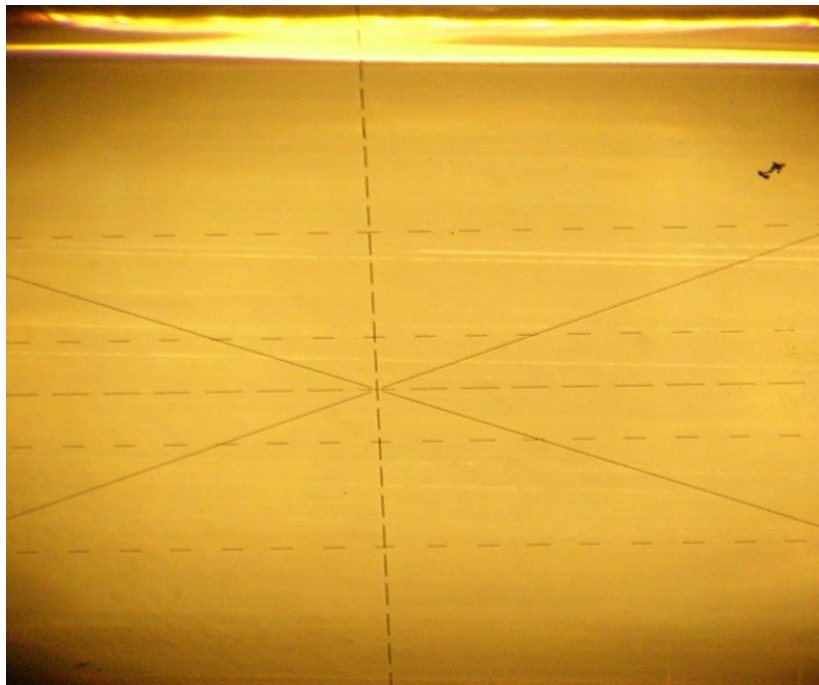Figure 2.3 − End view of a glass wafer when cutting with a diamond tool

Figure 2.4 − End view of a glass wafer during the cutting process
via controlled laser thermal cleaving

2.3. Laser beam machine equipment

To examine the mechanisms of laser thermal cleaving of brittle non-metallic materials, laser beam equipment was used, which was designed and developed with the applicant's involvement during the T-3 task "To develop and create technological complex for laser processing of materials and master its production" under the State Scientific and Technical Program "Laser Systems" [63, 70, 95].

The selection of a laser technology version for development and implementation, along with its application efficiency, is directly contingent upon the attributes of the fundamental laser equipment. Consequently, the development of laser beam equipment, incorporating YAG and CO_2 lasers, emerged as a critical objective, essential for providing technological support in the investigation of high-precision separation techniques of brittle non-metallic materials.

Throughout all operating modes of the device, process gas (mainly air) is used. The primary function of air is to protect the lens, while its secondary role involves creating an air-water mixture that acts as a refrigerant during the laser thermal cleaving of brittle non-metallic materials.

The device consists of a fixed assembly comprising two lasers and a coordinate table, which is governed by a computer numerical control (CNC) system (see Figures 2.5 and 2.6). The technical specifications of the machine, as outlined in Table 2.5, along with a detailed description of its components, are presented below.

The ILGN-802 emitter functions as a source of infrared radiation, characterized by a wavelength of 10.6 µm. The YAG KLT 00.03.00.000 SB emitter is composed of a quantron KLT 00.03.02.000 featuring an active element, a pulse pump lamp, and reflectors. It includes resonator components such as mirrors and holders, a shutter for radiation interruption, and a telescopic nozzle.

The ILGN-802 transmitter receives its power supply from the IPL-3 power supply source.

The equipment is constructed using the following structural assemblies:
Modul 1
– YAG emitter operating in a pulse mode (KLT 00.03.00.000);
– YAG laser power supply unit IPL-2-6000;
– cooling unit UO-1;
Modul 2
– ILGN-802 emitter operating in a continuous mode;
– CO_2 laser power supply unit IPL-3;
– cooling unit LSO-158A;

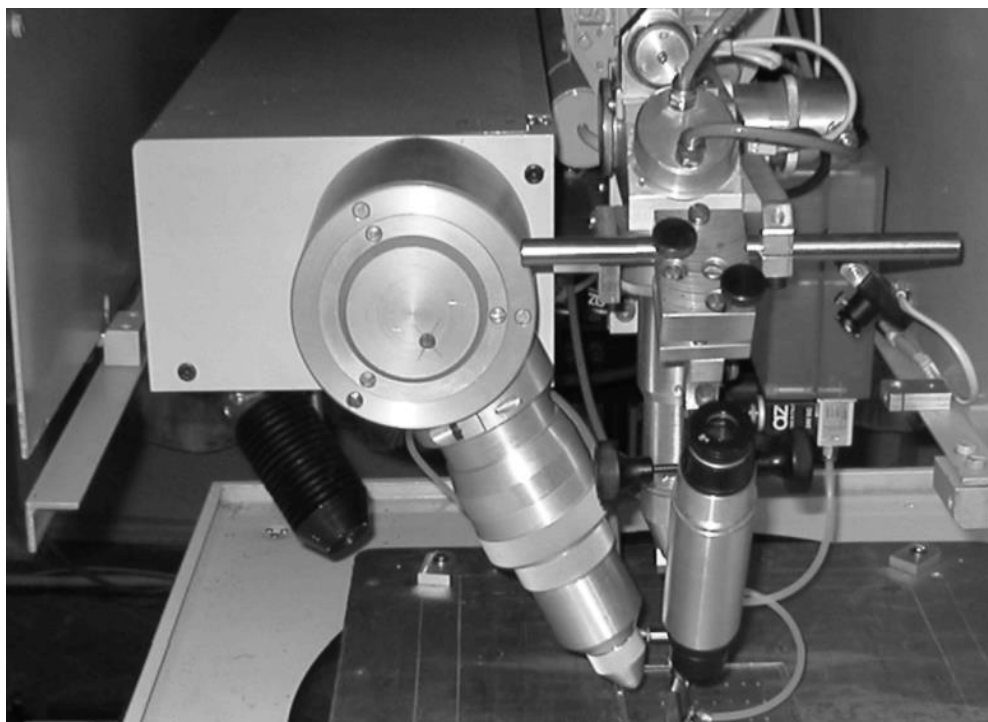Figure 2.5 – Assembled representation of laser beam machine equipment

Figure 2.6 – Overview of the operating area of the laser beam machine equipment

Table 2.5 – Specifications of the device

Wavelength of YAG laser radiation, µm	1.064
Pulse duration of YAG laser radiation, ms	0.5 ÷ 8
Range of YAG laser pulse repetition rate variation, Hz	1 ÷300
Maximum radiation energy in a YAG laser pulse, J	2 ÷ 30
Wavelength of CO_2 laser radiation, µm	10.6
Maximum power of CO_2 laser radiation, W	75
Continuous operation time of the device, h, min	4
Rotary table diameter, mm	500
Rotary table speed, rpm	0 ÷ 34
Maximum linear displacement along X and Y axes, mm	500
Accuracy of linear displacement along X and Y axes, mm	0.05
Maximum displacement speed along X and Y axes, mm/min	6000
Positioning accuracy, mm, max	0.05
Refrigerant	H_2O
Maximum power consumption from AC mains, kW	9
Weight of the workpiece, kg, max	5
Maximum mass of the device, kg, max	500
Length, mm	3500
Width, mm	3500
Height, mm	2000

Coordinate system
– coordinate table UKPT-2M;
– rotation unit KLT 02.06.000;
– laser rotation unit at 90° UPLI 90.00.00.000;
– casing KLT 00.02.00.000;
– video camera KRS S400;
– backlight unit TD 2.431.000;
– monitor MM-9M (TS-4410);
– CNC system SINUMERIC 802S;
– Pentium IV computer;
– control cabinet TS-8.

The IPL-2-6000 power supply unit is engineered for the synchronous generation of current pulses in the emitter lamps of the solid-state YAG laser model KLT 00.03.00.000, as well as for the management of its operating modes. The system delivers pumping power of up to 6000 W, allowing for frequency modulation of radiation in the range of $1 \div 300$ Hz, with pulse durations adjustable within $0.5 \div 8$ ms. The device UPLI 90.00.00.00.000 rotates the laser beam by 90°. This optical system comprises a configuration of lenses and mirrors.

The casing KLT 00.02.00.000 functions as a protective barrier against laser radiation exposure. The casing covers the laser housings and the laser beam rotation unit UPLI 90.00.00.00.000.

The KRS S400 video camera, MM-9M (TS-4410) monitor, and TD 2.431.000 backlight unit are used for the visualization of material processing.

The SINUMERIC 802S CNC system is engineered to manage stepper motors associated with the coordinate table (X, Y, φ coordinates), the stepper motor for the rotation unit, components of the pneumatic system, and protective shutters that obstruct the beam when it is essential to halt the supply of laser radiation to the processing area.

The computer is engineered to facilitate the execution of large-scale technological programs on machine equipment, which cannot be accomplished with the CNC system due to its RAM limitations. Additionally, it serves the purpose of storing and editing technological programs. The computer is capable of visualizing the processing zone and recording video information onto a hard disc.

The TS-8 control cabinet is a robust assembly designed to house the power supplies for both lasers and the cooling unit, the safety interlocking device, and components of the pneumatic system.

2.4. Experimental models of laser equipment

Experimental studies of double-beam laser thermocleavage processes were conducted using the advanced laser apparatus that was developed. Nonetheless, the design characteristics of the device hindered the successful execution of experimental studies in several instances, preventing the application of methodologies that could enhance the technology for high-precision separation of brittle nonmetallic materials.

This situation required the design and assembly of experimental setups for laser apparatus aimed at the relevant experimental investigations. In this instance, alongside the equipment provided, supplementary equipment was employed.

In conducting experimental studies, the CO_2 lasers LGN-703 and ILGN-709, along with the solid-state laser LTN-103, were utilized. The LGN-703 laser emitter produced radiation with an output power ranging from 30 to 40 W, while the ILGN-709 emitter generated radiation with an output power of 120 W, operating at a wavelength of 10.6 μm. The solid-state emitter LTN-103 is designed to generate radiation at a wavelength of 1.06 μm, allowing for a seamless adjustment of the output power in the range of 0 to 250 W.

Alongside the previously noted laser equipment, a five-axis stepper motor control device DSI-5 and a heat gun SKIL 8003 were used.

It is important to highlight that throughout the experimental process, several devices for laser thermal cleaving were developed and produced, with their availability being closely linked to the success of the research undertaken. The identified technical solutions have been secured through patents pertaining to utility models and methods for laser thermal cleaving of brittle nonmetallic materials [84–89].

A prototype of the setup developed by us [91] was used in order to investigate the impact of supplementary gas flows (specifically heated air) on the controlled laser thermocleavage process. Figure 2.7 provides a schematic representation of this setup.

The laser cutting model for brittle non-metallic materials includes the following components: CO_2 laser 1, focusing lens 2, coordinate table 3, defect application mechanism 4, refrigerant supply nozzle 5, heating and gas supply device 6 and vertical movement mechanism 7 with carriage 8. Focusing lens 2, defect application mechanism 4, refrigerant supply nozzle 5, and gas heating and supply device 6 are positioned on carriage 8. The setup is equipped with a coordinate table control unit 9.

The operation of unit 9 is managed through a process program that is input into computer 10. The designation 11 signifies a product composed of the material intended for processing.

The laser produces radiation that is extensively absorbed in the surface layers of the material undergoing processing (for the processing of silicate glasses and alumina ceramics, a CO_2 laser emitting radiation at a wavelength of 10.6 μm is used).
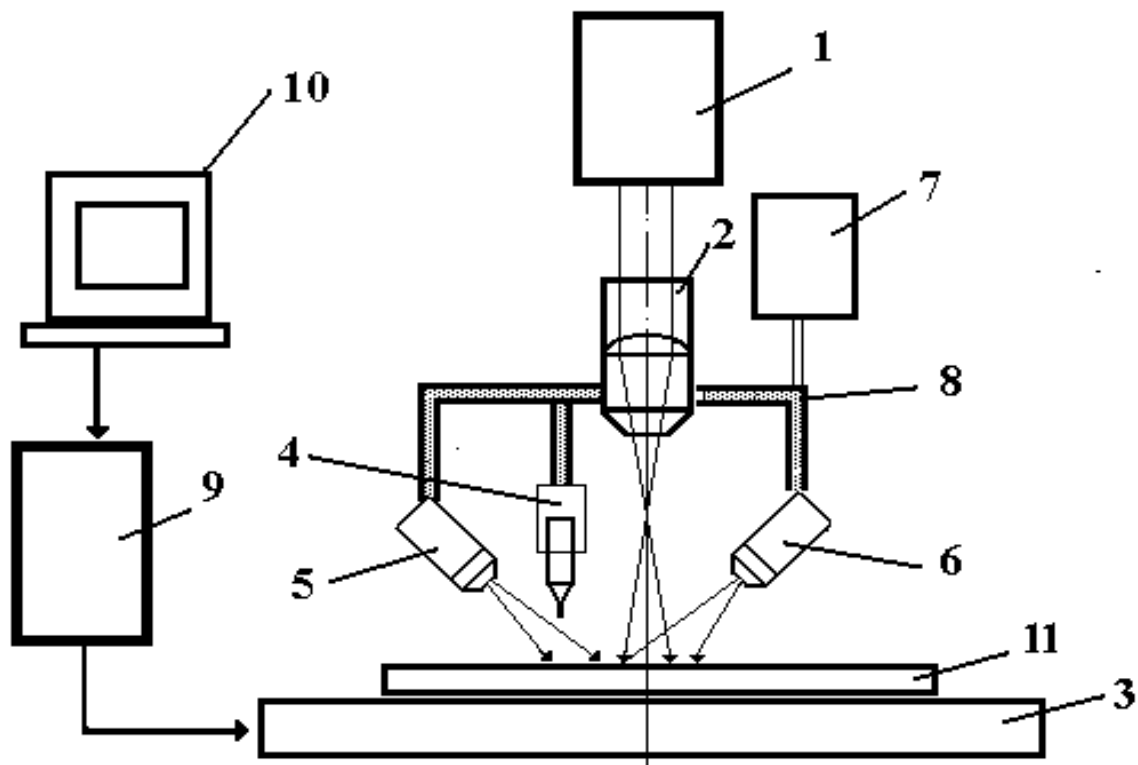
Figure 2.7 – Experimental model of the laser setup
for thermocleaving of brittle nonmetallic materials

A shutter (not depicted in Figure 2.7) is employed to prevent the irradiation of the sample, redirecting radiation away from the processing area during the process of positioning the product on the table, focusing the laser radiation, and fine-tuning the systems for delivering refrigerant, heated air, and the defect application mechanism.

The coordinate table promotes the relative displacement of laser beams and the workpiece within the horizontal plane. The mechanism for defect application is specifically engineered for the introduction of local defects along the thermocleavage line and features a device that facilitates the vertical movement of the cutter. The nozzle allows for the pressurized delivery of a fine air-water mixture into the processing area.

The heating and gas supply device is primarily designed for the extraction of refrigerant from the area subjected to laser radiation exposure. This device also offers preheating for the surface of the workpiece.

The computer software is adapted to modify the functioning of the control unit for the coordinate table and the vertical movement mechanism based on a predetermined technological program. This unit also regulates the refrigerant supply mechanism, manages the defect application mechanism, controls the heating and gas supply device, and adjusts the position of the damper that governs the laser radiation supply.

In order to explore the process of laser thermal cleaving along curvilinear trajectories, a prototype of a laser setup was used, characterized by the implementation of a five-coordinate control system of stepper drives [86]. Figure 2.8 presents a schematic diagram illustrating the model of this setup.
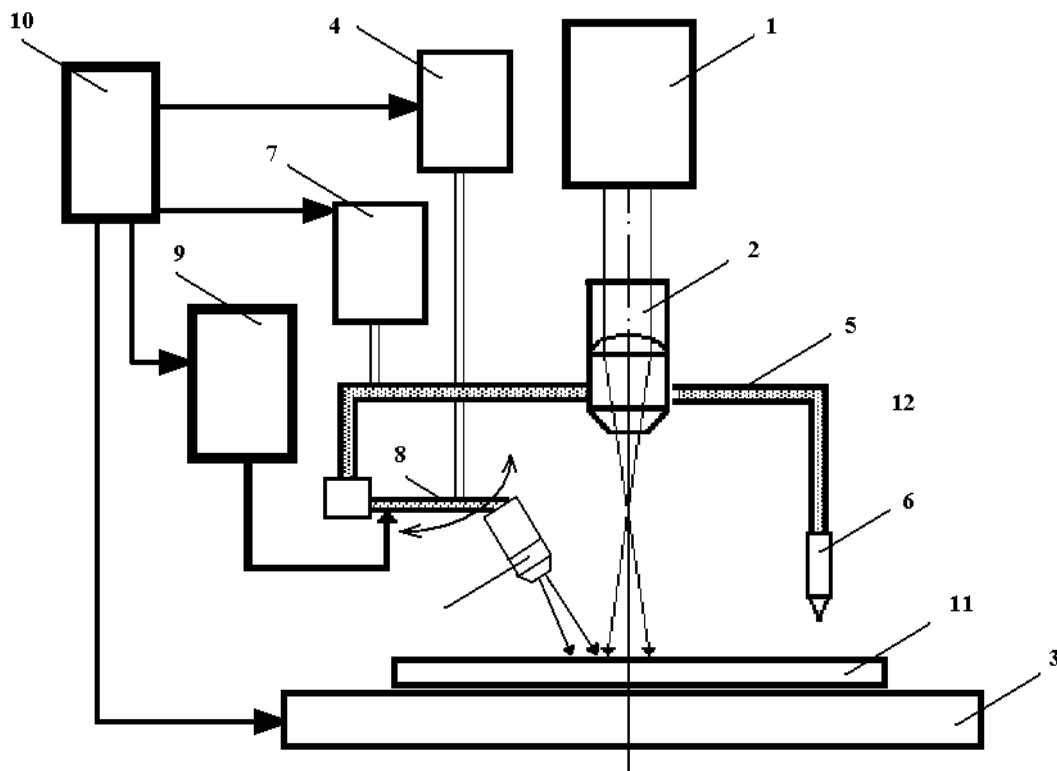
Figure 2.8 – Experimental model of the laser setup
for thermocleaving along curvilinear trajectories

The primary components of the prototype model include: CO_2 laser 1, focusing lens 2, coordinate table 3, vertical movement mechanism 4 with carriage 5, defect application mechanism 6, refrigerant supply unit 7, nozzle 8, and mechanism 9 for the horizontal movement of the nozzle, which ensures the cooling zone is positioned according to the specified horizontal coordinates. The configuration also includes a control unit 10. Position 11 specifies the product intended for processing.

The setup incorporates a mechanism for the horizontal movement of the nozzle, enabling independent motion and the direct supply of refrigerant to the laser radiation exposure line. This design enhances the precision of the splitting crack orientation along the laser radiation exposure line during cutting of curvilinear contours. The vertical movement mechanism enables the maintenance of optimal radiation power density during processing. This capability is crucial for the manufacturing of products from brittle non-metallic materials that are constrained by curvilinear contours of complex spatial shapes.

A prototype of the setup was created to study the processes of laser thermal cleaving of tubular-shaped brittle nonmetallic materials using various methods, including double-beam methods. The layout of the setup is illustrated in Figure 2.9 [84].
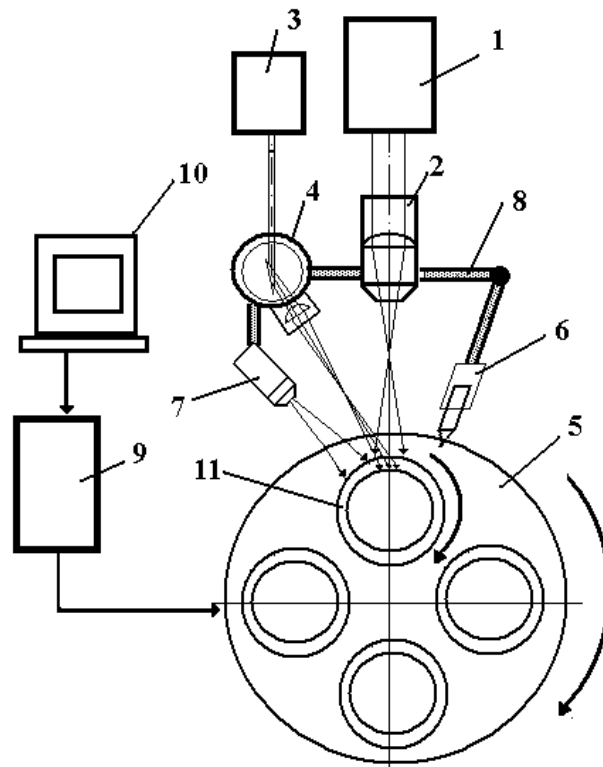

Figure 2.9 – Experimental model of the laser setup
for thermocleaving of tubular-shaped materials

The setup for laser cutting of brittle non-metallic tubular-shaped materials includes CO_2 laser 1, focusing lens 2, YAG laser 3, focusing lens 4, rotating drum 5, defect application mechanism 6, refrigerant feeder 7, and supporting bracket 8. The bracket 8 is equipped with focusing lenses 2 and 4, a defect application mechanism, and a refrigerant feeder. The setup includes a control unit 9. The control unit's operations are synchronised

through the technological program inputted into computer 10. Position 11 denotes a tubular product composed of the material designated for processing.

Laser 1 generates radiation at a wavelength that aligns with the surface absorption characteristics of the material designated for treatment. The radiation of laser 3 has a wavelength corresponding to the bulk absorption by the material. As previously mentioned, for the processing of silicate glass and alumina ceramics, it is appropriate to utilize a CO_2 laser emitting radiation at a wavelength of 10.6 microns as laser 1, and a YAG laser emitting radiation at a wavelength of 1.06 microns as laser 2.

The prototype model has lens 2, which is securely mounted on bracket 8 to focus the radiation from laser 1. In contrast, lens 4, intended for focusing the radiation from laser 3, is installed to allow for rotation. The rotating drum 5 is engineered for precise positioning of the work pieces 11 within the processing area. The individual work pieces 11 are sequentially positioned within the grooves of the drum 5. Simultaneously, the workpiece 11 situated in the working area undergoes rotation.

2.5. Properties of silicate glasses and alumina ceramics

The Terminology Commission of the USSR Academy of Sciences defined glass as "all amorphous bodies obtained by supercooling the melt, irrespective of their chemical composition and solidification temperature range, which, due to a gradual increase in viscosity, exhibit mechanical properties of solids, and the transition from liquid to glassy state should be reversible" [159 p.p.10].

Inorganic as well as organic substances can exist in a glassy form. The composition of inorganic glasses may encompass nearly all elements of the periodic table. Inorganic glasses can be classified into many categories based on their composition: elemental, oxide, halide, chalcogenide, and mixed [160, p. 130].

Oxide glasses are glasses primarily composed of oxygen-containing compounds. Oxide glasses are categorized into the following classes based on the type of glass-forming oxide: silicate glasses, borate glasses, phosphate glasses, germanate glasses, and borosilicate glasses.

Silicate glasses are the most significant oxide glasses, constituting 95 % of all mass-produced industrial glasses. In terms of prevalence, they are incomparable to glasses of other categories [159]. Silicate glasses are recognized as crucial technical materials, whose advancement and application significantly influence several fields of research and technology [161]. Reference [7] highlights the significant role of glass in electrovacuum manufacturing and instrumentation, using its superior vacuum, electrical insulation,

and thermal insulation qualities. Consequently, glass is extensively implemented in the production of structural components for electrovacuum and gas discharge devices, as well as in microelectronics.

As noted in [162], ceramics refer to any polycrystalline materials obtained through the sintering process of nonmetallic powders of natural or artificial origin.

A wide variety of ceramic materials exists, showcasing significant diversity. In [164, p. 5], a classification of ceramics is proposed, which is based on the presence of a specific chemical substance in the manufactured ceramic product, where the crystalline phase predominates in this type of ceramics.

This classification allows for the grouping of all existing types of ceramics into several primary classes:
 – ceramics composed of highly refractory oxides (oxide ceramics);
 – ceramics derived from silicates and aluminosilicates;
 – ceramics using titanium dioxide, titanates, zirconates, etc.;
 – spinel-based ceramics;
 – ceramics incorporating chromites of rare earth elements;
 – ceramics formulated from refractory oxygen-free compounds.

As observed in [164], among the diverse range of ceramic materials, oxide ceramics are the most widespread. Meanwhile, study [162] highlighted that the most important material for electronic engineering is alumina-oxide ceramics, which represent the most prevalent category of oxide ceramics. Alumina, or corundum, ceramics are polycrystalline materials primarily composed of aluminum oxide. This nomenclature is derived from the natural mineral corundum, which is essentially pure aluminum oxide, represented by the chemical formula Al_2O_3. In this context, "technical alumina ceramics are composed not solely of Al_2O_3; they may also include certain additives and impurities from raw materials. It is standard practice to refer to corundum ceramics as those containing 95 % or more Al_2O_3, with corundum being the primary crystalline phase" [163, p. 98].

In [163], it is found that alumina ceramics are extensively utilized across multiple technological domains, including radio-electronics, owing to their physical, mechanical, and electrophysical properties. The primary application area for alumina ceramics is in the production of integrated circuit substrates [162]. In [163], it is observed that following the development of transparent ceramics known as "Polycore", the scope of scientific and industrial applications for alumina ceramics was considerably broadened, particularly in the domains of aviation and space technology.

Thus, the choice of samples from silicate glasses and alumina-oxide ceramics as the main materials for studying the regularities of laser thermal cleavage processes is justified by the prevalence of these materials in various

applications. Both classes are recognized as common brittle nonmetallic materials utilized across numerous fields of human endeavor [7, 165]. This situation arises from the advantageous interplay of multiple technical properties of silicate glasses and alumina ceramics [160, 163].

Let us consider the main parameters characterizing the properties of silicate glasses and alumina ceramics. Understanding these parameters is essential for analyzing the physical principles underlying the laser thermo-cleavage processes of these materials. The parameters are as follows:

ρ is the density;

c is the specific heat capacity;

λ is the heat-conductivity coefficient;

α_T is the thermal linear expansion coefficient;

E is the Young's modulus;

ν is the Poisson ratio.

Table 2.1 [7] provides a summary of the properties of silicate glasses and alumina ceramics at room temperature.

The properties of materials are primarily influenced by their chemical composition, as detailed in Table 2.6 [7, 159]. The effect of each oxide on specific material properties is distinct and can be quantified by a numerical coefficient. The degree of influence of an oxide is proportional to its content in the material.

Table 2.6 – Chemical composition of certain types of silicate glasses and alumina ceramics

Material type	Chemical composition, %									
	SIO_2	AL_2O_3	MgO	Na_2O	CaO	K_2O	SO_3	Fe_2O_3	B_2O_3	Cr_2O_3
Sheet glass	71.7	2	4.1	14.6	6.7	0.32	0.5	0.08	–	–
Fused quartz	100	–	–	–	–	–	–	–	–	–
S52-1	68.7	3.5	–	4.4	–	4.4	–	–	19.0	–
Polycore (VK 100-1)	–	99.8	0.2	–	–	–	–	–	–	–
22XC (VK 94-1)	2.76	94.4	2.35	–	–	–	–	–	–	0.49

Given that laser thermal cleaving involves substantial temperature variations in the work material, it is essential to consider the temperature dependencies of various properties of silicate glasses and alumina ceramics when conducting numerical simulations within the context of the uncoupled quasi-static theory of thermoelasticity. The discussion pertains to the specific heat capacity and thermal conductivity of the materials previously mentioned.

The data presented in references [7, 165, 163, 166] indicates that the specific heat capacity of silicate glasses and alumina ceramics exhibits an increase as temperature rises. The specific heat capacity of silicate glasses is observed to increase by approximately 1.5 times from room temperature to the glass transition temperature. In contrast, the specific heat capacity of alumina ceramics increases by 1.3 times within the temperature range from room temperature to 1000 °C [7, 166].

According to reference [7], an increase in the temperature of silicate glasses from room temperature to the glass transition temperature results in an approximate twofold increase in their thermal conductivity. The thermal conductivity of alumina ceramics exhibits a significant reduction upon heating. Specifically, when the temperature varies from room temperature to 1000°C, a nearly fivefold decrease in thermal conductivity is recorded [163].

As shown by [7], the temperature dependence of additional characteristics of silicate glass and alumina ceramics is minimal and can be disregarded in future simulations of laser thermal cleaving processes.

The successful implementation of any laser thermal cleavage technology is contingent upon the occurrence of fracture resulting from the material's brittleness. With regard to reference [167], two primary types of fracture are identified: plastic and brittle. The initial emergence of these terms occurred as technical concepts applied in practice. In the context of physical theory, the phenomena of plastic and brittle fracture can be accurately described using the terms "shear fracture" and "cleavage fracture," respectively [163]. In [163], the brittleness of a material is characterized as the ratio of shear resistance to tensile strength. When the ratio exceeds one, the material is classified as brittle.

However, it should be noted that the brittleness of materials can be brittleness proper, both as a material property determined by the nature of interatomic interaction and the crystallochemical structure of the substance and as a brittle state of the material. The brittle state of a material is determined by such factors as the microstructure of the material and the conditions of its deformation. "Under certain external conditions (temperature, pressure), brittle materials acquire the ability to plastic deformation. This means that the rates of stress relaxation processes reach values not lower than the rate of application of these stresses" [130, c. 102].

Consequently, the temperature within the processing area during laser thermal cleaving must be restricted to levels that prevent the relaxation of thermoelastic stresses, which results from plastic deformation.

When determining the upper limit of permissible temperatures for glasses, select the glass transition temperature that corresponds to the specific type of glass. For silicate glass sheets, the glass transition temperature is 516 °C; for fused quartz, it is 1200 °C; and for glass S52-1, it is 522 °C [7].

In the case of alumina ceramics, the literature does not provide specific temperature values at which these materials transition to a plastic state. The complexity of the fracture mechanism in ceramic materials that include one or more crystalline phases, along with a glassy phase, is noteworthy [168]. Fracture may manifest either through the body of the glassy phase or along the crystalline structures. Under certain conditions, materials that possess a fully crystalline structure may experience fractures along grain boundaries while maintaining their overall integrity [163].

The condition for macroscopic plasticity of polycrystalline materials, as noted in [130], is the existence of multiple independent active slip systems. Simultaneously, it is noted that systems involving aluminum oxide are already present at approximately 1000 ˚C. Accordingly, it will be considered that for aluminum-oxide ceramics, the transition to the plastic state occurs at temperatures exceeding 1000 ˚C, which dictates the brittle fracture mechanism (separation) at temperatures below this threshold [130].

Given that laser thermal cleaving leads to brittle fracture, it is logical to utilize the tensile strength of specific silicate glass and alumina ceramics as a criterion for material fracture when modelling the associated processes.

It is important to note that strength refers to a material's ability to withstand mechanical failure [165]. Simultaneously, based on the magnitude of destructive loads, distinctions are made among tensile, bending, and compression strengths. It is observed in [165] that the strength of materials is influenced by the state of the product's surface, its dimensions, the surrounding environment, and temperature. Furthermore, it is found that the strength of glasses is influenced by their homogeneity, while the strength of ceramics is contingent upon their microstructure.

Theoretical estimates suggest that the strength value is approximately one tenth of the elastic modulus for the corresponding material [169]. The actual strength values are significantly lower. The theoretical strength of a solid body refers to the strength exhibited by a body possessing an ideal structure, free from damage and defects, at a temperature of absolute zero, subjected to quasi-static homogeneous tensile strain [169]. The theoretical strength of SiO_2 is approximately 10 GPa, while the theoretical strength of Al_2O_3 is 50 GPa [130].

The typical tensile strength values for silicate glasses range from 35 to 100 MPa, while for alumina ceramics, they range from 80 to 300 MPa [164, 163]. The low values of real strength can be explained by the Griffith

theory, which states that calculating the strength of a product requires consideration of microcracks on the surface and the significant stress concentration at the tips of these microcracks [130].

Reference [165] indicates that silicate glasses exhibit the lowest strength at a temperature of 200 °C. With rising temperatures, the strength of most ceramic materials notably diminishes; specifically, alumina ceramics experience a pronounced reduction in strength at temperatures exceeding 800 °C [163].

The durability of glasses and ceramics is influenced by the physical and chemical properties of the environment. Surface-active agents promote the development of pre-existing microcracks and contribute to the formation of additional ones. Water serves as an effective surface-active medium for silicate glasses and alumina ceramics [130, 165].

In accordance with [163], it is observed that the structural characteristics and porosity of ceramics play a significant role in determining their strength. The strength properties of ceramics decline as porosity increases, primarily due to the stress concentration surrounding the pores. Generally, fine-grained ceramics exhibit superior strength compared to coarse-grained ceramics, a phenomenon attributed to the reduced stress levels present at the grain boundaries. Defects and inhomogeneities in glass lead to a notable reduction in its strength [165].

CHAPTER 3. SIMULATION OF SINGLE-BEAM LASER THERMOCLEAVAGE PROCESSES AND DEVELOPMENT OF A SCHEME TO ENHANCE ITS STABILITY

3.1. Examination of the process underlying the production of splitting microcracks during controlled laser thermal cleaving

To clarify the mechanisms of laser thermal cleaving implemented by various technologies, the temperature and stress fields were computed for each version utilizing the finite element approach. The following presents the outcomes of simulating the processing of brittle nonmetallic materials using the CLT method and the through-the-thickness laser thermocleaving technique [63]. The technological parameters determined during experimental investigations of brittle nonmetallic material separation via the CLT method (using an air-water mixture as a refrigerant) and the through-the-thickness laser thermocleaving method are employed in the calculations (Table 3.1). Figure 3.1 illustrates the arrangement of laser beams and the refrigerant in accordance with the experimental settings.

Table 3.1 – Modes for laser thermal cleaving of silicate glass

Cross section shape and laser beam parameters	Refrigerant supply	Sample dimensions, mm		Cutting speed, mm/s	Laser power density, W/m^2
		thickness	transverse dimensions		
Circle R = 1.8 mm	absent	3	30x20	9	$1.57 \cdot 10^6$
	present			15	$1.57 \cdot 10^6$
Ellipse A = 9 mm B = 2.2 mm	absent			17	$1.28 \cdot 10^6$
	present			27	$1.28 \cdot 10^6$

The calculations employed the properties of sheet glass as presented in Table 2.1. The relationships between the coefficients of heat conductivity and specific heat capacity with respect to temperature were considered.

Furthermore, it was presumed that the parameters employed for the air-water mixture supply facilitated the cooling of the glass surface, with a heat transfer coefficient of 6800 W/m^2K [152].

Figure 3.2 shows the relationship between the stresses σ_{yy}, which act perpendicular to the separation plane, and the distance from the center of the laser beam section on the surface of the work material. The graphs exhibit a resemblance to the time sweep graphs of stress fields σ_{yy} at a specific point on the sample surface.
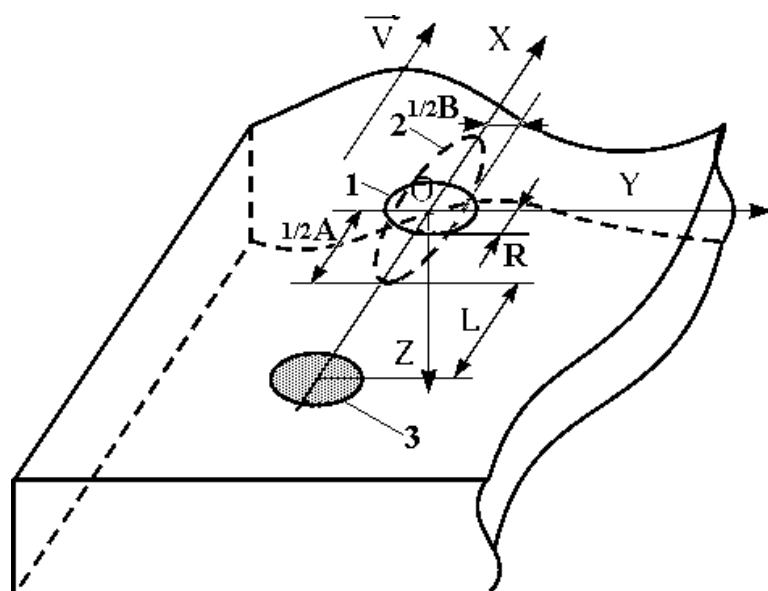
Figure 3.1 – Arrangement of laser beams and a refrigerant in the processing area
1 is the circular cross-section laser beam;
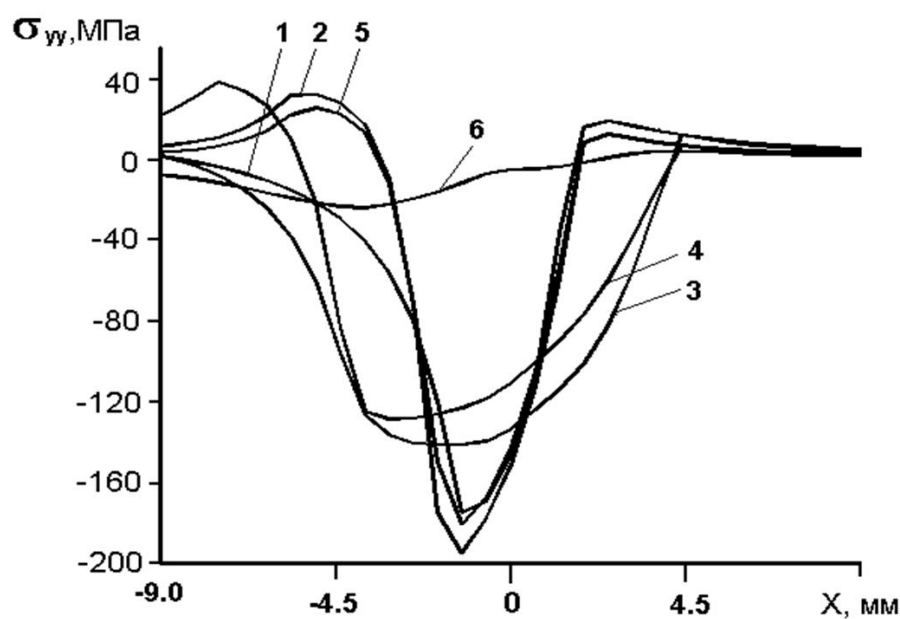2 is the elliptical cross-section laser beam; 3 is the refrigerant

Figure 3.2 – Stresses σ_{yy} on the material surface versus the distance
to the laser beam cross-section center

1 is the through-the-thickness thermocleaving with a circular cross-section beam at (Y=0); 2 is the CLT, with a circular cross-section beam at (Y=0); 3 is the through-the-thickness thermocleaving, with an elliptical cross-section beam at (Y=0); 4 is the CLT, with an elliptical cross-section beam at (Y=0); 5 is the CLT, with a circular cross-section beam at (Y=1 mm); 6 is the CLT, with an elliptical cross-section beam at (Y=1 mm)

Figure 3.3 presents the distribution of stress fields σ_{yy} in the separation plane of silicate glass when the material is exposed to laser radiation alone (through-the-thickness thermocleavage mode). Figure 3.4 illustrates the specified dependence obtained when the work material is subjected to both laser radiation and refrigerant simultaneously.
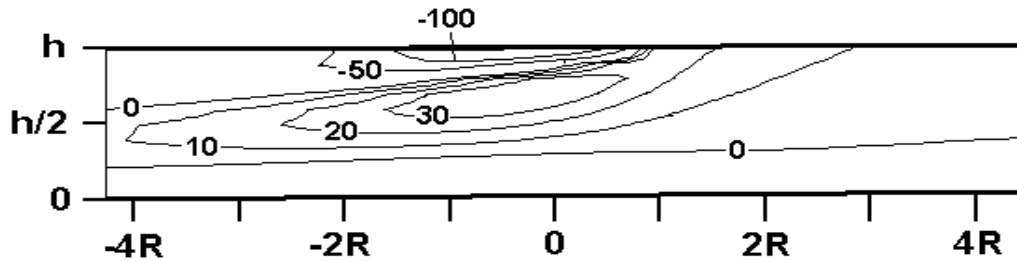

Figure 3.3 – Stress distribution σ_{yy} in the separation plane, MPa
(Through-the-thickness thermocleaving when exposed
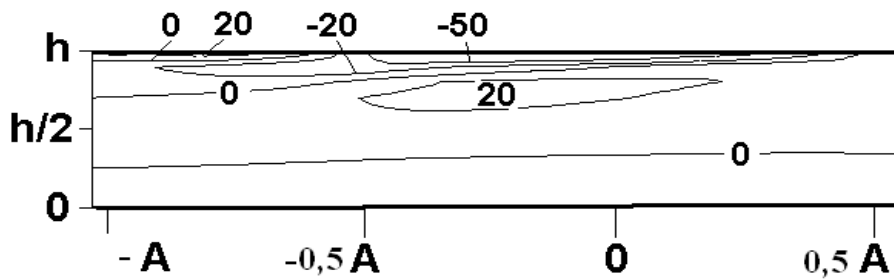to a circular cross-section beam)

Figure 3.4 – Stress distribution σ_{yy} in the separation plane, MPa
(CLT when exposed to an elliptical cross-section beam)

Comparing Figures 3.3 and 3.4 reveals that a notable compressive stress zone develops at the laser beam impact point in both cases, enveloped by a tensile stress zone at the front and depth of the material.

At CLT (Figure 3.4), unlike the mode of through-the-thickness thermal cleaving (Figure 3.3), an additional tensile stress zone is established in the upper layers of the sample, with its position influenced by the localization of the refrigerant exposure. This tensile stress zone is constrained by the compressive stress zone created by the laser beam.

Through the analysis of the distribution of thermoelastic fields, it was found that the initiation of the splitting microcrack occurs in the surface layers of the material from a crack-like defect in the microstructure within the tensile stress zone created due to the refrigerant supply. Further, the initial microcrack starts its movement and propagates to the compressive stress zone formed by laser radiation. Subsequently, the unsteady crack growth stops, and its further propagation is determined by the change in the spatial

distribution of tensile and compressive stress zones due to the mutual movement of the work material, laser beam and refrigerant.

Thus, the distribution of compressive stresses in the sample volume determines the shape and depth of microcrack development, the initialization and development of which occurs in the tensile stress zone generated in the refrigerant impact zone.

3.2. Analysis of the mechanism involved in the formation of a splitting microcrack during parallel laser thermal cleaving

Parallel laser thermal cleaving is a specific type of laser thermal cleaving characterized by the formation of a splitting crack that propagates parallel to the flat surface of the material being processed (Figure 3.5). During experimental studies, parallel laser thermal cleaving is performed by directing a laser beam onto the workpiece. The elliptical cross-section of the beam is aligned with its minor axis parallel to the movement direction of the laser beam in relation to the glass wafer (Figure 3.6).
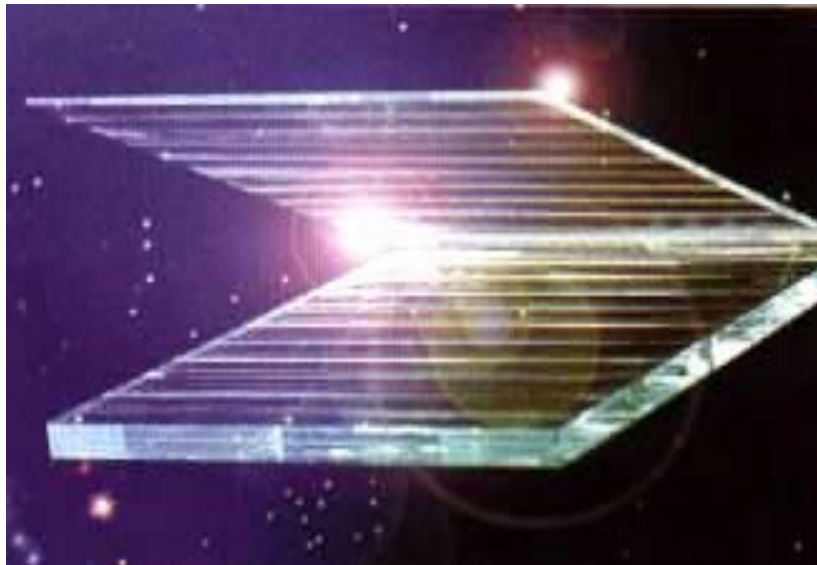

Figure 3.5 – Visual representation of a glass wafer produced
via parallel laser thermal cleaving [124]

The study focused on the characteristics of crack formation and progression along the surface, examining the distribution of thermoelastic fields generated in glass when subjected to heating by a laser beam with an elliptical cross-section, aligned with the minor axis in the direction of displacement [59]. The calculations were performed using the characteristics of silicate glass sheet given in Section 2.1. The thickness of the wafer was assumed to be h = 2 mm, the velocity of relative displacement of the laser

beam and the glass wafer $V = 16 \cdot 10^{-3}$ m/s. Calculations were performed with the following parameters of the laser beam of elliptical cross-section: major axis $B = 8 \cdot 10^{-3}$ m, minor axis $A = 1.2 \cdot 10^{-3}$ m, radiation power density $P_0 = 3 \cdot 10^6$ W/m^2.
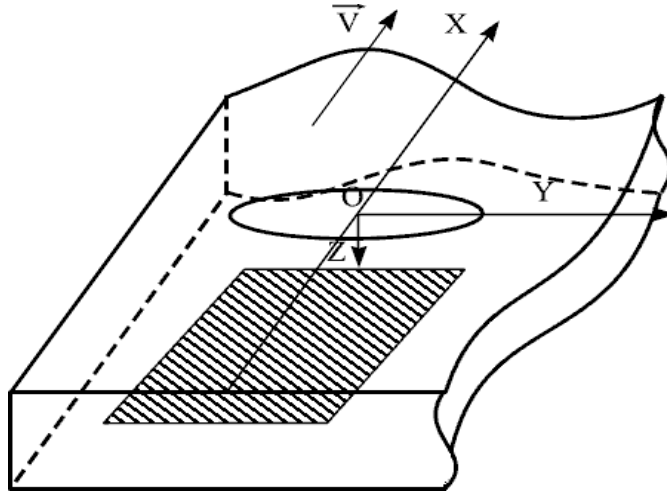

Figure 3.6 − Schematic illustrating the development of a splitting crack, parallel to the surface

Figure 3.7 illustrates the distribution of temperature fields created in the analyzed sample under the specified conditions. The solid lines represent isotherms corresponding to the temperature values indicated in the figures. The highest local temperature within the analyzed sample remains below the glass transition temperature, which is essential for effective glass separation through laser thermal cleaving.
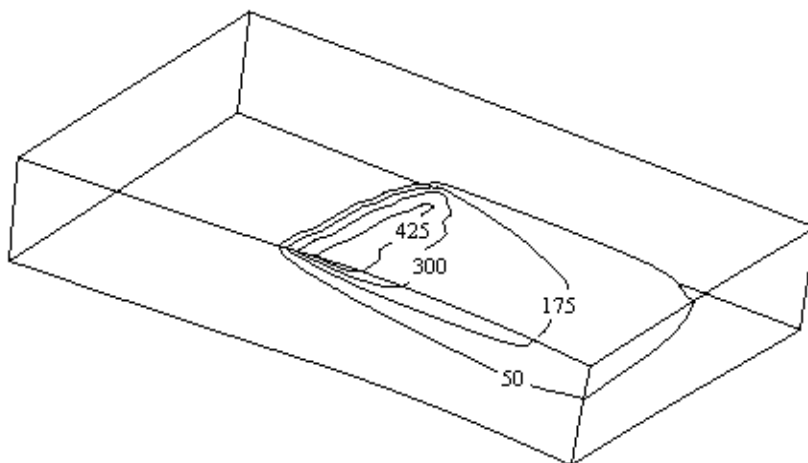

Figure 3.7 − Computational temperature distribution during parallel thermal cleaving, °C

Figure 3.8 shows the distribution of stress fields σ_{zz} that act perpendicular to the surface of the sample. A compressive stress zone is observed to form in front of the center of the elliptical laser beam. A tensile stress zone is established within the material, specifically at the depth corresponding to the backward displacement from the center of the elliptical cross-section of the laser beam. The magnitude of these stresses has the potential to initiate crack formation.
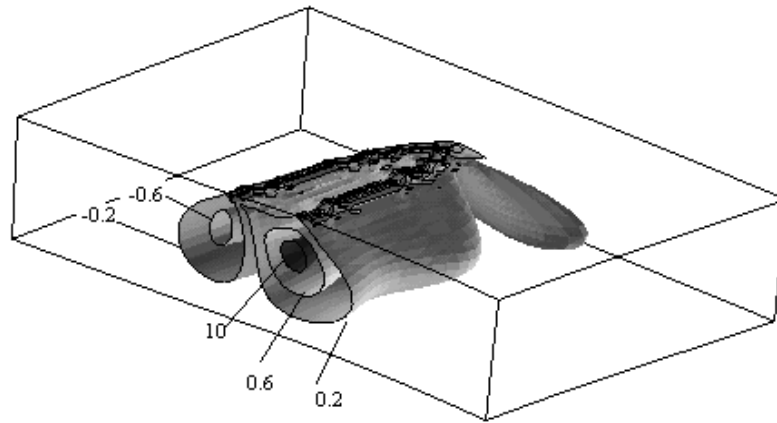

Figure 3.8 – Computational distribution of stresses σ_{zz}
during parallel thermal cleaving, MPa

It is important to highlight that, as suggested in [10], to enhance the probability of a crack developing parallel to the surface, it is beneficial to start its progression from an inclined microcrack situated at the appropriate depth. This recommendation arises from the observation that the strength of glass diminishes considerably when a microcrack appears, leading to tensile thermal stresses within the material that are sufficient for thermal delamination. Figure 3.9 demonstrates that, at the specified values of laser beam parameters, tensile stresses attain their peak at a depth of 0.5 mm.

In this scenario, a lag of their maximum from the center of the elliptical laser beam is observed at A/2, which subsequently results in the lag of the splitting crack noted in the experiment [10]. As the distance from the vertical plane that intersects the minor axis of the elliptical laser beam (Y = 0) increases, a gradual shift of the stress maximum towards the surface of the work material is noticed (Figure 3.10). This phenomenon accounts for the deflection spotted in the experimentally obtained cracks [10].

Figure 3.11 demonstrates that the tensile stresses σ_{yy} on the surface attain values around 20 MPa. It is important to note that the laser beam is shaped like an ellipse, with its minor axis aligned in the direction of displacement.
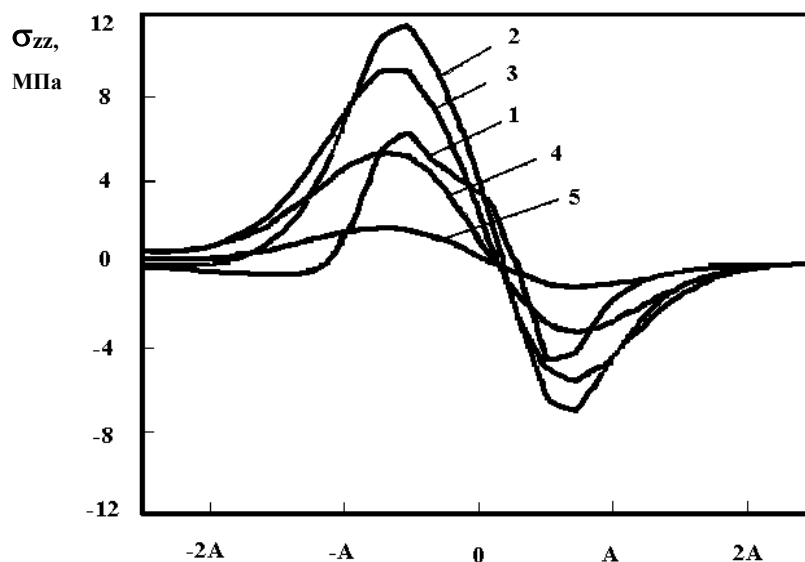
Figure 3.9 – Stresses σ_{zz} versus distance to the center of cross section
for the elliptical laser beam at Y = 0 mm
1 – Z = 0.2 mm; 2 – Z = 0.5 mm; 3 – Z = 0.8 mm; 4 – Z = 1.1 mm; 5 – Z = 1.3 mm

Figure 3.10 – Stresses σ_{zz} versus to the center of cross section
for the elliptical laser beam at Y = 4 mm
1 – Z = 0.2 mm; 2 – Z = 0.5 mm; 3 – Z = 0.8 mm; 4 – Z = 1.1 mm; 5 – Z = 1.3 mm

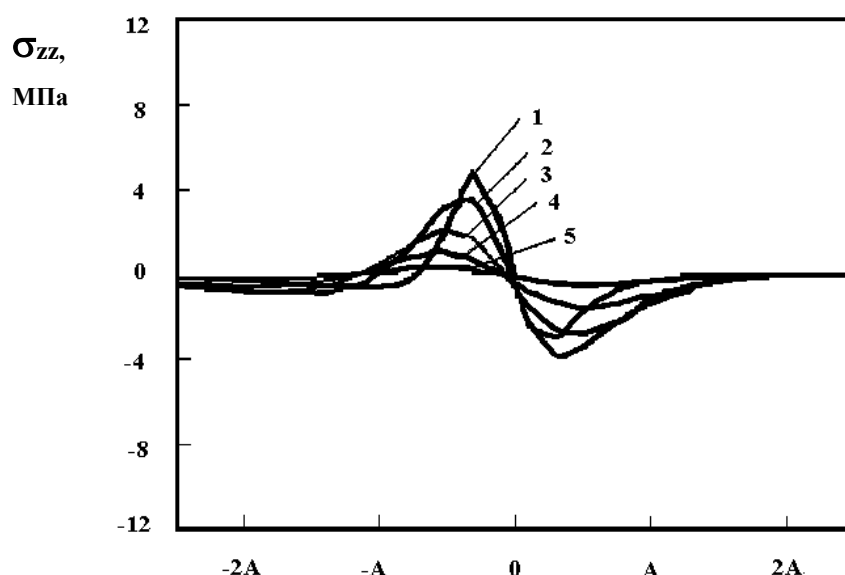Thus, the effective stress area σ_{zz} and the resulting stress on the sample in the direction perpendicular to the sample surface are higher than in the plane that intersects the minor axis of the elliptical laser beam. In this case, the process of through-the-thickness thermocleaving is a noticeable competition to the process of thermal cleaving. In practice, this is evident in the fact that even at minor deviations from the specified mode, thermal delamination evolves into through-the-thickness thermal cleaving [10].
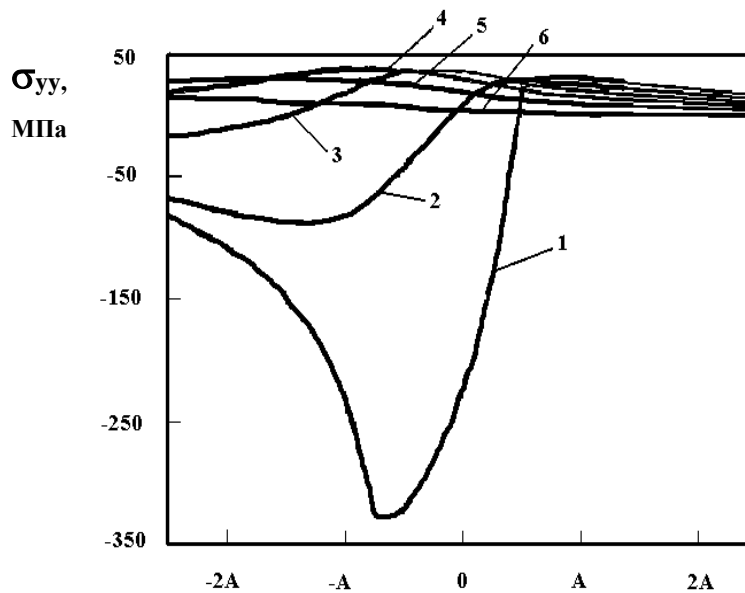
Figure 3.11 – Stresses σ_{yy} versus distance to the center of cross section
for the elliptical laser beam at Y = 0 mm
1 – Z = 0; 2 – Z = 0.2 mm; 3 – Z = 0.4 mm; 4 – Z = 0.6 mm;
5 – Z = 0.8 mm; 6 – Z = 1.1 mm

3.3. Laser separation through the controlled laser thermocleavage technique on quartz glasses synthesized via the sol-gel method

The advancement of contemporary industrial production requires the creation of not only innovative materials but also suitable technologies for their processing. Recently, the synthesis of quartz glasses using the sol-gel method has gained significant popularity. The sol-gel method enables the production of highly pure and activated quartz glasses, which are suitable for applications in fiber optics, optoelectronics, and laser technology [170]. In this connection, it seems relevant to investigate the potential application of CLT for cutting quartz glasses produced through the sol-gel method. It is important to highlight that the properties of these glasses closely resemble those of fused silica glass (Table 3.2). However, at the submicron scale, their structure differs from the structure of fused silica glass by greater randomness and a large number of defects [171]. Therefore, additional research is required prior to the application of CLT for cutting quartz glasses produced via sol-gel technology.

The analysis of literature regarding the dimensional processing of brittle nonmetallic materials in [2] revealed that gas-laser cutting is extensively utilized for cutting quartz glass. Nonetheless, the application of this technology entails significant energy expenses and lacks a high degree of precision. Furthermore, following the gas-laser cutting of quartz glass, it is necessary to conduct additional annealing of the products to eliminate any residual thermal stresses [2].

51

Table 3.2 – Properties of quartz sol-gel glasses

Glass parameter	Sol-gel glass
Density, kg/m^3	2201
Specific heat capacity, J/ kg·K	250
Thermal conductivity, W/m·K	0.7
thermal linear expansion coefficient, deg^{-1}·10^{-7}	5.7
Young's modulus, GPa	73
Poisson ratio	0.16

The high thermal stability of quartz glass (the coefficient of linear thermal expansion of quartz glass is an order of magnitude less than that of most industrial silicate glasses [7, 165]) complicates its separation via thermal cleaving. Nevertheless, research [10] indicated the successful implementation of laser thermal cleaving for cutting quartz glasses. It is noted that thermal cleaving of quartz glass can be realized both with and without a refrigerant.

The processing of quartz glass without refrigerant is achieved using a laser beam with an elliptical cross-section. The minor axis of the beam is aligned with the direction of movement. This method resembles the parallel laser thermal cleaving technique illustrated in Figure 3.6. However, it was demonstrated in [2] that this option of laser thermal cleaving of quartz glass exhibits low cutting accuracy, a feature typical of through-the-thickness laser thermal cleaving.

The study highlighted in [2] indicates that the processing option employing a circular laser beam for heating the cutting line, paired with sharp local cooling of the heating zone, demonstrates significantly greater effectiveness. In comparison to the previously discussed option, using CLT alongside a circular laser beam enhances the stability of the separation process, resulting in a twofold increase in processing speed and an accuracy improvement ranging from three to nine times [2].

We conducted experimental studies on the thermal cleaving processes of quartz gel glasses, utilizing this specific processing option where the positioning of the laser beam and refrigerant in the cutting plane coincides with the CLT scheme presented in Figure 3.1. [60, 64]. Thermal cleaving of quartz sol-gel wafers was conducted in the following manner. The quartz wafer designated for processing was maneuvered using a coordinate device in relation to the fixed laser emitter and a nozzle that supplied the refrigerant. The quartz surface was heated using CO_2 laser radiation. The heated surface of the glass underwent rapid cooling as it transitioned through the area of refrigerant exposure.

The experimental studies established the possibility in principle of generating a splitting microcrack in quartz sol-gel glass through the use of CLT.

Nonetheless, it is important to point out that the corresponding modes of microcracking exhibit increased sensitivity to the slightest variations in technological parameter values. This is evident in the experiment through the frequent failures of crack formation that occur with even minor deviations from the specified technological parameters during the processing mode.

To reveal the peculiarities of the CLT of sol-gel glasses according to the previously outlined methodology, a finite-element solution was conducted to address the distribution of thermoelastic fields in quartz wafers within the quasi-static formulation [60, 64]. The material parameters used in the calculations are provided in Tables 2.1 and 3.2. The calculations considered the relationship between the heat conductivity coefficient and specific heat capacity as a function of temperature [10, 165]. The technological parameters chosen for the calculations are presented in Table 3.3.

Table 3.3 – Technological parameters for laser processing of quartz sol-gel glass

Laser beam cross-section parameters	Laser power, W	Cutting speed, mm/s
Circle, R = 1 mm	35	60
Ellipse A = 3 mm, B = 1 mm	35	40

Calculations were performed for a wafer with geometric dimensions 20×10×0.5 mm.

Figure 3.12 illustrates the temperature fields generated in wafers of specified sizes during processing with laser beams of circular and elliptical cross-sections, while Figure 3.13 depicts the distribution of stresses σ_{yy} exerted in the material perpendicular to the cutting plane. Figure 3.12 reveals that both processing modes achieve comparable maximum temperatures, around 1200 °C, which is the maximum permissible for processing quartz glasses by the CLT method, as temperatures over this threshold render the glasses plastic [165].

Figure 3.13 shows a region of compressive stresses generated at the point of laser radiation exposure, which, when employing a circular cross-section beam, exhibits a greater stress magnitude and more pronounced localization in the separation plane.

Furthermore, Figure 3.13 demonstrates the formation of a tensile stress zone in the upper layers of the material, with its location dictated by the

refrigerant impact zone. This zone is constrained by the region of compressive stresses generated by the laser beam and is distinguished by marginally elevated values when employing a laser beam with an elliptical cross-section. In both options, the tensile stresses σ_{yy} acting perpendicular to the cutting plane are insufficient for the stable initiation of the splitting microcrack.
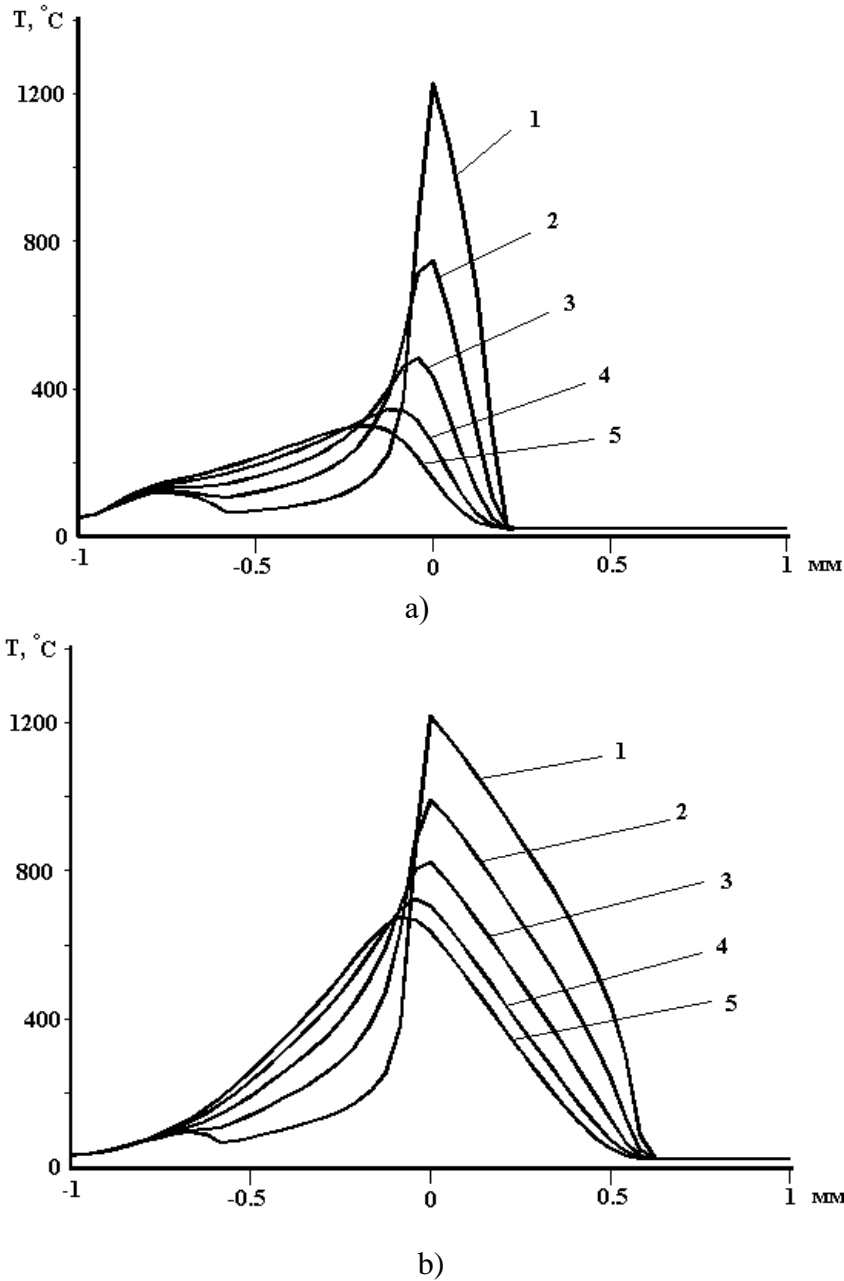

Figure 3.12 – Temperature as a function of distance
to the center of the laser beam cross-section
a) circular cross-section laser beam;
b) elliptical cross-section laser beam;
1 - Z = 0; 2 – Z = 0.1 mm; 3 – Z = 0.2 mm;
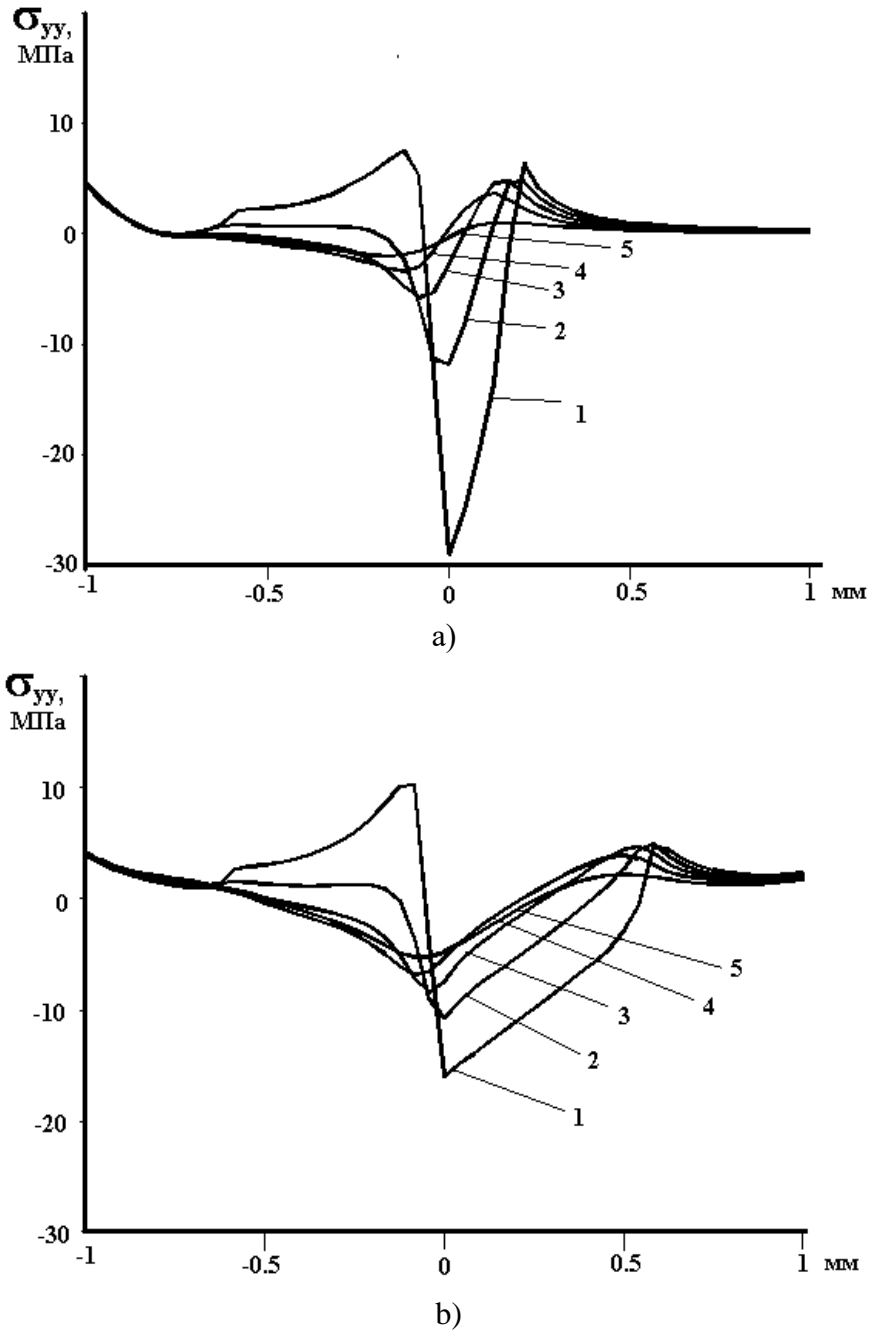4 – Z = 0.3 mm; 5 – Z = 0.4 mm

54

Figure 3.13 – Stresses σ_{yy} versus distance to the center
of the laser beam cross-section
a) circular cross-section laser beam;
b) elliptical cross-section laser beam;
1 - Z = 0; 2 – Z = 0.1 mm; 3 – Z = 0.2 mm;
4 – Z = 0.3 mm; 5 – Z = 0.4 mm

The analysis of thermoelastic field distribution indicates that the initiation of a splitting microcrack should occur in the tensile stress zone on the material's surface. In this scenario, additional technological operations are required to initiate the microcrack.

In [10], it is observed that the preliminary deposition of a defect on the surface of quartz glass is insufficient to attain the desired outcome, as it leads

to an increase in the proportion of absorbed energy within the damaged area and the subsequent melting of the defect. A successful solution for enhancing the reliability of microcrack nucleation is proposed in the same work.

The process involves the preliminary heat treatment of the quartz glass surface at the initial point of the trajectory using a stationary laser beam, followed by rapid cooling and the introduction of a defect in the refrigerant supply area. This method has yielded positive results in the processing of quartz sol-gel glasses.

Consequently, the research findings indicate that there are no significant differences in the separation of sol-gel-derived quartz glass and fused silica glass through laser thermal cleaving. The implementation of the thermocleavage process necessitates specific measures to facilitate the nucleation of a splitting microcrack.

3.4. Distinctive characteristics of laser thermal cleaving under the simultaneous influence of laser radiation, refrigerant, and hot airflow on the material surface

As stated in Chapter 1, a notable drawback of CLT is the limited reliability of the separation process, particularly in modes with a small distance from the boundary of the laser impact zone to the front of the cooling zone. Analysis of the CLT process revealed multiple factors contributing to the instability of cracking. The refrigerant's significant influence on the thermal-physical conditions within the laser impact zone leads to frequent failures in the development of splitting microcracks.

A consequence of this situation is that CLT does not ensure reliable separation when the splitting microcracks are positioned at a close distance from each other, such as in the production of miniature items. The development of the subsequent splitting microcrack is frequently halted when the refrigerant, residual from the deposition of previous microcracks, intersects with the impact trajectory of the laser beam.

According to reference [161], the impact of a liquid on the surface of heated glass results in the formation of a vapor film. During the subsequent cooling of the glass, the thickness of the film decreases. The liquid transitions from the film boiling stage to the nucleate boiling stage, followed by convection cooling. Simultaneously, both film and nucleate boiling exhibit a low heat transfer coefficient, attributed to the low thermal conductivity of steam. The same study highlights that the heat exchange process during the cooling of a heated glass surface by atomized liquid is primarily influenced by the hydrodynamics of the refrigerant as it flows over the material surface. This process is characterized by the formation of a thin liquid film that is

continuously renewed by the influx of new refrigerant. Under specific conditions, particularly when the refrigerant supply speed is sufficiently high, the liquid on the surface does not reach the boiling point. In this scenario, the heat exchange conditions on the surface are mainly determined by the flow rate of the liquid across the surface. The heat transfer coefficient is elevated when the atomized liquid impacts the glass surface at high velocities. The stability of heat transfer also depends on the velocity of the liquid. At lower velocities, the heat transfer mode exhibits instability, whereas at higher velocities, it becomes stable and can be adjusted.

Thus, an important factor is that on the cooling surface of the material, influenced by the refrigerant, there emerges not only a region characterized by stable intensive cooling but also a region exhibiting unstable weak cooling, which arises from the refrigerant's flow over the surface (Figure 3.14). Simultaneously, the pre-cooling of the material sections subjected to laser irradiation in this area demonstrates instability and a low cooling rate, attributed to the insufficiently high speed of liquid movement across the material surface, which consequently undermines the reliability of the cracking process.
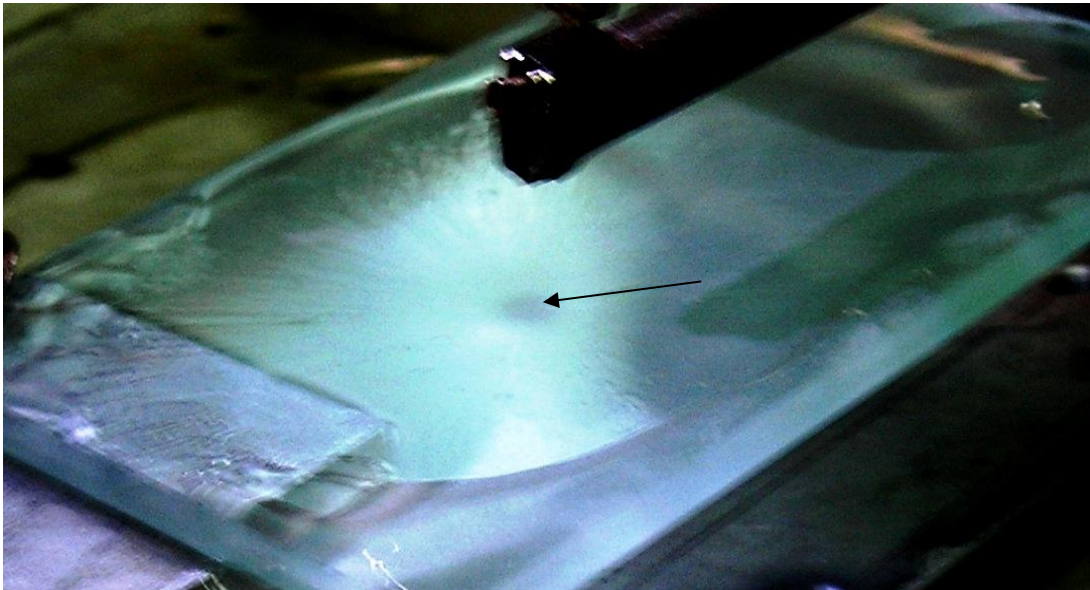

Figure 3.14 – Visual representation of glass wafers exposed to refrigerant

The arrow indicates the area of stable intensive cooling, which is surrounded by a liquid film generated from the refrigerant flowing over the surface

The identified drawbacks lead to the inefficiency of the technology in question, necessitating further investigation into the process and the formulation of a strategy aimed at enhancing the reliability and quality of the separation of brittle nonmetallic materials.

The findings from a series of studies demonstrated the rationale behind the combined effect of laser radiation, refrigerant, and hot airflow on the surface of materials [94].

Experimental investigations into laser cleaving processes were conducted using a prototype of a laser processing setup, as illustrated in Figure 2.5.

Figure 3.15 schematically illustrates the mutual arrangement of the laser radiation exposure area, the refrigerant-cooled zone, and the area heated by hot airflow, as used in the experiments [73].

Figure 3.15 includes the following components: 1 is the laser beam, 2 is the refrigerant, 3 is the hot airflow, 4 is the work piece composed of brittle non-metallic material. 5 is the laser beam cross-section in the cutting plane, 6 is the area of intense cooling by the refrigerant, 7 is the liquid film of the spreading refrigerant, 8 is the region of hot airflow. The horizontal arrow signifies the direction of product movement.
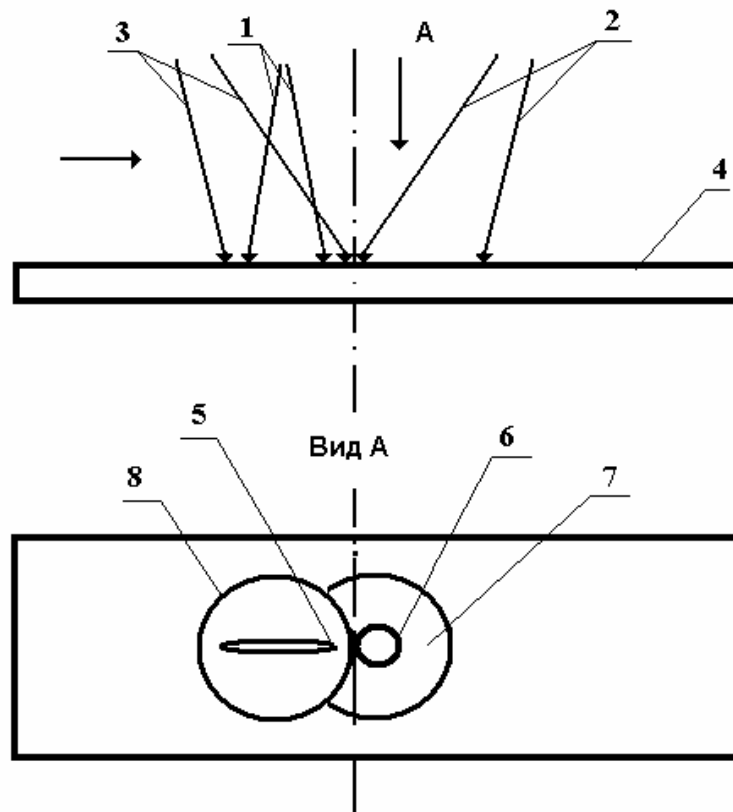

Figure 3.15 – Mutual arrangement of the laser radiation exposure area, cooling zone and the area heated by hot airflow

The separation of brittle nonmetallic materials is accomplished through the sequential execution of the operations detailed in the proposed processing scheme.

The initial blank is positioned on the coordinate table. A defect is introduced at the beginning of the processing line. Subsequently, the laser beam is directed to the segment of the processing contour that contains the deposited defect.

The product is afterwards transported along the processing line utilizing a coordinate table, which is aligned with the laser beam, heated air supply device, and nozzle. The absorption of laser radiation in the surface layer results in the heating of the wafer. The refrigerant is delivered to the zone that has been preheated through the application of laser radiation and the flow of hot air. Additionally, the area affected by the laser is situated within the zone influenced by the hot airflow. The glass wafer is concurrently subjected to heating from two surface heat sources: CO_2 laser radiation and a hot airflow, followed by cooling with the refrigerant. The refrigerant zone exerts a significant influence on the formation of temperature fields, facilitated by stable and intensive cooling.

In the course of the experiments, parallel separating cuts were made on M3 glass samples which had a thickness of $3 \div 5$ mm with a spacing of 5 mm between each cut. An ILGN-802 laser operating at a radiation wavelength equal to 10.6 microns and a radiation power of $40 \div 60$ W was used. During glass separation, the laser radiation was focused into beams of elliptical cross-section with a major axis of $A = 6 \div 12$ mm, and a minor axis of $B = 0.5 \div 2$ mm. The airflow was heated to a temperature of $200 \div 300$ °C before being introduced into the processing zone. The cutting speed of the samples was $10 \div 30$ mm/s.

Experimental studies revealed that the hot airflow removes the refrigerant from the laser beam impact zone, thereby preventing the introduction of additional refrigerant. This mechanism ensures the stabilization of thermophysical conditions within the laser impact zone.

To clarify the peculiarities of the CLT process influenced by the combined effects of laser radiation, refrigerant, and hot airflow on the material surface, we addressed the issue of thermoelastic field distribution through the application of the finite element method [94, 171].

The calculations were performed using the data regarding the properties of silicate glass sheet as outlined in Section 2.1, along with the specified parameters of the laser beam cross-section: major axis $A = 6 \cdot 10^{-3}$ m, minor axis $B = 1.4 \cdot 10^{-3}$ m; laser radiation power $P = 40$ W, diameter of the nozzle of the hot air supply device $D = 3$ mm, distance from the nozzle to the surface $Z = 10$ mm. The hot air temperature was set at 250 °C. An enhanced cooling zone was established in a circular form with a diameter of 3 mm. The calculations were carried out for a wafer with size dimensions of 24×12×3 mm. The traverse speed of the workpiece relative to the laser beams was assumed to be 10 mm/s.

Figure 3.16 illustrates the calculated temperature fields generated in the sample under study due to the treatment outlined in Figure 3.15, while Figure 3.17 depicts the corresponding distribution of stresses σ_{yy} acting perpendicular to the cutting plane. Figure 3.16 indicates that when the sample's surface is simultaneously subjected to laser radiation, refrigerant, and hot airflow, a localized area of elevated temperatures (approximately 500 °C) arises from the laser's influence. Additionally, a broader region on the material's surface exhibits temperatures ranging from 200 °C to 250 °C, which is attributed to the impact of the hot airflow.
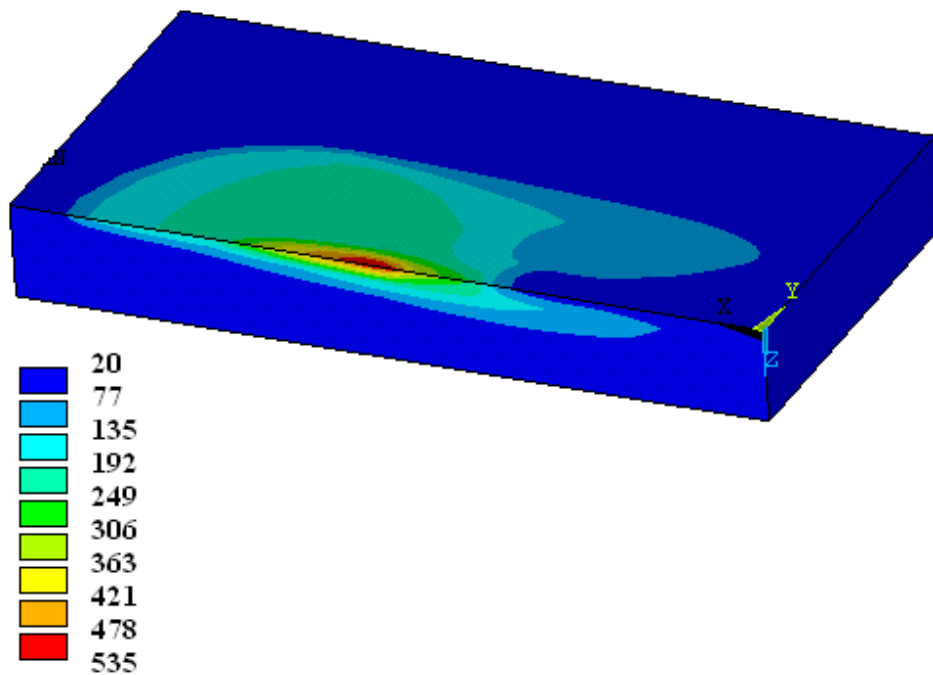

Figure 3.16 – Temperature distribution (°C) on the material surface resulting from the combined influence of laser radiation, hot airflow, and a refrigerant

Upon examining Figure 3.17, it becomes evident that the incorporation of hot airflow does not result in any significant variations in the spatial distribution of tensile and compressive stress zones when compared to the conditions observed at CLT. Consequently, it can be concluded that the mechanism underlying the formation and progression of the splitting microcrack is identical in both scenarios examined (Section 3.1).

Alongside the calculations of thermoelastic fields generated by the combined influence of laser radiation, refrigerant, and hot airflow on the material surface, analogous calculations were conducted for options that differed from the previous ones by the lack of hot gas flow.
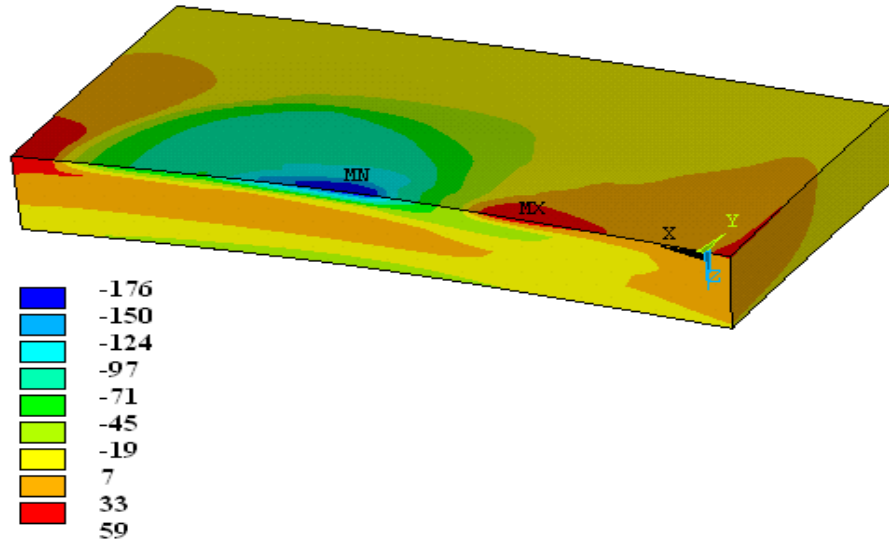
Figure 3.17 – Stress distribution σ_{yy} (MPa) on the material surface resulting from the combined influence of laser radiation, hot airflow, and a refrigerant

Figure 3.18 illustrates the relationship between the distribution of stresses σ_{yy}, which act perpendicular to the separation plane, and the distance to the centers of laser beam cross-sections on the sample surface.
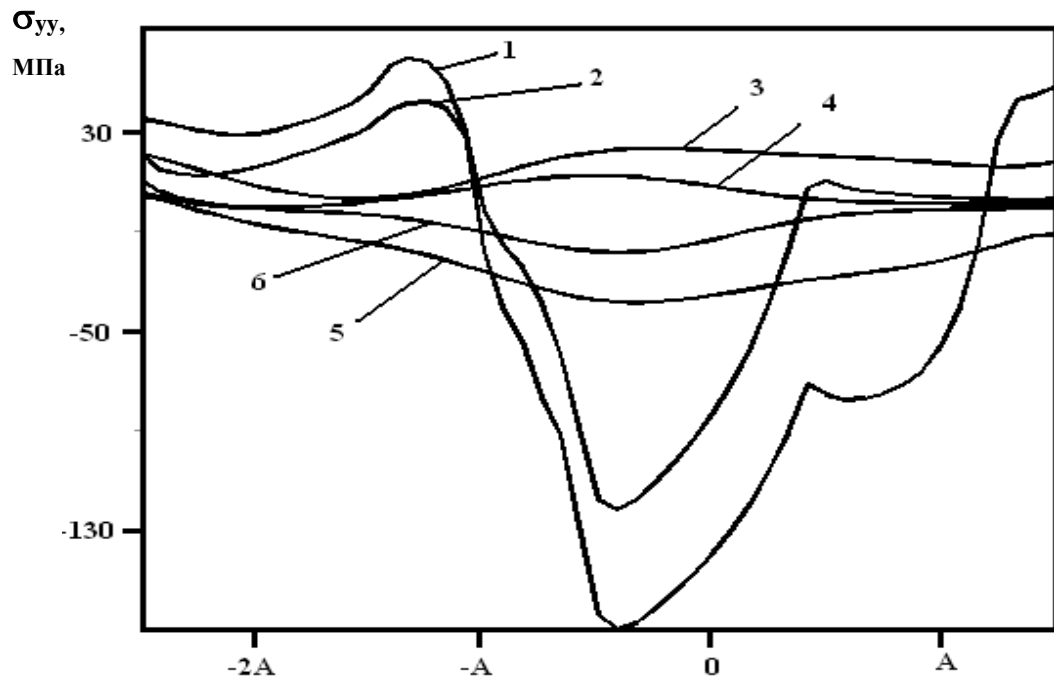

Figure 3.18 – Stresses σ_{yy} as a function of distance to the center of the laser beam cross-section (Y = 0 mm)
1 – Z = 0; 3 – Z = H/2; 5 – Z = -H (CLT with additional exposure to hot airflow);
2 – Z = 0; 4 – Z = H/2; 6 – Z = -H (CLT without exposure to hot airflow)

61

As previously mentioned, the graphs shown in Figure 3.18 resemble the time sweep of the stress fields σ_{yy} at specific locations within the sample.

When analyzing the relationships illustrated in this figure, it becomes evident that the most notable variations in the spatial distribution of stresses generated during processing, both with and without hot airflow, are found in the surface layers of the material. The observed differences are characterized by a significant rise in compressive stresses within the area subjected to laser radiation exposure, measuring (–169 MPa and –121 MPa, respectively. Additionally, there is an increase in tensile stresses in the region exposed to refrigerant, recorded at 59 MPa and 42 MPa, respectively. The rise in stresses is attributed to the elevation of the maximum temperature in the processing area from 412 °C to 509 °C.

Therefore, by using the supplementary effect of hot airflow, it facilitates not only the removal of refrigerant from the area affected by laser radiation but also enhances tensile stresses as a result of preheating. This consequently enhances the stability of microcrack formation.

The study [114] also employs preheating of the material along the laser thermocleavage path. However, for this purpose, the authors of this patent use a second laser, which proves to be economically impractical given that the expenses associated with hot air sources are considerably less than those of lasers (in our experimental investigations, we utilized a heat gun SKIL 8003).

3.5. Examination of laser cleaving processes in quartz glass as part of linear fracture mechanics

The simulation of laser processing within the framework of thermoelasticity theory, excluding the consideration of an initiating defect and a laser-induced crack in the material, limits the applicability of the results for precise calculations of the technological parameters involved in the laser cleaving of quartz glass. This is due to the significant impact that both the initiating defect and the laser-induced crack have on the distribution of stress fields. Furthermore, it is important to recognize that the assessment of the spatial localization of thermoelastic fields does not enable us to ascertain with the required precision whether the crack induced by the laser will propagate in a stable manner. To address this issue, it is essential to identify the critical state based on the principles of fracture mechanics [155, 173].

In [20], an effort was undertaken to apply fracture mechanics criteria for the analysis of laser cleaving in quartz glass. The calculations were conducted under the assumption of an infinite plate that is weakened by a semi-

infinite crack. The approximation notably diminishes the precision of calculations regarding the modes of laser-induced crack formation in quartz glass, thereby rendering the results unsuitable for precise calculations of the technological parameters associated with this process.

As referenced in [172, 174], algorithms were developed for the 2-D and 3-D simulation of the thermally induced crack formation process, utilizing the principles of thermoelasticity and linear fracture mechanics through the finite element remeshing technique. The finite element remeshing suggested by the authors of [172, 174], guided by the computed values of the stress intensity factor at the crack tip, greatly enhances the precision of modelling laser cleaving in brittle nonmetallic materials.

In this regard, it is logical to explore the laser cleaving of quartz glass through the perspective of thermoelasticity theory and linear fracture mechanics, while considering the parameters of the initiating defect and employing the finite element remeshing technique outlined in [172, 174].

The simulation of laser cleaving of quartz wafers was conducted using the algorithm established in references [172, 174] (see Figure 3.19). The fields of thermal stresses were determined within the context of the uncoupled thermoelasticity problem, employing a quasi-static formulation and employing the finite element method [139].

The conditions for laser-induced crack growth are as follows: the calculated stress intensity factor K_I at the crack tip must surpass the critical stress intensity factor K_{IC}, and the stresses at the crack tip must be tensile [172]. The critical stress intensity factor K_{IC} represents a mechanical property of a material that defines its ability to resist the propagation of a normal-fracture crack in brittle fracture [173, 155].

Special elements modelling stress singularity at the crack tip were used to enhance the accuracy of K_I calculations. In order to achieve the root asymptotics at the crack tip, the nodes of isoparametric elements were adjusted by a quarter of the element side towards the tip [172, 173].

The diagram in Figure 3.20 illustrates the impact zones of the laser and refrigerant within the cutting plane. Position 1 indicates the laser beam, position 2 denotes the refrigerant, position 3 identifies the crack, and position 4 represents the glass wafer. The horizontal arrow in the figure illustrates the movement direction of the workpiece in relation to the laser beam and the refrigerant.

This research provides the calculations for quartz glass and sheet-like silicate glass to facilitate comparative analysis. The characteristics of these materials are detailed in Table 2.1. The critical stress intensity coefficients K_{IC} for sheet-like silicate glass and quartz glass are measured at 0.5 MPa m$^{1/2}$ and 0.7 MPa m$^{1/2}$, respectively.

```
┌─────────────────────────────────┐
│      Specifying input data       │
└─────────────────────────────────┘
                 ⇓
┌─────────────────────────────────┐
│      Finite element model        │
│          construction            │
└─────────────────────────────────┘
                 ⇓
┌─────────────────────────────────┐
│  Calculation of temperature fields  │
└─────────────────────────────────┘
                 ⇓
┌─────────────────────────────────┐
│    Calculation of thermoelastic   │
│          stress fields            │
└─────────────────────────────────┘
                 ⇓
┌─────────────────────────────────┐
│  Calculation of stress intensity  │
│           factor $K_I$            │
└─────────────────────────────────┘
                 ⇓
        No
         ◇─────────────────────────◇
          \      $K_I > K_{IC}$      /
           ◇───────────────────────◇
                 ⇓      Yes
┌─────────────────────────────────┐
│     Changing the position of the  │
│   crack tip and the finite element │
│            remeshing              │
└─────────────────────────────────┘
                 ⇓
┌─────────────────────────────────┐
│   Interpolation of the tempera-   │
│  ture field onto a new finite ele- │
│            ment mesh              │
└─────────────────────────────────┘
                 ⇓
┌─────────────────────────────────┐
│    Changing the position of the   │
│     heating and cooling zones     │
└─────────────────────────────────┘
                 ⇓
┌─────────────────────────────────┐
│        Results processing         │
└─────────────────────────────────┘
```
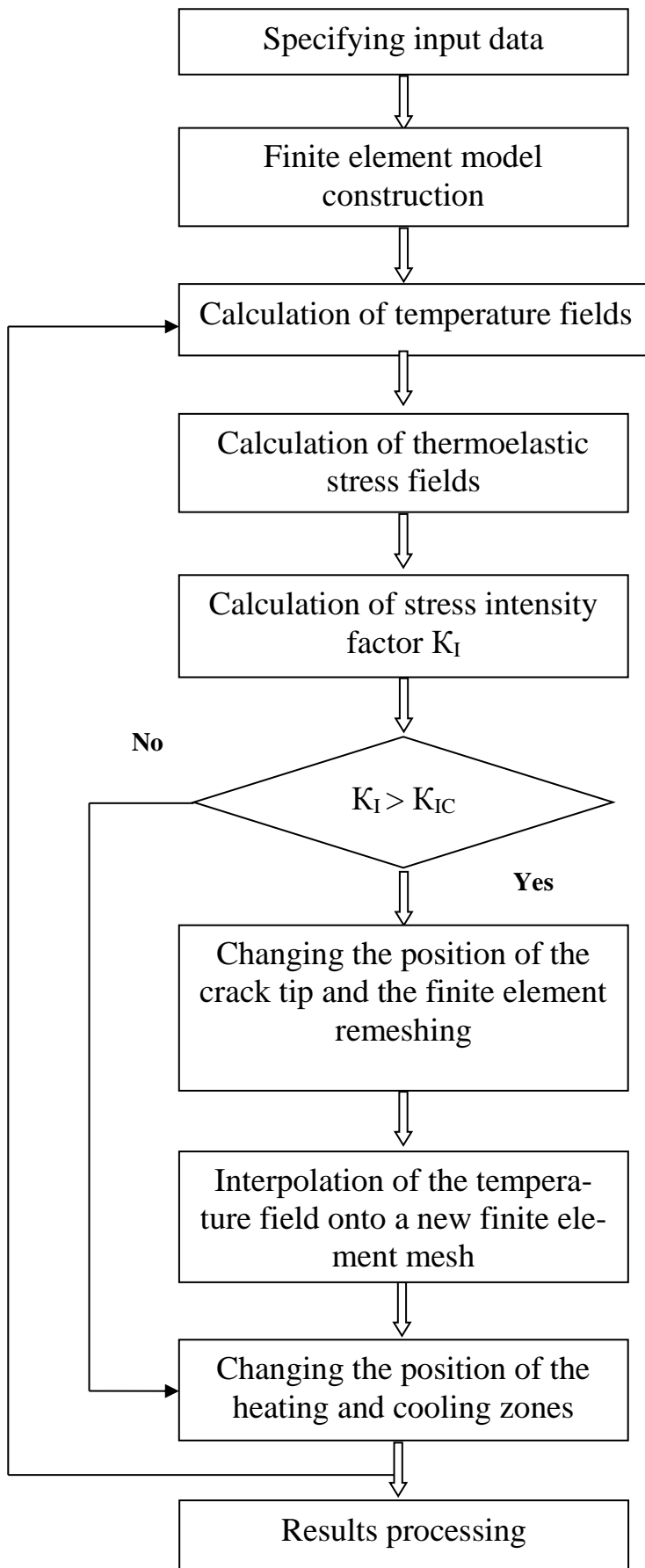
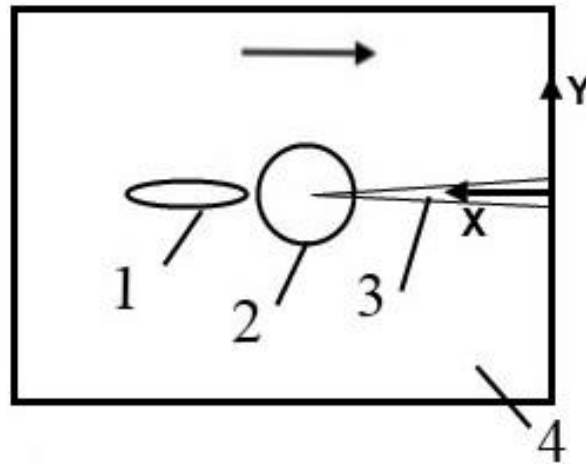Figure 3.19 – Algorithm for finite element simulation of laser cleaving
in quartz glass

Figure 3.20 – Layout of laser and refrigerant impact areas
in the cutting plane of the glass wafer

Calculations were performed for rectangular wafers with geometric dimensions of 15×20×1 mm. Simulation was carried out for the scenario involving exposure to laser radiation at a wavelength of 10.6 μm.

The parameters of the laser beam were set as follows: major axis $A = 6 \cdot 10^{-3}$ m and minor axis $B = 2 \cdot 10^{-3}$ m. The wafer movement speed in relation to the laser beam and refrigerant was established at $v = 15$ mm/s. It was determined that the parameters for the air-water mixture supply would effectively cool the glass surface, achieving a heat transfer coefficient of 7000 W/m²K [161]. The radius of the refrigerant spot was measured at $R_h = 3$ mm, while the length of the initiating crack was adjusted between 0.75 mm and 1.5 mm.

Note that the temperature in the processing area during laser cleaving should remain within limits that prevent the relaxation of thermoelastic stresses. The upper limit of permissible temperatures for glasses is determined by the glass transition temperature specific to each glass type. For quartz glass, this temperature is 1473 K, while for sheet-like silicate glass, it is 789 K [7].

During the numerical experiment, the laser radiation power values required to heat the material to the glass transition temperature were established based on the specified processing parameters and sample geometry. For quartz glass thermal cleaving, the maximum allowable laser radiation power is $P = 30$ W, while for sheet-like silicate glass, it is $P = 10$ W.

Figures 3.21 to 3.26 present the results of the calculations. Figures 3.21 – 3.23 illustrate the calculated curves for two distinct cases: 1 represents the thermal cleaving of quartz glass, while 2 depicts the thermal cleaving of sheet-like silicate glass. In the comparative analysis of laser thermal cleaving

of quartz glass and sheet-like silicate glass, the length of the initiating crack was maintained at 1 mm, and the finite element remeshing technique was not employed, resulting in a constant crack length throughout the analysis.
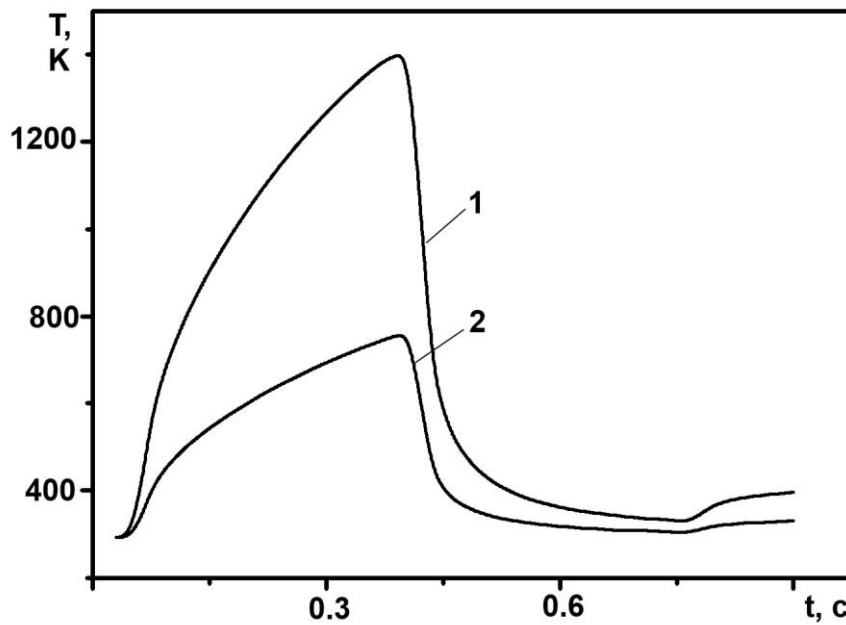
Figure 3.21 – Calculated temperature values T at the crack tip

As previously mentioned, under the specified processing parameters, the material reached the glass transition temperatures of quartz and sheet-like silicate glass (refer to Figure 3.21).
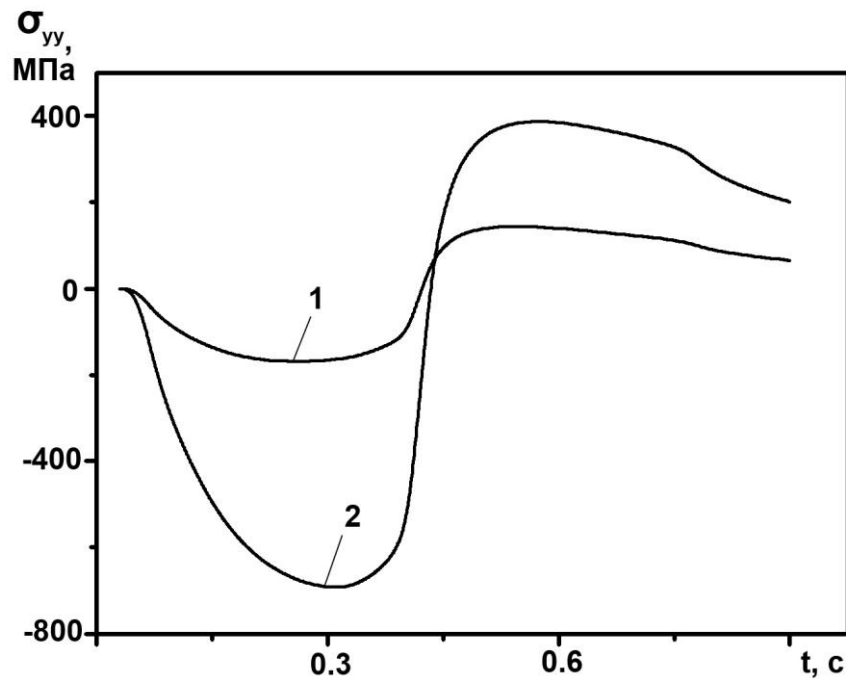
Figure 3.22 – Calculated values of elastic stresses σ_{yy} at the crack tip

The graphs depicted in Figure 3.22 clearly demonstrate that during the laser thermal cleaving of quartz and sheet-like silicate glasses, notable compressive stresses develop at the tip of the initiating defect due to the effects of laser heating. The maximum compressive stress values at the tip of the initiating defect are –168 MPa for quartz glass and –692 MPa for sheet-like silicate glass.

Furthermore, the influence of the refrigerant leads to the development of tensile stresses at the tip of the initiating defect, with maximum values reaching 143 MPa for the simulation involving quartz glass and 388 MPa for the sheet-like silicate glass, as illustrated in Figure 3.22.

The graphs presented in Figure 3.23 indicate that two maxima of stress intensity coefficients are consistently established at the tip of the initiating crack. The second maximum of stress intensity coefficient values suggests that for quartz glass, the value is 0.82 MPa $m^{1/2}$, while for sheet-like silicate glass, it is 2.14 MPa $m^{1/2}$. This corresponds to tensile stresses at the crack tip, implying that both necessary conditions for the initiation of crack development are fulfilled.

When comparing the magnitude of thermoelastic stresses and the stress intensity factors at the crack tip during the thermal cleaving of sheet-like and quartz glasses, it is evident that for quartz glass, the maximum values of the stress intensity factor are 2.6 times lower. It is important to consider that the comparison is conducted at varying maximum temperature values in the processing area (see to Figure 3.21).
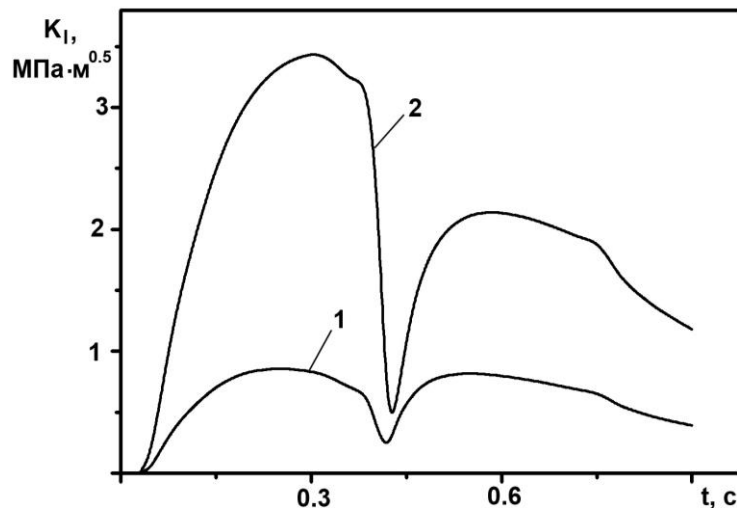

Figure 3.23 – Calculated values of stress intensity factor K_I at the crack tip

It is noteworthy that the selected processing modes provide virtually minimal necessary values of the stress intensity factor when cutting quartz glass. Thus, a slight increase in processing speed or a slight decrease in laser power will prevent the stress intensity factor at the crack tip from attaining

the critical stress intensity factor values, ultimately resulting in the failure of the laser-induced crack formation process during the experiment. The primary factor contributing to the low values of stress intensity factors at the crack tip is the significantly lower coefficient of linear thermal expansion of quartz glass, which is an order of magnitude less than that of the majority of commercial silicate glasses.

To study the influence of the initiating defect parameters on the process of laser-induced crack initiation, calculations of stress values and stress intensity factors at the crack tip were performed for different values of the initiating defect length using the finite element remeshing technique.

Figures 3.24 – 3.26 illustrate the calculated curves corresponding to various initiating defect lengths. Specifically, 1 represents the curves for a initiating defect length of L = 0.75 mm, 2 corresponds to L = 1 mm, and 3 depicts the curves for L = 1.5 mm.
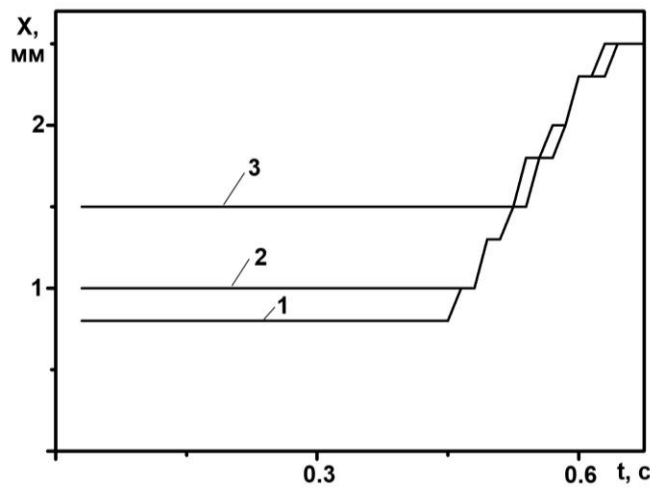

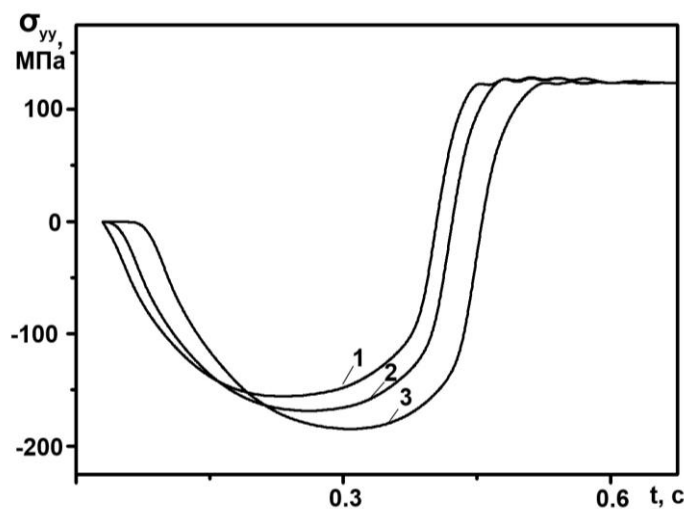Figure 3.24 – Calculated values of X coordinates at the crack tip

Figure 3.25 – Calculated values of elastic stresses σ_{yy} at the crack tip

68

In all three calculated cases, it is observed that laser-induced cracks originate from initiating defects (see Figure 3.24). It is important to consider the significant impact that the length of the initiating defect has on the magnitude of thermoelastic stresses and the stress intensity factors at the crack tip, as illustrated in Figures 3.25 – 3.26.
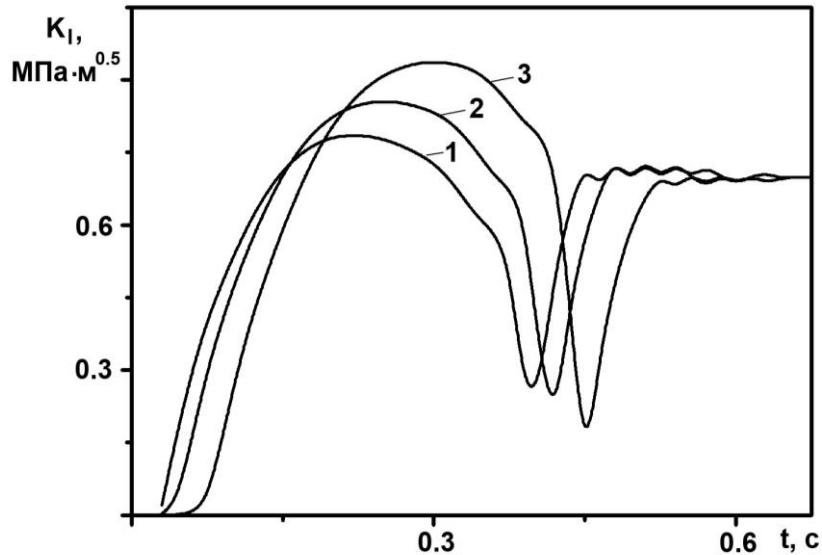

Figure 3.26 – Calculated values of stress intensity factor K_I at the crack tip

Thus, at an initiating defect length of L = 0.75 mm, the maximum stress intensity factor is K_I = 0.79 MPa m$^{1/2}$; for L = 1 mm, the maximum stress intensity factor increases to K_I = 0.86 MPa m$^{1/2}$; at L = 1.5 mm, the maximum stress intensity factor reaches K_I = 0.94 MPa m$^{1/2}$.

Thus, by increasing the length of the initiating defect, it is possible to enhance the probability of laser-induced crack initiation, which is crucial for developing the modes of laser thermal cleaving of quartz glasses. The application of 3-D simulation technology for the thermally induced crack formation process, within the context of thermoelasticity theory and linear fracture mechanics, utilizing a finite element remeshing technique, enables the execution of essential calculations for the technological modes of laser thermal cleaving of quartz glasses, while considering the parameters of the initiating defect.

3.6. Peculiar aspects of controlled laser thermal cleaving of crystalline silicon

The works focused on the study of controlled laser thermal cleaving of various crystals are especially noteworthy (see, for example, [17]). It is important to highlight that in these studies, the numerical simulation of thermoelastic fields is conducted within a two-dimensional framework and does

not consider the anisotropic nature of the elastic properties of crystals. Simultaneously, it is recognized that the dynamics of different physical processes, even within cubic crystals, can undergo qualitative changes when compared to isotropic media [175, 176]. In this context, it appears logical to conduct a three-dimensional simulation of the controlled laser thermal cleaving process in a cubic silicon crystalline system, while considering its anisotropic properties.

The finite element method [139] was employed to simulate the processes involved in laser thermal cleaving of silicon wafers. In the simulation of controlled laser thermal cleaving, the initial step involved calculating the temperature fields. Subsequently, the focus shifted to determining the thermoelastic stresses that arise due to the effects of laser radiation and refrigerant interaction with silicon. This sequence of simulations yields results within the context of the uncoupled thermoelastic problem in a quasi-static formulation. From a physical perspective, the quasi-static formulation of the thermoelastic problem involves the assumption that the stress state is established significantly quicker than thermal equilibrium is attained [152].

The maximum tensile stress criterion was selected as the determining factor for the direction of crack propagation [153]. The laser microcrack propagates in a direction that is perpendicular to the maximum tensile stress application, as per this criterion. A crack propagating in the tensile zone is considered to cease its growth upon reaching the compression zone.

For the calculations, the density, specific heat capacity, thermal conductivity coefficient, and coefficient of linear thermal expansion of silicon were assumed to be $\rho = 2330$ kg/m^3, C = 758 J/(kg·K), $\lambda = 109$ W/ (m·K), $\alpha = 2.33 \cdot 10^{-6}$ K^{-1}, respectively [177, 178].

The calculation of thermoelastic fields generated in a monocrystalline silicon wafer due to sequential laser heating and refrigerant exposure was performed for three distinct options: I – three-dimensional analysis of an isotropic plate, II – three-dimensional analysis of an anisotropic plate cleaved in the (100) plane, III – three-dimensional analysis of an anisotropic plate cleaved in the (111) plane.

The expression of Hooke's law for anisotropic materials can be represented in matrix form [167, 179]

$$\sigma_i = \sum C_{ik}\left(\varepsilon_k - \varepsilon_k^t\right),$$

where

$$\sigma_1 = \sigma_{xx},\ \sigma_2 = \sigma_{yy}, \sigma_3 = \sigma_{zz},\ \sigma_4 = \sigma_{xy},\ \sigma_5 = \sigma_{yz},\ \sigma_6 = \sigma_{xz},$$

represent stresses, while

$$\varepsilon_1 = \varepsilon_{xx}, \; \varepsilon_2 = \varepsilon_{yy}, \varepsilon_3 = \varepsilon_{zz}, \; \varepsilon_4 = 2\varepsilon_{xy}, \; \varepsilon_5 = 2\varepsilon_{yz}, \; \varepsilon_6 = 2\varepsilon_{xz},$$

denote elastic deformations, and

$$\varepsilon_1^t = \alpha_x \Delta T, \; \varepsilon_2^t = \alpha_y \Delta T, \varepsilon_3^t = \alpha_y \Delta T, \; \varepsilon_4^t = 0, \; \varepsilon_5^t = 0, \; \varepsilon_6^t = 0,$$

stand for temperature deformations.

For cubic crystals, if the directions of acting forces leading to tensile and shear stresses are combined with the main crystallographic directions <100>, the matrix $\{C_{ik}\}$ takes the following form [167]

$$\{C_{ik}\} = \begin{pmatrix} C_{11} & C_{12} & C_{12} & 0 & 0 & 0 \\ C_{12} & C_{11} & C_{12} & 0 & 0 & 0 \\ C_{12} & C_{12} & C_{11} & 0 & 0 & 0 \\ 0 & 0 & 0 & C_{44} & 0 & 0 \\ 0 & 0 & 0 & 0 & C_{44} & 0 \\ 0 & 0 & 0 & 0 & 0 & C_{44} \end{pmatrix}.$$

The matrix $\{C_{ik}\}$ for the case when the wafer is cleaved in the <111> plane can be expressed as follows [179]

$$\{C_{ik}\} = \begin{pmatrix} C_{11} - \dfrac{m}{2} & C_{12} + \dfrac{m}{6} & C_{12} + \dfrac{m}{3} & 0 & 0 & -\dfrac{m}{3\sqrt{2}} \\[2mm] C_{12} + \dfrac{m}{6} & C_{11} - \dfrac{m}{2} & C_{12} + \dfrac{m}{3} & 0 & 0 & \dfrac{m}{3\sqrt{2}} \\[2mm] C_{12} + \dfrac{m}{3} & C_{12} + \dfrac{m}{3} & C_{11} - \dfrac{2m}{3} & 0 & 0 & 0 \\[2mm] 0 & 0 & 0 & C_{44} + \dfrac{m}{6} & \dfrac{m}{3\sqrt{2}} & 0 \\[2mm] 0 & 0 & 0 & \dfrac{m}{3\sqrt{2}} & C_{44} + \dfrac{m}{3} & 0 \\[2mm] -\dfrac{m}{3\sqrt{2}} & \dfrac{m}{3\sqrt{2}} & 0 & 0 & 0 & C_{44} + \dfrac{m}{3} \end{pmatrix},$$

where

$$m = C_{11} - C_{12} - 2C_{44}.$$

The following elastic rigidity constants were used for the calculations: $C_{11} = 1.656 \cdot 10^5$ MPa, $C_{12} = 0.6386 \cdot 10^5$ MPa, $C_{44} = 0.7953 \cdot 10^5$ MPa [180].

For modeling the controlled laser thermal cleaving of an isotropic silicon wafer, Young's modulus $E = 1.9 \cdot 10^5$ MPa, Poisson's ratio $v = 0.42$ (option I a) were considered as per [179]. Besides, Young's modulus and Poisson's ratio determined by the following equations were employed (option I b): $E = 1/S_{11}$, $v = -S_{12}/S_{11}$, where S_{11} and S_{12} are the coefficients of the flexibility matrix equal to $7.68 \cdot 10^{-3}$ GPa^{-1} and $-2.14 \cdot 10^{-3}$ GPa^{-1} [167].

Figure 3.27 illustrates the positions of the laser and refrigerant impact zones within the cutting plane, along with the configurations of their cross-sections. Position 1 indicates the laser beam, position 2 denotes the refrigerant, position 3 represents the silicon wafer, while positions 4 and 5 illustrate the cross-sections of the laser beam and the refrigerant's zone of influence on the cutting plane, respectively.
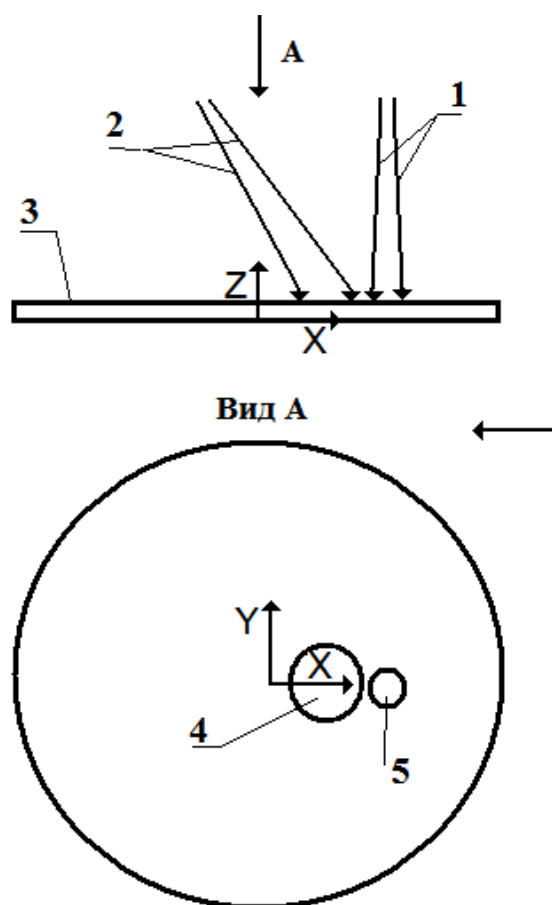

Figure 3.27 − Arrangement of laser and refrigerant impact areas in the cutting plane

The horizontal arrow in the figure indicates the movement direction of the workpiece relative to the laser beam and the refrigerant.

Calculations were performed for discs with a radius of 15.5 mm and thicknesses of h = 0.2 mm and h = 0.4 mm. The radius of the laser spot is R = 0.5 mm, and the power of the radiation is P = 60 W. The wafer movement speed relative to the laser beam and the refrigerant was set at v = 10 mm/s and v = 100 mm/s. Calculating thermoelastic fields in samples of varying sizes, processing speeds, and laser radiation power presents no fundamental challenges.

Simulation was conducted for exposure cases involving laser radiation at wavelengths of 1.06 μm and 0.808 μm. The selection of laser radiation at a wavelength of 1.06 μm for numerical simulation was necessitated by the requirement for experimental validation of the simulation outcomes. The investigation of laser radiation parameters at a wavelength of 0.808 μm for numerical calculations is significant due to silicon's substantial absorption of radiation at this wavelength. Currently, there are laser emitters available that possess adequate power to facilitate the process of controlled laser thermal cleaving. Moreover, experimental studies on the separation of silicon wafers into crystals, as detailed in [175], utilized a setup incorporating a laser that generated radiation at the specified wavelength.

As previously stated, calculations were conducted for three distinct options for comparative analysis: an isotropic plate, a plate cleaved in the (100) plane, and a plate cleaved in the (111) plane. The study modelled the effects of laser radiation exposure at wavelengths of 1.06 μm and 0.808 μm on plates with thicknesses of 0.2 mm and 0.4 mm, which were in motion relative to the laser at velocities of 10 mm/s and 100 mm/s.

The results of the calculations are presented in Tables 3.4 and 3.5, as well as Figures 3.28 and 3.29.

Table 3.4 – Calculated values for the maximum and minimum temperatures in the wafer undergoing processing

Temperature in the wafer , K	laser radiation at a wavelength of 1.06 μm				laser radiation at a wavelength of 0.808 μm			
	h = 0.2 mm		h = 0.4 mm		h = 0.2 mm		h = 0.4 mm	
	v = 10 mm/s	v = 100 mm/s	v = 10 mm/s	v = 100 mm/s	v = 10 mm/s	v = 100 mm/s	v = 10 mm/s	v = 100 mm/s
maximum	507	427	508	419	1640	1154	1095	804
minimum	297	293	304	293	320	293	331	293

Analysis of the data presented in Table 3.4 and Figure 3.28 indicates that the maximum temperature values for all design modes remain below the

melting point of silicon. This condition is essential to prevent brittle fracture of the wafer due to thermoelastic stresses. The maximum temperature is observed during the processing of a thin wafer (h = 0.2 mm) at a low speed (v = 10 mm/s) for radiation at a wavelength of 0.808 μm. The significant impact of a high thermal conductivity coefficient on the development of temperature fields during the laser thermal cleaving of silicon wafers is noteworthy.

The thermal conductivity of silicon leads to a notable reduction in the maximum temperature during the processing of thick samples, as opposed to thinner samples, when utilizing radiation at a wavelength of 0.808 μm. The observed change is approximately 30 % when analyzing the cutting of samples with thicknesses of 0.2 mm and 0.4 mm. It is important to highlight that the use of radiation at a wavelength of 1.06 microns as a technological tool result in a weakly expressed effect, attributed to the volumetric nature of absorption of this radiation by crystalline silicon.

Table 3.5 and Figure 3.29 present the calculated maximum tensile and compressive stresses in the processing area during controlled laser thermal cleaving for three distinct options. I is the three-dimensional analysis of an isotropic plate (Ia is based on the data of [178], IIb is based on the data of [167]); II is the three-dimensional analysis of an anisotropic plate cleaved in plane (100); III is the three-dimensional analysis of an anisotropic plate cleaved in plane (111).

Table 3.5 – Calculated values for the maximum tensile and compressive stresses in the processing area

| Option	Maximum stresses in the processing area σ_y, MPa	laser radiation at a wavelength of 1.06 μm				laser radiation at a wavelength of 0.808 μm			
		h = 0.2 mm		h = 0.4 mm		h = 0.2 mm		h = 0.4 mm	
		v = 10 mm/s	v = 100 mm/s	v = 10 mm/s	v = 100 mm/s	v = 10 mm/s	v = 100 mm/s	v = 10 mm/s	v = 100 mm/s
I a	tensile	8.2	1.7 (5.4)	7.3	0.9 (5.9)	49.7	10.0 (33.1)	24.0	2.9 (20.2)
	compressive	−46.4	−27.9	−45.8	−26.1	−296	−178	−172	−102
I b	tensile	5.6	1.2 (3.7)	5.0	0.6 (4.0)	33.8	6.8 (22.6)	16.4	2.0 (13.8)
	compressive	−31.7	−19.1	−31.4	−17.8	199	−122	−118	−69.5
II	tensile	6.3	1.3 (4.2)	5.6	0.7 (4.6)	38.5	7.9 (26.0)	18.6	2.0 (16.1)
	compressive	−36.1	−21.3	−35.6	−19.6	−223	−135	−129	−75.1
III	tensile	6.7	1.4 (4.4)	5.8	0.6 (4.8)	40.4	8.1 (27.4)	19.4	2.2 (16.8)
	compressive	−38.7	−22.7	−38.0	−20.8	−240	−143	−139	−80.1
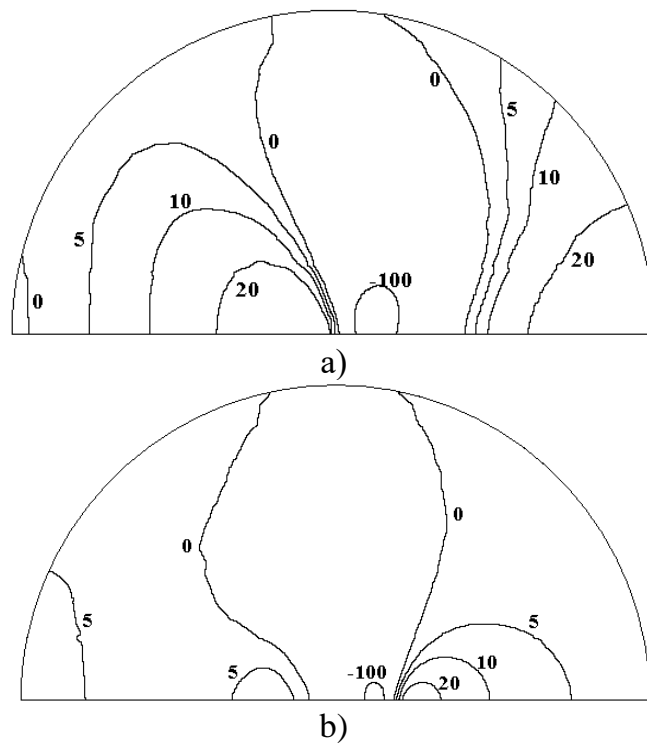
Figure 3.28 – Temperature field distribution on the surface of the silicon wafer cleaved
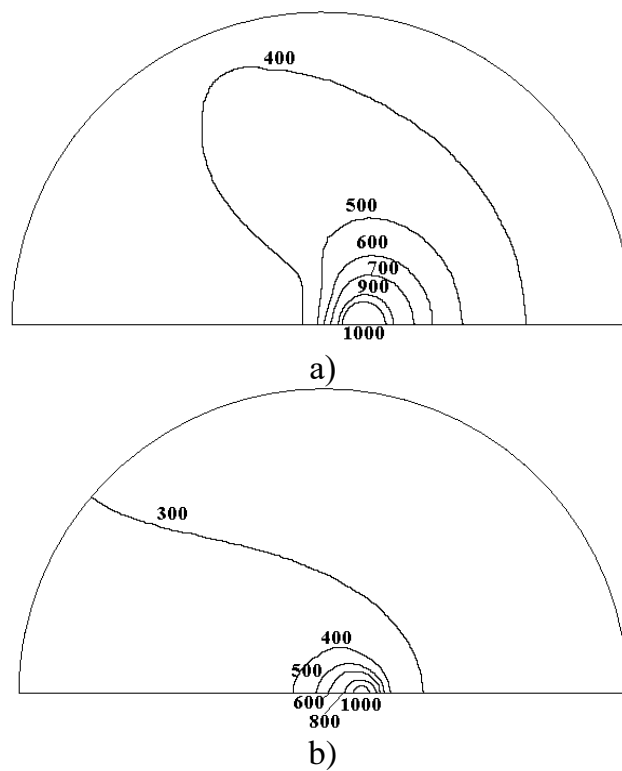in plane (111), K
a) v=10 mm/s, b) v=100 mm/s

Figure 3.29 – Field distribution of thermal stresses on the surface of the silicon wafer
cleaved in plane (111), MPa
a) v=10 mm/s, b) v=100 mm/s

The data presented in Table 3.5 indicates that employing an isotropic model for the controlled laser thermal cleaving of anisotropic materials, such as silicon, produces considerable inaccuracies. In comparing the maximum tensile stresses in the cutting plane of the plate cleaved along the (100) plane, it is observed that the isotropic model results in errors of 48 % and 16 % for options Ia and Ib, respectively. Modelling the processing of the plate cleaved in the (111) plane results in errors of 39 % and 20 % for options Ia and Ib, respectively.

It should be noted that the difference in maximum tensile stress values in plates cleaved along the (100) and (111) planes ranges from 3 % to 10 %, aligning well with the findings of [179]. It is essential to consider this variation in stress values when determining the parameters of the separation process, such as adjusting the cutting speed or laser power.

Attention must be directed towards the specific characteristics of spatial localization of thermoelastic fields during high-speed controlled laser thermal cleaving. When cutting at a speed of 100 mm/s, a zone of tensile stresses develops in the area of laser radiation exposure prior to the zone of compressive stresses (see Figure 3.29). These tensile stresses are significantly greater in magnitude than those in the zone of refrigerant exposure. The values of these stresses are presented in parentheses in Table 3.5.

Experimental studies employing laser radiation at a wavelength of 1.06 μm were conducted to validate the results of the numerical simulation. Figure 3.30 presents an end view of the silicon wafer that has been separated via a controlled laser thermocleavage technique. The experimental results demonstrated the effectiveness of the employed simulation technique.
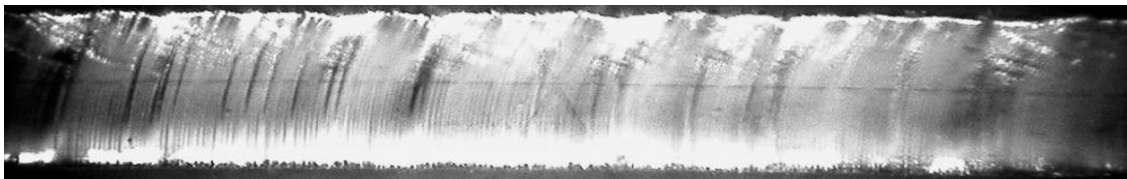

Figure 3.30 – End view of a silicon wafer separated
via controlled laser thermal cleaving

Thus, the results indicate that the anisotropy of the elastic properties of silicon wafers must be considered in simulations of laser thermal cleaving processes.

Analysis of laser cleaving of silicon wafers along the (110) plane
The calculation of thermoelastic fields presented above was conducted for wafers cleaved in the (100) and (111) planes, although it is important to note that silicon single crystals cleaved in the (110) plane are also used in practice.

Thus, the matrix $\{C_{ik}\}$ for the (110) cut can be expressed as follows:

$$\{C_{ik}\} = \begin{pmatrix} \dfrac{C_{11}}{2} + \dfrac{C_{12}}{2} + C_{44} & \dfrac{C_{11}}{2} + \dfrac{C_{12}}{2} - C_{44} & C_{12} & 0 & 0 & 0 \\[2mm] \dfrac{C_{11}}{2} + \dfrac{C_{12}}{2} - C_{44} & \dfrac{C_{11}}{2} + \dfrac{C_{12}}{2} + C_{44} & C_{12} & 0 & 0 & 0 \\[2mm] C_{12} & C_{12} & C_{11} & 0 & 0 & 0 \\[2mm] 0 & 0 & 0 & C_{44} & 0 & 0 \\[2mm] 0 & 0 & 0 & 0 & C_{44} & 0 \\[2mm] 0 & 0 & 0 & 0 & 0 & \dfrac{C_{11}}{2} - \dfrac{C_{12}}{2} \end{pmatrix}.$$

Calculations were conducted for discs with a radius of 15.5 mm and thicknesses of h = 0.2 mm and h = 0.4 mm. The laser spot radius is R = 0.5 mm, and the radiation power is P = 60 W. The speed of the wafer movement relative to the laser beam and the refrigerant were selected as v = 10 mm/s and v = 100 mm/s. Simulation was conducted for cases of exposure to laser radiation at wavelengths of 1.06 μm and 0.808 μm.

The findings of the calculations are presented in Table 3.6 and Figures 3.31 – 3.33. The values of the maximum thermoelastic tensile and compressive stresses generated in the silicon wafer for the three processing options under examination are presented in Table 3.6.

Table 3.6 – Calculated values for maximum tensile and compressive stresses in the processing area

Option	Maximum stresses in the processing area, MPa	laser radiation at a wavelength of 1.06 μm				laser radiation at a wavelength of 0.808 μm			
		h = 0.2 mm		h = 0.4 mm		h = 0.2 mm		h = 0.4 mm	
		v = 10 mm/s	v = 100 mm/s	v = 10 mm/s	v = 100 mm/s	v = 10 mm/s	v = 100 mm/s	v = 10 mm/s	v = 100 mm/s
I	tensile	7.9	1.6	6.9	0.8	48.1	9.8	23.2	2.6
	compressive	–43.4	–25.4	–40.3	–21.0	–273	–164	–153	–89.3
II	tensile	9.3	2.0	7.8	1.1	57.3	12.1	26.1	3.6
	compressive	–49.1	–28.5	–42.6	–22.1	–309	–185	–163	–94.6
III	tensile	8.5	1.7	7.3	0.9	52.2	10.3	24.5	2.9
	compressive	–46.8	–27.0	–41.7	–21.5	–294	–175	–158	–92.0

Figures 3.31 – 3.33 illustrate the field distributions of thermal stresses for wafers with a thickness of h = 0.2 mm, processed at a speed of v = 10 mm/s, under the influence of laser radiation at a wavelength of 0.808 μm.

It is important to highlight that the lack of thermal conductivity anisotropy in silicon crystals results in the calculated temperature values in the processing area and the patterns of their formation for cuts (110), (100), and (111) being identical when the same treatment parameters and wafer sizes are chosen.
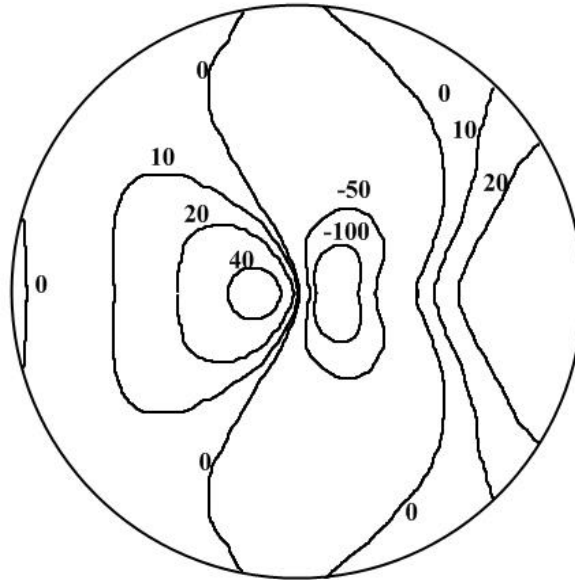
Figure 3.31 – Field distribution of thermal stresses on the surface of the silicon wafer when the laser beam progresses towards [1$\bar{1}$0], MPa
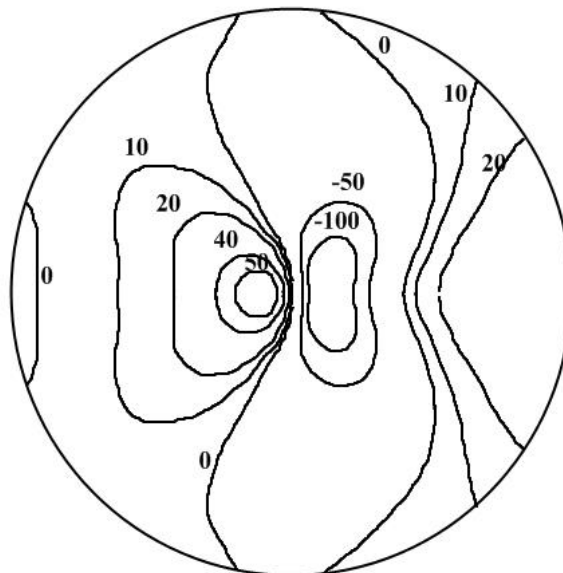

Figure 3.32 – Field distribution of thermal stresses on the surface of the silicon wafer when the laser beam progresses towards [001], MPa

The analysis of the data given in Table 3.6 shows that the highest values of tensile stresses are reached during thermal cleaving of cut (110) when the laser beam is moved towards [001] (II processing option), and the lowest values are reached when the laser beam is moved towards [1$\bar{1}$0] (I processing option). The difference in the values of maximum tensile stresses formed during processing towards [001] and [1$\bar{1}$0] ranges from 11 % to 28 %. This difference in the values of tensile stresses should be taken into account when selecting the parameters of the laser thermal cleaving process.

We should distinctly observe the unique characteristics of the spatial localization of the thermoelastic fields generated during the laser thermal cleaving of cut (110) towards [1$\bar{1}$1] (see Figure 3.33). The distribution of thermoelastic fields generated in this operating mode exhibits a slight asymmetry concerning the line of exposure to laser radiation. The asymmetry of the thermoelastic stress fields arises from the asymmetry of the Young's modulus surface cross-section relative to direction [1$\bar{1}$1] (see [178]), and this factor must be considered when determining the parameters for thermal cleaving.
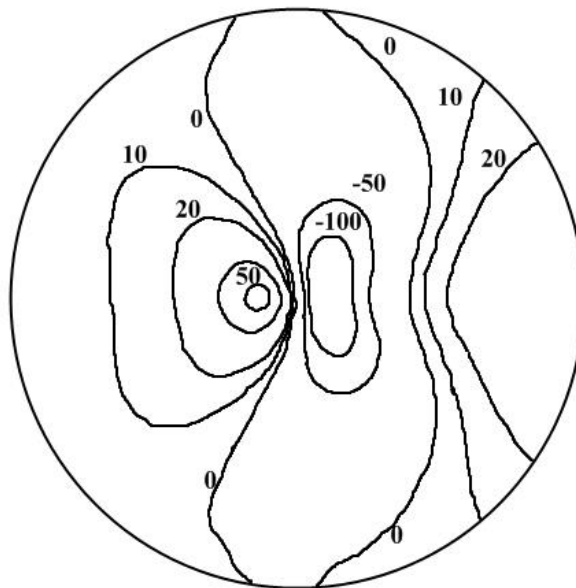

Figure 3.33 − Field distribution of thermal stresses on the silicon wafer surface when the laser beam progresses towards [1$\bar{1}$0], MPa

3.7. Peculiar aspects of controlled laser thermal cleaving of crystalline quartz

Considerable attention is given to analyzing the unique characteristics of laser thermal cleaving in different crystals. This research area is important because traditional crystal separation methods result in substantial material

loss and contamination of surfaces used in the process. The studies that examine the controlled laser thermal cleaving of quartz crystals are especially noteworthy [16, 47]. The examination of the nuances in this technology's application within quartz crystal processing is significant due to the extensive industrial use of quartz crystal components, which exceeds an annual consumption of 1 billion dollars [181]. These studies highlight the essential importance of considering the crystallographic orientation of the material being processed when determining the parameters for laser thermal cleaving. Nevertheless, the authors focus solely on the anisotropy of thermal expansion in quartz crystals, neglecting the influence of crystallographic direction on other properties of these crystals. In this context, it is logical to explore the unique aspects of the controlled laser thermal cleaving process of crystalline quartz, considering the anisotropic characteristics of thermal expansion, thermal conductivity, and elastic properties of the crystals.

The finite element method was employed to simulate the laser thermal cleaving of quartz plates [139]. Initially, the temperature fields were computed, followed by the determination of the thermoelastic stresses induced by the interaction of laser radiation and refrigerant on the crystalline quartz wafer. This simulation algorithm establishes the outcomes derived from the uncoupled thermoelasticity problem within the quasi-static formulation [152]. The criterion of maximum tensile stresses was employed to analyze the results obtained [153].

Calculations were conducted for square wafers with geometric dimensions of 20×20×1.5 mm and 20×20×0.75 mm. Simulation was performed for the scenario involving exposure to laser radiation at a wavelength of 10.6 μm. The radius of the laser radiation spot was 1.5 mm, and the power of the radiation was 50 W. The speed of wafer movement in relation to the laser beam and the refrigerant were selected as v = 5 mm/s and v = 15 mm/s.

Standard initial orientations of square-shaped crystal samples were employed for simulation [182]. In the analysis of the three examined cuts, the directions of the laser beam travel were aligned with the crystallographic axes present in the corresponding cutting plane (see Figure 3.34). Following the guidelines outlined in [182], two letters representing the crystallographic axes of the crystalline element were employed to specify the cuts. The first letter indicated the axis aligned with the thickness of the sample, while the second letter referred to the axis aligned with the length of the sample.

The square samples used in the zy-cut analysis clearly provide a sufficient basis to concentrate only on the processing option along the X axis. Consequently, the analysis of thermoelastic fields generated in a single-crystal quartz wafer due to sequential laser heating and refrigerant exposure was conducted for five distinct options: I is the zy-cut analysis, involving the

movement of the laser beam along the X-axis; II is the yx-cut analysis, with the laser beam also moved in the X-axis direction; III is the yx-cut analysis, where the laser beam is directed along the Z-axis; IV is the xy-cut analysis, pertaining to the movement of the laser beam in the Z-axis direction; V is the xy-cut analysis, focusing on the movement of the laser beam in the Y-axis direction.
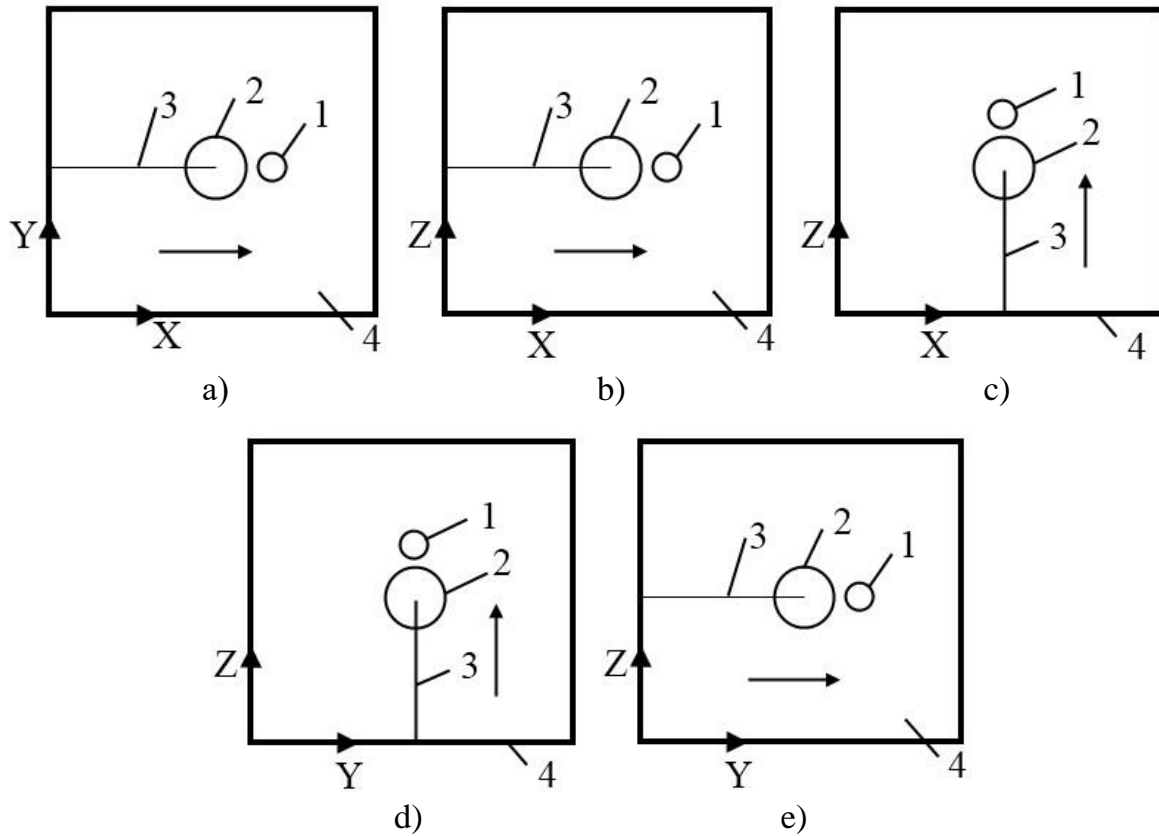

Figure 3.34 – Layouts of laser and refrigerant exposure zones in cutting plane

Figure 3.34 illustrates the arrangement of laser and refrigerant impact zones within the cutting plane for the five processing options examined in this study. Position 1 denotes the laser beam, position 2 refers to the refrigerant, position 3 signifies the laser-induced crack, and position 4 pertains to the quartz plate. The horizontal arrow in the figure illustrates the movement direction of the workpiece in relation to the laser beam and the refrigerant.

In the calculations, the density and specific heat capacity of crystalline quartz were assumed to be $\rho = 2643$ kg/m^3 and $C = 741$ J/kg·K, respectively. The simulation considered the variations in physical properties of crystalline quartz across different crystallographic directions. The thermal conductivity coefficients and linear thermal expansion values for crystalline quartz were

taken as $\lambda\| = 12.3$ W/m·K, $\alpha\| = 9\cdot10^{-6}$ K^{-1} along the third-order symmetry axis Z, while $\lambda^{\perp} = 6.8$ W/m·K, $\alpha^{\perp} = 14.8\cdot10^{-6}$ K^{-1} were noted for the direction perpendicular to the axis Z, respectively [178, 180].

Low-temperature quartz is classified within the trigonal system, leading to its elastic properties being characterized by six independent components of the elastic modulus tensor. The matrix entry for the zy-cut is detailed as follows [183]

$$\{C_{ik}\} = \begin{pmatrix} C_{11} & C_{12} & C_{13} & C_{14} & 0 & 0 \\ C_{12} & C_{11} & C_{12} & -C_{14} & 0 & 0 \\ C_{13} & C_{12} & C_{33} & 0 & 0 & 0 \\ C_{14} & -C_{14} & 0 & C_{44} & 0 & 0 \\ 0 & 0 & 0 & 0 & C_{44} & C_{14} \\ 0 & 0 & 0 & 0 & C_{14} & \dfrac{C_{11}-C_{12}}{2} \end{pmatrix}.$$

The matrix $\{C_{ik}\}$ for the yx-cut can be expresses as

$$\{C_{ik}\} = \begin{pmatrix} C_{11} & C_{13} & C_{12} & -C_{14} & 0 & 0 \\ C_{13} & C_{33} & C_{13} & 0 & 0 & 0 \\ C_{12} & C_{13} & C_{11} & C_{14} & 0 & 0 \\ -C_{14} & 0 & C_{14} & C_{44} & 0 & 0 \\ 0 & 0 & 0 & 0 & \dfrac{C_{11}-C_{12}}{2} & -C_{14} \\ 0 & 0 & 0 & 0 & -C_{14} & C_{44} \end{pmatrix}.$$

Correspondingly, for the xy-cut, the matrix $\{C_{ik}\}$ is of the form

$$\{C_{ik}\} = \begin{pmatrix} C_{33} & C_{13} & C_{13} & 0 & 0 & 0 \\ C_{13} & C_{11} & C_{12} & 0 & 0 & C_{14} \\ C_{13} & C_{12} & C_{11} & 0 & 0 & -C_{14} \\ 0 & 0 & 0 & \dfrac{C_{11}-C_{12}}{2} & -C_{14} & 0 \\ 0 & 0 & 0 & -C_{14} & C_{44} & 0 \\ 0 & C_{14} & -C_{14} & 0 & 0 & C_{44} \end{pmatrix}.$$

82

The following elastic rigidity constants were used for calculations: C_{11} = 86.75·10⁹ MPa, C_{12} = 5.95·10⁹ MPa, C_{13} = 11.91·10⁹ MPa, C_{14} = −17.8·10⁹ MPa, C_{33} = 107.2·10⁹ MPa, C_{44} = 57.8·10⁹ MPa [178, 180].

To determine the contribution of anisotropy of various properties of crystalline quartz to the formation of temperature fields and thermal stresses during controlled laser thermal cleaving, four sets of material properties were employed for each of the five calculation options:

– a set of features that considers the relationship of thermal conductivity coefficients, coefficients of linear thermal expansion, and elastic properties of quartz crystals with respect to the crystallographic direction;

– a set of features that considers the relationship of only the thermal conductivity coefficients with respect to the crystallographic direction;

– a set of features that considers the relationship of only the coefficients of linear thermal expansion with respect to the crystallographic direction;

– a set of features that considers the relationship of only the elastic properties of quartz crystals with respect to the crystallographic direction.

The values for Young's modulus and Poisson's ratio provided in [181] were used to simulate the controlled laser thermal cleaving of an isotropic quartz wafer. The thermal conductivity coefficient and linear thermal expansion coefficient were calculated as the arithmetic mean of their values along the Z-axis and in the perpendicular direction.

As previously stated, for the comparative analysis, calculations were conducted for five distinct processing options of square-shaped crystalline elements with standard initial orientation. Additionally, four different sets of material features were applied for each processing option, considering the anisotropy of quartz crystals to varying extents.

The outcomes of the conducted calculations are presented in Tables 3.7 and 3.8, along with Figures 3.35–3.37.

Table 3.7 – Calculated values of maximum temperatures in the wafer

Pro-cessing option	Maximum temperature in the wafer T, K			
	h = 0.75 mm		h = 1.5 mm	
	v = 5 mm/s	v = 15 mm/s	v = 5 mm/s	v = 15 mm/s
I	1546	991	1116	820
II, V	1468	1013	1163	909
III, IV	1523	1049	1202	933

Table 3.7 displays the calculated maximum temperature values for a set of features, considering the anisotropic nature of thermal conductivity in quartz crystals.

Note that all calculated temperature values remain below the melting point of crystalline quartz. This condition is essential for the occurrence of brittle fracture in the wafer due to thermoelastic stresses. The calculated options indicate that the lower temperature values are associated with the operating mode of thick wafers (h = 1.5 mm) at a high speed (v = 15 mm/s).
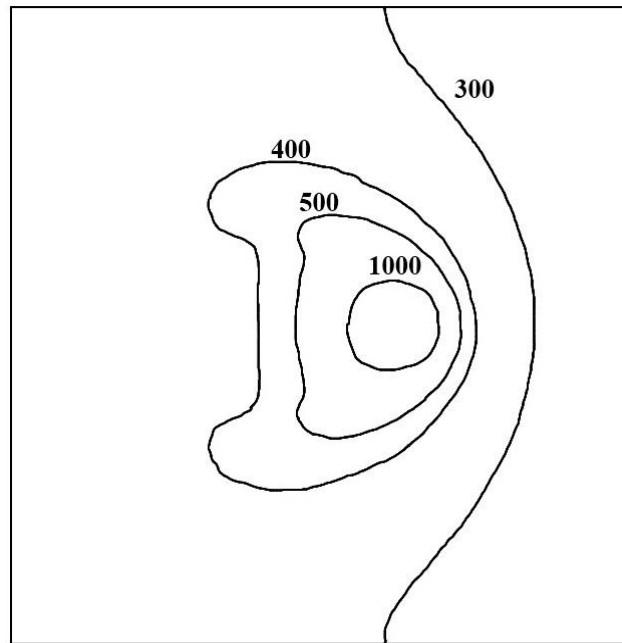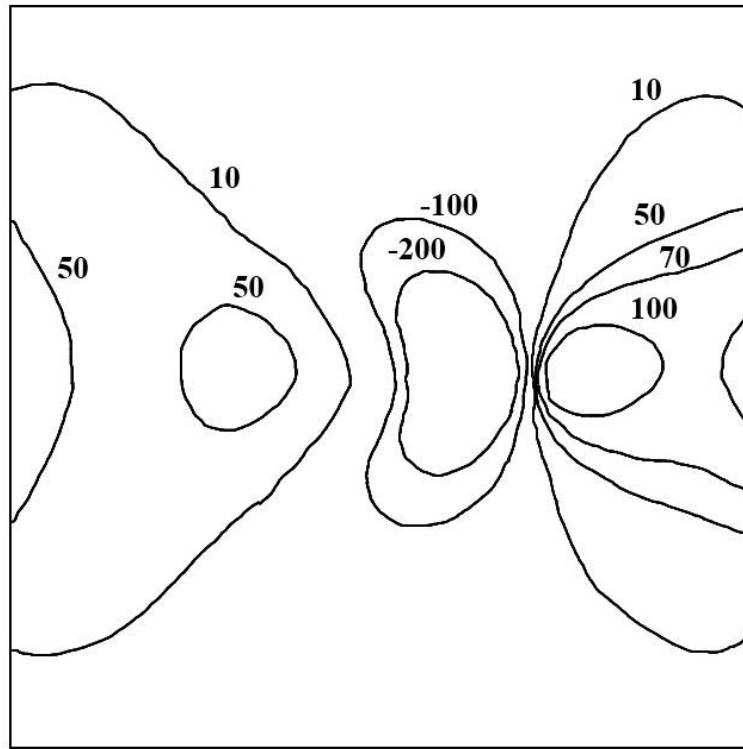

a
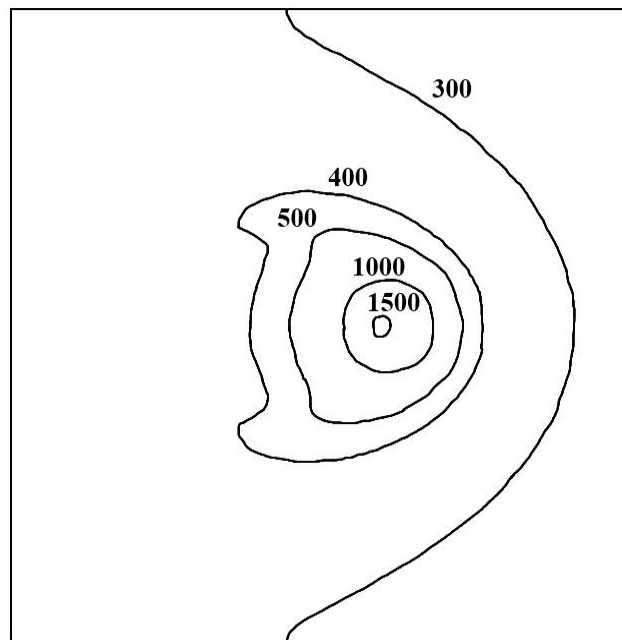
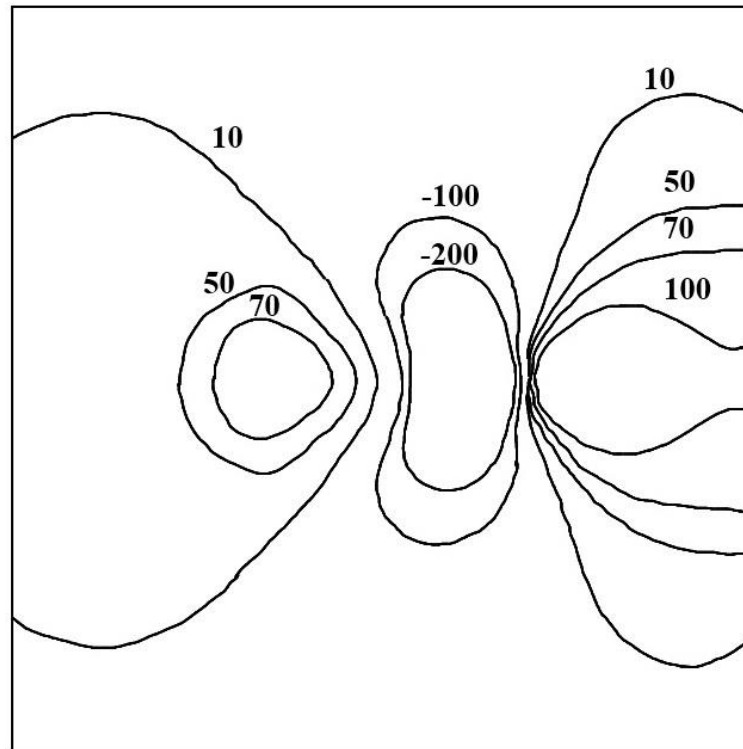
b

Figure 3.35 – Temperature field distribution on the quartz wafer surface
(v = 5 mm/s, h = 0.75 mm), K
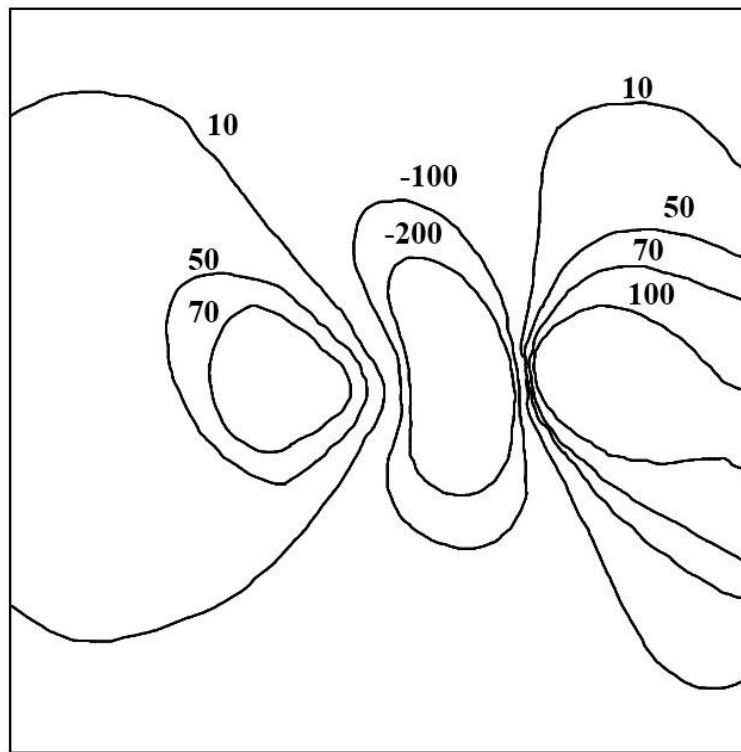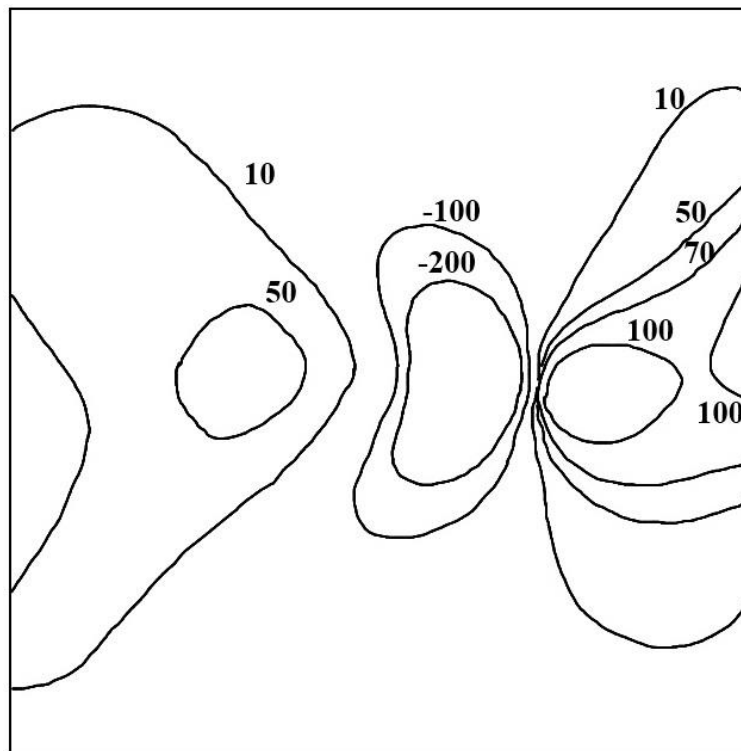a) processing options II and V, b) processing options III and IV

84

a)

b)

Figure 3.36 – Field distribution of thermal stresses on the quartz wafer surface
(v = 5 mm/s, h = 0.75 mm), MPa
a) processing option II, b) processing option III

Figure 3.37 − Field distribution of thermal stresses on the quartz wafer surface
(v = 5 mm/s, h = 0.75 mm), MPa
a) processing option IV, b) processing option V

Table 3.8 – Calculated values of maximum tensile and compressive stresses within the processing area

Option	Maximum stresses in the processing area, MPa	a set of features a)				a set of features b)			
		h = 0.75 mm		h = 1.5 mm		h = 0.75 mm		h = 1.5 mm	
		v = 5 mm/s	v = 15 mm/s	v = 5 mm/s	v = 15 mm/s	v = 5 mm/s	v = 15 mm/s	v = 5 mm/s	v = 15 mm/s
I	tensile	83.8	31.8	42.9	23.5	72.4	27.7	36.4	23.7
	compressive	641.9	328.4	414.2	262.5	550.0	278.4	337.8	211.3
II	tensile	63.5	21.1	33.2	26.5	69.5	27.0	40.5	31.3
	compressive	512.7	287.6	355.9	244.1	559.9	322.1	414.2	294.5
III	tensile	85.1	38.8	56.2	43.2	70.4	30.2	48.0	35.8
	compressive	607.3	388.4	459.1	335.2	528.4	314.1	395.2	618.0
IV	tensile	93.1	42.4	73.0	55.1	70.4	30.2	48.0	39.8
	compressive	628.5	377.3	480.8	355.3	528.4	314.1	395.2	286.5
V	tensile	65.7	22.7	34.3	26.3	69.5	27.0	40.5	31.3
	compressive	520.9	292.9	356.0	245.4	559.9	322.1	414.2	294.5
		a set of features c)				a set of features d)			
I	tensile	88.2	33.9	47.9	27.8	60.2	23.4	32.8	22.7
	compressive	669.4	377.8	473.9	326.3	449.5	253.6	312.5	215.7
II	tensile	49.6	16.4	22.3	14.2	88.4	33.1	47.2	34.5
	compressive	410.3	224.6	256.0	166.7	587.2	330.1	409.9	282.3
III	tensile	87.2	36.1	54.0	42.5	64.2	24.8	31.9	16.2
	compressive	590.2	335.0	418.7	295.5	512.0	284.5	348.7	232.2
IV	tensile	87.2	36.1	54.0	42.5	69.1	27.2	37.2	22.3
	compressive	590.2	335.0	418.7	295.5	524.8	294.3	357.7	244.1
V	tensile	49.6	16.4	22.3	14.2	87.2	33.7	47.2	33.9
	compressive	410.3	224.6	256.0	166.7	597.1	334.2	412.8	284.8

The anisotropy of thermal conductivity in quartz requires distinct attention to the temperature fields generated in the square-shaped elements for three cases of the five processing options analyzed in this study:

– the first case involves cutting the crystal wafer perpendicular to the Z-axis, with the cutting line positioned in the plane perpendicular to this axis (option I);

– the second case entails cutting the crystal wafer perpendicular to the Z-axis, with the cutting line positioned in the plane parallel to this axis (options II and V);

– the third case involves cutting the crystal wafer along the-Z axis, with the cutting line positioned in the plane parallel to this axis (options III and IV).

The analysis of the data presented in Table 3.7 indicates that the minimum temperature values occur during the processing of the zy-cut (processing option I). This phenomenon can be attributed to the significantly higher heat transfer coefficient along the Z-axis of quartz crystals compared to their values in the directions perpendicular to this axis ($\lambda\|$ exceeds $\lambda\perp$ by almost a factor of two).

The processing of the yx- and xy-cuts is associated with higher temperature values when the laser beam is moved along the Z-axis (III and IV processing options). It is important to highlight that these values are only marginally elevated compared to the temperature values generated during the processing of the same cuts when the laser beam travels along the X-axis and Y-axis, respectively (II and V processing options). Consequently, the greatest disparity between processing options III and II for the calculation parameters is limited to 3.6 %, whereas the difference between options III and I amounts to 12.1 %.

Table 3.8 presents the calculated values of the maximum tensile and compressive stresses generated in the processing area for the five examined processing options. The calculations allow us to assert that simulating controlled laser thermal cleaving of quartz crystals necessitates careful consideration of the anisotropy of all properties that affect the formation of thermoelastic fields in the sample. Considering just one of the material's anisotropic characteristics results in considerable errors. For instance, when considering solely the anisotropy of thermal conductivity in assessing the tensile stresses in the processing area for the examined modes, the error amounts to 34.2 %. If we take into account only the anisotropy of thermal expansion, the error increases to 46.4 %. Furthermore, when only the anisotropy of elastic properties is considered, the error escalates to 62.5 %.

The analysis of the data presented in Table 3.8 indicates that the maximum tensile stress values occur during the thermal cleaving of the yx- and xy-cuts when the laser beam is directed along the Z axis (processing options III and IV). The elevated temperature values observed during the implementation of processing options III and IV (see Table 3.7) contribute signifi-

cantly to this phenomenon when compared to other processing options. Furthermore, the development of elevated tensile stresses during the implementation of processing options III and IV is facilitated by increased values of the linear thermal expansion coefficient in the direction perpendicular to the plane of the laser-induced crack, as opposed to the values observed during the processing of the yx- and xy-cuts along the X and Y axes, respectively (processing options II and V).

The low temperature values in the processing area, combined with the minimal linear thermal expansion coefficient in the direction perpendicular to the laser-induced crack plane, result in reduced tensile stresses during the implementation of the II and V processing options. Tensile stresses generated at the zy-cut separation during processing option I exceed the calculated stresses for options II and V, while being lower than those for options III and IV. This outcome can be attributed to, firstly, the low temperature values in the processing area (see Table 3.7), and secondly, the significant values of the linear thermal expansion coefficient in the direction that is perpendicular to the plane of the laser-induced crack.

The results obtained highlight the critical significance of the anisotropic nature of thermal conductivity in quartz crystals, as well as the anisotropy of their thermal expansion, on the magnitude of thermoelastic stresses generated during the controlled laser thermal cleaving of this material. Nonetheless, the existence of anisotropy in elastic properties requires a distinct examination of all five options for the processing of square-shaped crystal elements with the standard initial orientation explored in this study. It is essential to focus on the unique characteristics of the spatial localization of the thermoelastic fields generated during the laser thermal cleaving of the xy-cut (IV and V modes). Figure 3.37 demonstrates that the distribution of thermoelastic fields generated during the controlled laser thermal cleaving of the xy-cut exhibits asymmetry in relation to the line of laser radiation exposure. The asymmetry of the elastic stress fields in practice results in an undesirable deviation of the laser-induced crack from the processing contour, which must be considered when selecting the parameters of thermal cleaving.

To validate the outcomes of the numerical simulation, experimental investigations were carried out employing laser radiation at a wavelength of 10.6 μm. Figure 3.38 presents an end view of the quartz wafer separated via the controlled laser thermal cleaving technique. The experimental results demonstrated the effectiveness of the simulation technique employed.

Thus, the findings indicate that it is essential to consider the anisotropic behavior of the thermal expansion, as well as the anisotropic characteristics of thermal conductivity and elastic properties in quartz crystals.

The simulation outcomes can inform the selection of parameters and enhance the process of precision separation of quartz wafers in the fabrication of crystal elements.
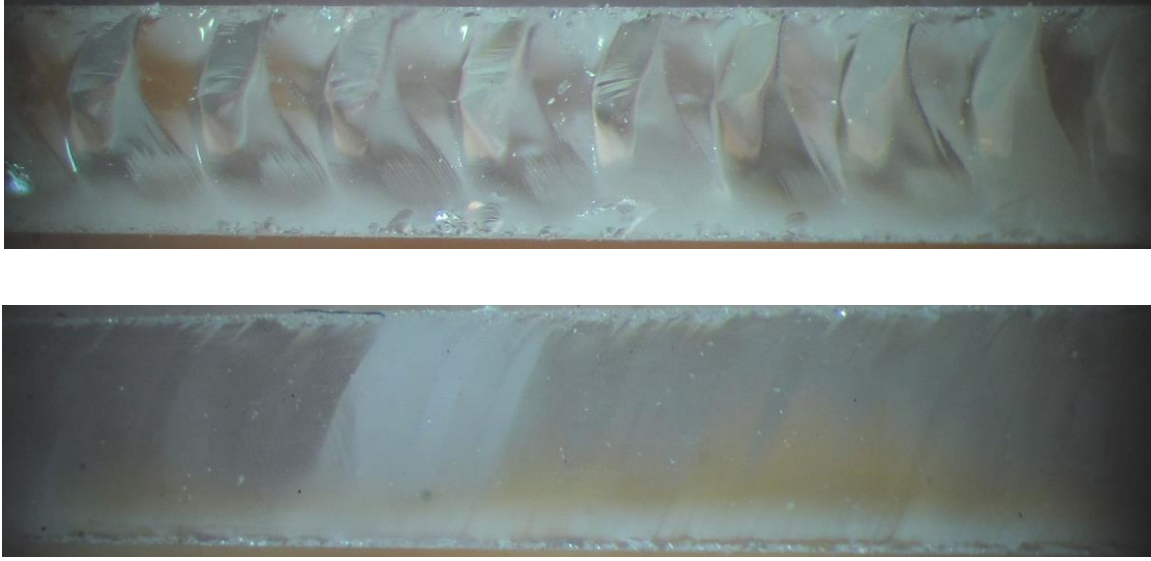

Figure 3.38 − End view of quartz wafers separated
through controlled laser thermal cleaving

Peculiar aspects of controlled laser thermal cleaving of crystalline quartz

In practical applications, quartz crystals of AT- and BT- cuts are the most commonly used [184]. In this context, we examined the unique characteristics of the laser thermal cleaving process for AT- and BT-cut quartz crystals.

Any arrangement of a crystal element with regard to the X, Y, Z axes can be achieved through a sequence of successive rotations from one of the initial orientations of this crystal element. For an AT-cut, a rotation of 35^0 is executed, while for a BT-cut, a rotation of 49^0 is carried out [185] (see Figure 3.39).

The matrix $\{C_{ik}\}$ for the AT-cut can be expressed as follows

$$\{C_{ik}\} = \begin{pmatrix} 86.74 & -8.25 & 27.15 & -3.66 & 0 & 0 \\ -8.25 & 129.77 & -7.42 & 5.70 & 0 & 0 \\ 27.15 & -7.42 & 102.83 & 9.92 & 0 & 0 \\ -3.66 & 5.70 & 9.92 & 38.61 & 0 & 0 \\ 0 & 0 & 0 & 0 & 68.78 & 2.57 \\ 0 & 0 & 0 & 0 & 2.57 & 28.96 \end{pmatrix} \cdot 10^9 \text{ Pa.}$$
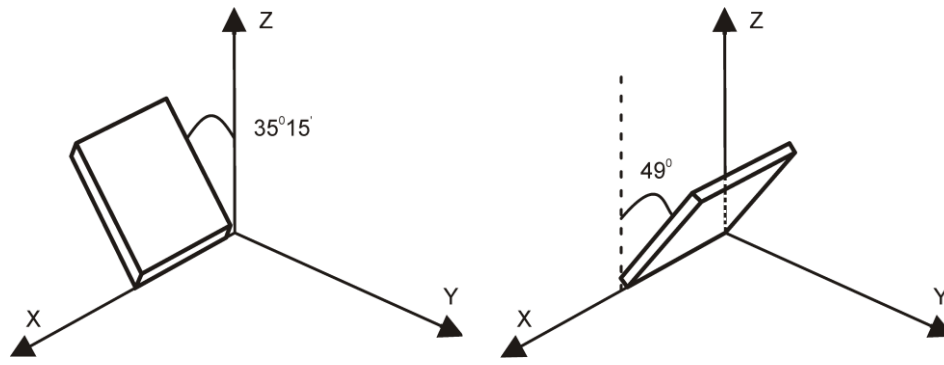
Figure 3.39 – AT- and BT-cuts of the crystalline quartz

Correspondingly, for the BT-cut, the matrix $\{C_{ik}\}$ is of the form

$$\{C_{ik}\} = \begin{pmatrix} 86.74 & 27.53 & -8.63 & 0.057 & 0 & 0 \\ 27.53 & 98.24 & -5.67 & -12.80 & 0 & 0 \\ -8.63 & -5.67 & 130.86 & 0.17 & 0 & 0 \\ 0.057 & -12.80 & 0.17 & 40.36 & 0 & 0 \\ 0 & 0 & 0 & 0 & 29.87 & -6.49 \\ 0 & 0 & 0 & 0 & -6.49 & 67.87 \end{pmatrix} \cdot 10^9 \text{ Pa}$$

The calculation of thermoelastic fields generated in a quartz wafer due to sequential laser heating and refrigerant exposure was carried out for four different options: I is the AT-cut analysis with the laser beam orientated parallel to the X-axis; II is the AT-cut analysis with the laser beam orientated perpendicular to the X-axis; III is the BT-cut analysis with the laser beam orientated parallel to the X-axis; IV is the BT-cut analysis with the laser beam orientated perpendicular to the X-axis.

The thermoelastic stress fields generated in quartz wafers during laser cleaving were calculated using the finite element method, adhering to the uncoupled thermoelastic problem within the quasi-static formulation [139, 152].

Calculations were conducted for square wafers with geometric dimensions of 20×20×1.5 mm and 20×20×0.75 mm. The simulation process was performed for the scenario involving exposure to laser radiation at a wavelength of 10.6 μm. The radius of the laser radiation spot was R = 1.5 mm, and the power of the radiation was P = 50 W. The wafer movement speed in relation to the laser beam and refrigerant was set at v = 5 mm/s and v = 15 mm/s.

The outcomes of the computations are presented in Tables 3.9 – 3.10 and Figures 3.40 – 3.41.

Table 3.9 presents the maximum temperature values recorded in the quartz wafer for the four processing options analyzed. The values for maximum thermoelastic tensile and compressive stresses are provided in Table 3.10.

Table 3.9 – Calculated values of maximum temperatures in the wafer undergoing processing

Option	Maximum temperature in the wafer T, K			
	h = 0.75 mm		h = 1.5 mm	
	v = 5 mm/s	v = 15 mm/s	v = 5 mm/s	v = 15 mm/s
I	1520	994	1125	842
II	1538	1005	1136	847
III	1502	999	1135	862
IV	1531	1018	1156	871

Table 3.10 – Calculated values of maximum tensile and compressive stresses in the processing area

Option	Maximum stresses in the processing area, MPa	h = 0.75 mm		h = 1.5 mm	
		v = 5 mm/s	v = 15 mm/s	v = 5 mm/s	v = 15 mm/s
I	compressive	650	343	431	281
	tensile	85	33	45	22
II	compressive	717	381	483	319
	tensile	100	40	53	34
III	compressive	605	322	401	264
	tensile я	77	27	42	19
IV	compressive	563	316	395	272
	tensile	74	31	50	30

Figures 3.40 and 3.41 illustrate the distributions of temperature fields and thermal stresses for wafers with a thickness of h = 0.75 mm, processed at a speed of v = 5 mm/s.

The review of the data in Table 3.9 suggests that the anisotropic characteristics of quartz crystal properties, when considering AT- and BT- cuts, do not have a substantial impact on the peak temperature values within the processing area. Significantly more critical elements include parameters like processing speed and the geometric dimensions of the wafer being processed. Consequently, the variations induced by the anisotropy of thermophysical properties result in maximum temperature differences that do not exceed 3 %. In contrast, the differences arising from processing speed and sample geometry for the chosen design parameters can reach up to 45 %.

The analysis of the data values presented in Table 3.10 indicates that both the processing speed and the geometric dimensions of the wafer significantly affect the thermoelastic stresses generated in the processing area. The variations resulting from these factors contribute to a disparity in the maximum tensile stress values, ranging from 50 % to 80 %. The anisotropy of quartz crystal properties significantly influences the maximum values of thermoelastic stresses in the processing area. Consequently, the observed differences in the maximum values of tensile stresses surpass 35 %. It is essential to consider this variation in tensile stress values when determining the parameters for the laser thermal cleaving process.
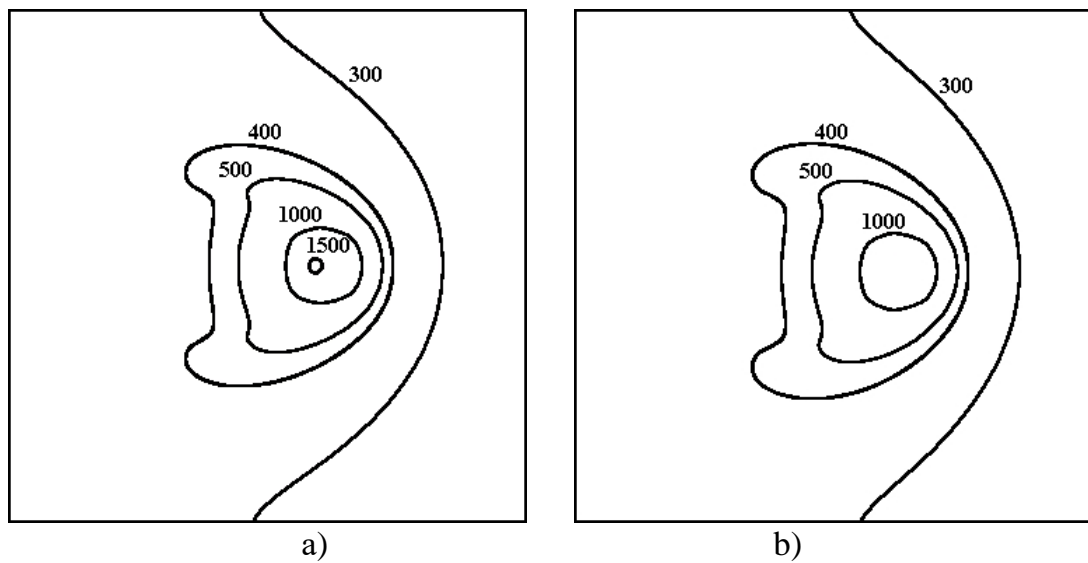

Figure 3.40 – Temperature field distribution on the crystalline quartz surface: a) option I; b) option III
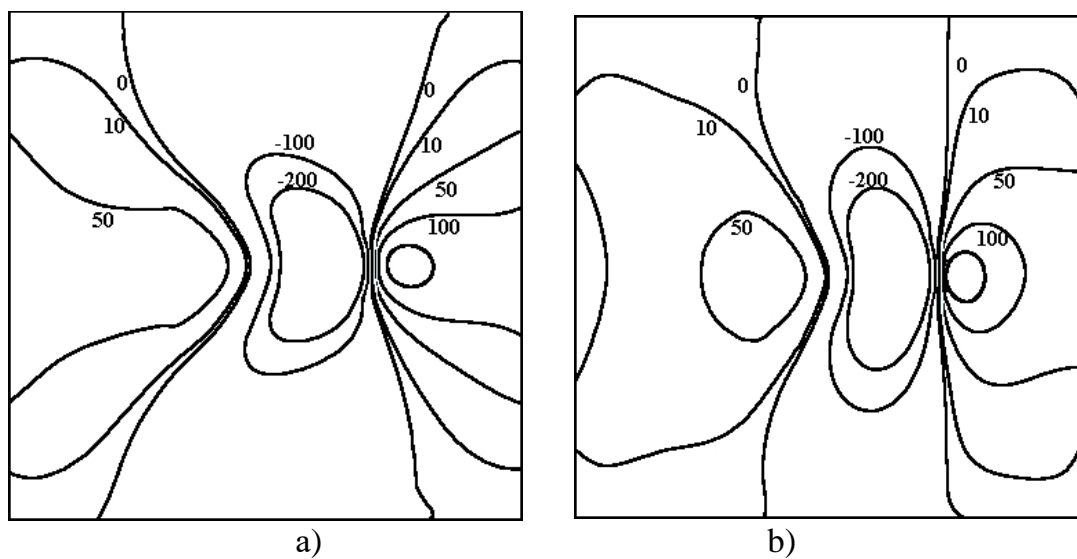

Figure 3.41 – Thermoelastic stress field distribution on the crystalline quartz surface: a) option I; b) option III

The results reveal the importance of considering the anisotropic properties of quartz crystals when determining the parameters for laser thermal cleaving of AT- and BT-cut quartz wafers.

3.8. Simulation of laser processing for diamond crystals

Diamond stands out as a highly promising material for the development of next-generation equipment. The distinct physical characteristics guarantee reliable performance in the demanding environments of devices utilizing it [210]. In examining the present landscape of technology for processing super hard materials, it becomes evident that laser processing offers considerable benefits compared to alternative techniques for cutting diamond crystals. The benefits of this technology primarily encompass its high-power density and the localized effect attained through the concentration of laser radiation on the material being processed. This capability allows for the creation of narrow cuts with minimal thermal influence, all while maintaining a high level of productivity in dimensional processing. Furthermore, it is important to highlight the significant technological performance of laser radiation, which enables the automation of the treatment process while maintaining high quality [1].

As stated in [187], it is particularly noteworthy to investigate the efficiency of laser processing of diamonds in various crystallographic directions, specifically when laser radiation is directed along the third- and fourth-order symmetry axes. Regrettably, the referenced study conducts the simulation of temperature fields using a one-dimensional approach, which considerably undermines the reliability of the numerical estimates obtained.

The paper [188] presents the results of a three-dimensional simulation of hole formation induced by laser radiation along the third and fourth order symmetry axes of diamond crystals.

This study elucidates the distinctive effects of laser radiation on diamond crystals along three crystallographic orientations (aligned with the symmetry axes of the second, third, and fourth order) during the relative motion of the laser beam and the affected surface.

The application of laser on diamond crystals during dimensional processing results in a substantial rise in temperature, accompanied by phase transitions. Figure 3.42 illustrates a generalized schematic of phase transformations in diamond crystals induced by laser radiation [187].

According to this schematic, laser cutting of diamond crystals leads to their graphitization, evaporation, recrystallisation, and the production of diamond polycrystals. The examination of all aforementioned changes in

simulation poses considerable challenges; hence, this study employed a simplified model of diamond transformations induced by laser radiation: diamond $\Rightarrow$ phase transition $\Rightarrow$ graphite $\Rightarrow$ evaporation. The intensive graphitization stage of diamond crystals is considered to occur when the material attains a temperature of 2300 K.
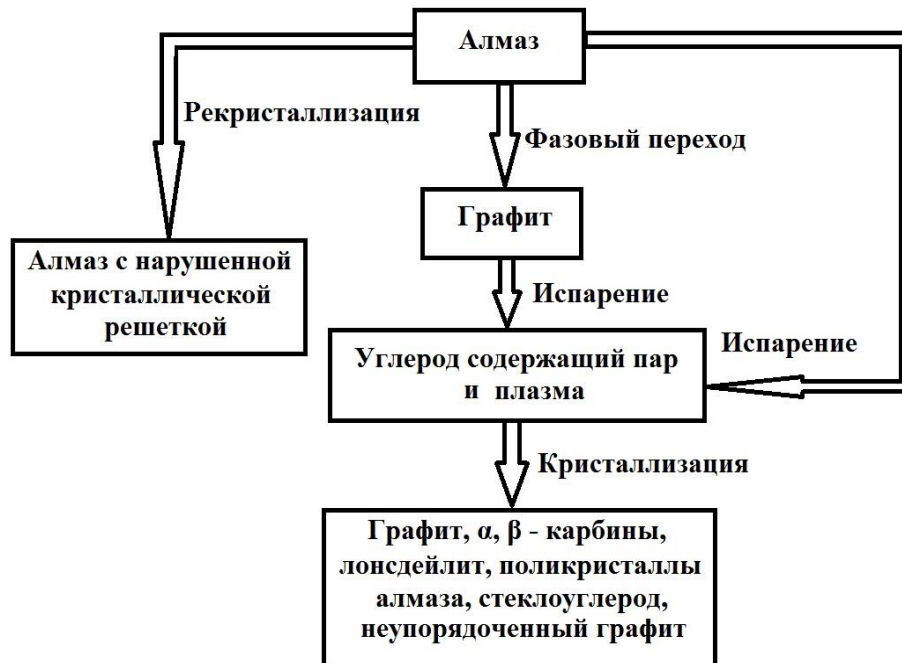

Figure 3.42 – Schematic representation of transformations of diamond induced by laser radiation

The finite element method [139] was employed to examine the characteristics of laser processing in diamond crystals. The simulation of the diamond–graphite phase transition involved cyclic verification of the attainment of the graphitization temperature by the material's points, followed by the allocation of graphite thermophysical properties to the relevant regions of the finite element model. The precise alignment of hexagonal graphite planes parallel to the (111) planes of diamond crystals was considered, irrespective of the direction of the incident laser radiation.

In the calculations, the density, specific heat capacity, and thermal conductivity coefficient of diamond and graphite were assumed to be equal to the following values: ρ_a = 3520 kg/m³, ρ_g = 2300 kg/m³; C_a = 854 J/kg·K, C_g = 994 J/kg·K; λ_a = 427 W/m·K, $\lambda_g^{\perp}$ = 88 W/m·K, $\lambda_g\|$ = 355 W/m·K [187]. The symbol $\lambda_g^{\perp}$ stands for the thermal conductivity coefficient of graphite in the direction that is perpendicular to the hexagonal faces, while the symbol $\lambda_g\|$ indicates the thermal conductivity coefficient of graphite in the direction that is parallel to the hexagonal faces.

The calculation of temperature fields generated in diamond crystals due to laser heating was conducted for four distinct options: I is the three-dimensional analysis influenced by laser radiation along the second-order symmetry axis (L2), II is the three-dimensional analysis influenced by laser radiation along the third-order symmetry axis (L3), III is the three-dimensional analysis influenced by laser radiation along the fourth-order symmetry axis (L4), IV is the three-dimensional analysis excluding graphitization effects under the influence of laser radiation.

The process of laser heating of diamond crystals was simulated following the scheme illustrated in Figure 3.43, with 1 indicating the laser beam and 2 representing the diamond sample. The arrow, accompanied by the designation $\vec{v}$ in the figure, shows the direction of movement of the workpiece in relation to the laser beam.

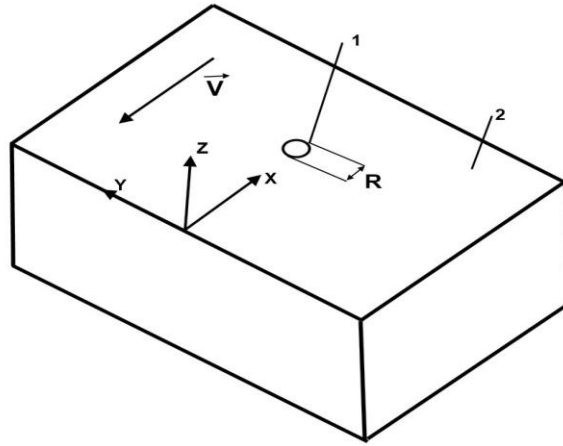Figure 3.44 illustrates the partitioning of the crystal into finite elements.

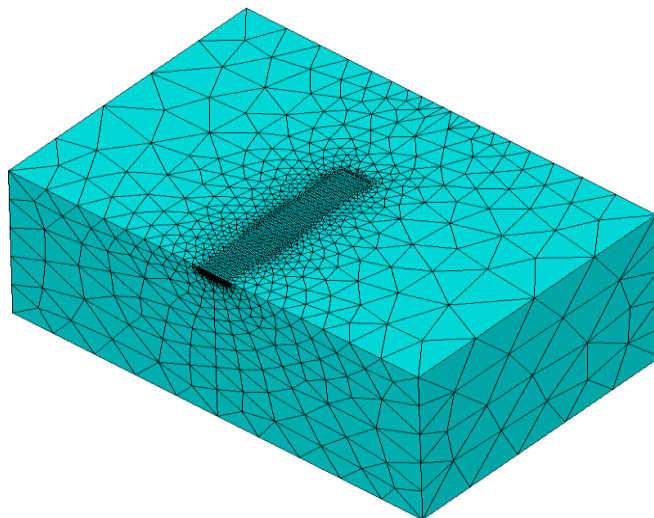Figure 3.43 − Arrangement of the laser beam within the processing area

Figure 3.44 – Finite element partitioning of the computational domain

96

Calculations were performed for a sample shaped as a rectangular parallelepiped with geometric dimensions of 2×3×1.5 mm, using the specified values of technological processing parameters: laser power density $P_0 = 1.8 \cdot 10^{10}$ W/m², radius of the laser beam cross-section R = 0.05 mm. The modulus of the relative velocity of the laser beam and the sample was V = 7 mm/s.

As previously stated, the simulation was conducted under four distinct sets of conditions: I is the laser beam is orientated along the L2 axis, II is the laser beam is orientated along the L3 axis, III is the laser beam is orientated along the L3 axis, IV is the diamond-graphite phase transition was excluded from the simulation. The findings of the calculations are provided in Figures 3.45 – 3.48.
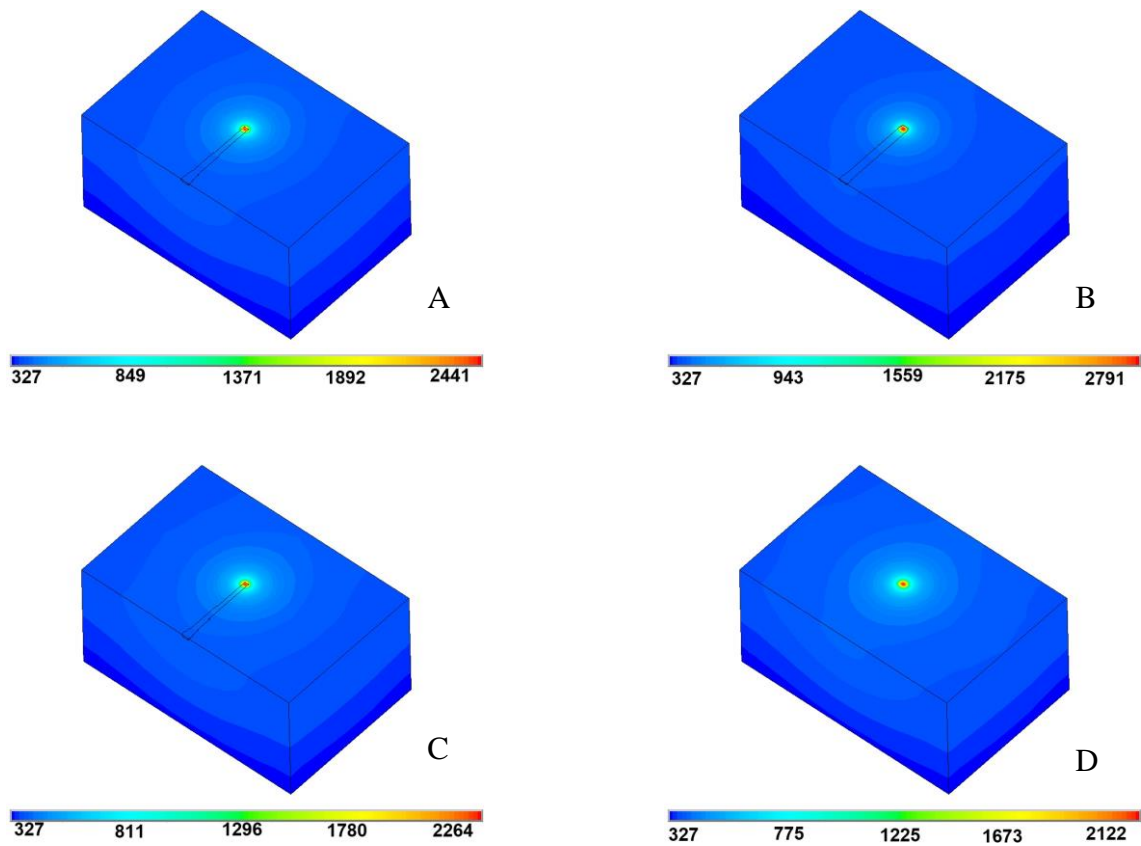

Figure 3.45 – Temperature distribution in diamond crystal, K
A – processing option I, B – processing option II,
C – processing option III, D – processing option IV

Figure 3.45 illustrates the computed distributions of temperature fields generated in diamond crystals during laser processing, while Figures 3.46 and 3.47 present the calculated time dependences of temperature at the center of the beam cross-section.
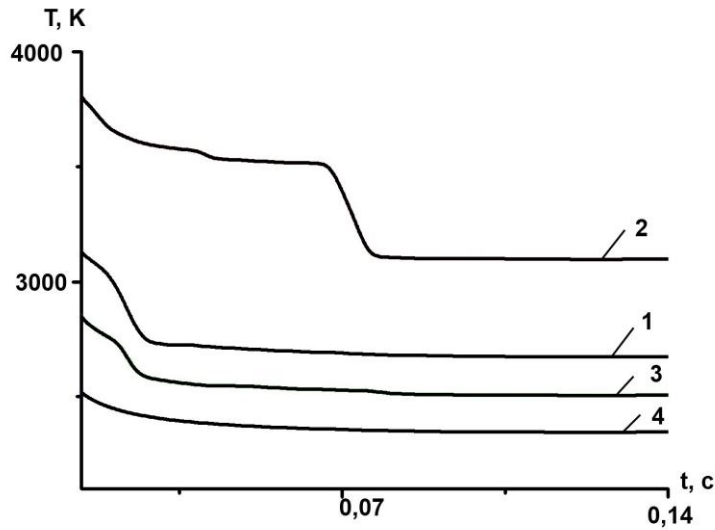
Figure 3.46 − Calculated temperature variation over time at the center
of the beam cross-section
1 – processing option I, 2 – processing option II, 3 – processing option III,
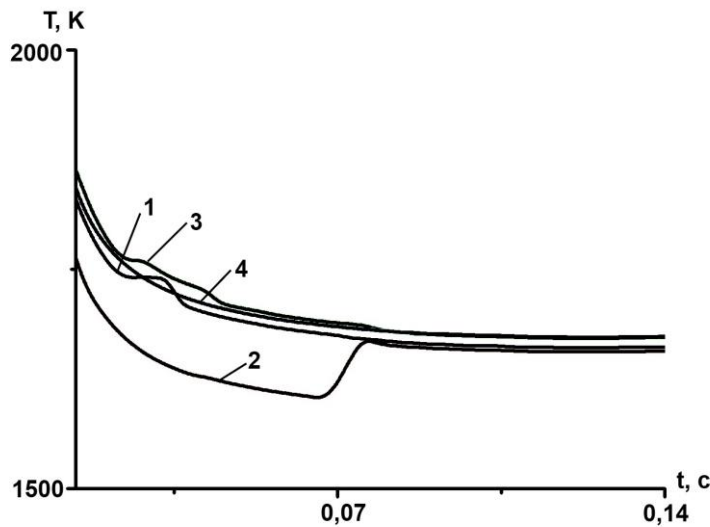4 – processing option IV
(Z = 0, Y = 0)

Figure 3.47 − Calculated temperature variation over time at the center
of the beam cross-section
1 – processing option I, 2 – processing option II, 3 – processing option III,
4 – processing option IV
(Z=-2·10-5, Y=0)

Upon examination of the data provided in Figures 3.45 and 3.46, it is evident that the temperature within the laser processing area attains its peak values when the laser beam aligns parallel to the L3 axis, with the maximum temperature recorded at the transition to stationary mode being 3099 K.

When exposed to laser radiation along the axes L2 and L4 of the crystal, the observed maximum temperature values are 2675 K and 2506 K, respectively. The temperature in the laser impact area was recorded as the lowest in the simulation, excluding the diamond-graphite phase transition, with the maximum temperature in stationary mode reaching 2346 K. Figure 3.47 illustrates that there is no notable difference in the temperature values obtained across all four simulation options when achieving the steady-state mode of cutting at a short distance from the surface along the laser beam axis.

Figure 3.48 demonstrates the computed configurations of graphitization regions on the surface of a diamond crystal. The data indicates that the largest cut width occurs when the laser beam is aligned with the L3 axis, while the narrowest cut width is observed when the crystal is irradiated along the L4 axis. The graphitization region created during processing along the L4 axis exhibits a clear asymmetry in relation to the displacement line of the laser beam's cross-sectional center.
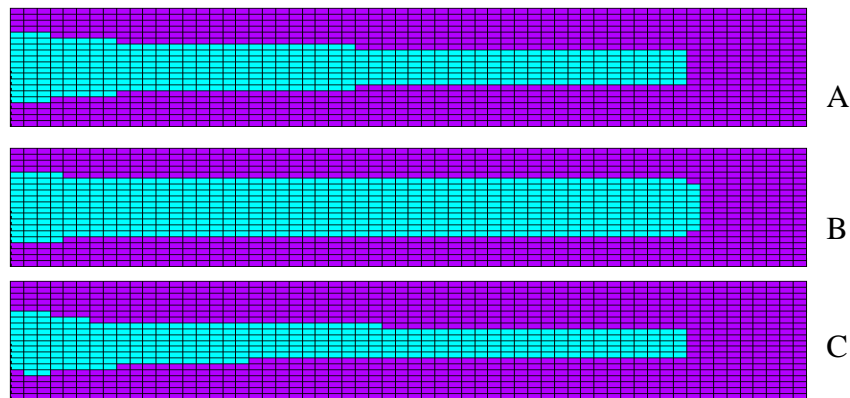

Figure 3.48 – Computed configuration of the graphitization region on the surface of a diamond crystal
A – processing option I,
B – processing option II,
C – processing option III

The revealed features of the formation of temperature fields and graphitization regions can be attributed to the consideration of the strict orientation of hexagonal graphite faces parallel to the (111) planes of diamond during the simulation process. The anisotropic nature of graphite's thermophysical properties explains why the temperature in the processing area and the cut width attain their maximum values when laser radiation is directed along the L3 axis, while the minimum values occur when it is oriented along the L4 axis. The temperature values and parameters of the graphitization region for the diamond crystal processing option with laser radiation along the L2 axis are situated in an intermediate range compared to the values derived from the other two processing options discussed here.

The noted disparity in temperature values and substance parameters inside the graphitization region must be considered while determining laser processing settings.

Peculiar aspects of thermoelastic field formation during laser processing of diamond crystals

The localization features of thermoelastic stress fields that are generated in diamond crystals under laser exposure in the aforementioned crystallographic orientations require consideration.

The calculation of thermoelastic stress fields generated in diamond crystals due to laser impact was performed using the finite element method within the context of the unrelated thermoelasticity problem in a quasi-static framework [139, 152, 153]. The process of simulating the diamond–graphite phase transition was conducted following the algorithm outlined in [189].

Diamond is classified within the cubic system, which allows for the characterization of its elastic properties through three independent components of the elastic modulus tensor. The elastic rigidity constants used for calculations are as follows: C_{11} = 1079 GPa, C_{12} = 124 GPa, C_{44} = 578 GPa [190]. Simultaneously, the values for Young's modulus and Poisson's ratio provided in [191] were used to simulate the laser treatment of an isotropic diamond plate.

The calculation of thermoelastic fields generated in diamond crystals due to laser irradiation was conducted for four distinct options: I is the analysis of the effects of laser radiation along the second-order symmetry axis (L2), II is the analysis of the effects of laser radiation along the third-order symmetry axis (L3), III is the analysis of the effects of laser radiation along the fourth-order symmetry axis (L4), IV is the analysis of the effects of laser radiation without considering graphitization and anisotropy properties of diamond crystals. At the same time, the simulation for the first three calculation options was executed with an emphasis on graphitization.

Calculations were carried out for a sample shaped as a rectangular parallelepiped with geometric dimensions of 2 mm×3 mm×1.5 mm, using the specified values of technological processing parameters: laser radiation power density P_0 = 1.8 × 10^{10} W/m², the laser beam cross-section radius R = 0.05 mm. The modulus of the relative velocity of the laser beam and the sample was V = 7 mm/s.

The results of the performed calculations are presented in Table 3.11 and Figure 3.49. In Table 3.11, σ_{xx} denotes the stresses acting along the X-axis, and σ_{yy} represents the stresses acting along the Y-axis, as depicted

in Figure 3.43. Figure 3.49 shows the calculated field distributions of thermal stresses in the case of laser processing of diamond crystals along the fourth-order symmetry axis.
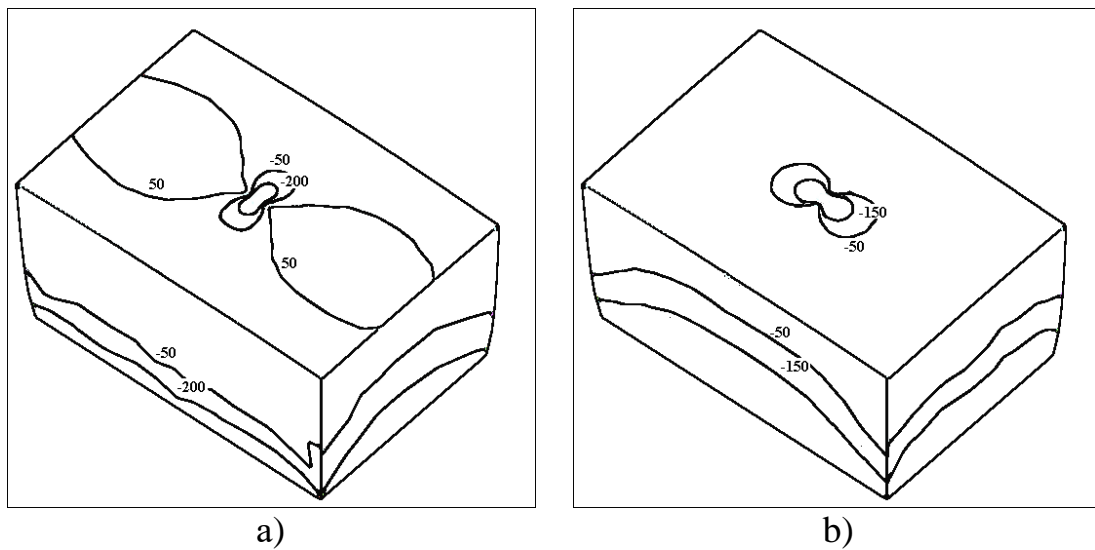

a)   b)

Figure 3.49 – Field distribution of thermoelastic stresses in diamond during
its processing along the L4 axis: a) σ_{xx} stresses; b) σ_{yy} stresses

Table 3.11 – Outcomes related to the calculations associated with the simulation of laser processing on diamond crystals

Processing option / Maximum stresses in the processing area, MPa		I 110	II 111	III 100	IV
σ_{xx}	tensile	98	90	96	95
	compressive	1230	1850	1070	1020
σ_{yy}	tensile	117	95	91	110
	compressive	1460	2090	1260	1200

The examination of the data presented in Table 3.11 indicates that considering the anisotropy of diamond crystal properties and the graphitization process significantly influences the values of thermoelastic stresses in the laser processing area. This leads to the conclusion that employing an isotropic model for the laser processing of diamond crystals results in significant errors. In comparing the maximum stresses generated in the diamond crystal processing area along the L2 axis, it is evident that employing the isotropic model results in an error of up to 18 %. When simulating the diamond crystal processing along the L3 and L4 axes, the observed errors are 45 % and 14 %, respectively. Furthermore, it is important to highlight that

101

the variation in the maximum stress values generated during processing along various symmetry axes spans from 8 % to 42 %. It is essential to consider this variation in tensile stress values when determining the parameters for laser processing of diamond crystals.

3.9. Enhancing the effectiveness of laser controlled thermal cleaving of silicate glasses using the photoelastic technique

During the implementation of laser cleaving, variations from the established processing parameters can arise due to factors such as inconsistencies in refrigerant supply, a decrease in laser radiation power density, and the presence of defects in the material being processed, among others.

The combination of these factors results in the disruption of the splitting crack's development, necessitating ongoing visual monitoring to ensure timely intervention in the separation process or adjustments to processing parameters.

To automate the management of splitting crack development and the dynamic alteration of processing parameters during the laser cutting of silicate glasses, the use of the photoelastic approach is recommended.

One of the criteria for analyzing the initiation and progression of a splitting crack is the excess of the stresses in the material beyond its tensile strength. For brittle materials, the subsequent criteria can be chosen as applicable stresses: the criterion for the maximum normal stresses, according to which the cause for material failure is considered to be the highest of the three principal main normal stress; the criterion for maximum tangential stresses, according to which it is assumed that the limit state of the material occurs when the highest tangential stress reaches its permissible value, which is determined from tensile-compression experiments ($\sigma_{eq}=\sigma_1-\sigma_3$); the criterion for specific potential energy of shape alteration, when the dangerous state occurs once the specific potential energy of shape alteration reaches its limit value, which is determined from simple tensile-compression experiments (comparison is based on equivalent on Mises stresses).

The polarization-optical method, also known as the photoelastic method, relies on a physical and mechanical phenomenon. In this process, linearly-polarized waves, as they traverse a deformed element of a transparent model, experience a phase shift or optical travel difference. The extent of this shift is contingent upon the stress-strain state of the element. The interference pattern derived from the superimposition of these waves allows for the extraction of information regarding the magnitude and spatial distribution of stresses or deformations present in the material being analyzed. This method's practical application is demonstrated in several studies [192–196].

A prototype setup was developed to dynamically ascertain the values of thermoelastic stresses, allowing for subsequent adjustments of the processing parameters. The schematic representation of this setup is illustrated in Figure 3.50 [197].
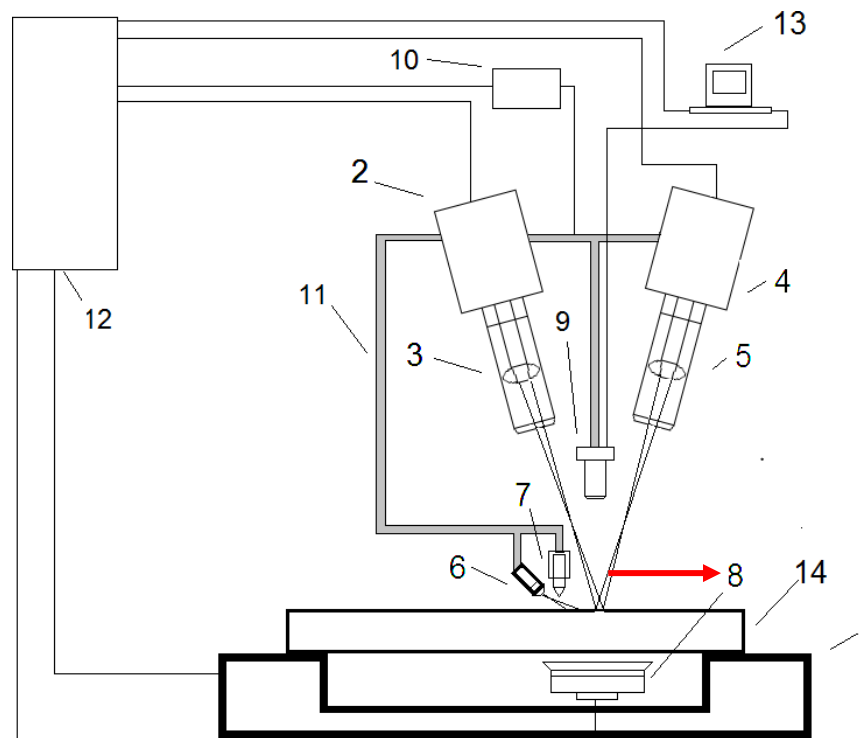

Figure 3.50 – Setup for laser cutting of silicate glasses:
1 is the coordinate table, 2 is the laser, 3 is the focusing lens, 4is the laser,
5 is the focusing lens, 6 is the refrigerant supply unit, 7 is the defect mechanism,
8 is the polarized light source, 9 is the video camera with analyzer,
10 is the vertical displacement mechanism, 11 is the carriage,
12 is the set-up control unit, 13 is the computer

A video camera equipped with an analyzer and a polarized light source is used to visualize the distribution of thermoelastic stresses in the developed prototype. The acquired image allows for the analysis of the resulting isochromes and isoclines, leading to the calculation of thermoelastic stresses. If required, adjustments can be made to the technological parameters of processing, such as radiation power density, processing speed, and refrigerant supply intensity.

Figure 3.51 illustrates the interference patterns achieved through controlled laser thermal cleaving with this prototype setup. The patterns are acquired without a crack (Figure 3.51. a), with a nonthrough crack (Figure 3.51. b), and with a through-the-thickness splitting crack (Figure 3.51. c).
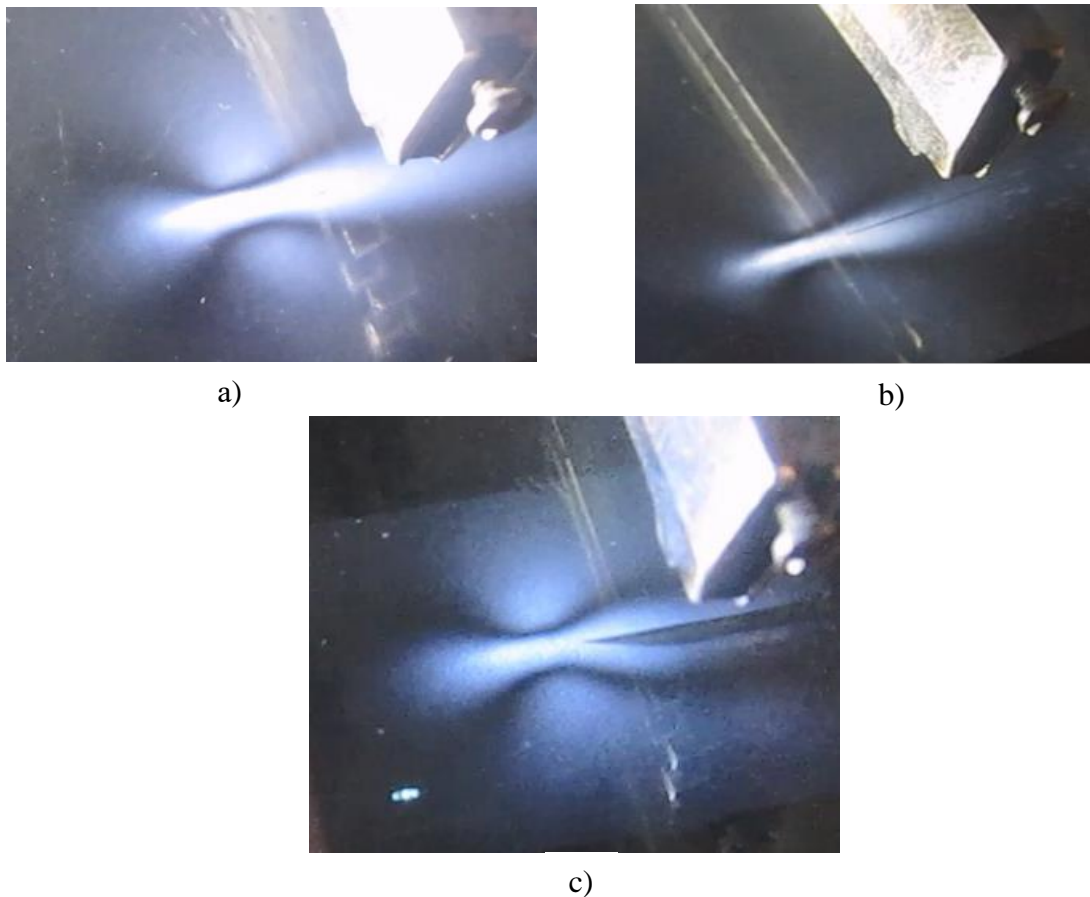
a)

b)

c)

Figure 3.51 − Images of the processing area captured using
the photoelastic technique
a is the area of laser beam and refrigerant exposure, b is the non-through
thickness splitting crack, c is the through-the-thickness splitting crack

Figures 3.52 and 3.53 illustrate the computed stress distributions in the sample at a specific moment, highlighting the conditions with and without a nonthrough splitting crack. The computations were executed using the finite element method.

The design parameters for processing silicate glass and its properties were selected based on the experimental findings. Given that the motion of the beam and the refrigerant occurs along the center of the sample, and considering the symmetry on either side of the separation plane, the representation of the fields is provided for half of the sample. The front face of the sample represents a section along the material separation plane.

The analysis of Figures 3.52a and 3.52b reveals a pronounced region of tensile stresses on the material's surface in the refrigerant supply area, characterized by a rapid cooling effect on the material. The peak stresses are concentrated along the path of the laser beam or beams, as well as the impact of the refrigerant. The crack nucleation takes place at the material's surface. The area of tensile stresses, resulting from the influence of the refrigerant, penetrates deeply into the material and is constrained from beneath by the

104

areas of compressive stresses generated by the laser beams. The development of the nucleated crack is constrained within these regions, preventing it from penetrating deeply into the material.
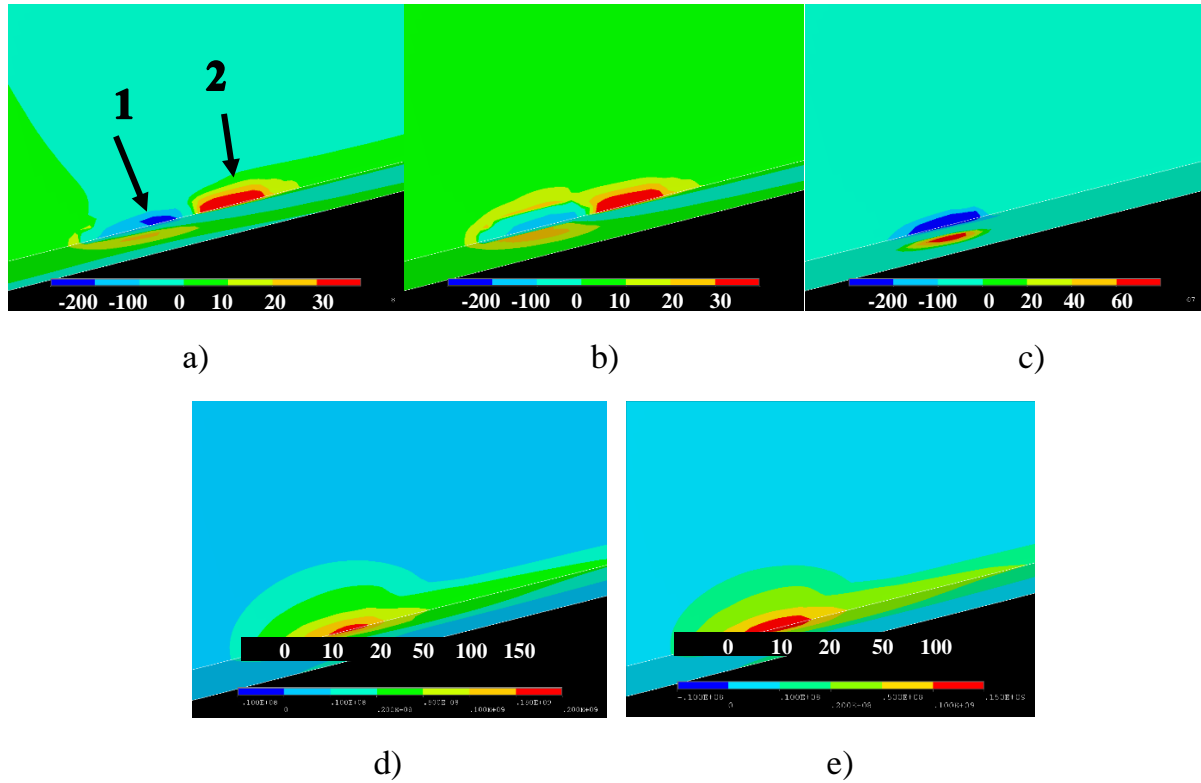

Figure 3.52 – Distribution of thermoelastic fields in the sample (MPa) during laser processing in the absence of a splitting crack:
a) stresses σ_{22} perpendicular to the separation plane,
b) principal stresses σ_1, c) principal stresses σ_3,
d) stress intensity $\sigma = \mathrm{MAX}\left(\left|\sigma_1 - \sigma_2\right|, \left|\sigma_2 - \sigma_3\right|, \left|\sigma_3 - \sigma_1\right|\right)$,
e) von Mises equivalent,
1 is the laser radiation exposure area, 2 is the refrigerant exposure area

The interference pattern reveals regions of significant compressive and tensile stresses, indicated by zones exhibiting heightened intensity of transmitted light. The analysis of this image alongside the computed distribution of stress intensity (specifically, the maxima of the difference of principal stresses) and the Mises distribution of equivalent stresses leads to the conclusion that the intensity of transmitted light is directly related to the magnitude of stresses. As the value of stresses increases, so does the intensity of the polarized light. Nonetheless, distinguishing between the areas of compressive and tensile stresses based on these images proves to be challenging.

Figures 3.51a and 3.51b illustrate that a dark band is observed along the boundaries of a splitting crack. This phenomenon can be attributed to the existence of a free surface that is perpendicular to the surface of the material,

as well as the near-zero stress values in the vicinity of the crack faces. This observation is further validated by numerical simulation within the context of linear fracture mechanics, as depicted in Figure 3.53.
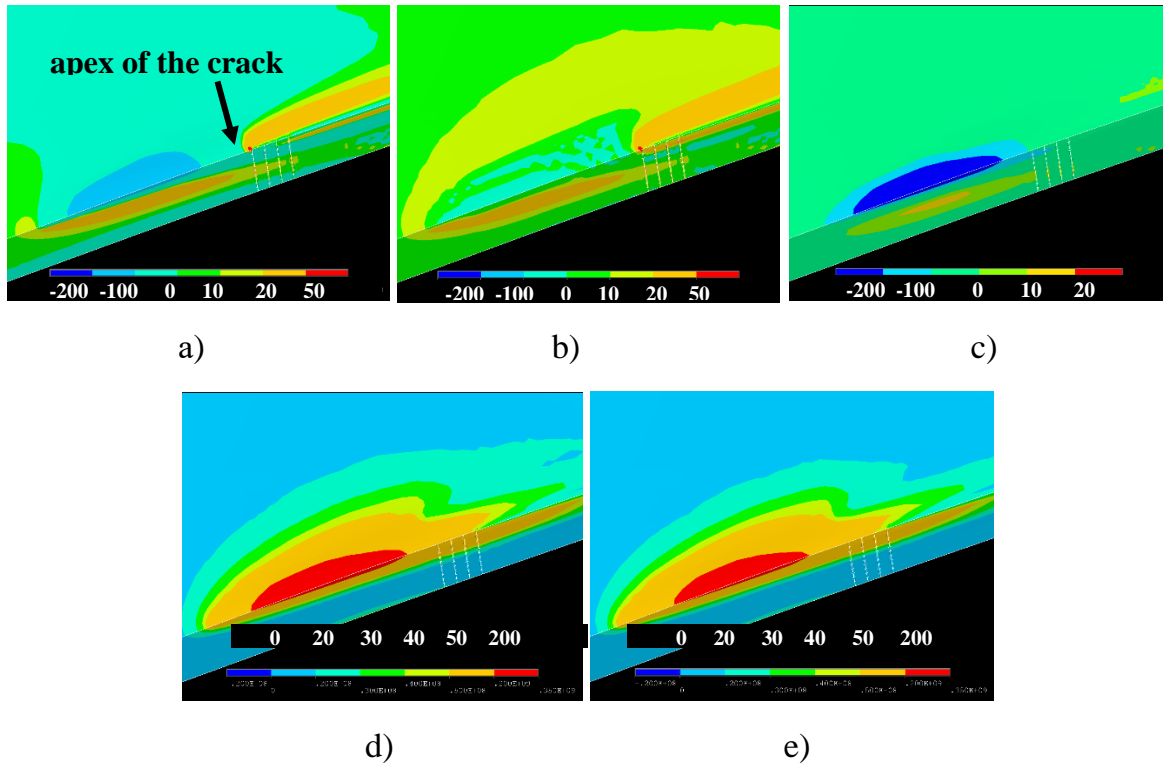

Figure 3.53 – Distribution of thermoelastic fields in the sample (MPa) during laser processing in the presence of a splitting crack in the material
a) stresses σ_{22} perpendicular to the separation plane,
b) principal stresses σ_1, c) principal stresses σ_3,
d) stress intensity $\sigma = \mathrm{MAX}\left(\left|\sigma_1 - \sigma_2\right|, \left|\sigma_2 - \sigma_3\right|, \left|\sigma_3 - \sigma_1\right|\right)$,
e) von Mises equivalent

By examining the intensity of the transmitted polarized light in the region where the refrigerant is present, one can determine whether a splitting crack is present or not. A distinct dark band along the material processing line signifies the existence of a crack, whereas a consistent area of uniform intensity allows us to confirm its absence. This enables the creation of a computer program that can dynamically identify the presence of a splitting crack during the controlled laser thermocleaving of silicate glasses. It does this by analyzing images captured by a video camera and can adjust the processing parameters or halt the technological process as required.

CHAPTER 4. CONTROLLED DOUBLE-BEAM LASER THERMAL CLEAVING OF BRITTLE NON-METALIC MATERIALS

When processing brittle non-metallic materials using laser thermo-cleavage methods, CO_2 laser radiation at a wavelength of 10.6 μm is predominantly employed. This wavelength is effectively absorbed in the thin surface layers of silicate glasses and alumina ceramics, serving as the primary technological tool (Section 1).

The application of radiation from solid-state lasers emitting at a wavelength of 1.06 μm for the high-precision processing of silicate glasses and alumina ceramics has not been sufficiently adopted. This is primarily due to the minimal absorption of such radiation in these materials, leading to inefficiencies in the processing methods employed [7]. The utilization of radiation at a wavelength of 1.06 μm is advantageous for the processing of thick wafers composed of silicate glass and alumina ceramics. This advantage arises from the volumetric absorption characteristics of the specified wavelength within these materials.

In the analysis of existing literature and our experimental studies, it was observed that the efficiency of the separation process for brittle nonmetallic materials, when using radiation at a wavelength of 1.06 microns, was found to be insufficiently high.

The current most effective method for high-precision processing of brittle nonmetallic materials, known as CLT, presents a notable disadvantage that limits its broader implementation. The limitation of the depth of the splitting microcrack when using laser radiation at a wavelength of 10.6 μm is attributed to its considerable absorption by the surface layers of silicate glasses and alumina ceramics.

The most effective solution for various challenges in laser technology is achieved through double-beam processing methods, which involve the simultaneous exposure of materials to two laser radiation beams of differing wavelengths. The results of studies on the threshold behavior of metal cutting using the combined radiation of a CO_2 laser and a pulsed YAG laser, as presented in [198], indicate that the enhancement in process efficiency is attributable to the implementation of double-beam technology.

It is essential to develop a new double-beam method aimed at high-precision processing of brittle nonmetallic materials. This method should incorporate the primary advantages of CLT while enabling an increase in the depth of penetration of the splitting microcrack. The proposed method involves a double-beam approach for laser-controlled thermal cleaving of brittle nonmetallic materials. This technique employs simultaneous radiation from a solid-state YAG laser operating at a wavelength of 1.06 μm and a CO_2 laser emitting at a wavelength of 10.6 μm, along with a refrigerant [67, 89].

It is important to highlight that the application of established double-beam techniques for laser thermal cleaving [123, 134] renders the solution to the specified task unfeasible. This is due to the use of YAG laser radiation at a wavelength of 1.06 μm for the formation of a scribe channel, which results in the inability to achieve the edge quality typical of CLT. The controlled double-beam laser thermal cleaving closely resembles the previously established double-beam method for thermal cleaving of ceramic-metal structures [134].

The characteristics of heating nonmetallic materials when exposed to laser radiation of varying wavelengths were examined in [199–201]. The study presented in [199] demonstrated the potential to alter the structure of the temperature field within the sample volume across a broad range, particularly when examining the characteristics of semiconductor heating under double-frequency laser exposure. A conclusion was reached in [201] regarding the mutual influence of radiation at various frequencies on the thresholds of pulsed optical breakdown of the gallium arsenide surface, accompanied by a proposed model for a qualitative explanation of this phenomenon. It is important to recognize that the aforementioned papers just offer insights into the configurations of temperature fields; this alone does not suffice for a thorough investigation into the mechanisms behind the formation of splitting microcracks during double-beam laser thermal cleaving.

The development of a double-beam technique for controlled thermal cleaving demanded further investigation into the mechanisms behind the formation of splitting microcracks when brittle nonmetallic materials are subjected to laser radiation at varying wavelengths. This required numerical simulation of temperature fields and stress distribution throughout the double-beam processing.

At the same time, it became evident that a preliminary investigation into the mechanisms of double-beam thermal cleaving of metal-ceramic structures, which had previously been well examined experimentally, was justified.

4.1. Simulation of double-beam laser thermal cleaving of metal-ceramic structures

In modern technologies, a range of techniques for joining heterogeneous materials, including ceramics and glass with metals, is extensively employed. Metal-ceramic structures exhibit significant potential owing to their elevated mechanical strength and capability for operation under high-temperature conditions. Products made from this type of material include ceramic substrates designed for hybrid integrated circuits featuring a metallized surface. The current methodologies for processing structural materials

in microelectronics and instrument engineering rely on metal-cutting equipment equipped with abrasive tools. Cutting modes are established empirically, taking into account the physical and mechanical properties of materials, the geometric dimensions of samples, and the accuracy requirements for their processing.

Alternative methods of dimensional processing, such as thermochemical, electro erosion, chemical-catalytic, and ultrasonic techniques, have not achieved widespread use in industrial technology. This is primarily due to the challenges associated with their implementation in production environments and their associated low labor productivity [202]. The examination of double-beam laser thermal cleaving processes in metal-ceramic structures is significant, serving both as a foundational step in understanding the mechanisms of controlled double-beam thermal cleaving and possessing intrinsic value on its own. An experimental and theoretical investigation into the thermal cleaving of ceramic-metal structures was conducted in references [134, 57].

As indicated in [57], during the process of laser separation of a bilayer sample, laser beam 1 (Figure 4.1) passes through ceramic layer 3 and is subsequently absorbed by metallic layer 4, resulting in heating of that layer. The thermal conductivity results in heat transfer into the non-metallic layer from the metallized surface side. The radiation energy from beam 2, absorbed in the surface layer of ceramic 3, is used for heating purposes.

Figure 4.1 – Arrangement of laser beams in the context of double-beam processing for metal-ceramic structures

The physical modelling of the laser separation of metal-ceramic structures presented in [57] accurately represents the primary characteristics of the process. However, it fails to consider the impact of bulk absorption of alumina ceramics by laser radiation at a wavelength of 1.06 μm on the resulting distribution of thermoelastic fields. The model presented in [57] was used in [203] to examine the separation process of a multilayer metal coating on a ceramic wafer.

To address volumetric heat generation, we conducted measurements of the extinction coefficient. This coefficient represents the sum of the true absorption coefficient, which indicates the fraction of radiant energy absorbed, and the coefficient that accounts for primary beam energy loss resulting from other processes, mainly scattering [157]. The extinction coefficient was determined through the measurement of transmission coefficients of YAG laser radiation incident on alumina ceramic wafers of varying thickness, without a metal coating, using the IMO-2H laser power meter (Section 2.2) as outlined in [158].

In the refined model of the process described in [62], the ceramic wafer is subjected to heating from two surface heat sources positioned on the surface of alumina ceramics and at the "ceramic-metal" interface, along with a bulk source generated by laser radiation at a wavelength of 1.06 μm, where the intensity distribution with respect to depth follows the Bouguer-Lambert law. This model outlines the process of double-beam splitting of metal-ceramic structures using the finite element method. It addresses the distribution of thermoelastic fields generated during the heating of a bilayer material by laser sources, considering the volume absorption of laser radiation at a wavelength of 1.06 μm by alumina ceramics.

The properties of alumina ceramics given in Section 2.1 were used in the calculations. Furthermore, the temperature dependencies of the thermal conductivity coefficients for ceramics and gold were considered [9, 140, 142, 158]. The modulus of elasticity, Poisson's ratio, and thermal expansion coefficient for gold were assumed to be equal to E = 80.6 GPa, $\nu = 0.422$; $\alpha_T = 165 \cdot 10^{-7}$ K^{-1}, respectively.

The parameters of the laser beam used in the calculations were as follows: major axis A = $4 \cdot 10^{-3}$ m, minor axis B = $1 \cdot 10^{-3}$ m for an elliptical beam cross-section, with a radiation wavelength of 10.6 μm and a radiation power of 30 W; the radius of the YAG laser radiation spot R = 200 μm, also with a radiation power of 30 W. Calculations were conducted for a bilayer material consisting of ceramic and gold, with the ceramic layer H having a thickness of 1 mm and the gold layer h measuring 20 μm. The sample's movement

speed in relation to the laser beams was set at 30 mm/s. The ceramic substrate has geometric dimensions of 20×10×1 mm, while the metal layer measures 20×10×0.02 mm.

To ensure a comparative analysis, the distribution of thermoelastic fields was computed solely under the influence of the CO_2 laser, using the same values of technological parameters as those applied in the simulation of double-beam processing. Figure 4.2 illustrates the temperature distribution curves at the surface of the ceramic layer (Z = 0), at its midpoint (Z = H/2), and at the ceramic-gold interface (Z = H). The solid lines demonstrate the isotherms associated with the temperature values shown in the figures.
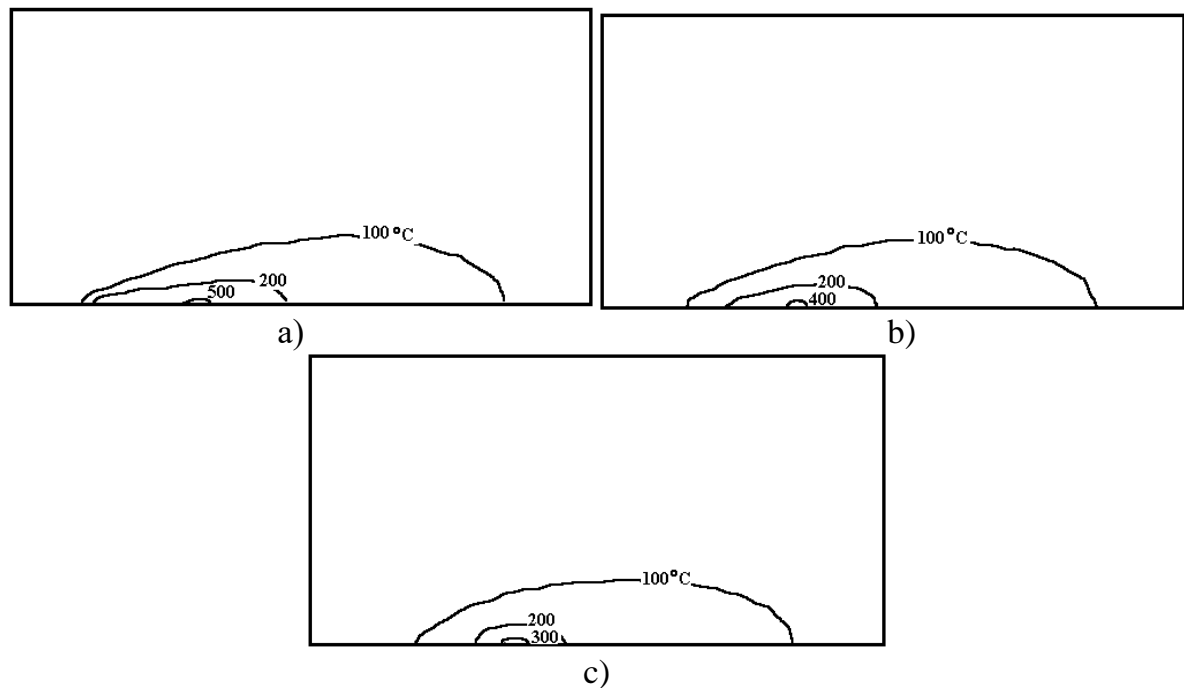
Figure 4.2 – Distribution of temperature fields in metallized ceramics during double-beam processing
A) Z = 0; B) Z = H/2; C) Z = H

As Z increases from 0 to H in the analyzed sample, the computed temperature values in the area of CO_2 laser exposure show a decline. This phenomenon is attributed to the surface absorption of radiation at a wavelength of 10.6 μm, coupled with the low thermal conductivity of alumina-oxide ceramics.

The spatial temperature distribution influenced by the bulk effect of YAG-laser radiation remains relatively constant throughout the depth of the material. Simultaneously, starting at Z = H/2, the influence of CO_2 laser does not notably alter the location of isotherms with high temperature values. It

is important to emphasize that the highest calculated temperature values remain below 611°C. Consequently, the relaxation of stresses near microstructure defects in alumina ceramics due to plastic strains presents challenges, leading to potential brittle separation of the metal-ceramic sample as a result of crack propagation.

Figures 4.3 and 4.4 illustrate the distribution of stresses σ_{yy} that act perpendicular to the sample's separating plane on the surface of the metal-ceramic structure at three locations: at the surface (Z = 0), in the middle (Z = H/2), and at the ceramic–gold interface (Z = H). This is presented for two processing variants: double-beam and the variant using only CO_2 laser exposure.
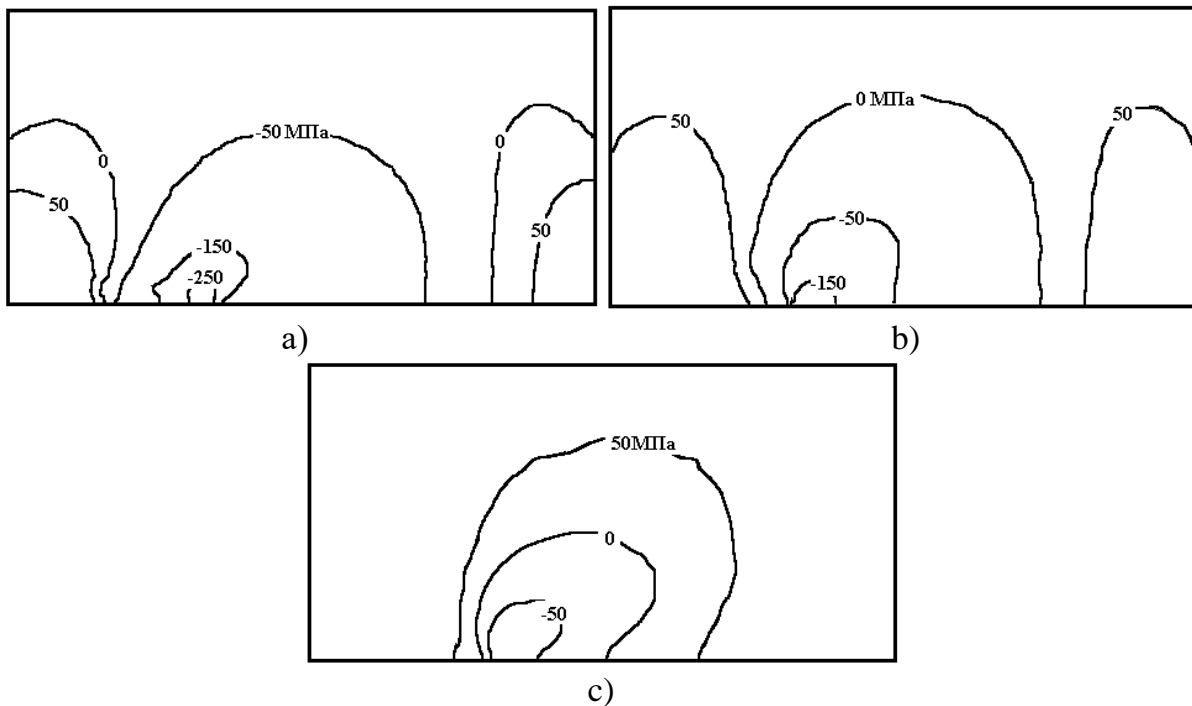

Figure 4.3 – Distribution of stress fields σ_{yy} in metallized ceramics during double-beam processing
a) Z = 0; b) Z = H/2; c) Z = H

The data presented in Figures 4.3 and 4.4 clearly indicate that there are notable differences in the contributions of CO_2 laser and YAG laser radiation to the resulting stress distribution at various depths. At the surface of the sample, the stresses induced by the CO_2 laser radiation attain significant levels. However, from the midpoint of the sample, the stresses identified by the YAG laser radiation exhibit elevated values; these stresses attain significant levels at the ceramic–gold interface, attributed to the absorption of laser radiation in the metal layer that has traversed the ceramic at a wavelength of 1.06 μm. It is important to observe that on the surface of the bilayer metal-ceramic structure, the isolines of elevated stresses encompass broader areas

in the region subjected to CO_2 laser exposure. In contrast, the stress zones resulting from the second laser exposure are less extensive, attributed to the larger geometrical dimensions of the laser beam cross-section at a wavelength of 10.6 μm. Consequently, the formation of the splitting crack along the laser impact line takes place in the surface layers of alumina ceramics and is influenced by the stresses generated by the laser radiation at a wavelength of 10.6 μm.
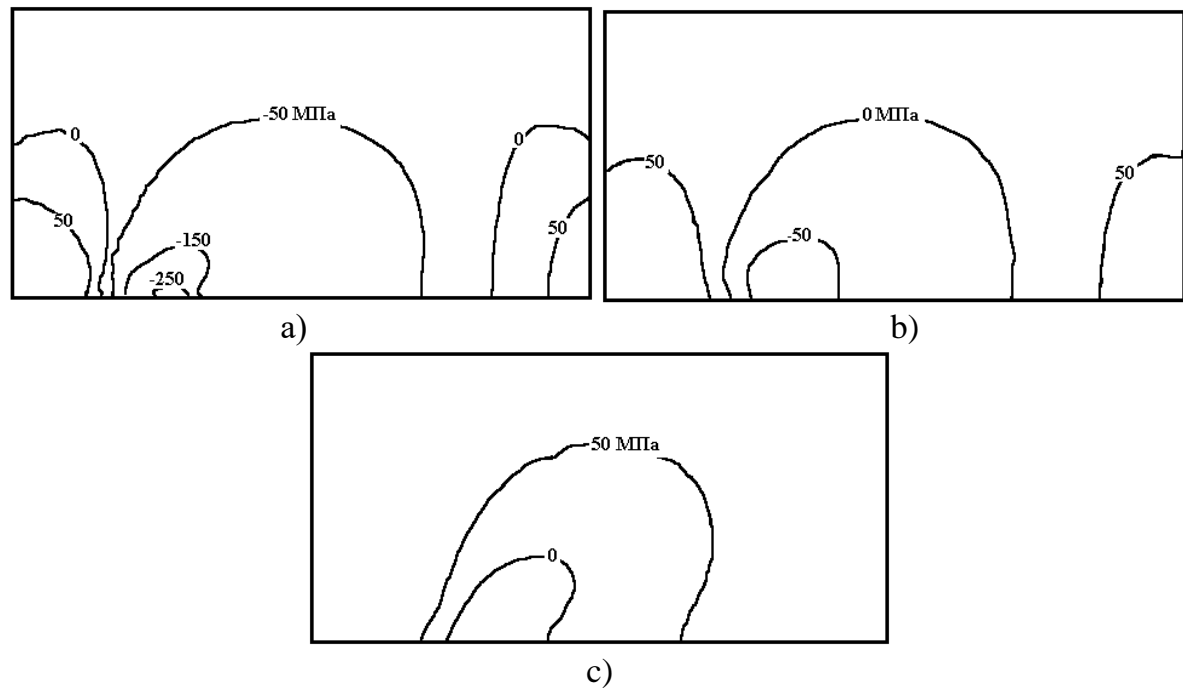

Figure 4.4 – Distribution of stress fields σ_{yy} in metallized ceramics
during CO_2 laser processing
a) Z = 0; b) Z = H/2; c) Z = H

However, based on the analysis of stress distribution in the deeper layers of the material, it can be concluded that the stresses induced by laser radiation at a wavelength of 1.06 μm are significant for the propagation of the splitting crack into the material.

These stresses arise from the reduction of crack deviations from the separating plane and its stricter vertical orientation, which is observable not only at the ceramic-gold interface, as indicated in reference [57], but also within the alumina-oxide ceramic layers closer to the surface.

Note that the technology of double-beam processing of metal-ceramic structures, examined in detail in this section, exemplifies the successful implementation of selective laser radiation impact at varying wavelengths on materials exhibiting diverse physical and chemical properties.

Nonetheless, this technology fundamentally represents a variant of through-the-thickness laser thermal cleaving and is consequently marked by the drawbacks typical of this laser processing technique.

The logical development of this method involves the application of concurrent double-frequency laser impact on the material being treated, in conjunction with the refrigerant. This represents an innovative approach to the processing of brittle non-metallic materials through the technique of controlled double-beam laser thermal cleaving.

4.2. Examination of the mechanisms involved in controlled double-beam laser thermal cleaving of brittle non-metallic materials

This section outlines the findings from the numerical simulation regarding the process of controlled double-beam laser thermal cleaving. The study was conducted considering the impact of bulk absorption by the material of laser radiation at a wavelength of 1.06 μm on the overall distribution of thermoelastic fields, specifically in scenarios involving simultaneous exposure of the work material to CO_2 and YAG laser radiation along with a refrigerant [67].

Figure 4.5 displays the layout of laser beams alongside the arrangement of the refrigerant within the cutting plane. Position 1 indicates the laser beam at a wavelength of 1.06 μm, position 2 signifies the laser beam at a wavelength of 10.6 μm, and position 3 stands for the refrigerant feeding zone.
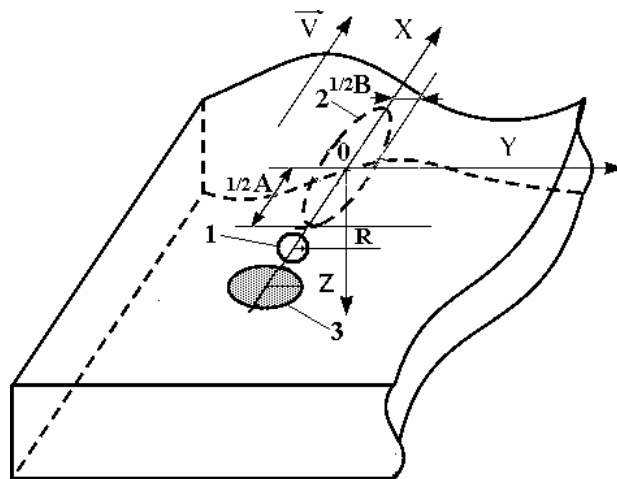

Figure 4.5 – Arrangement of laser beams and a refrigerant within the cutting plane during double-beam controlled thermal cleaving

Following this layout, the material is concurrently heated by a local surface heat source at the point of incidence of the beam at a wavelength of 10.6 microns, along with a bulk source generated by laser radiation at a wavelength of 1.06 microns.

The movement of the sample results in the surface heated by the laser beams experiencing cooling, as it enters the region exposed to the refrigerant.

The mechanism of double-beam thermal cleaving was elucidated using the finite element method, considering the temperature dependence of thermophysical characteristics. The problem addressed the distribution of thermoelastic fields generated by the combined effects of CO_2 laser and YAG laser radiation, along with refrigerant application, on the material.

The calculations were performed considering the properties of silicate glass sheet as discussed in Section 2.1. The parameter values selected for the simulation of the laser beams were as follows: major axis $A = 6 \cdot 10^{-3}$ m, minor axis $B = 2 \cdot 10^{-3}$ m for a beam of elliptical cross-section with a radiation wavelength of 10.6 μm and a radiation power of 15 W; radius of the YAG laser radiation spot $R = 1 \cdot 10^{-3}$ m, its radiation power 20 W. The calculations were carried out for a wafer with geometrical dimensions 20×10×5 mm. The velocity of the workpiece relative to the laser beams V is assumed to be 10 mm/s.

Figure 4.6, a presents the outcomes of the temperature field calculations within the volume of the examined sample during double-beam processing, while Figure 4.7, a illustrates the related stress distribution σ_{yy} acting perpendicular to the separating plane.
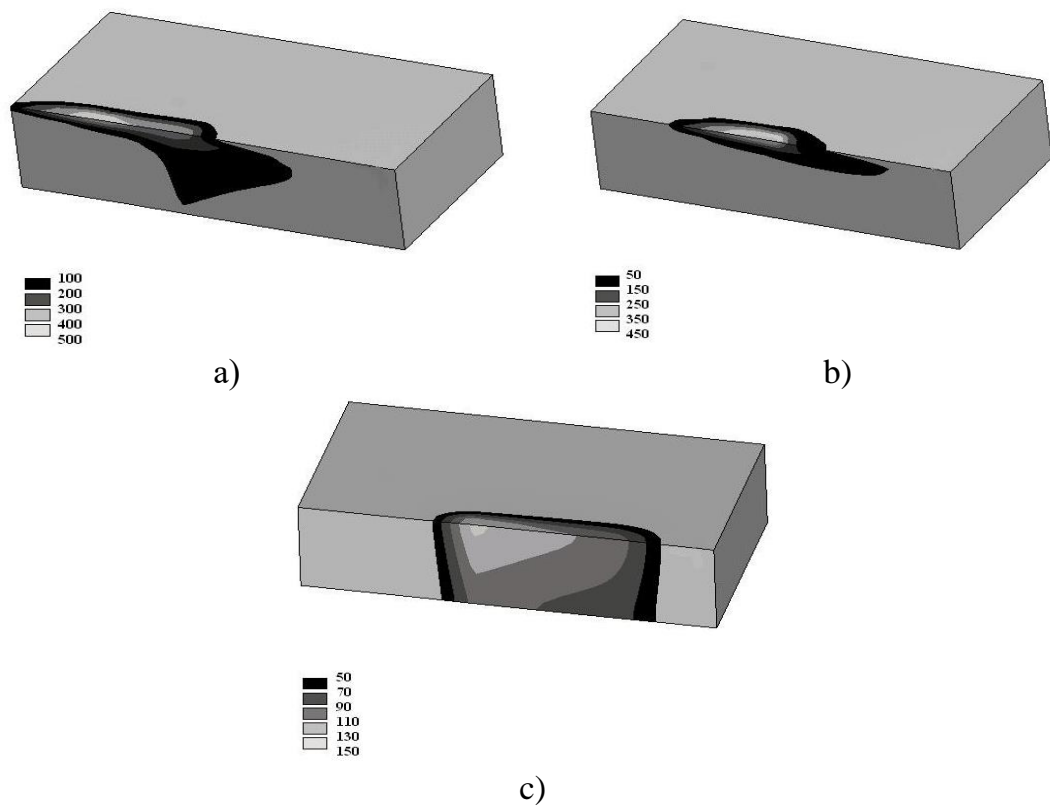

Figure 4.6 – Temperature distribution within the volume of the sample, ºC
a) double-beam exposure; b) CO_2 laser and refrigerant exposure;
c) YAG laser exposure

115

To facilitate additional comparative analysis, calculations of the thermoelastic field distribution were conducted for the single-beam CLT procedure (Figures 4.6, b and 4.7, b) and the YAG-laser-only material treatment procedure (Figures 4.6, c and 4.7, c). The identical values of the process parameters used in the calculations were those chosen in the simulation of double-beam processing.
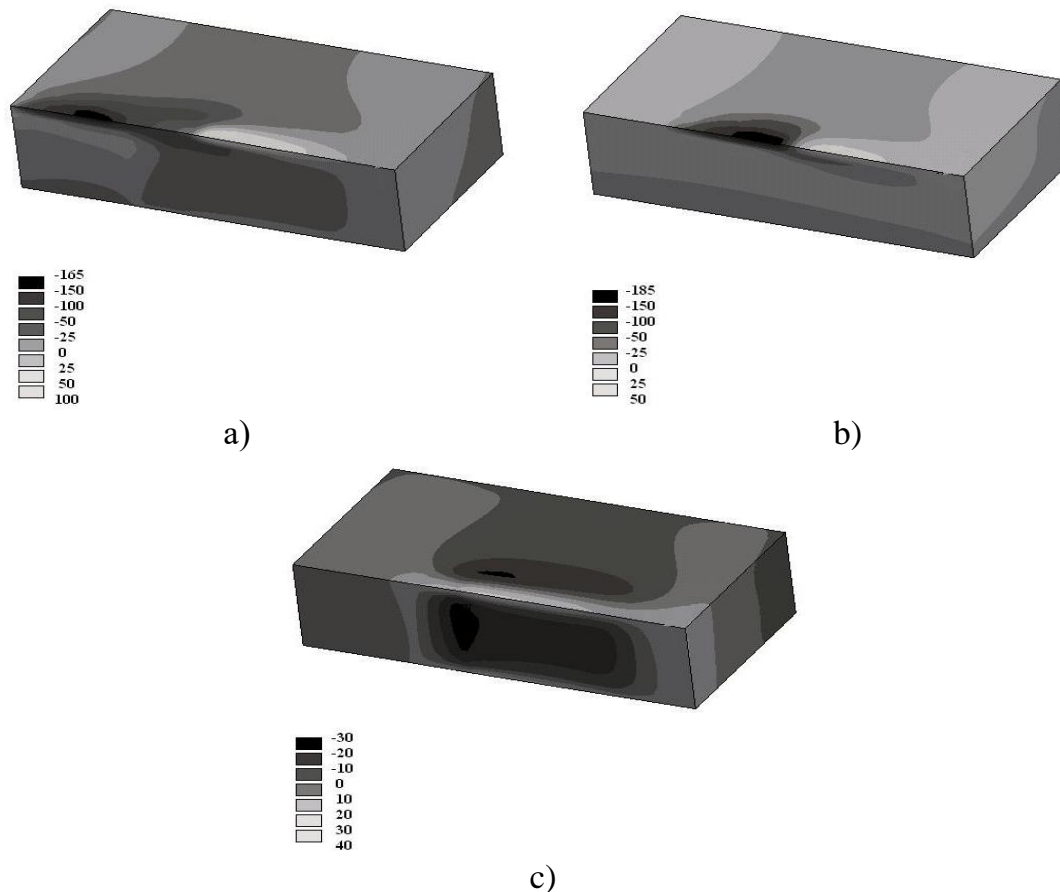

a)

b)

c)

Figure 4.7 – Stress distribution σ_{yy} within the volume of the sample, MPa
a) double-beam exposure; b) CO_2 laser and refrigerant exposure;
c) YAG laser exposure

Figures 4.8 and 4.9 demonstrate the relationships between temperature and stress σ_{yy} relative to the distance from the center of the elliptical section of the laser beam in the cutting plane for CLT and controlled double-beam laser thermal cleaving. These relationships are similar to the time sweep of the temperature and stress fields for points of the sample positioned at varying depths.

As previously stated, the primary criterion for optimizing process parameters using data on temperature fields is the maximum temperature value in the processing zone, which determines the failure mechanism of brittle nonmetallic materials.
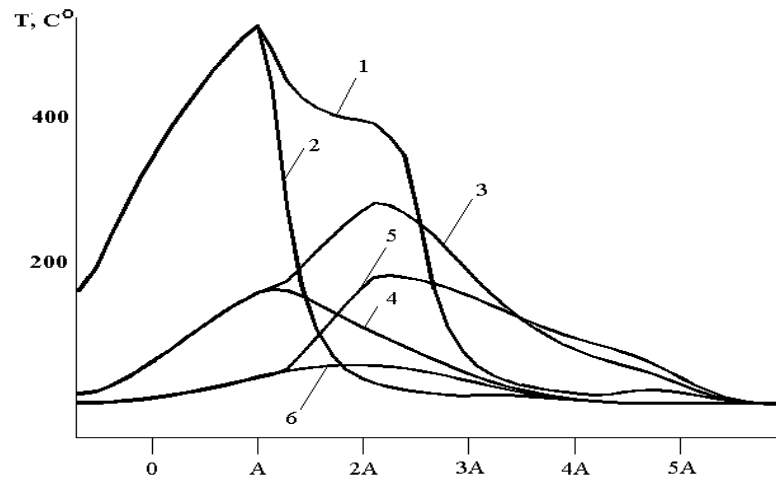
116

Figure 4.8 – Temperature dependence on the distance to the center of the cross-section
of the elliptical laser beam in the sample at various depths (at Y = 0 mm)
1 is the double-beam thermal cleaving Z = 0;
2 is the single-beam thermal cleaving Z = 0;
3 is the double-beam thermal cleaving Z = 0.2H;
4 is the single-beam thermal cleaving Z = 0.2H;
5 is the double-beam thermal cleaving Z = 0.1H;
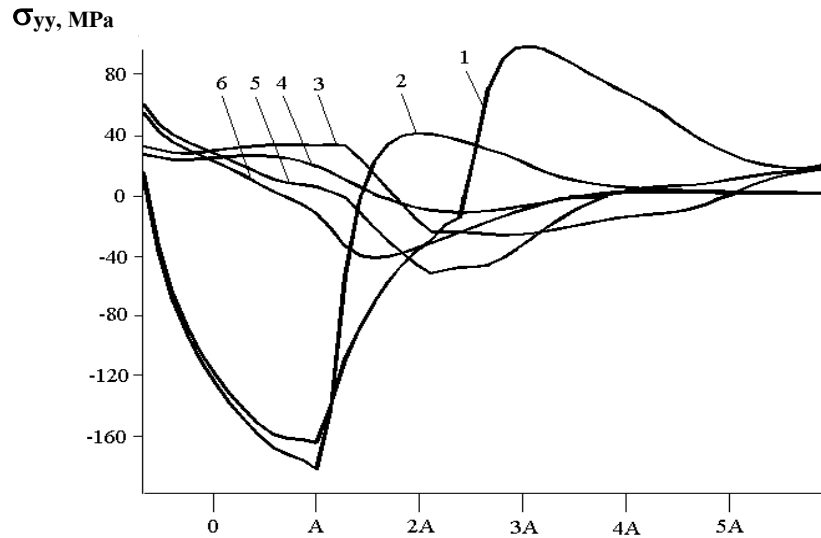6 is the single-beam thermal cleaving Z = 0.1H

Figure 4.9 – Dependence of stresses σ_{yy} on the distance to the center of the
cross-section of the elliptical laser beam in the sample at various depth (at Y = 0 mm)
1 is the double-beam thermal cleaving Z = 0;
2 is the single-beam thermal cleaving Z = 0;
3 is the double-beam thermal cleaving Z = 0.2H;
4 is the single-beam thermal cleaving Z = 0.2H;
5 is the double-beam thermal cleaving Z = 0.1H;
6 is the single-beam thermal cleaving Z = 0.1H

117

Let us reiterate that when processing silicate glass, we can select the glass transition temperature as the upper limit of permissible temperatures (for sheet glass produced through vertical drawing – 516 °C), which influences the brittle mechanism of material separation at lower temperatures. The analysis presented in Figures 4.6 and 4.8 demonstrates that the specified condition for the chosen processing parameters is satisfied across all three scenarios examined. As anticipated, the maximum temperature reaches the maximum values during double-beam exposure, while the lowest value of the maximum temperature is associated with the exposure of the material only to YAG laser radiation.

When comparing the distributions of stress fields σ_{yy} shown in Figures 4.7 and 4.9 – 4.11, it becomes evident that in both single-beam and double-beam processing, the nucleation of the splitting microcrack takes place within the surface layers of the material, starting from a microstructural defect situated in the region of tensile stresses generated by the influence of the refrigerant.
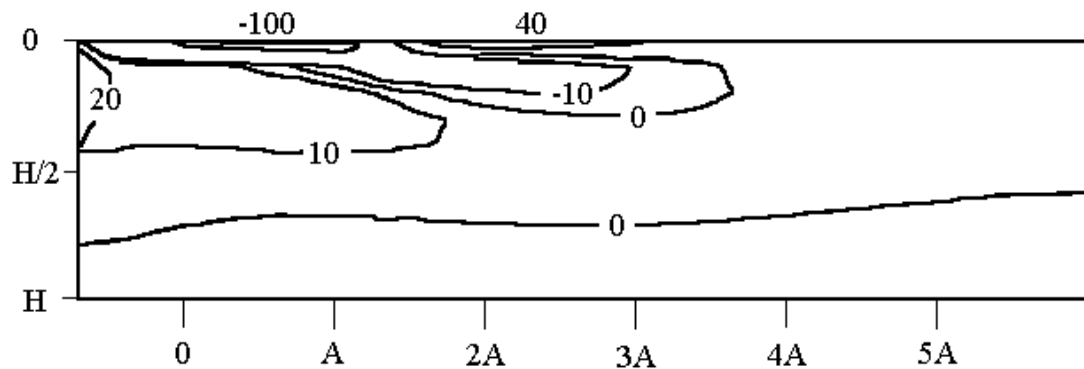

Figure 4.10 – Distribution of stress fields σ_{yy} (MPa) in the sample's separating plane during single-beam thermal cleaving at $Y = 0$
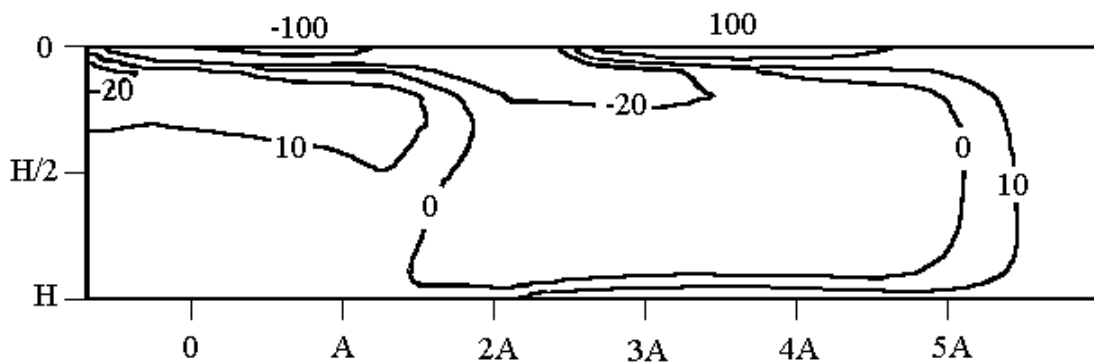

Figure 4.11 – Distribution of stress fields σ_{yy} (MPa) in the sample's separating plane during double-beam thermal cleaving at $Y = 0$

The initial microcrack subsequently propagates to the region of compressive stresses generated by laser radiation. Following this, the unsteady crack growth ceases, and its further progression is influenced by the changes in the spatial distribution of tensile and compressive stress regions, stemming from the interactions between the material, laser radiation, and the refrigerant. This aspect of the mechanism underlying the development of splitting microcracks aligns with the previously provided description for CLT.

Nonetheless, in the context of double-beam processing, the region experiencing compressive stresses is situated within the deeper layers of the material. Consequently, employing double-beam technology enables the formation of deeper microcracks compared to the single-beam processing method. This is due to the spatial arrangement of compressive stress regions within the sample volume, which influences the depth of penetration of the induced microcrack into the material.

Furthermore, it is important to note that in the refrigerant feeding zone, the tensile stress values during double-beam processing significantly exceed those observed during single-beam processing. Consequently, the stability of microcrack nucleation is notably enhanced during double-beam processing. This detail holds significant relevance when processing materials in orthogonal orientations.

As laser beams approach the sample's edge, the area of substantial compressive stresses caused by the intense heating from CO_2 laser radiation diminishes significantly. Consequently, the development of microcracks transitions into an uncontrolled state, leading to a deviation of the crack from its initial trajectory.

In double-beam processing, a region characterized by significant compressive stresses is established throughout nearly the entire depth of the sample. Concurrently, the magnitude of these compressive stresses is considerably greater than that observed in single-beam thermal cleaving. The microcrack subsequently becomes uncontrolled as it nears the edge of the sample, resulting in a decrease in edge defects.

During the analysis of stress fields generated in the material solely by YAG laser radiation, it was observed that at a sufficiently high-power density of radiation, despite its weak absorption, thermoelastic stresses of significant magnitude and spatial configuration are produced in the material, enabling the realization of laser thermal cleaving.

However, as illustrated in Figure 4.7, c, the spatial distribution of stresses σ_{yy} indicates that the conditions for through-the-thickness thermal cleaving are satisfied, which is associated with several notable disadvantages previously discussed in the first chapter when outlining its characteristics.

4.3. Development of an effective scheme for controlled double-beam laser thermal cleaving

Following the analysis of thermoelastic fields presented in Section 4.2, a conclusion was drawn regarding the practicality of employing double-beam action for the development of an innovative technique aimed at the separation of brittle non-metallic materials, specifically through controlled double-beam controlled laser thermal cleaving.

It is necessary to point out that, based on the calculation results (Figures 4.10–4.11), during double-beam exposure, the area of tensile stresses concentrated in the refrigerant exposure region is confined by the combined area of compressive stresses. This zone is created due to the overlapping regions where compressive stresses occur as a consequence of exposure to laser radiation at wavelengths of 10.6 μm and 1.06 μm, respectively.

In this scenario, accurately positioning the laser beam at a wavelength of 1.06 μm along the cutting line between the area affected by the laser beam at a wavelength of 10.6 μm and the area influenced by the refrigerant is essential for creating a combined zone of considerable compressive stresses. The spatial configuration of this zone is established in the surface layers due to the influence of CO_2 laser, while the YAG laser affects the deeper layers of the material.

Consequently, the significant impact of compressive stresses on the shape and depth of the microcrack, when employing the outlined arrangement of laser beams and the refrigerant, facilitates the development of a spatial configuration of thermoelastic stress fields. This configuration results in an enhanced depth of microcrack penetration in comparison to the single-beam processing method.

The developed method addresses a technical challenge by enhancing the quality of product separation from brittle non-metallic materials characterized by significant end face heights under thermoelastic stress. This improvement is realized through the implementation of deep splitting microcracks of specific dimensions, which effectively eliminate noticeable deviations of the separation line from the trajectory of laser radiation during the final material separation process.

The area of laser radiation exposure, characterized by a wavelength that aligns with the volume absorption of the material being processed, must be positioned along the cutting line. This line lies between the region where the laser beam interacts with the wavelength that achieves maximum absorption in the thin surface layer of the material and the area where refrigerant is applied.

Figure 4.12 illustrates the mutual arrangement of the laser beam impact areas and the refrigerant-cooled area [89].
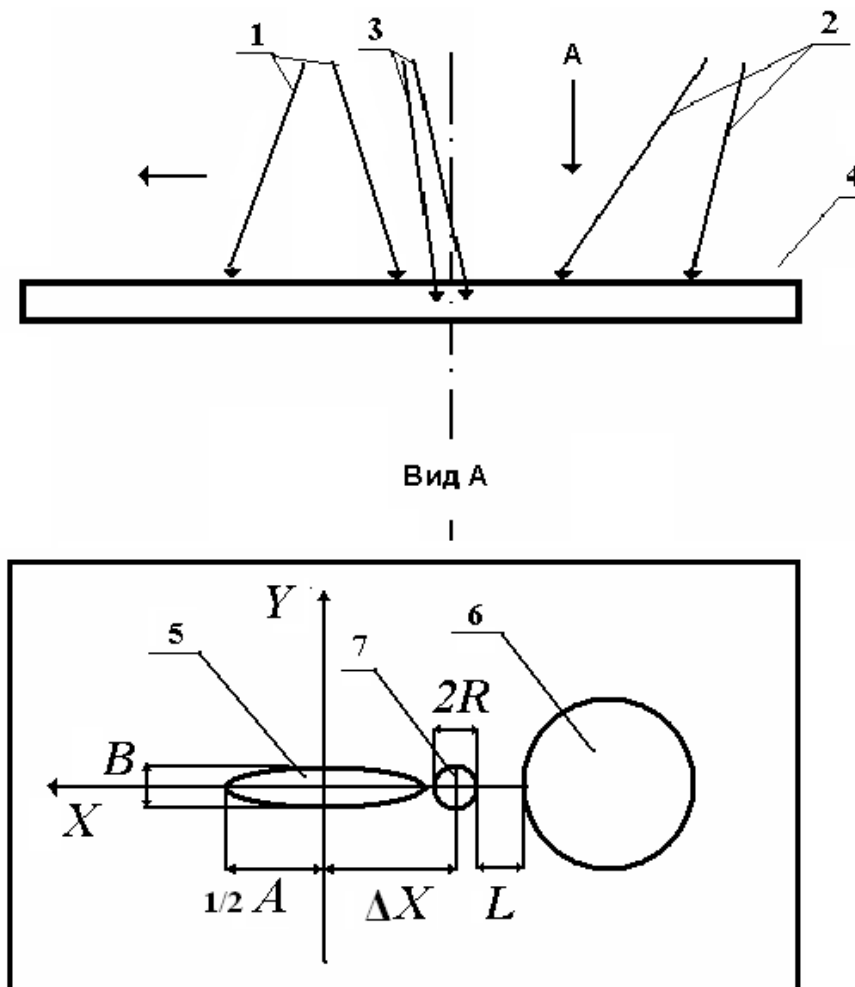
Figure 4.12 – Arrangement of the impact area for laser beams in conjunction
with the refrigerant-cooled area

The positions indicated in the figure represent the following: 1 is the laser beam at a wavelength of 10.6 μm, 2 is the refrigerant, 3 is the laser beam at a wavelength of 1.06 μm, 4 is the workpiece composed of brittle non-metallic material, 5 is the cross-section of laser beam 1 in the cutting plane, 6 is the refrigerant exposure area, 7 is the cross-section of laser beam 2. The horizontal arrow denotes the direction of movement for the workpiece.

Under experimental conditions, the procedure for controlled double-beam laser thermal cleaving is executed as outlined below. The initial blank of material 4 is positioned on the coordinate table.

A defect, such as a stab or cut, is introduced at the initial stage of the processing line. Subsequently, laser beam 1 is aimed at the defect's location, after which the coordinate table initiates the movement of workpiece 4 along the processing line. Simultaneously, refrigerant is introduced into the zone that has been preheated by laser radiation at a wavelength of 10.6 microns. Additionally, laser beam 3, which emits radiation at a wavelength of

1.06 microns, is positioned along the cutting line between laser beam 1 and the refrigerant exposure area.

A splitting microcrack is initiated at refrigerant supply point 2, originating from the applied defect. The microcrack develops within the tensile stress zone created by the influence of the refrigerant, as analyzed in the previous section regarding thermoelastic fields.

Furthermore, the initial microcrack propagates, extending into the region of compressive stresses generated by the combined influence of the laser beam at a wavelength that aligns with the maximum absorption of radiation in the thin surface layer of the material, as well as the laser beam at a wavelength that corresponds to the bulk absorption of radiation by the material.

Once the non-stationary crack growth ceases, its subsequent progression is influenced by the alterations in the spatial arrangement of tensile and compressive stress zones, which arise from the interaction between the work material and the laser beams.

Following the outlined sequence of operations, experimental studies were conducted to assess the effectiveness of the controlled double-beam thermo-cleavage method for separating 5 mm thick wafers of silicate glass sheets.

The laser technological equipment described in Chapter 2 was utilized throughout the experimental work.

The CO_2 laser beam focused on the glass surface, forming an elliptical spot characterized by a major axis of A = $6 \cdot 10^{-3}$ m and a minor axis of B = $2 \cdot 10^{-3}$ m. The measured distance L was determined to be 3 mm. The YAG laser's radiation beam centered on the glass surface, forming a circular spot with a radius of R=$1 \cdot 10^{-3}$ m.

The research revealed the dependencies of laser microcrack depth, which is formed during double-beam laser thermal cleaving, on several factors: the speed of relative movement between the laser beams and the work material (Figure 4.13), the power of laser radiation at a wavelength of 10.6 μm (Figure 4.14), and the power of laser radiation at a wavelength of 1.06 μm (Figure 4.15).

Figures 4.13 – 4.15 demonstrate that the depth of the microcrack exhibits a nearly linear relationship with both the rate of thermal cleaving and the laser power, applicable for wavelengths of 1.06 μm and 10.6 μm. A small section in Figure 4.15 stands out, where an increase in laser power leads to a notable decrease in microcrack depth, attributed to the excessive heating of the material and subsequent melting.
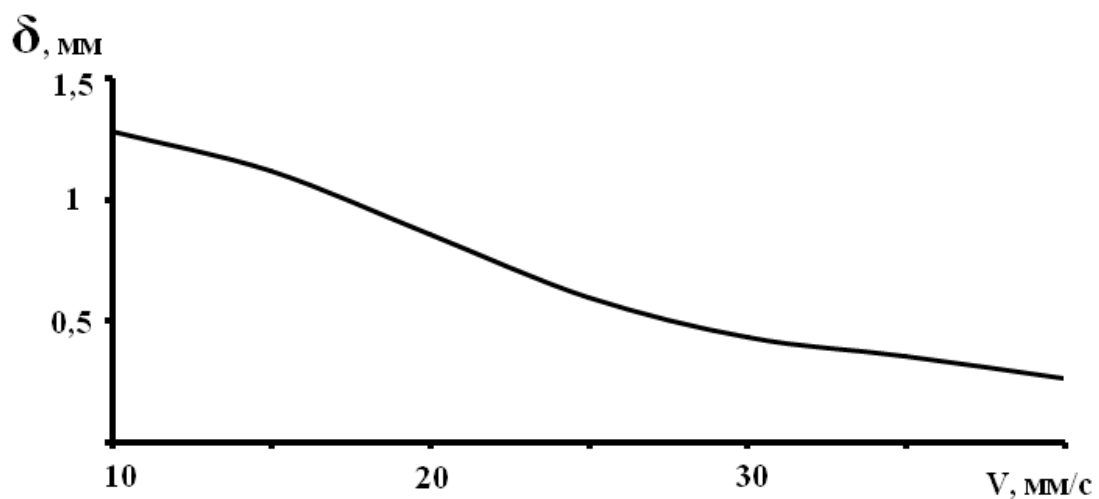
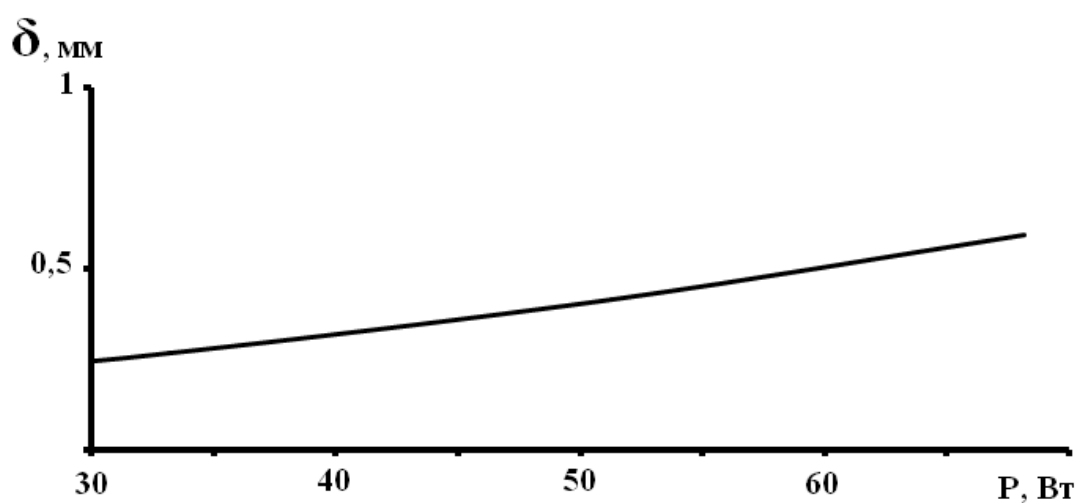Figure 4.13 – Microcrack depth versus processing speed

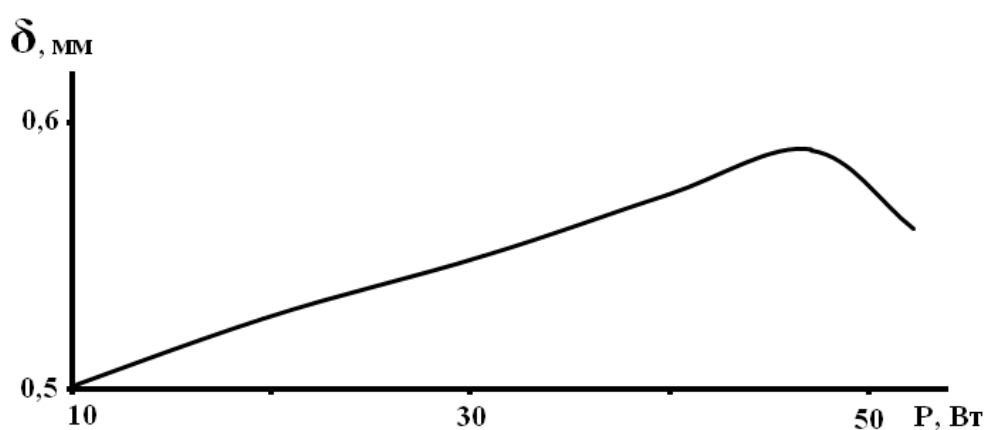Figure 4.14 – Microcrack depth versus YAG laser power

Figure 4.15 – Microcrack depth versus CO_2 laser power

It is crucial to focus on Figure 4.16, illustrating how the depth of laser microcracks varies with the positioning of laser beams on the glass surface. The variable ΔX represents the distance between the centers of the laser

beams, and in the graph, it assumes a negative value when the YAG laser beam is situated between the refrigerant exposure area and the CO_2 laser beam. Figure 4.16 illustrates that the peak values of microcrack depth occur when the center of the YAG laser beam is shifted towards the refrigerant exposure area. A notable reduction in microcrack depth, followed by a complete halt in cracking, is observed when the center of the YAG laser beam is shifted in the opposite direction.
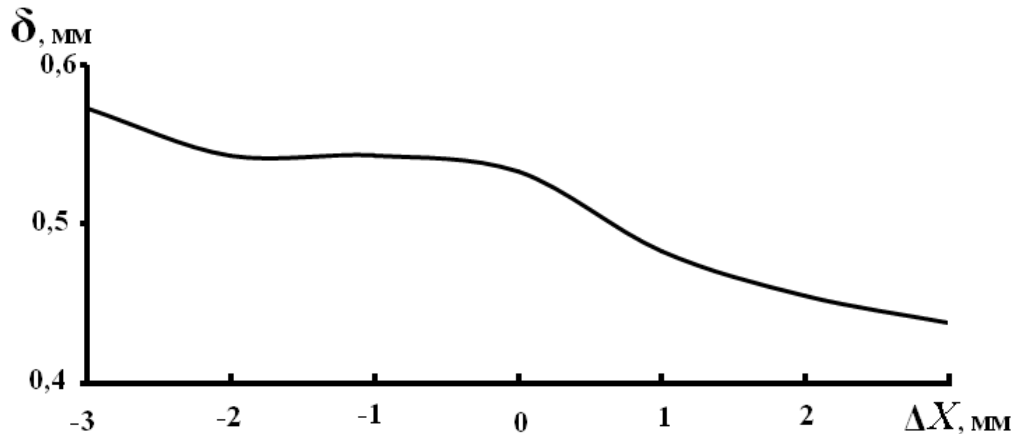

Figure 4.16 – Microcrack depth versus mutual arrangement of laser beams

The experimental results align well with the numerical simulations of thermoelastic fields presented in Section 4.2, leading to the conclusion that the penetration depth of the splitting microcrack can be adjusted during double-beam impacts on silicate glass. Experimental confirmation indicated that positioning a laser beam at a wavelength of 1.06 μm along the cutting line between regions subjected to laser radiation at 10.6 μm and the refrigerant optimizes the depth of the laser microcrack.

4.4. Laser thermal cleaving of thick alumina-oxide ceramics

Ceramic products offer several advantages over metal and polymer products, which are influenced by the unique interatomic interactions present in the chemical compounds that constitute ceramics. The benefits encompass significant elasticity, hardness, and a notable resistance to plastic deformation [130]. Nevertheless, the characteristics of ceramics present challenges in their processing. Simultaneously, the cutting of samples from alumina ceramics with a thickness of 1 ÷ 2 mm using CLT provides good quality results. However, when attempting to process ceramic sheets thicker than 6 mm with this method, achieving the formation of a high-quality splitting microcrack becomes challenging. In this context, it appears beneficial to adjust the CLT method for cutting ceramic wafers up to 10 mm thick and to investigate the mechanism behind their separation.

Experimental investigations into the thermal cleaving of 10 mm thick alumina ceramic wafers were conducted utilizing laser technological equipment [65]. The positioning of the laser beam and the refrigerant in relation to the cutting plane aligned with the schematic presented in Figure 3.1. The workpiece intended for processing was positioned in conjunction with the coordinate table, moving in relation to the fixed CO_2 laser and the nozzle that delivered the refrigerant. The alumina wafer was heated by the absorption of CO_2 laser radiation in the surface layer. The heated surface of alumina ceramics underwent rapid cooling in the refrigerant impact area. The results obtained through experimentation served as the foundation for concluding that it is fundamentally possible to achieve microcracks of sufficient depth for mechanical final cleaving when cutting plates that are up to 10 mm thick. Figure 4.17 presents a photograph depicting a sample of alumina ceramics that have been separated through the process of laser thermal cleaving.

The key distinction of the developed technology compared to the established CLT technology lies in the fact that it involves heating the surface layers of the sample to temperatures that surpass the melting point of alumina ceramics. As the cooling process progresses, the molten layers solidify, leading to the development of a principal microcrack.

Figure 4.17 – Sample of alumina ceramics after laser thermal cleaving

To clarify the unique aspects of the mechanism of laser thermal cleaving of thick ceramic wafers as outlined in the aforementioned scheme, the challenge of determining the thermoelastic fields was addressed. The calculations used the properties of ceramics presented in Table 2.1, considering the relationships between the thermal conductivity coefficient and specific heat capacity as they vary with temperature.

Calculations were conducted for a plane-parallel wafer measuring 20×20×10 mm, using the following parameters for the laser beam: beam cross-section radius $R = 1 \cdot 10^{-3}$ m and radiation power $P = 70$ W. The laser beam's movement speed relative to the surface of alumina ceramic was set at 2 mm/s.

125

Figure 4.18 illustrates the calculated temperature fields generated in the examined alumina ceramic sample due to CO_2 laser processing. Figure 4.19 presents the associated stress distribution, denoted as σ_{yy}, which acts perpendicular to the separation plane.
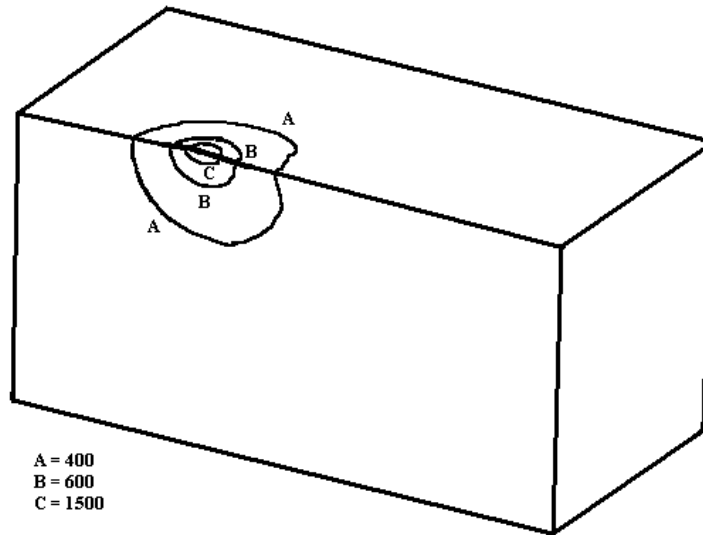

A = 400
B = 600
C = 1500

Figure 4.18 – Temperature distribution in alumina ceramics during single-beam processing with CO_2 laser, °C
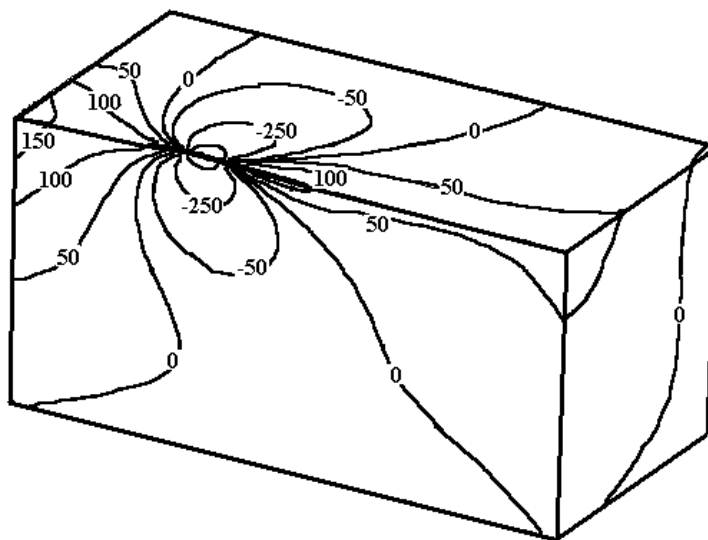

Figure 4.19 – Distribution of stresses σ_{yy} in alumina ceramics during single-beam processing with CO_2 laser, MPa

Figure 4.18 shows that under the specified processing parameters within the laser radiation exposure zone, the temperature attains levels that surpass the melting point of alumina ceramics. The isotherms related to ele-

126

vated temperature values are situated within the surface layers. This phenomenon is attributed to the significant absorption of radiation at a wavelength of $\lambda = 10.6$ μm occurring in the material's surface layer.

Upon analyzing the stress distribution σ_{yy} depicted in Figure 4.19, it is reasonable to conclude that the nucleation of the splitting microcrack takes place in the melt zone, attributed to tensile stresses generated during the solidification process of the material. The microcrack's further penetration into the sample's depth is attributed to tensile stresses generated by the refrigerant supply.

The ultimate depth of the resulting microcrack is influenced primarily by the area of compressive stresses surrounding the tensile stress zone, which is induced by laser interaction, rather than by the configuration of isotherms related to the melting temperature and isolines that represent the geometric location of points with maximum tensile stress in the refrigerant supply area. During the solidification of molten surface layers of ceramics due to intensive cooling, a microcrack is generated. The final shape of this microcrack is influenced by the spatial distribution of tensile and compressive stress zones, which are created by the effects of the refrigerant and laser radiation, respectively.

The results from the prior study on double-beam thermal cleaving of silicate glasses support the hypothesis that employing the double-beam method, i.e., integrating surface heating via radiation at a wavelength of 10.6 μm with bulk heating through radiation at a wavelength of 1.06 μm, can enhance the separation process characteristics of thick ceramics [66].

The double-beam thermocleavage method presented in Figure 4.1 was employed for subsequent investigations. Following this scheme, an alumina ceramic wafer was positioned in relation to stationary CO_2 and YAG lasers, along with a nozzle specifically designed for refrigerant supply. The wafer was subjected to surface heating through radiation emitted by the CO_2 laser beam. The YAG laser beam, with its intensity distribution along the depth following the Bouguer-Lambert law, was nearly entirely absorbed as it traversed the thickness of the ceramic sample, resulting in significant bulk heating of the material. Subsequently, the area heated by laser beams underwent rapid cooling in the refrigerant exposure area. Experimental studies revealed that double-beam processing can generate a splitting microcrack of greater depth than single-beam processing.

Thermoelastic field calculations related to the outlined double-beam processing scheme were executed using the same technological parameter values as those applied in single-beam processing. The radius of the YAG laser beam cross-section was considered to be R = $1{\cdot}10^{-3}$ m, and the radiation power was set at P = 100 W. Figure 4.20 illustrates the outcomes of the

127

temperature field calculations within the examined alumina ceramics sample, resulting from the double-beam processing. Meanwhile, Figure 4.21 presents the computed distribution of stresses σ_{yy} that are acting perpendicular to the separation plane.

Figure 4.20 demonstrates that the isotherms corresponding to the melting temperature of the alumina ceramics are located in deeper layers compared to those observed in the single-beam processing.

A = 400
B = 600
C = 1500
D = 1900
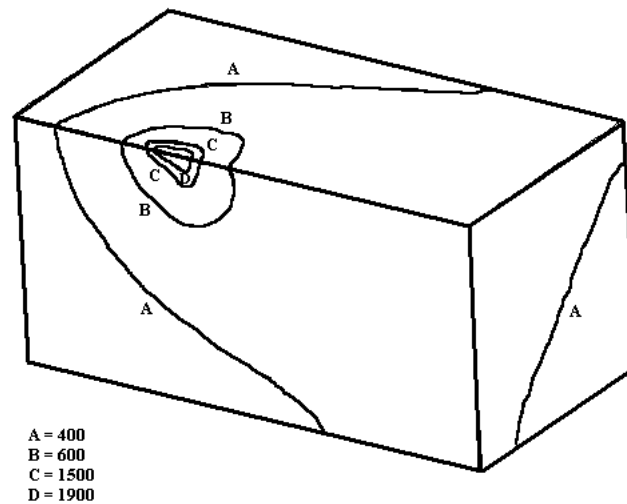
Figure 4.20 – Temperature distribution in alumina ceramics
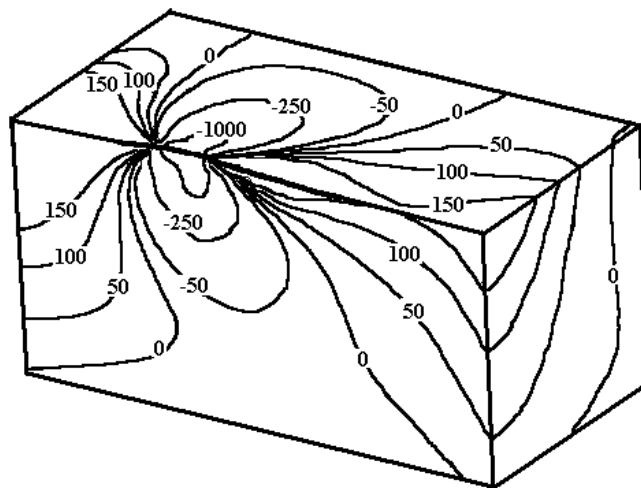during double-beam processing, °C

Figure 4.21 – Distribution of stresses σ_{yy} in alumina ceramics
during double-beam processing, MPa

The observed displacement results from the bulk absorption of YAG laser radiation in the ceramic, specifically at a wavelength of $\lambda = 1.06$ μm. Upon examining the distribution of stress fields σ_{yy}, as illustrated in Figure

4.21, it can be concluded that the microcrack, similar to the scenario of single-beam processing, emerges during the solidification of the molten surface layers of ceramics. Simultaneously, the region of tensile stresses adequate for the development of a splitting microcrack is situated in deeper layers of the material compared to processing that relies on only CO_2 laser radiation.

4.5. Double-beam laser technique for creating rounded edges in glass products

Currently, several techniques for precision laser processing of brittle nonmetallic materials have been established, including the method of asymmetric laser thermal cleaving. This approach facilitates the creation of an oblique crack featuring rounded edges. The authors in [24] propose several different variants for the realization of this method. This study investigates the formation of asymmetric distributions of thermoelastic fields in silicate glass samples, using the effects of laser radiation at a wavelength of 10.6 μm, which is absorbed in the thin surface layers of the material being treated. In one instance, an asymmetric distribution is attained by heating the material surface with an elliptical laser beam positioned at an angle to the direction of relative displacement. In another instance, this distribution is achieved through the displacement of the refrigerant in.

The investigation into the process of achieving rounded edges on glass products through the use of two laser beams with varying wavelengths of 10.6 μm and 1.06 μm has been conducted [67, 68].

Figure 4.22 illustrates the mutual arrangement of laser beams and the refrigerant on the surface of the material being processed.
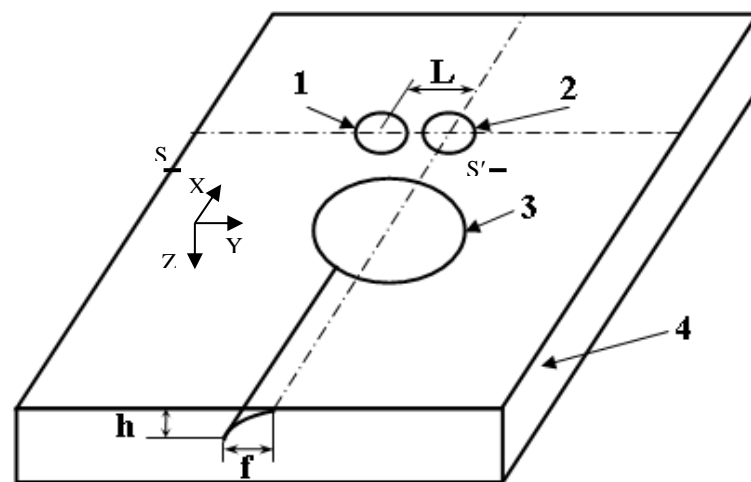

Figure 4.22 – Arrangement of laser beams and the refrigerant
1 is the YAG laser; 2 is the CO_2 laser;
3 is the refrigerant; 4 is the glass wafer

Experimental investigations were conducted to analyze the relationship between the depth h and deviation f of the crack from the processing line, considering various values of the mutual displacement of laser beams L and processing speed v. Experimental studies were conducted on laser technological equipment that comprises two lasers with varying emission lengths.

The 4 mm thick glass wafer designated for treatment is maneuvered by a coordinate table in relation to fixed laser beams and the refrigerant. The CO_2 laser beam, characterized by a wavelength of $\lambda = 10.6$ μm, was configured on the surface as a circle with a diameter of 3 mm. In contrast, the YAG laser beam, at a wavelength of $\lambda = 1.06$ μm, was also arranged in a circular form but with a diameter of 2 mm. Additionally, the refrigerant was introduced to the surface as a finely dispersed air-water mixture, featuring a diameter of 5 mm. Simultaneously, the CO_2 laser beam and the refrigerant were positioned on the surface of the wafer along the processing line, maintaining a distance of 4 mm between their centers. The alignment of the YAG laser beam was adjusted in relation to the CO_2 laser beam, specifically along a line that is perpendicular to the processing line. The separation L between the centers of the laser beams was adjusted from 0 to 2 mm. The power of the laser beam was $P_1 = 30$ W for the CO_2 laser and $P_2 = 100$ W for the YAG laser. Both lasers were utilized in a continuous operational mode.

Figure 4.23 presents the experimental dependencies of crack depth h and experimental dependencies of crack deviation f at different processing speeds for YAG laser displacement values L equal to 0.5 mm, 1 mm and 1.5 mm.
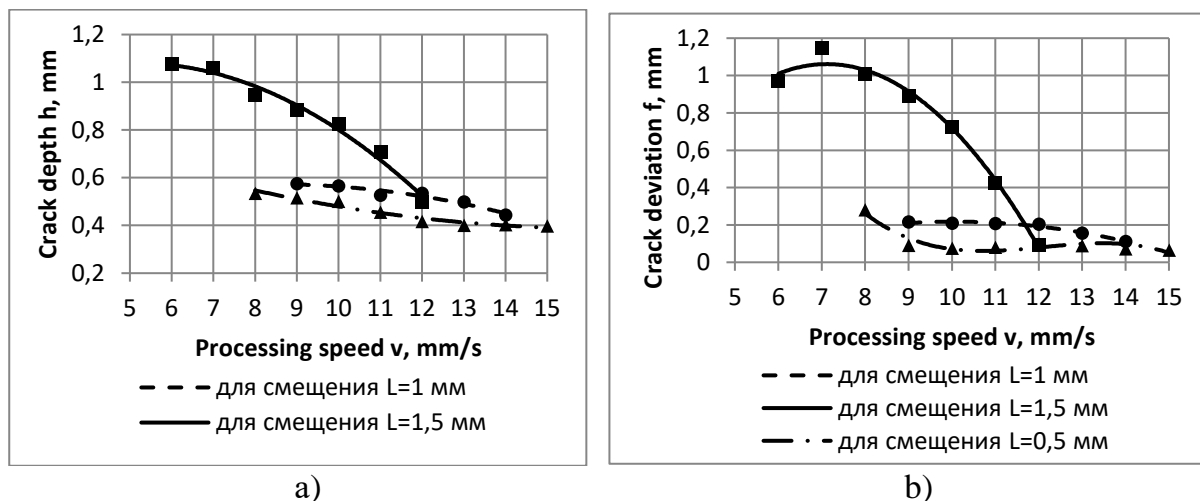

a)   b)

Figure 4.23 – Experimental correlation of crack depth (a) and deviation (b) for laser beam displacement values ranging from L = 0.5 to 1.5 mm

Figure 4.24 shows analogous dependencies for the YAG laser displacement value L set at 2 mm.

For each specified processing speed, several samples were obtained and measurements of crack depths and deviations were recorded for each sample, from which the average value was derived. Crack nucleation takes place on the surface of the material in the region where the refrigerant is supplied, specifically at the point of impact of the CO_2 laser beam. Subsequently, the crack propagates deep within the material, deviating towards the YAG laser beam line, and halts its progression at varying depths depending on the operating mode. The ultimate separation can be achieved through final cleaving methods, including mechanical, thermal, and ultrasonic techniques.
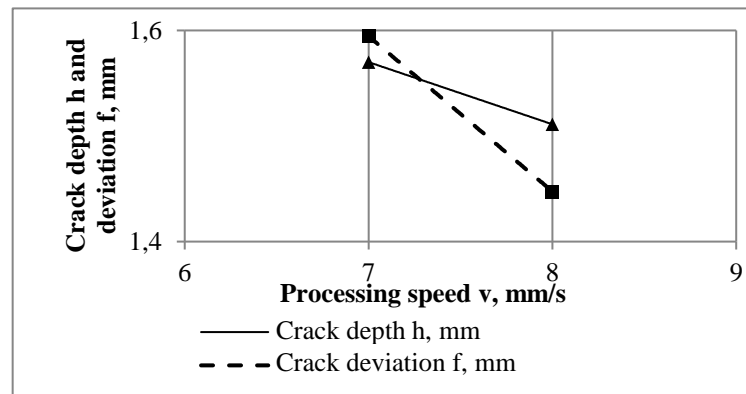
Figure 4.24 – Experimental correlation of crack depth and deviation
for a laser beam displacement of L = 2 mm

Figure 4.25 illustrates the end-face profile of the split sample.

a)   b)
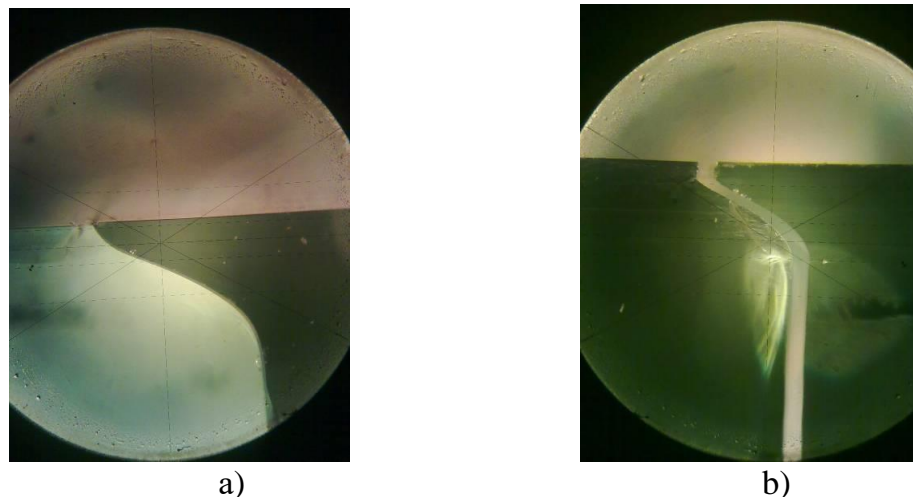
Figure 4.25 – End-face profile of the split sample
a) is for the processing parameters of v = 8 mm/s, L = 1.5 mm
b) is for the processing parameters of v = 7 mm/s, L = 2 mm

A chamfer is observed at the end of one segment of the split sample, while a protrusion is noted at the end of the other segment. Analysis of the

dependencies illustrated in Figures 1–3 reveals that as processing speed increases, there is a notable decrease in both the depth of the crack and the deviation from the processing line. The range of speeds for stable crack nucleation and development varies depending on the different values of displacement L of the YAG laser beam from the processing line. Therefore, for a displacement of L = 0.5 mm, the range for the specified parameters of the laser beams is between 9 and 20 mm/sec. The depth of the crack diminishes as the speed increases, whereas the deviation of the crack from the impact line of the CO_2 laser beam stays relatively constant. At a velocity of 8 mm/s, the crack propagates through the full thickness of the sample, indicating the occurrence of through-the-thickness thermal cleaving, with a notable increase in crack deviation. At reduced velocities within the zone of CO_2 laser beam interaction, the surface temperature surpasses the glass transition threshold, leading to the formation of a microcrack network upon subsequent cooling, while no crack propagation is detected. No crack nucleation occurs at speeds exceeding 20 mm/s. It is important to observe that for a specific displacement L at velocities of 9 and 10 mm/s, the crack profile differs from the overall representation illustrated in Figure 4.25.

Figure 4.26 demonstrates that crack nucleation initiates on the surface of the sample along the CO_2 laser beam line, subsequently leading to crack propagation that extends deeper and deviates towards the YAG laser line. At a certain depth, the crack once more shifts towards the CO_2 laser beam line, creating an unusual "wave" formation. For a displacement of L = 1 mm, stable nucleation and development of an oblique crack is observed within a velocity range of 9–14 mm/s.
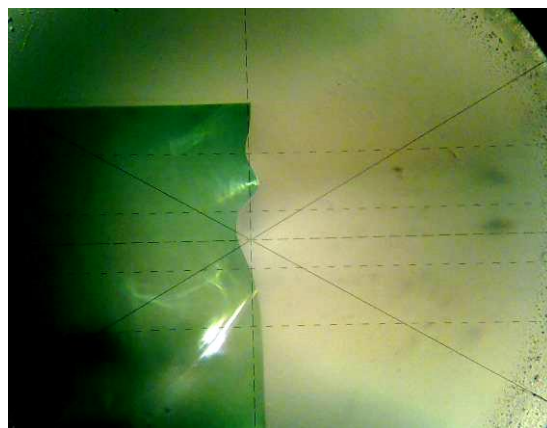

Figure 4.26 – Representation of a "wavy" crack

For L = 1.5 mm, we have 7 to 11 mm/s. At a processing speed of 6 mm/s, a consistent growth of an oblique crack is still noted; however, a network of microcracks develops on the surface due to overheating, resulting in a reduction of the crack deviation value. At a processing speed of

12 mm/s, the effect of the YAG laser becomes imperceptible, while the crack created by the CO_2 laser beam progresses in depth nearly perpendicular to the surface. For a displacement of 2 mm, the velocity range was relatively limited, spanning from 7 to 8 mm/sec. The values of deviation and crack depth are at their maximum in this instance.

Consequently, the findings indicate that the suggested approach of double-beam asymmetric laser thermal cleaving enables the effective production of silicate glass products featuring rounded edges. The parameters for rounded edges can be adjusted by altering the technological operating modes.

It is important to highlight another effect observed during the study. To assess the depth h and deviation f following the formation of an oblique crack, a secondary crack was introduced perpendicular to the processing line prior to the final cleaving of the sample, using solely the CO_2 laser beam and the refrigerant. The crack was placed complying with the guidelines outlined in Figure 4.22 from right to left. At the base of the oblique crack protrusion, a consistent nucleation and development of a crack parallel to the surface of the work material is noted, indicating that a parallel laser thermal cleaving process is being executed. A parallel crack is noted to emerge when the deviations of the oblique crack f surpass 0.6 mm, with the relative displacement of laser beams L set at 1.5 and 2 mm. The nucleation of the parallel crack takes place precisely at the base of the protrusion in this instance. By modifying the deviation and depth of the oblique crack, one can induce the formation of a parallel crack at a specified depth.

Simulation of the procedure of double-beam asymmetric thermal cleaving of brittle non-metallic materials

The simulation of laser thermocleaving processes relies on thermal-strength analysis tools that are suitable for conducting strength analysis derived from the solutions to the heat conduction problem. In this scenario, thermal and strength analyses are conducted in a sequential manner, aligning with the approach used to address the uncoupled thermoelasticity problem within a quasi-static framework. At the initial phase of finite element modelling for the process of double-beam asymmetric laser thermal cleaving, the temperature field distribution within the sample is computed, followed by the calculation of thermoelastic stress fields derived from the obtained temperature fields.

The CO_2 laser beam, characterized by its energy absorption in a thin surface layer of the material, is modelled as a circular surface heat source with a diameter of 3 mm and a power of 20 W. The YAG laser beam, which transfers energy to the sample volume, is represented as a circular bulk heat source with a diameter of 2 mm and a power of 80 W.

A silicate glass wafer with a thickness of 4 mm and geometric dimensions of 20x20 mm was selected as the sample for analysis. The refrigerant was delivered to the surface as a finely dispersed air-water mixture, characterized by a diameter of 5 mm. Simultaneously, the CO_2 laser beam and the refrigerant were positioned on the surface of the wafer along the processing line, maintaining a distance of 4 mm between their centers.

The material processing speed v, as illustrated in Figure 4.22, was set at 10 mm/s.

Figure 4.27 presents the temperature distribution at a specific moment along the line where the centers of the laser beams (Y-axis) are located during the execution of double-beam asymmetric laser thermal cleaving, as outlined in Figure 4.22.
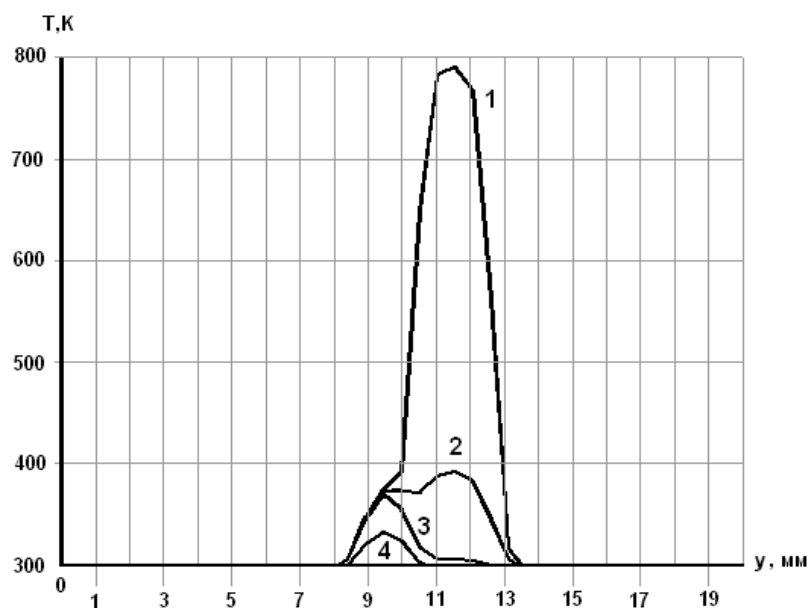
Figure 4.27 – Temperature distribution along the line where the centers of CO_2 and YAG laser beams are positioned, K

The YAG laser displacement value L was selected to be 2 mm. The CO_2 laser beam was centered at the coordinate y = 11.5 mm, while the YAG laser beam was centered at y = 9.5 mm. Numeral 1 represents the temperature distribution along the OY axis on the surface of the material, numeral 2 indicates the distribution at a depth of z = 0.4 mm, numeral 3 corresponds to a depth of z = 0.8 mm, and numeral 4 pertains to a depth of z = 2 mm.

The presented temperature distributions indicate that there is significant local heating of the sample surface in the region exposed to CO_2 laser radiation, with a peak temperature of 775 K observed, remaining below the glass transition temperature. The additional thermal energy resulting from heat

conduction penetrates deeply into the material. The sample experiences uniform heating across its entire thickness when exposed to YAG laser radiation. Concurrently, the temperature readings are significantly lower compared to the region affected by CO_2 laser radiation. It is important to highlight that starting at a depth of 0.8 mm from the sample surface, the effect of CO_2 laser radiation on the temperature distribution within the sample is nearly nonexistent, with the heating of the material primarily occurring due to YAG laser radiation. The temperature distribution pattern in relation to the CO_2 laser exposure line exhibits asymmetry. The asymmetry in the temperature distribution results in an asymmetric distribution of thermoelastic stress.

Figure 4.28 shows the distribution of the main thermoelastic stresses σ_1 at a fixed moment in time along the line SS', which is perpendicular to the processing line and passes through the area subjected to refrigerant exposure.
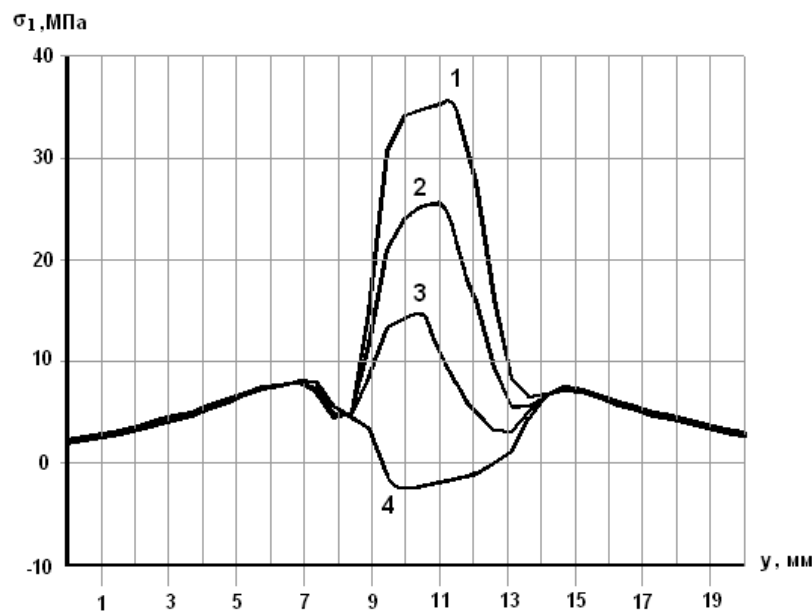
Figure 4.28 – Thermoelastic stress distribution σ1 along the line perpendicular to the processing line (Y-axis), intersecting the refrigerant exposure area, MPa

Numeral 1 denotes the stress distribution along the line on the surface of the material, numeral 2 represents the stress at a depth of $z = 0.1$ mm, numeral 3 corresponds to the stress at a depth of $z = 0.2$ mm, and numeral 4 signifies the stress at a depth of $z = 0.4$ mm.

The analysis of the presented distribution reveals a zone of significant tensile stresses on the material's surface in the refrigerant supply region, where there is an abrupt cooling of the material.

At the same time, the maximum of stresses is predominantly located along the line of CO_2 laser impact (coordinate y=11.3 mm). The probability

of crack nucleation increases with elevated tensile stress values. Consequently, crack nucleation and propagation will occur in regions where tensile stresses reach their peak. Given that the maximum tensile stresses manifest on the surface of the sample where it is exposed to the refrigerant, crack nucleation takes place on the material's surface. The main stress values σ_1 and σ_{yy} are equal in magnitude, leading to the initial crack propagation occurring in a direction perpendicular to the material's surface, a phenomenon confirmed by experimental observations. The region of tensile stresses resulting from the refrigerant's action penetrates significantly into the material, constrained from below by the compressive stress zones created by laser beams. The presence of these zones restricts the progression of the nucleated crack into the material's depths.

The dependencies of the main stresses σ_1 on the y-coordinate, as illustrated in Figure 4.28, indicate that the stress maxima shift from the CO_2 laser impact line to the YAG laser impact line. Specifically, at a depth of z = 0.35 mm, the maximum tensile stress is found at the point with the y-coordinate y = 9.7 mm.

This shift occurs due to the absorption of radiation energy at the material's depth, which significantly affects the distribution of stress fields in the deeper layers of the sample. The maximum stress values observed at the depth of the sample are lower than those recorded on the surface. Consequently, the nucleation of the splitting crack takes place on the surface of the sample within the region subjected to CO_2 laser exposure. As the crack advances deeper into the material, it shifts towards the YAG laser impact line and, upon reaching the compressive stress zone, halts its progression. The value of the crack deviation is established by the relative displacement of the laser beams L. By marking the points along the SS' lines at various depths where the tensile stresses reach their maximum values, we can derive the shape of the oblique crack illustrated in Figure 4.29, which aligns closely with the experimental observations.
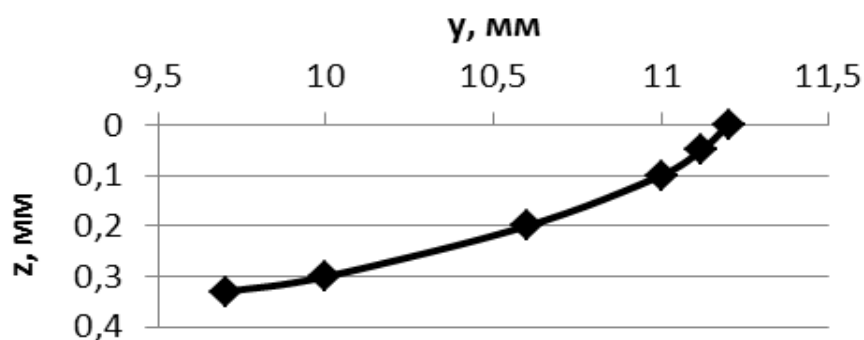

Figure 4.29 – Design form of the crack

4.6. Analysis of laser thermal cleaving of materials using beams of special geometry

The traditional approach for implementing the method of controlled laser cleaving can be seen in Figure 4.30. This process involves the surface heating of the material using laser beam 1, followed by the cooling of this area with refrigerant 2.
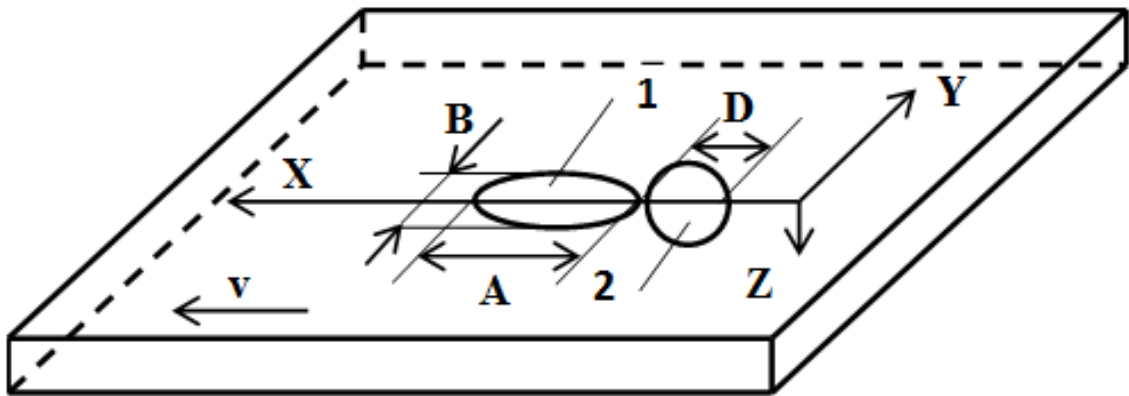

Figure 4.30 – Layout of elliptical laser beam and the refrigerant
in the cutting plane

A microcrack is consequently generated in the refrigerant feed area, tracing the path of the laser beam along the processing line [7, 24]. The ultimate separation is executed through mechanical, thermal, or ultrasonic final cleaving methods.

A finite-element solution was previously conducted regarding the distribution of thermoelastic fields in a silicate glass sheet during the controlled laser thermal cleaving process using CO_2 laser radiation [53, 58−61,]. The scheme is illustrated in Figure 4.30. The problem was addressed using a quasi-static formulation as outlined in [139]. The examination of the distribution of stress fields σ_{yy} revealed that within the area affected by the laser beam, considerable compressive stresses develop, surrounded both at the surface and within the material by a region of tensile stresses. In the upper layers of the sample, an additional area of tensile stresses develops, with its position dictated by the localization of the refrigerant's impact. The region of tensile stresses is constrained from below by the compressive stresses generated by the laser beam.

Through the analysis of the distribution of thermoelastic fields, it was determined that the initiation of splitting microcracks occurs in the surface layers of the material, originating from a crack-like defect within the microstructure in regions of tensile stresses induced by the supply of refrigerant.

Additionally, the initial microcrack begins to move and propagate towards the region of compressive stresses induced by laser radiation. Once the unsteady crack growth ceases, its subsequent advancement is influenced by the alteration in the spatial distribution of tensile and compressive stress regions, which results from the interaction among the work material, the laser beam, and the refrigerant.

However, this approach presents a drawback. When the heating and cooling line (i.e., the X-axis in Figure 4.30) is positioned near the sample's lateral boundary, the presence of microdefects at the edge can lead to a sharp deviation of the microcrack from the processing line towards the lateral boundary, potentially reaching the boundary itself, followed by a halt in the microcrack's progression. Consequently, cutting must occur at a considerable distance from the lateral boundary, leading to an increase in production waste.

Accordingly, it appears relevant to explore new or refine current techniques for separating brittle non-metallic materials so that processing can be carried out as close to the sample's edges as possible.

The finite element method was employed to determine the thermoelastic fields generated in samples of brittle nonmetallic materials during the process of controlled laser thermal cleaving.

All calculations were performed for silicate glass samples with geometrical dimensions of 40x40 mm and thickness of 3 mm.

The processing speed of the material for all subsequent schemes aimed at achieving the controlled laser thermal cleaving process was established at 15 mm/sec. This relatively low processing speed was selected to facilitate graphical representation and analysis of the spatial distribution of elastic stress fields in a glass plane-parallel wafer. The rise in processing speed leads to a reduction in the tensile stress zone, influenced by the refrigerant's exposure along the wafer's depth, alongside the compressive stress zone that surrounds it from beneath, caused by the heating of the material, and the movement of these zones towards the surface layers of the material. This consequently leads to challenges in the qualitative illustrative representation of field patterns.

The main criterion for optimizing process parameters, based on information about temperature fields, is the maximum temperature values within the processing area, which dictate the fracture mechanism of the sample. In silicate glass processing, the glass transition temperature (for silicate glass sheet – 789 K) represents the upper limit for permissible temperatures at which the brittle separation mechanism is realized.

Given that laser thermal cleaving leads to brittle fracture, it is logical to utilize the tensile strength of silicate glass as a criterion for material fracture when simulating the relevant processes. In the examination of crack nucleation and propagation, a tensile strength of 25 MPa was selected. [152, 204].

In order to conduct a comparative analysis, calculations were carried out on the thermoelastic fields produced during controlled laser thermal cleaving, specifically for laser beams that are elliptical, semi-ring, and crescent-shaped.

The controlled laser thermal cleaving process was simulated using an elliptical beam, following the scheme demonstrated in Figure 4.30.

Figure 4.31 illustrates the spatial distribution of the thermoelastic fields σ_{yy} at a specific moment in time resulting from the implementation of this scheme.

Considering that the motion of the beam and the refrigerant occurs along the center of the sample, the symmetrical nature on either side of the $Y = 0$ plane allows for the representation of the fields to be shown for only half of the sample. The front face of the sample represents the cut in the $Y = 0$ plane. A CO_2 laser was used as the radiation source, operating at a wavelength of $\lambda = 10.6$ μm, which is known for its significant absorption by the surface layers of the sample, with a power of $P = 30W$.
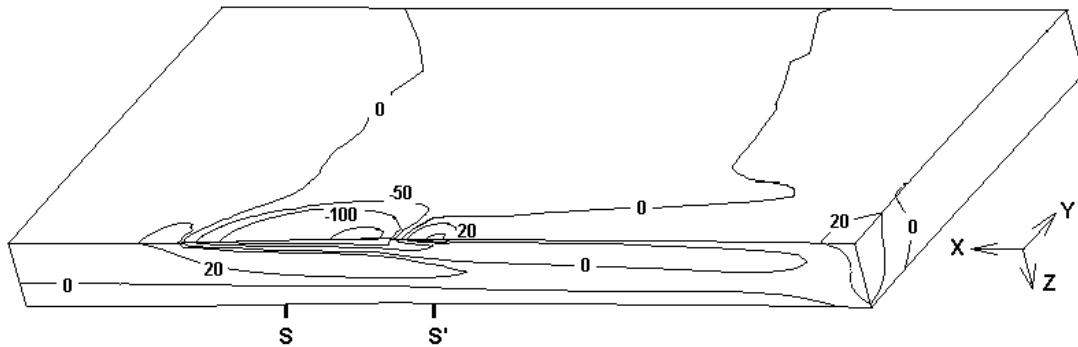
Figure 4.31 – Distribution of thermoelastic fields σ_{yy} (MPa) in the sample using an elliptical laser beam

The dimensions of the large and small axes are $A = 10$ mm and $B = 5.4$ mm, respectively. The diameter of the refrigerant's area of influence on the material's surface is 3 mm and remains constant across all the methods outlined below.

The maximum calculated values of the sample temperatures do not exceed 747 K.

Figure 4.31 depicts the locations S and S′, which denote the positions along the X-axis of the laser beam and the centers of the refrigerant, respectively. The examination of the spatial distribution of thermoelastic fields de-

picted in figure σ_{yy} indicates that, as previously mentioned, a region of considerable tensile stresses emerges in the area of the refrigerant supply. The tensile stress values surpass the strength limit of the glass. A microcrack is initiated and progresses within this zone. This region is bounded at the front and bottom by a zone characterized by substantial compressive stresses induced by the movement of the laser beam. However, from the lateral perspective, this region is not constrained by significant compressive stresses, particularly when the processing occurs along or near the sample boundary.

Microdefects and microcracks located at the boundaries of the sample serve as stress concentrators. Consequently, during processing near the lateral boundary of the sample, areas of considerable tensile stresses are generated at the tips of microcracks and microdefects. Additionally, the direction of the main microcrack's growth shifts towards these microdefects and microcracks. To mitigate this effect, it is recommended to establish a region of substantial compressive stresses not only in the area preceding and below the tensile stress zone created by the refrigerant, but also along its lateral boundaries.

The elastic stress fields arising during single-beam controlled laser thermal cleaving with a CO_2 laser beam featuring a semi-ring-shaped cross-section were calculated.

The implementation scheme for this method is presented in Figure 4.32. Position 1 indicates the shape of the laser source spot on the material surface, while position 2 stands for the refrigerant. The external radius of the ring is 2.5 mm, while the internal radius measures 1.7 mm. Laser radiation power is measured at 20 W. The centers of the semi-ring and the refrigerant impact zone are aligned.
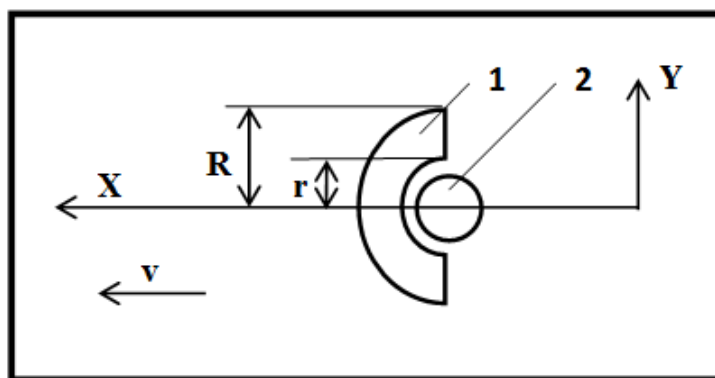

Figure 4.32 – Schematic illustrating the arrangement of laser beams
and a refrigerant in the cutting plane

Figure 4.33 provides the spatial distribution of the thermoelastic fields σ_{yy} resulting from the implementation of this scheme. The depiction of the

fields is provided for half of the wafer and is presented at an enlarged scale for a specific section of the wafer to enhance clarity. The position S indicated in the figure denotes the location of the center of the laser beam and the refrigerant along the X-axis.

A region of strong compressive stresses appears in the area where laser radiation interacts with the sample surface, constraining the area of refrigerant influence not only from the front and bottom but also from the sides. However, it should be noted that the maximum temperature values on the material surface of 738 K are generated not along the processing line (X-axis), but rather at the edges of the laser beam. Along the processing line, the temperature values are observed to be 150 degrees lower than these maximum values. The low temperature values along the processing line, combined with the minimal heat penetration area along the X-axis, lead to the conclusion that in the refrigerant supply area, the stresses σ_{yy} do not evolve into tensile stresses.
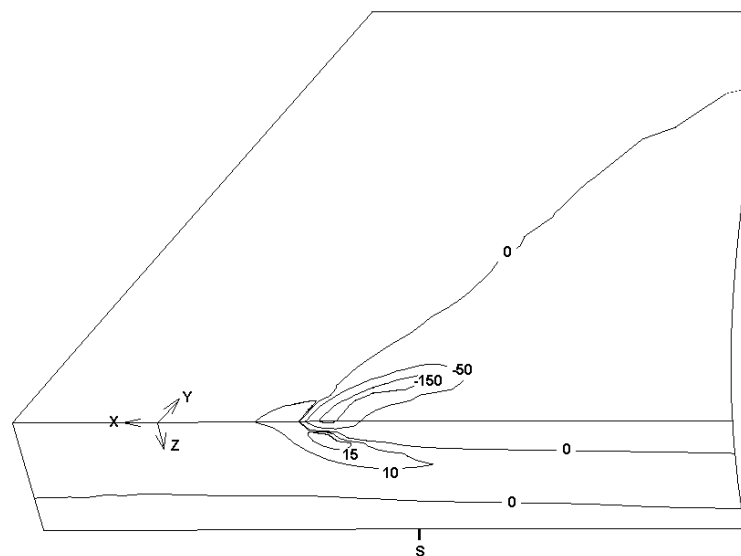
Figure 4.33 – Distribution of thermoelastic fields σ_{yy} (MPa)
in the sample using a semi-ring laser beam

In prior studies referenced as [66, 67, 71, 74], the authors reported findings on the process of double-beam laser thermal cleaving applied to brittle nonmetallic materials. This process involves the simultaneous irradiation of the workpiece using two laser beams of different wavelengths. One beam is selected for its ability to achieve intense absorption in the surface layers of the sample, while the other is chosen for its effectiveness in volumetric absorption within the material being processed. The technology for double-beam thermal cleaving of brittle non-metallic materials enables the formation of a specified distribution of thermoelastic stress fields, applicable not only in a thin surface layer but also throughout the entire depth of the

work material. This results in enhanced quality and accuracy of processing, significantly minimizing the deviation of microcracks from the material's separation line by increasing their depth.

Using the findings from these studies, we computed the distribution of thermoelastic fields within the sample during the double-beam laser thermal cleaving process. This process employed CO_2 and YAG laser beams, characterized by a semi-ring cross-section. The beams exhibit analogous shapes and geometrical dimensions as depicted in the schematic presented in Figure 4.32. The centers of the laser beams align with the refrigerant.

The CO_2 laser beam radiation, at a wavelength of 10.6 μm, is absorbed by the surface layer, resulting in the heating of the glass wafer's surface. The continuous YAG laser beam, at a wavelength of 1.06 μm, passes through the glass volume and experiences partial absorption, resulting in bulk heating of the sample. In this process, the glass wafer is subjected to heating via a local surface heat source, replacing the CO_2 laser radiation, while a bulk heating source is generated by laser radiation at a wavelength of 1.06 μm. CO_2 laser radiation power is 15 W, while YAG laser radiation power is 140 W.

Figure 4.34 illustrates the spatial distribution of the thermoelastic fields σ_{yy} that arise from the implementation of this scheme.

The presented distribution indicates that the use of a bulk source results in the establishment of a tensile stress zone in the refrigerant supply area, with the lateral and bottom regions of this area constrained by zones exhibiting considerable compressive stresses. The maximum tensile stress values are below the strength threshold of the glass, indicating that crack nucleation will not occur.
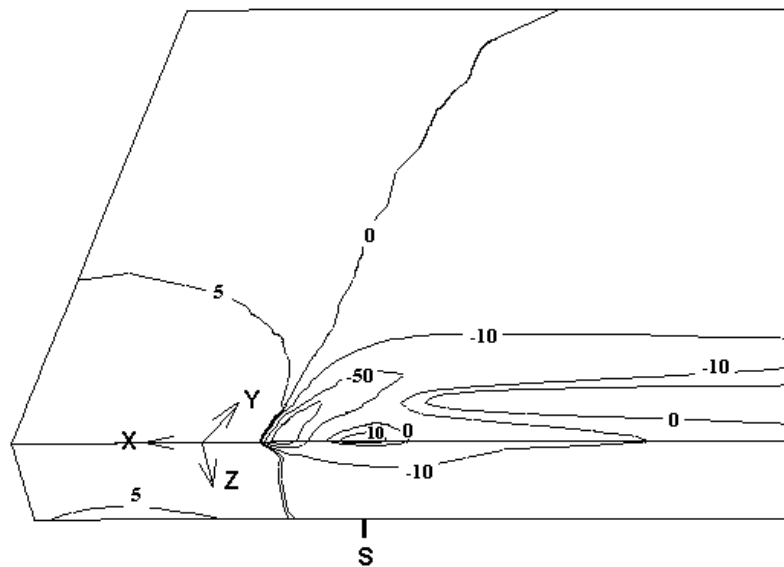

Figure 4.34 – Distribution of thermoelastic fields σ_{yy} (MPa)
in the sample when using semi-ring CO_2 and YAG laser beams

To achieve the specified objective, it is essential to maintain a substantial heating area on the material surface throughout the processing line, similar to the application of elliptical laser beams. Concurrently, it is important to provide additional heating to the sample at the sides of the refrigerant supply area. This approach will create a zone of considerable compressive stresses, which will prevent microcracks from deviating near the lateral boundary of the sample.

To accomplish this goal, it is necessary to use a laser beam featuring a crescent-shaped cross section [204]. The implementation scheme of this method can be seen in Figure 4.35.

Position 1 indicates the shape of the laser source spot on the material surface, while position 2 denotes the refrigerant. The subsequent processing parameters were selected for the calculations. The inner contour of the beam is defined as a circle with a radius of r = 1.7 mm. The outer contour is characterized as an ellipse, with the major and minor axes measuring A = 10 mm and B = 5.4 mm, respectively. The power of the laser radiation is 26 W.
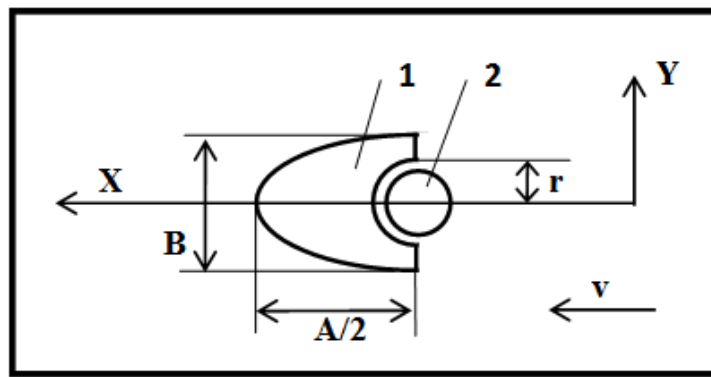
Figure 4.35 – Layout of laser beams and a refrigerant in the cutting plane

Figure 4.36 illustrates the spatial distribution of thermoelastic fields σ_{yy} that emerge from the implementation of this scheme. The graphic representation of the fields is displayed for half of the wafer. The position S in the figure indicates the location of the center of the laser beam and the refrigerant along the X-axis. The maximum temperature recorded in the sample is 760 K or lower.

The presented distribution suggests that within the refrigerant supply area, there exists a zone of tensile stresses that is adequate for the initiation of a microcrack. The front and bottom are surrounded by an area of considerable compressive stresses, which influence the formation of microcracks along the processing line and at depth. Simultaneously, a region of considerable compressive stresses develops on the lateral side of the refrigerant supply area. This area facilitates the control of the microcrack's deviation

from the line along which the material splits during processing near the sample's lateral boundary. In essence, it enables the prevention of the microcrack's deviation towards the lateral boundary when microdefects and microcracks are present on it.
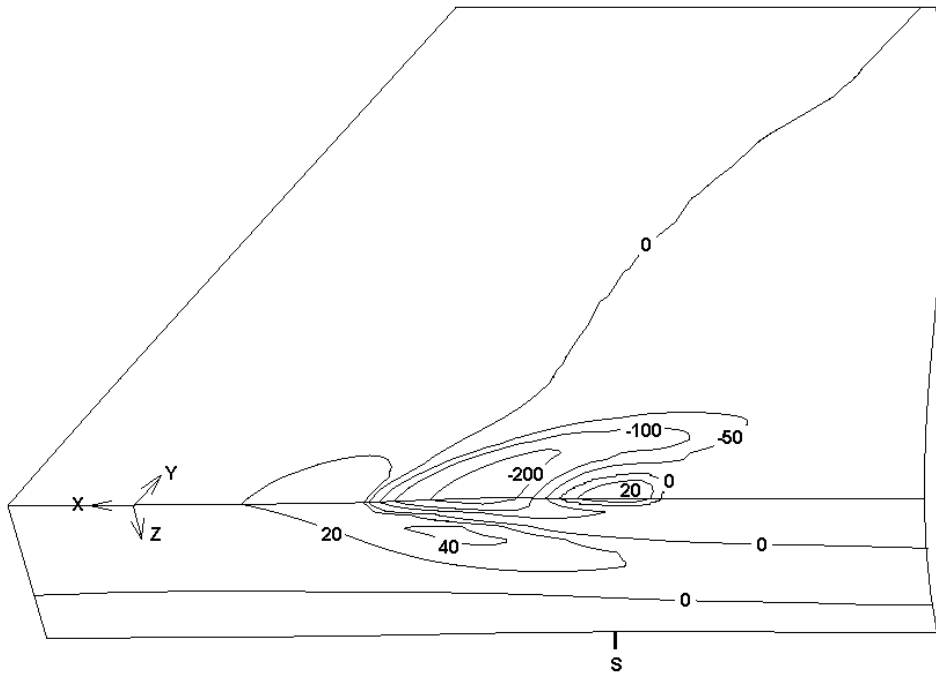
Figure 4.36 – Distribution of thermoelastic fields σ_{yy} (MPa)
in the sample using a semi-ring laser beam

A method for double-beam laser thermal cleaving using CO_2 and YAG laser beams with a crescent-shaped cross-section is proposed based on the findings obtained. The implementation scheme for this method is provided in Figure 4.35. The geometrical dimensions of the beam cross-sections and the locations of their centers are in alignment. The inner contour of the beam is defined as a circle with a radius of $r = 1.7$ mm. The outer contour is characterized as an ellipse, with major and minor axes measuring $A = 10$ mm and $B = 5.4$ mm, respectively. CO_2 laser exhibits a radiation power of $P = 18$ W, while the YAG laser demonstrates a radiation power of $P = 140$ W.

Figure 4.37 illustrates the spatial distribution of thermoelastic fields σ_{yy} resulting from the implementation of this scheme. The graphic representation of the fields is displayed for half of the wafer. The maximum temperature value in the sample is 755 K or lower.

The displayed distribution indicates that, similar to the earlier scenario, a region of significant compressive stresses emerges at the front and on the lateral side of the refrigerant supply area This phenomenon is attributed to the surface heating of the material by the CO_2 laser beam, which influences the progression of microcracks along the material processing line (X-axis).

144

The region of refrigerant exposure exhibits a zone of tensile stresses, with values significantly exceeding those observed during CO_2 laser exposure alone, measuring approximately 48 MPa.
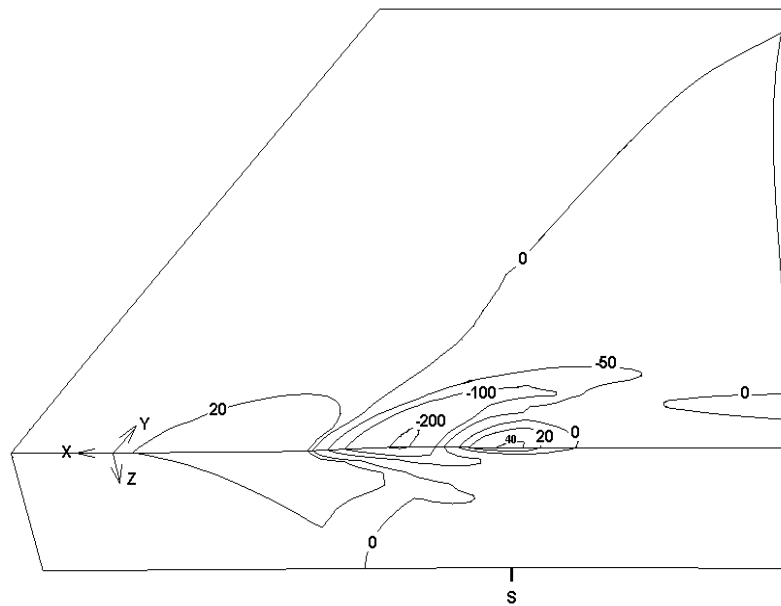
Figure 4.37 – Distribution of thermoelastic fields σ_{yy} (MPa) in the sample using crescent-shaped CO_2 and YAG laser beams

Table 4.1 presents the computed values of maximum temperatures on the material surface, T_{max}, along with the tensile stresses, $\sigma_{yy\ max}$, in the refrigerant exposure area for various configurations of the controlled laser thermocleaving process.

Table 4.1 – Calculated values of maximum temperatures (T_{max}) on the material surface and tensile stresses ($\sigma_{yy\ max}$) in the area of refrigerant exposure for various schemes of the controlled laser thermocleaving process

	Laser beam power, W	T_{max}, K	$\sigma_{yy\ max}$, MPa
an elliptical CO_2 laser beam	30	747	53
a semi-ring CO_2 laser beam	20	738	–
the integrated use of semi-ring beams generated by CO_2 and YAG lasers	15 (CO_2) 140 (YAG)	760	15
a crescent-shaped CO_2 laser beam	26	760	35
the integrated use of crescent-shaped beams generated by CO_2 and YAG lasers	18 (CO_2) 140 (YAG)	755	48

When comparing the maximum tensile stress values in the refrigerant supply region across the schemes outlined in Table 4.1, it is observed that, with the exception of the first scheme, the highest values are recorded when employing the last method.

This, consequently, guarantees a high level of stability in the microcrack nucleation process. In double-beam processing, the bulk absorption of YAG laser radiation by the material results in the compressive stress area being situated in the deeper layers of the material. A compressive stress region develops throughout the entire thickness of the material within the tensile stress area generated by the refrigerant. The spatial arrangement leads to a notable enhancement in the depth of the splitting microcrack compared to single-beam processing.

4.7. Examination of laser cleaving in bilayer structures of silicon wafers and glass substrates

Bilayer structures composed of monocrystalline silicon and glass are extensively used in the fabrication of semiconductor microelectromechanical devices, with electrostatic bonding serving as a primary technology for sample manufacturing [205, 206].

A study in [205] examined the laser cleaving process of bilayer structures consisting of silicon and glass, considering the anisotropic elastic properties of monocrystalline silicon and employing a laser beam at a wavelength of 1.06 μm, focused from the glass layer side.

Here we present the results of numerical simulation regarding the laser cleaving of bilayer structures made of monocrystalline silicon and glass. This process involves laser heating using beams at wavelengths of 1.06 μm and 10.6 μm, along with exposure to a refrigerant. The outcomes of the simulation relating to the single-beam laser treatment of a bilayer structure using a beam at a wavelength of 1.06 microns, both with and without the application of refrigerant impact, are also presented. The analysis was carried out for both the scenario involving treatment from the glass layer side and the scenario involving laser treatment from the monocrystalline silicon side. The simulation was performed in a three-dimensional setting for three cuts of silicon crystals used in the creation of bilayer structures: (100), (110), (111).

The process of laser cleaving of bilayer structures composed of monocrystalline silicon and glass was analyzed through finite-element modelling, focusing on the uncoupled thermoelastic problem within a quasi-static framework [139]. The criterion of maximum tensile stress was applied to ascertain the direction of crack development induced by the laser [153].

In the modelling process, it was assumed that the thermal conductivity coefficient, specific heat capacity, and density of LK5 glass and monocrystalline silicon remain constant. The values used were $\lambda_1 = 1.13$ W/m·K, $C_1 = 795$ J/kg·°C, $\rho_1 = 2270$ kg/m³ for glass, and $\lambda_2 = 10^9$ W/m·K, $C_2 = 758$ J/kg·°C, $\rho_2 = 2330$ kg/m³ for silicon, respectively. The temperature

dependencies of the linear thermal expansion coefficients for LC5 glass and monocrystalline silicon were considered. The reflection and absorption coefficients of monocrystalline silicon and optical glass for laser radiation at wavelengths of 1.06 μm and 10.6 μm were used in the calculations. The modulus of elasticity and Poisson's ratio for glass were taken as $E_1 = 68.5$ GPa, $\nu_1 = 0.184$. The constants of elastic rigidity for crystalline silicon used in the modelling are as follows: $C_{11} = 165.6 \cdot$ GPa, $C_{12} = 63.9 \cdot$ GPa, $C_{44} = 79.5 \cdot$ GPa [167, 177–180, 205–207,].

The calculations were performed for the following parameters of laser beams: the radius of the radiation spot $R_1 = 1 \cdot 10^{-3}$ m for a beam with a radiation wavelength $\lambda_1 = 1.06$ μm and radiation power $P_0 = 200$ W; the radius of the radiation spot $R_2 = 1 \cdot 10^{-3}$ m for a beam with a radiation wavelength $\lambda_2 = 10.6$ μm and radiation power $P_0 = 10$ W. The calculations were conducted for bilayer disks made of monocrystalline silicon and glass with radius R = 15.5 mm (the thickness of silicon layer was $H_1 = 0.5$ mm, the thickness of the glass layer was $H_2 = 0.5$ mm). The speed of the sample movement relative to the laser beams and refrigerant was equal to V = 10 mm/s.

For the comparative analysis, we performed calculations of thermoelastic field distributions for six different options concerning the spatial arrangement of the laser and refrigerant impact areas:

a) laser cleaving of a bilayer structure under sequential laser heating using beams at wavelengths of 1.06 μm and 10.6 μm, alongside exposure to a refrigerant from the side of monocrystalline silicon (see Figure 4.38, where the horizontal arrow indicates the direction of the workpiece movement relative to the laser beams and the refrigerant);

b) laser cleaving of a bilayer structure during sequential laser heating using a beam at a wavelength of 1.06 μm, followed by exposure to a refrigerant from the side of monocrystalline silicon (see Figure 4.39);

c) laser cleaving of a bilayer structure via laser heating using a beam at a wavelength of 1.06 μm directed from the side of monocrystalline silicon (see Figure 4.40);

d) laser cleaving of a bilayer structure through sequential laser heating using beams at wavelengths of 1.06 μm and 10.6 μm, in conjunction with exposure to a refrigerant from the side of the glass layer;

e) laser cleaving of a bilayer structure during sequential laser heating using a beam at a wavelength of 1.06 μm, coupled with exposure to a refrigerant from the side of the glass layer;

f) laser cleaving of a bilayer structure under laser heating using a beam at a wavelength of 1.06 μm from the side of the glass layer.

147

Figure 4.38 – Spatial arrangement of the impact areas
of laser radiation and a refrigerant (option A)
1 is the laser beam with a wavelength of 1.06 μm, 2 is the laser beam with a wave-
length of 10.6 μm, 3 is the refrigerant, 4 is the bilayer structure composed of mono-
crystalline silicon 5 and glass 6, 7 is the cross-section of laser beam 1 in the cutting
plane, 8 is the cross-section of laser beam 2 in the cutting plane,
9 is the refrigerant exposure area.

Figure 4.39 – Spatial arrangement of the impact areas
of laser radiation and a refrigerant (option B)
1 is the laser beam with a wavelength of 1.06 μm, 2 is the refrigerant,
3 is the bilayer structure composed of monocrystalline silicon 4 and glass 5, 6 is the
cross-section of laser beam 1 in the cutting plane,
7 is the refrigerant exposure area.

The mutual location of the impact areas of laser beams and a refrigerant for processing options D, E, F coincide with options A, B, C, respectively, considering their influence from the side of the glass layer.

The calculation of thermoelastic fields in the bilayer structure was conducted for each of the six options regarding the spatial arrangement of the laser and refrigerant impact areas. This analysis considered six distinct scenarios, incorporating the anisotropy of the silicon layer: I a is the cut analysis (100) in the [001] direction; I b is the cut analysis (100) in the [011] direction; II a is the cut analysis (110) in the [1−10] direction; II b is the cut analysis (110) in the [001] direction; II c is the cut analysis (110) in the [1−11] direction, III is the cut analysis (111) in the [1−10] direction.
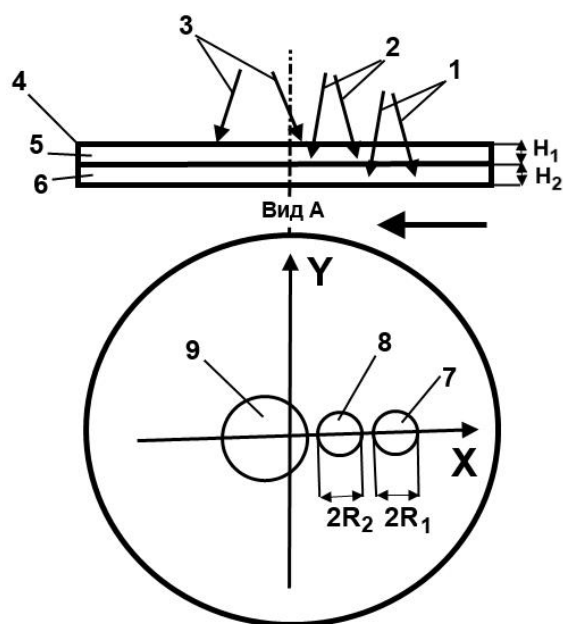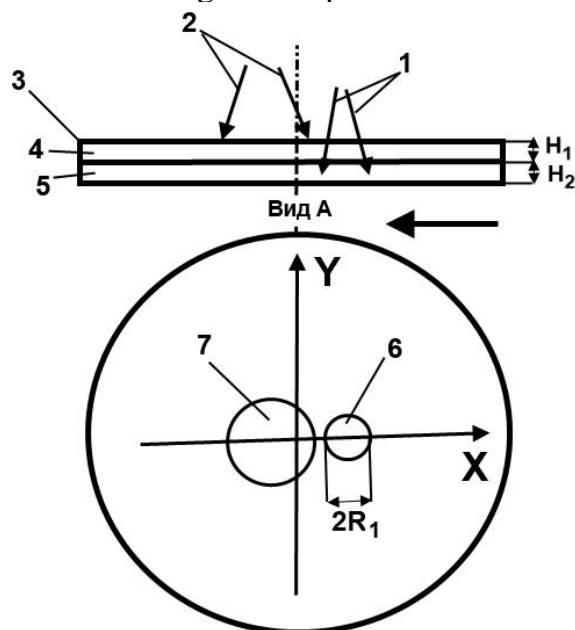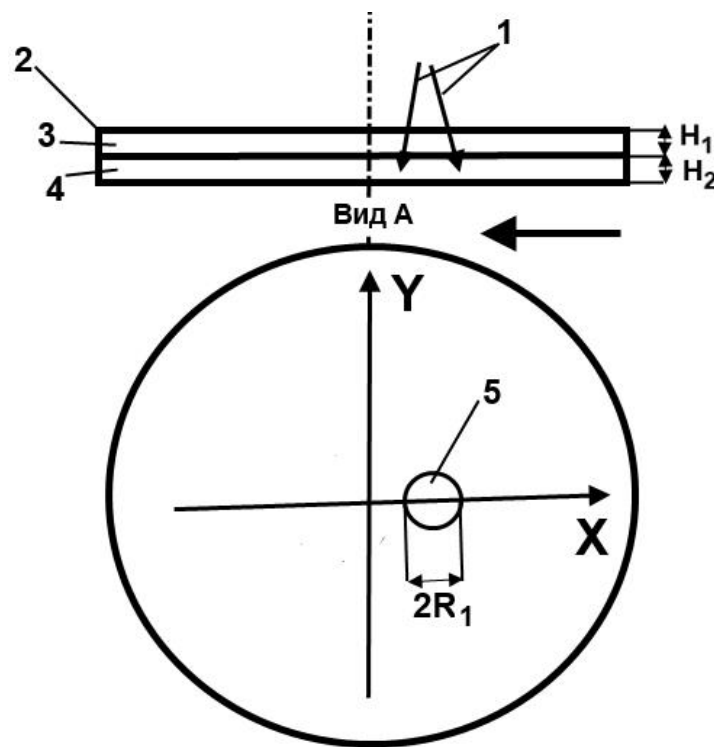
Figure 4.40 – Spatial arrangement of the impact areas
of laser radiation and a refrigerant (option C)
1 is the laser beam with a wavelength of 1.06 μm, 2 is the bilayer structure
composed of monocrystalline silicon 3 and glass 4,
5 is the cross-section of laser beam 1 in the cutting plane.

The outcomes of the calculations are presented in Tables 4.2–4.3 and Figures 4.41–4.44. Table 4.2 details the computed values for maximum and minimum temperatures within the analyzed bilayer structure. Table 4.3 outlines the computed values for maximum tensile and compressive stresses in the processing area.

149

Table 4.2 – Calculated values for maximum and minimum temperatures in the bilayer structure

Temperature in the bilayer structure T, K	Arrangement options for laser radiation and refrigerant impact areas					
	A	B	C	D	E	F
maximum	696	563	645	777	718	733
minimum	294	294	297	294	295	298

Table 4.3 – Calculated values of maximum tensile and compressive stresses in the processing area of the bilayer structure

Type of silicon cut	Maximum stresses σ_{yy} in the processing area, MPa	Arrangement options for laser radiation and refrigerant impact areas					
		A	B	C	D	E	F
Ia	tensile	56	40	35	48	42	40
	compressive	140	113	127	164	169	163
Ib	tensile	60	43	38	52	43	46
	compressive	138	113	125	161	169	161
IIa	tensile	58	42	39	52	40	46
	compressive	150	120	137	176	181	176
IIb	tensile	67	49	39	56	45	47
	compressive	166	134	151	202	208	202
IIc	tensile	65	47	42	57	43	52
	compressive	157	127	142	187	195	187
III	tensile	72	52	40	56	43	46
	compressive	178	142	162	208	214	208

Figures 4.41 – 4.44 illustrate the distributions of temperature fields and thermoelastic stress fields generated in the bilayer structure for each of the six scenarios of the spatial arrangement of the laser radiation and refrigerant impact areas during cutting in the [001] direction of the (100) cut of mono-crystalline silicon (type Ia), considering the anisotropy of the silicon layer in the bilayer structure. In the context of Figures 4.41 – 4.42, the letters a), b), and c) represent options A, B, and C regarding the spatial arrangement of the areas influenced by laser radiation and the refrigerant. Figures 4.43 and 4.44 illustrate the spatial arrangement of the laser radiation and refrigerant impact areas, with letters a), b), and c) representing options D, E, and F, respectively.
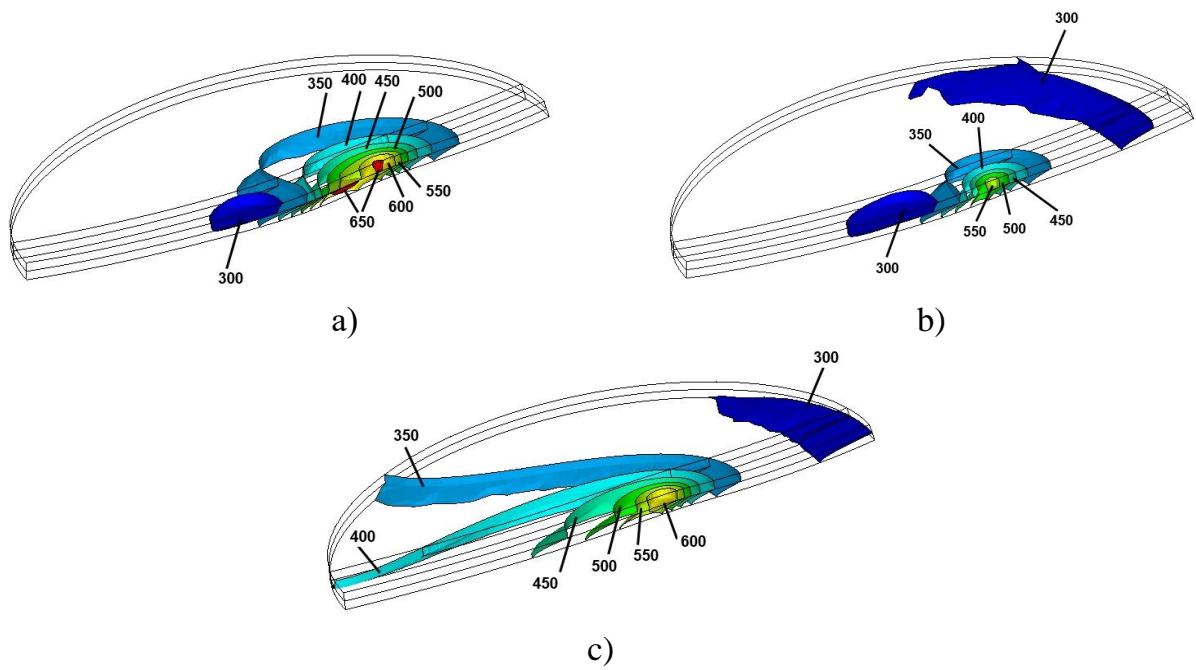
Figure 4.41 – Temperature distribution within the volume of the bilayer sample
when subjected to treatment from the monocrystalline silicon side, K
a) double-beam exposure with a refrigerant;
b) exposure to YAG laser and a refrigerant; c) YAG laser exposure

Figure 4.42 – Distribution of stresses σ_{yy} within the volume of the bilayer sample
subjected to treatment from the monocrystalline silicon side, MPa
a) double-beam exposure with a refrigerant;
b) exposure to YAG laser and a refrigerant; c) YAG laser exposure

151

Figure 4.43 – Temperature distribution within the volume of the bilayer sample
subjected to treatment from the glass layer side, K
a) double-beam exposure with a refrigerant;
b) exposure to YAG laser and a refrigerant; c) YAG laser exposure

Figure 4.44 – Distribution of stresses σ_{yy} within the volume of the bilayer sample
subjected to treatment from the glass layer side, in MPa
a) double-beam exposure with a refrigerant;
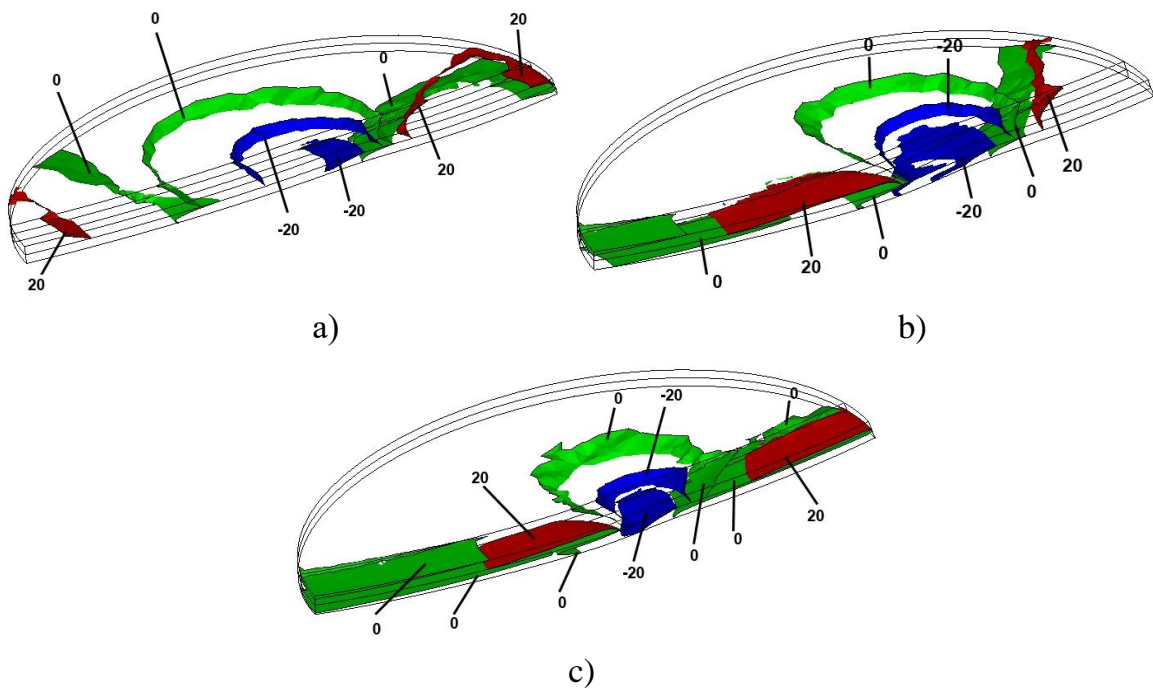b) exposure to YAG laser and a refrigerant; c) YAG laser exposure

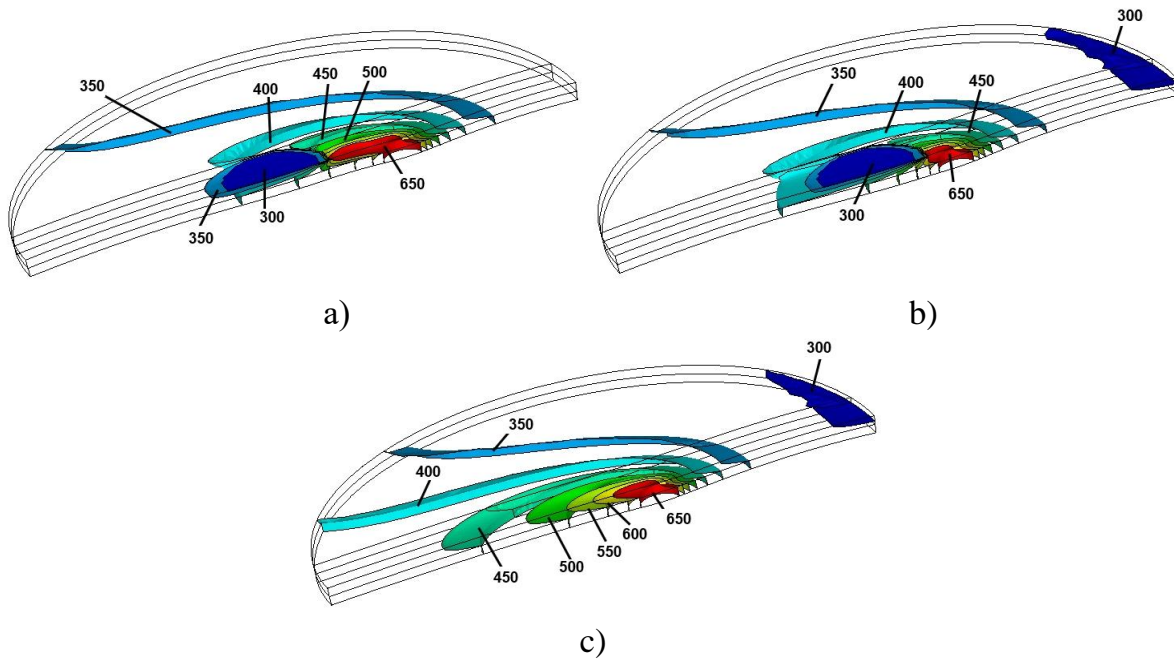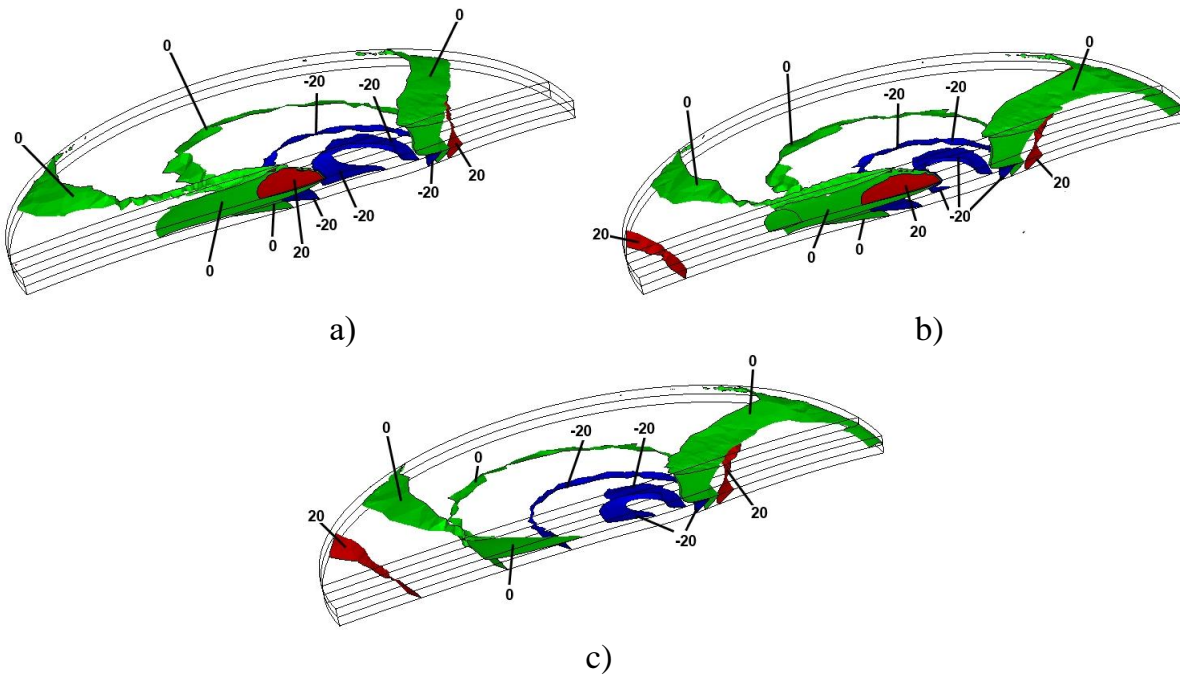The lack of thermal conductivity anisotropy in silicon crystals results in identical calculated temperature values in the laser processing area for cuts (110), (100), and (111) when the same processing parameters are selected. It is essential to consider the notable disparity in the thermal conductivity coefficients of silicon and glass. In the analysis of the results, it is reasonable to consider the substantial impact of the absorption and reflection coefficients of monocrystalline silicon and glass for radiation at wavelengths of 1.06 μm and 10.6 μm on the specific features of temperature field localization and their computed values.

The data shown in Table 4.2 indicates that the maximum temperature values for all six simulation modes remain below the glass softening temperature. This finding is crucial for determining the technological parameters for laser processing of bilayer structures composed of monocrystalline silicon and glass, as it relies on information about temperature fields [67]. Consequently, the computed temperature values fall within the range required for the occurrence of brittle fracture in the bilayer wafer due to thermoelastic stresses. The maximum temperature values are defined by the double-beam operating modes (696 K for option A and 777 K for option D, respectively). The minimum temperature values in the treatment area are observed in the single-beam configuration using a refrigerant (563 K for option B and 718 K for option E, respectively).

Figure 4.41a demonstrates the existence of two distinct local regions exhibiting elevated temperature values during double-beam processing from the perspective of monocrystalline silicon: one within the volume of the silicon wafer where YAG laser exposure occurs, and the other at the layer boundary corresponding to CO_2 laser exposure. The application of the double-beam scheme, influenced by the glass layer, results in the creation of a single continuous region exhibiting elevated temperature values within the volume of the bilayer structure (Figure 4.41a). In the implementation of the single-beam scheme using a YAG-laser ($\lambda_1 = 1.06$ μm) for the treatment of monocrystalline silicon, both with and without the application of a refrigerant, a region of elevated temperatures is generated solely within the silicon layer (Figures 4.41b and 4.41c). The implementation of single-beam processing options, influenced by the glass layer, along with double-beam interactions, results in the development of a region exhibiting elevated temperature values across two layers concurrently (Figures 4.43b and 4.43c).

As previously mentioned, Table 4.3 presents the computed values of the maximum tensile and compressive stresses generated in the processing area during laser cleaving. This data corresponds to six options of the spatial arrangement of the laser and refrigerant impact areas, as well as six distinct scenarios that consider the anisotropy of the silicon layer.

The analysis of the data (Table 4.3) indicates that the variation in maximum tensile stress values in bilayer structures attributed to silicon anisotropy can be as high as 30 %. The variation in maximum tensile stress values resulting from the spatial arrangement of the laser radiation and refrigerant impact areas can be as high as 80 %.

The highest tensile stress values are attained for the combination (III, A) when addressing the (111) cut, with the laser beams and refrigerant moving in the [1−10] direction from the monocrystalline silicon side. The combination (Ia, C) produces the lowest tensile stress values for the (100) cut when the laser beam, at a wavelength of 1.06 μm, is oriented in the [001] direction from the monocrystalline silicon side. The computed tensile stress values in the processing area are 72 MPa and 35 MPa.

Considering the previously outlined differences in the magnitudes of thermoelastic stresses, it is logical to select the technological parameters for the separation process of bilayer structures via laser cleaving, such as adjusting the processing speed or the power of the laser radiation.

Attention must be given to the features that govern the spatial localization of thermoelastic fields generated from the laser cleaving of bilayer structures, particularly when implementing six calculated options of the spatial arrangement of the areas affected by laser radiation and a refrigerant. Upon examining Figures 4.42 and 4.44, it is evident that the implementation of options using the refrigerant results in the formation of considerable tensile stresses on the surface of the sample within the impact area (Figures 4.42a, 4.42b, 4.44a, 4.44b). In single-beam processing scenarios, notable tensile stress regions develop within the bilayer structure, albeit at a considerable distance from the laser beam center (Figures 4.42c and 4.44c). This will result in instability during the laser cleaving process and may cause laser-induced cracks to deviate from the intended processing line.

It is also essential to focus on the spatial configurations of the boundary between tensile and compressive stresses in bilayer structures within the processing area (see isosurfaces at σ_{yy}=0). These configurations can serve as indicators for predicting the success of crack propagation originating on the surface of the first layer in the refrigerant exposure area across both layers. The most effective approach in this scenario involves employing laser cleaving of the bilayer structure, using sequential laser heating with beams at wavelengths of 1.06 μm and 10.6 μm, along with refrigerant exposure from the monocrystalline silicon side (Figure 4.42a).

Laser cleaving of bilayer structures comprising silicon wafers and glass substrates when the workpiece is subjected to laser beams at wavelengths equal to 0.808 μm and 10.6 μm

This section presents the outcomes of finite-element modelling concerning the laser cleaving of bilayer structures composed of monocrystalline silicon and glass, using laser heating with beams at wavelengths of 0.808 μm and 10.6 μm, alongside exposure to a refrigerant. The application of laser radiation parameters at a wavelength of 0.808 μm for modelling purposes is significant, as silicon exhibits a strong absorption of radiation at this wavelength.

The findings from the calculations are detailed in Tables 4.4–4.5 and illustrated in Figures 4.45–4.48.

Table 4.4 – Calculated values of maximum and minimum temperatures in the bilayer structure

Temperature in the bilayer structure T, K	Arrangement options for laser radiation and refrigerant impact areas					
	A	B	C	D	E	F
maximum	784	675	782	856	845	863
minimum	295	294	298	295	295	299

Table 4.5 – Calculated values of maximum tensile and compressive stresses in the processing area of the bilayer structure

Type of silicon cut	Maximum stresses σ_{yy} in the processing area, MPa	Arrangement options for laser radiation and refrigerant impact areas					
		A	B	C	D	E	F
Ia	tensile	64	46	42	63	46	59
	compressive	185	148	172	231	239	230
Ib	tensile	68	49	45	60	45	63
	compressive	184	149	170	229	240	227
IIa	tensile	65	46	49	69	47	63
	compressive	199	158	185	249	256	285
IIb	tensile	76	56	49	72	56	63
	compressive	220	176	205	287	297	285
IIc	tensile	73	53	53	67	50	70
	compressive	209	168	194	265	277	265
III	tensile	81	59	48	65	49	67
	compressive	235	187	219	298	307	297

Figure 4.45 – Temperature distribution within the volume of the bilayer sample when subjected to treatment from the side of monocrystalline silicon, K
a) double-beam exposure with a refrigerant; b) exposure to a laser at a wavelength of 0.808 µm and a refrigerant; c) exposure to a laser at a wavelength of 0.808 µm
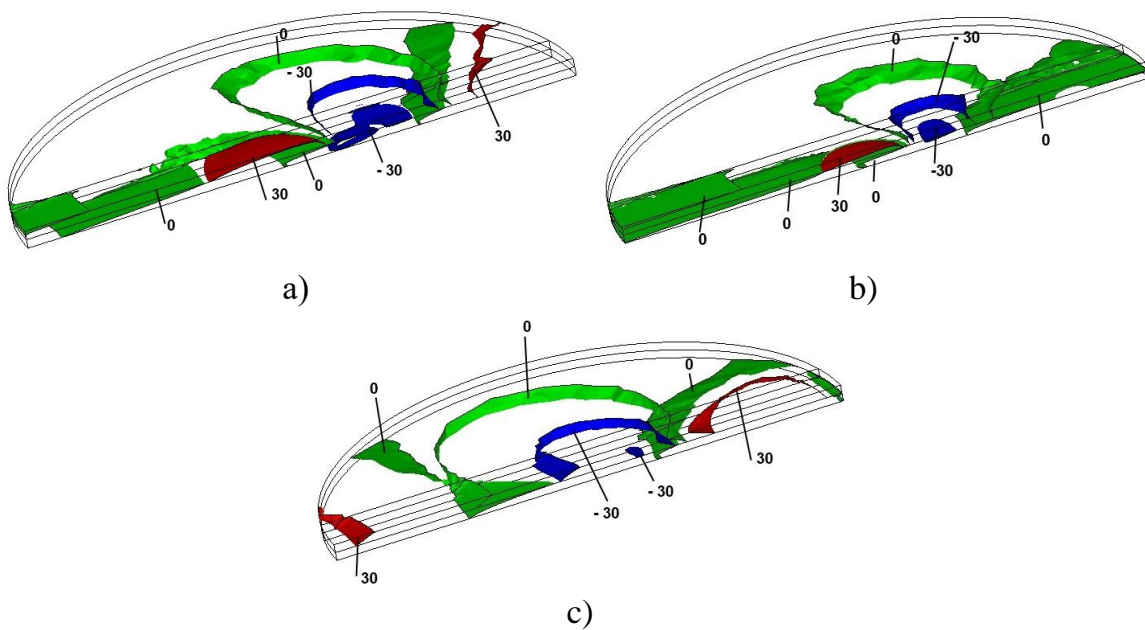
Figure 4.46 – Distribution of stresses σ_{yy} within the volume of the bilayer sample subjected to treatment from the side of monocrystalline silicon, MPa
a) double-beam exposure with a refrigerant; b) exposure to a laser at a wavelength of 0.808 µm and a refrigerant; c) exposure to a laser at a wavelength of 0.808 µm
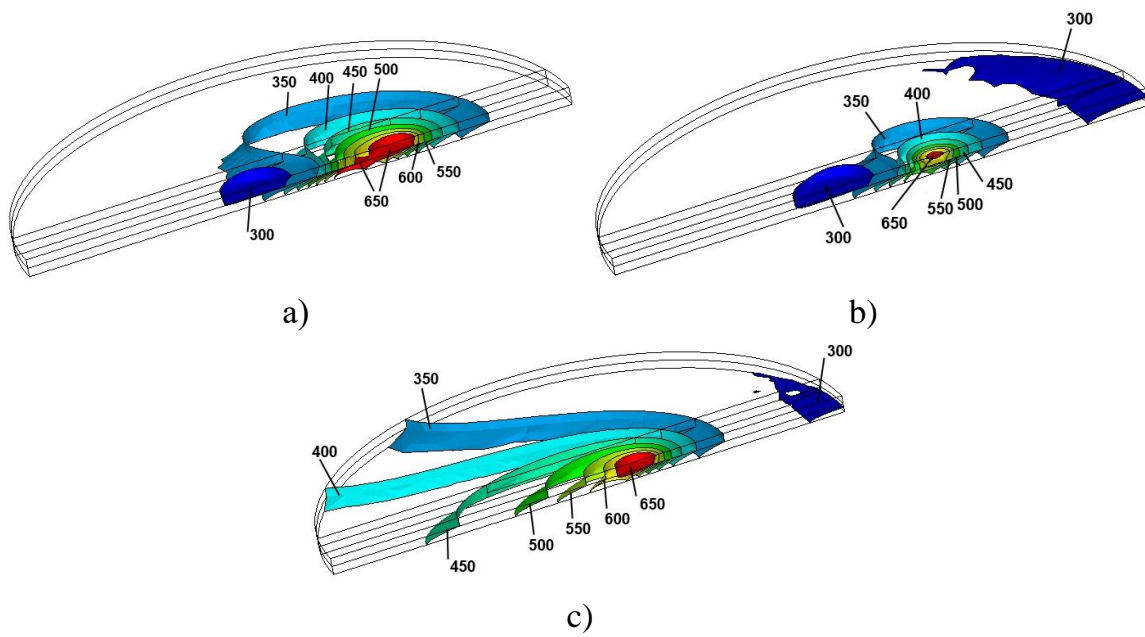
156
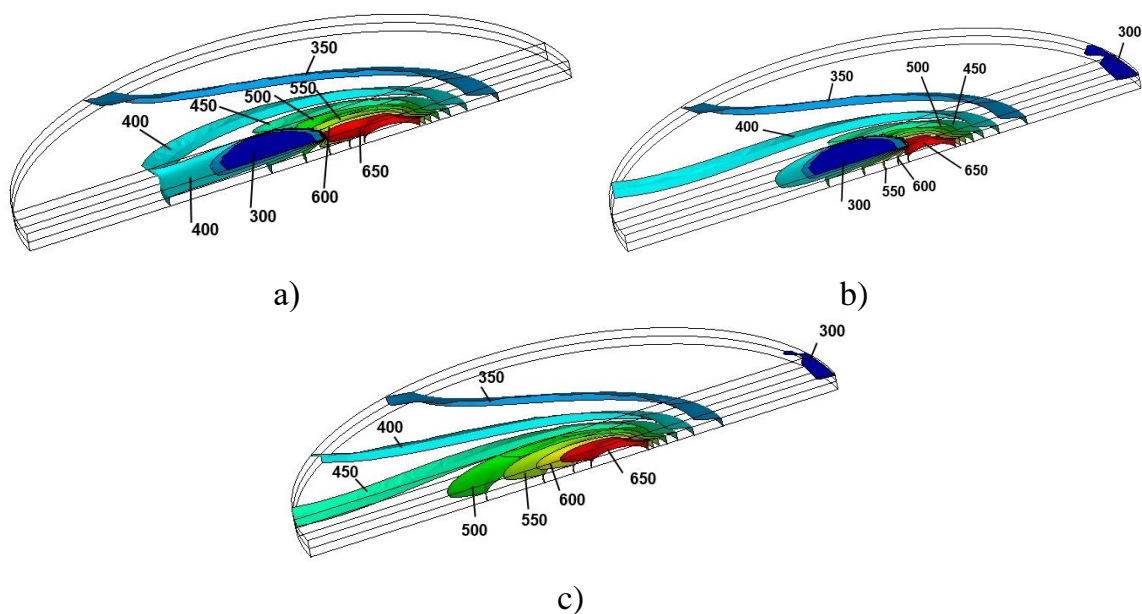
Figure 4.47 – Temperature distribution within the volume of the bilayer sample
subjected to treatment from the glass layer side, K
a) double-beam exposure with a refrigerant; b) exposure to a laser at a wavelength of
0.808 µm and a refrigerant; c) exposure to a laser at a wavelength of 0.808 µm

Figure 4.48 – Distribution of stresses σ_{yy} within the volume of the bilayer sample
subjected to treatment from the glass layer side, MPa
a) double-beam exposure with a refrigerant; b) exposure to a laser at a wavelength of
0.808 µm and a refrigerant; c) exposure to a laser at a wavelength of 0.808 µm
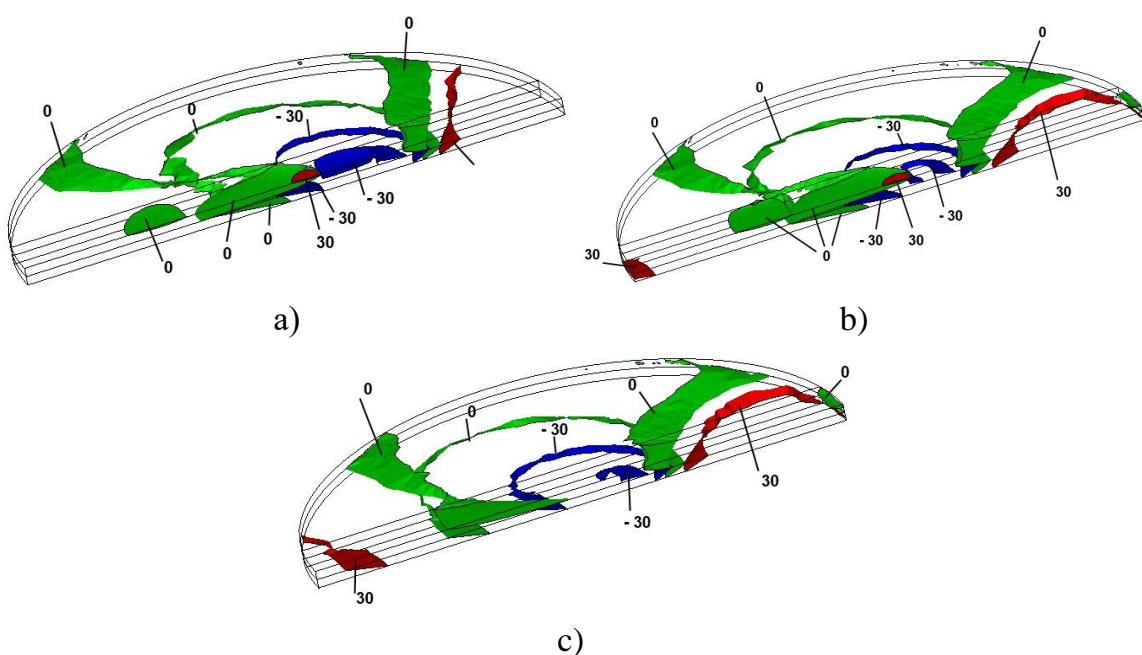
The calculated values of maximum and minimum temperatures in the
bilayer structure under examination are presented in Table 4.4. The values
of maximum tensile and compressive stresses in the processing area are
given in Table 4.5.

Figures 4.45 – 4.48 illustrate the distributions of temperature fields and thermoelastic stress fields generated in the bilayer structure for each of the six options of the spatial arrangement of the laser radiation and refrigerant impact areas during cutting along the [001] direction of the (100) cut of monocrystalline silicon (type Ia).

In this instance, as illustrated in Figures 4.45–4.46, the letters a), b), and c) represent options A, B, and C regarding the spatial arrangement of the laser radiation and refrigerant impact areas. In Figures 4.47–4.48, letters a), b), c) represent options D, E, F concerning the spatial arrangement of the laser radiation and refrigerant impact areas, respectively.

The data presented in Table 4.4 reveals that the maximum temperature values for all six simulation modes remain below the glass softening temperature. Consequently, the computed temperature values fall within the range required for the occurrence of brittle fracture in the bilayer wafer due to thermoelastic stresses.

In general, the peculiarities of temperature field localization presented in Figures 4.45 and 4.47 coincide with the simulation outcomes of the laser cleaving process for bilayer structures composed of silicon and glass. This is observed when employing laser radiation at a wavelength of 1.06 μm, while also considering the heightened absorption of radiation at 0.808 μm by silicon.

As noted earlier, Table 4.5 presents the computed values of the maximum tensile and compressive stresses generated in the processing area during laser cleaving. This data corresponds to six options of the spatial arrangement of the laser and refrigerant impact areas, as well as six distinct scenarios that consider the anisotropy of the silicon layer.

The analysis of the data (refer to Table 4.5) shows that the variation in maximum tensile stress values in bilayer structures attributed to silicon anisotropy amounts to 28 %. The variation in maximum tensile stress values resulting from the spatial arrangement of the laser radiation and refrigerant impact zones can be as high as 55 %.

The highest tensile stress values are attained for the combination (III, A) when addressing the (111) cut, with the laser beams and refrigerant moving in the [1$\bar{1}$0] direction from the monocrystalline silicon side. The combination (Ia, C) produces the lowest tensile stress values for the (100) cut when the laser beam, at a wavelength of 1.06 μm, is oriented in the [001] direction from the monocrystalline silicon side.

The determined values of the associated tensile stresses in the processing zone are 81 MPa and 42 MPa. Considering the previously discussed variations in thermoelastic stress values, it is logical to select the technological parameters for the separation of bilayer structures through laser cleaving, such as adjusting the processing speed or the power of the laser radiation.

Let us pay attention to the peculiarities of spatial localization of thermoelastic fields formed as a result of laser cleaving of bilayer structures at realization of different options of spatial arrangement of zones of influence of laser radiation and a refrigerant. Considering Figures 4.46 and 4.48, it can be seen that in case of realization of options with the use of refrigerant in the zone of its impact on the surface of the sample, tensile stresses of considerable magnitude are formed (see Figures 4.46a, 4.46b, 4.48a, 4.48b). In the case of single-beam processing variants, the areas of significant tensile stresses are also formed in the bilayer structure, but at a considerable distance from the laser beam center (see Figures 4.46c and 4.48c). In practice, this will result in instability during the laser cleaving process, potentially causing laser-induced cracks to deviate from the intended processing line. The examination of the spatial configuration of the boundary between tensile and compressive stresses in bilayer structures within the processing area (see isosurfaces at $\sigma_{yy} = 0$) facilitates the prediction of crack propagation success in both layers of the bilayer structure. The most effective method in this scenario seems to be the application of laser cleaving on the bilayer structure, using sequential laser heating and refrigerant exposure from the monocrystalline silicon side (see Figures 4.46a and 4.46b). It is important to highlight that analogous characteristics were detected in the simulation of the laser cleaving process for bilayer structures composed of silicon and glass, using laser radiation at a wavelength of 1.06 μm.

4.8. Laser thermal cleaving of sapphire using crescent-shaped beams

Nowadays, sapphire is widely used across various industrial domains. It exhibits characteristics such as remarkable transparency, resistance to ultraviolet radiation, durability against mechanical damage, tolerance to high temperatures, exceptional dielectric properties, a crystal lattice that facilitates epitaxial layer growth, a low friction coefficient, and several additional attributes. Sapphire finds application in optical and optoelectronic devices, serving as a material for the creation of viewing windows, lenses, prisms, and light guides across a wide range of radiation and temperature conditions. Additionally, it is used in the production of casings for specialized lamps and protective covers for navigation devices. The notable benefits of sapphire substrate include its inert nature, capacity to function under elevated temperatures, and resilience to mechanical stresses. At present, numerous industrial establishments globally are engaged in the production of epitaxial heterostructures utilizing aluminum, gallium, and indium nitrides, aimed at the mass manufacturing of LEDs and transistors on sapphire substrates. The

yearly production of LEDs and transistors on sapphire substrates reaches billions of units annually. Consequently, the advancement of manufacturing technology for sapphire substrate devices holds significant importance.

This section delves into the use of crescent-shaped beams within the framework of the controlled laser thermal cleaving process, employing sapphire crystals as a focal point for analysis.

A comparative analysis was conducted on the thermoelastic fields in sapphire wafers during single-beam and double-beam controlled laser thermal cleaving, using beams with circular and crescent-shaped cross-sections. Based on the transmission spectrum of sapphire as detailed in sources [208] and [209], continuous radiation at a wavelength of 10.6 µm, which is efficiently absorbed by the surface layers of the material, was employed for single-beam thermal cleaving. In the context of double-beam thermal cleaving, a laser emitting at a wavelength of 5 µm was selected as the secondary source of radiation characterized by bulk absorption. The configuration of the beam arrangement is illustrated in Figure 4.49. The arrow denotes the trajectory of the wafer's motion in relation to the laser beams.
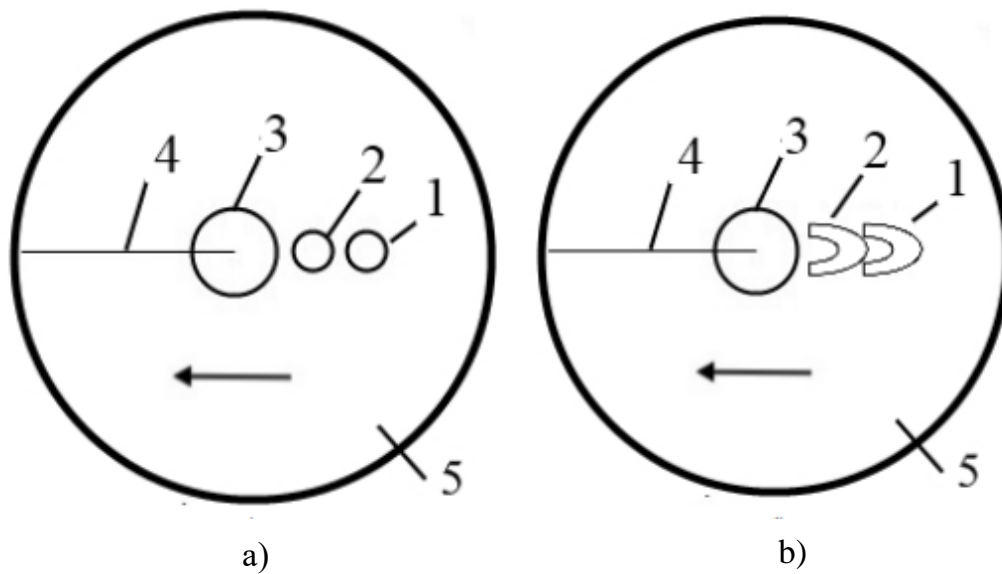
Figure 4.49 – Arrangement of laser radiation and refrigerant impact areas
in the cutting plane: a) is the circular beam; b) is the crescent-shaped beams
1 is the laser beam with a wavelength of 10.6 µm, 2 is the laser beam with
a wavelength of 5 µm, 3 is the refrigerant, 4 is the laser-induced microcrack,
5 is the sapphire wafer

Calculations were performed for wafers with a radius of 15.5 mm. The selected wafer thicknesses were 0.2 mm, 0.4 mm, and 1 mm, with a processing speed set at 10 mm/s.

The parameters of laser beams were as follows: a circular beam with a radius of 1.5 mm; a crescent-shaped beam featuring an outer contour that is a semi-ellipse with semi-major and semi-minor axes measuring 3.4 mm and

1.5 mm respectively, and an inner contour that is a semi-ellipse with semi-major and semi-minor axes measuring 1.7 mm and 0.75 mm respectively. The sizes of the crescent-shaped beams were chosen to ensure that, with constant radiation power densities across all calculations, the maximum tensile stress values in the processing area remained equivalent for both crescent-shaped and circular beams. The thermophysical properties of sapphire necessary for calculations are detailed in references [208] and [209].

The simulation of the laser thermal cleaving process was conducted within the context of thermoelasticity theory, employing the finite element method [139]. In the initial phase of addressing the problem, the temperature distributions within the sample were computed. Subsequently, the focus shifted to determining the thermoelastic stresses generated by the effects of laser radiation and refrigerant interaction on the surface of sapphire wafers. This sequence of simulations yields results within the context of the uncoupled problem of thermoelasticity, presented in a quasi-static formulation. From a physical perspective, the quasi-static formulation of the thermoelastic problem involves the assumption that the stress state is established at a rate significantly faster than the attainment of thermal equilibrium. The criterion of maximum tensile stress was selected as the determining factor for the direction of crack development [153].

According to this criterion, the laser microcrack propagates in the direction perpendicular to the maximum tensile stress. The consideration was given that the crack propagating in the tensile zone ceases its progression upon reaching the compressive zone. The analysis was performed considering the anisotropy of thermal and elastic properties of sapphire for wafers cleaved in the following planes: I – cut (0001) or C-plane; II – cut ($1\bar{1}02$) or R-plane. The matrix $\{C_{ik}\}$ of which, when considering the crystallographic structure of sapphire, will take the form [23]:

$$\{C_{ik}\} = \begin{pmatrix} C_{11} & C_{12} & C_{13} & C_{14} & 0 & 0 \\ C_{12} & C_{11} & C_{13} & -C_{14} & 0 & 0 \\ C_{13} & C_{13} & C_{33} & 0 & 0 & 0 \\ C_{14} & -C_{14} & 0 & C_{44} & 0 & 0 \\ 0 & 0 & 0 & 0 & C_{44} & C_{14} \\ 0 & 0 & 0 & 0 & C_{14} & \dfrac{C_{11}-C_{12}}{2} \end{pmatrix}$$

The following elastic rigidity constants were used for the calculations: $C_{11} = 4.97 \cdot 10^5$ MPa, $C_{12} = 1.626 \cdot 10^5$ MPa, $C_{13} = 1.172 \cdot 10^5$ MPa, $C_{14} = -0.229 \cdot 10^5$ MPa, $C_{33} = 4.981 \cdot 10^5$ MPa, $C_{44} = 1.472 \cdot 10^5$ MPa [210].

For a wafer cut along the plane $(1\bar{1}02)$ plane, i.e., the R-plane, the matrix is represented as follows:

$$\{C_{ik}\} = \begin{pmatrix} 128.3 & -7.7 & -7.67 & 0.072 & 6.13 & -6.16 \\ -7.7 & 130.15 & -7.76 & 4.5 & -0.6 & -1.38 \\ -7.67 & -7.76 & 130.13 & 4.5 & -1.38 & -0.58 \\ 0.072 & 4.5 & 4.5 & 34.47 & -4.8 & -4.8 \\ -6.13 & -0.6 & -1.38 & -4.8 & 33.6 & 4.78 \\ -6.16 & -1.38 & -0.58 & -4.8 & 4.78 & 33.6 \end{pmatrix} \cdot 10^9 \text{ Pa}$$

Figures 4.50 and 4.51 illustrate the distribution of thermoelastic stress fields on the surface of a 0.2 mm thick sapphire wafer during the processes of single-beam and double-beam laser thermal cleaving. The patterns observed in the field when employing circular and crescent-shaped beams exhibit similarities and are generally indicative of the process involved in controlled laser thermal cleaving. A zone of significant compressive stresses is established in the vicinity of laser irradiation, which subsequently transition into tensile stresses in the area where the refrigerant is supplied.

This zone serves as the locus for the initiation and growth of the splitting crack. An area characterized by tensile stresses is established in advance of the laser beam, with the value of these stresses intensifying as one moves closer to the edges of the sample. This may result in a negative outcome, specifically the nucleation of a crack originating from the weakened edge, which subsequently propagates towards the region subjected to laser exposure.

Tables 4.6 and 4.7 present the calculated values of maximum tensile stresses in the refrigerant exposure area of the sample.

Table 4.6 – Calculated values of maximum tensile stresses in the refrigerant exposure area in the sample using circular laser beams

Wafer thickness, mm	Stress, MPa			
	Single-beam thermal cleaving		Double-beam thermal cleaving	
	cut (0001)	cut $(1\bar{1}02)$	cut (0001)	cut $(1\bar{1}02)$
h = 0.2	235	87.7	284	101
h = 0.4	95.8	26.6	131	36.2
h = 1	31.3	7.6	52.9	12.7

The calculation data provided in Tables 4.6 and 4.7 clearly indicate that the maximum tensile stress values in the refrigerant exposure area of the sample, when using laser beams with the specified parameters, remain virtually unchanged.

Figure 4.50 – Field distribution of thermal stresses (MPa) on the surface of a sapphire wafer when exposed to laser radiation with a wavelength of 10.6 μm, considering the anisotropic nature of thermal properties
a) is the cut (0001) or C-plane, beam cross-section is circular;
b) is the cut ($1\bar{1}02$) or R-plane, beam cross-section is circular;
c) is the cut (0001) or C-plane, crescent-shaped beam;
d) is the cut ($1\bar{1}02$) or R-plane, crescent-shaped beam.

163
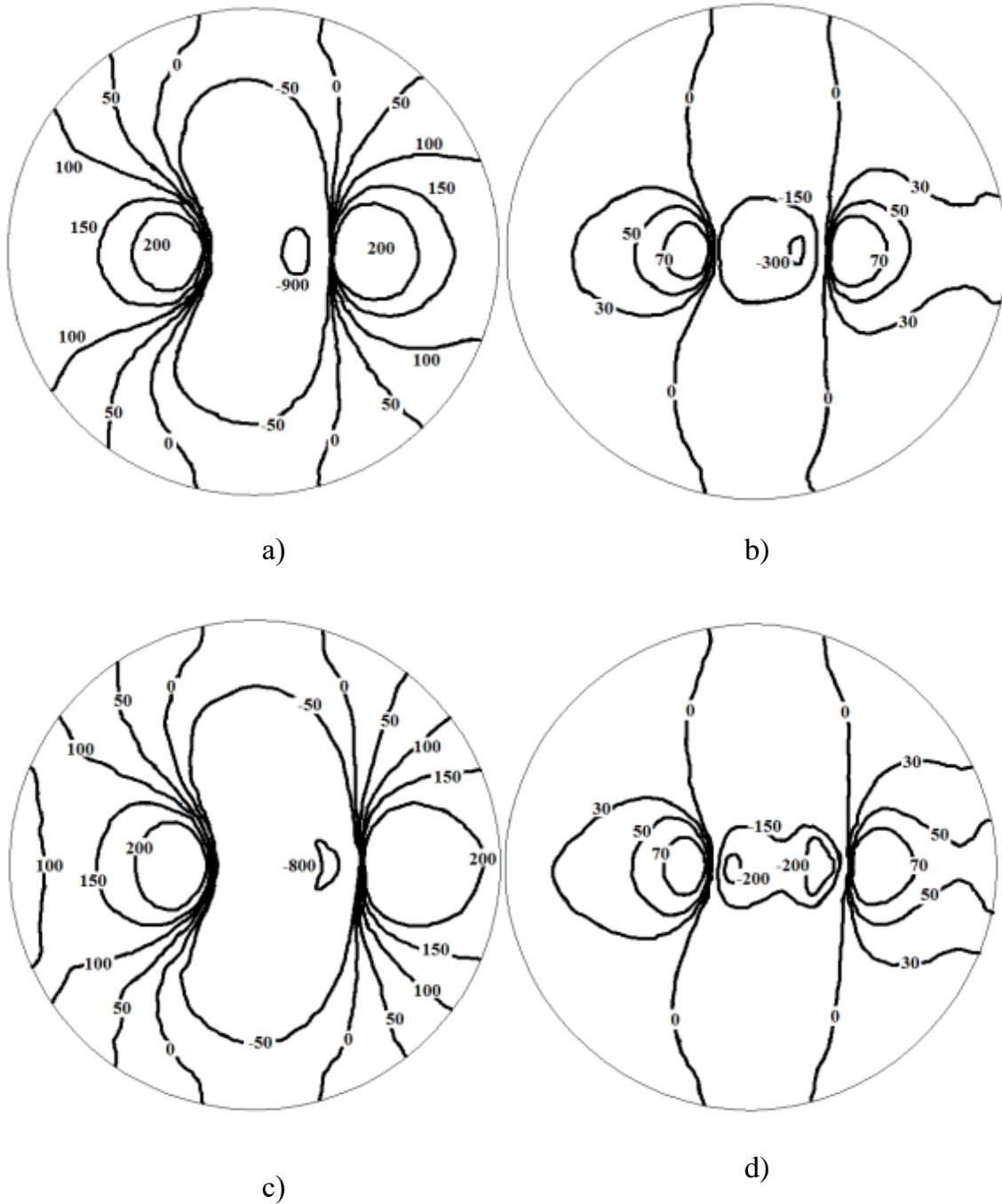
Figure 4.51 – Field distribution of thermal stresses (MPa) on the sapphire wafer surface subjected to concurrent exposure to laser radiation at wavelengths of 10.6 μm and 5 μm, considering the anisotropy of thermal properties

a) is the cut (0001) or C-plane, beam cross-section is circular;

b) is the cut ($1\overline{1}02$) or R-plane, beam cross-section is circular;

c) is the cut (0001) or C-plane, crescent-shaped beam;

d) is the cut ($1\overline{1}02$) or R-plane, crescent-shaped beam.

Table 4.7 – Calculated values of maximum tensile stresses in the refrigerant exposure area of the specimen using crescent-shaped laser beams

Wafer thickness, mm	Stress, MPa			
	Single-beam thermal cleaving		Double-beam thermal cleaving	
	cut (0001)	cut ($1\bar{1}02$)	cut (0001)	cut ($1\bar{1}02$)
h = 0.2	238	82	279	93.4
h= 0.4	99	26.7	130	34.7
h = 1	30.1	7	53.2	12.5

The findings from the temperature calculations are presented in Tables 4.8 and 4.9, as well as in Figures 4.52 and 4.53.

Table 4.8 – Calculated values of maximum temperatures in the sample when using circular laser beams

Wafer thickness, mm	Temperature, K			
	Single-beam thermal cleaving		Double-beam thermal cleaving	
	cut (0001)	cut ($1\bar{1}02$)	cut (0001)	cut ($1\bar{1}02$)
h = 0.2	1511	1780	1572	1795
h = 0.4	935	1025	963	1040
h= 1	619	607	630.6	617.5

Table 4.9 – Calculated values of maximum temperatures in the sample when using crescent-shaped laser beams

Wafer thickness, mm	Temperature, K			
	Single-beam thermal cleaving		Double-beam thermal cleaving	
	cut (0001)	cut ($1\bar{1}02$)	cut (0001)	cut ($1\bar{1}02$)
h = 0.2	1299	1342	1304	1420
h = 0.4	820.4	813.7	822.6	814
h= 1	564.8	542	566.8	540

Figure 4.52 illustrates the computed temperature distribution on the surface of a 0.2 mm thick sapphire wafer during single-beam laser thermal cleaving, while Figure 4.53 presents analogous distributions for double-beam cleaving.

The temperature field distribution on the surface, when employing both beam types, along with the stress distribution, exhibits similarities and is typically indicative of the controlled laser thermal cleaving process. The surface of the wafer undergoes considerable heating in the area subjected to laser radiation.
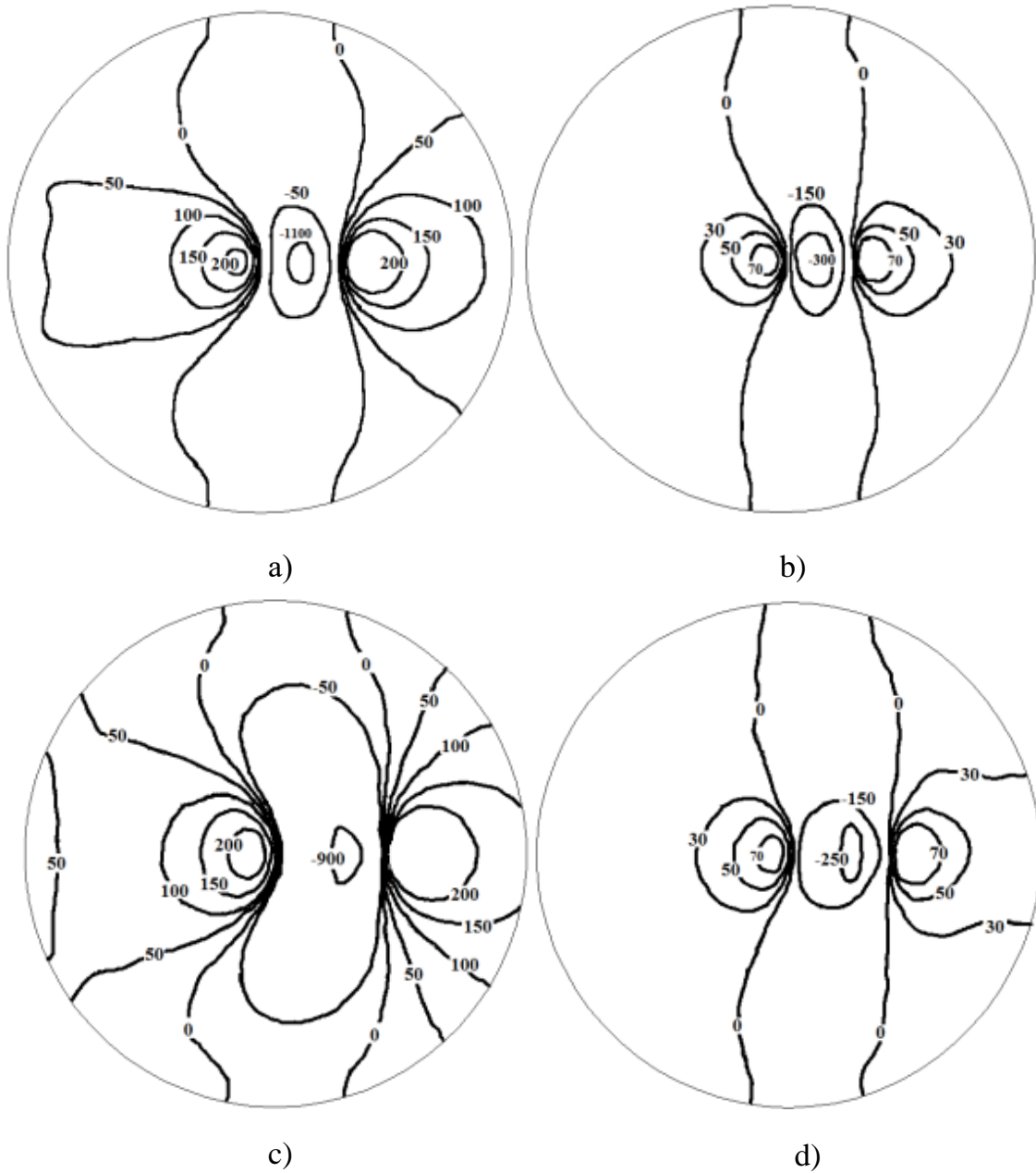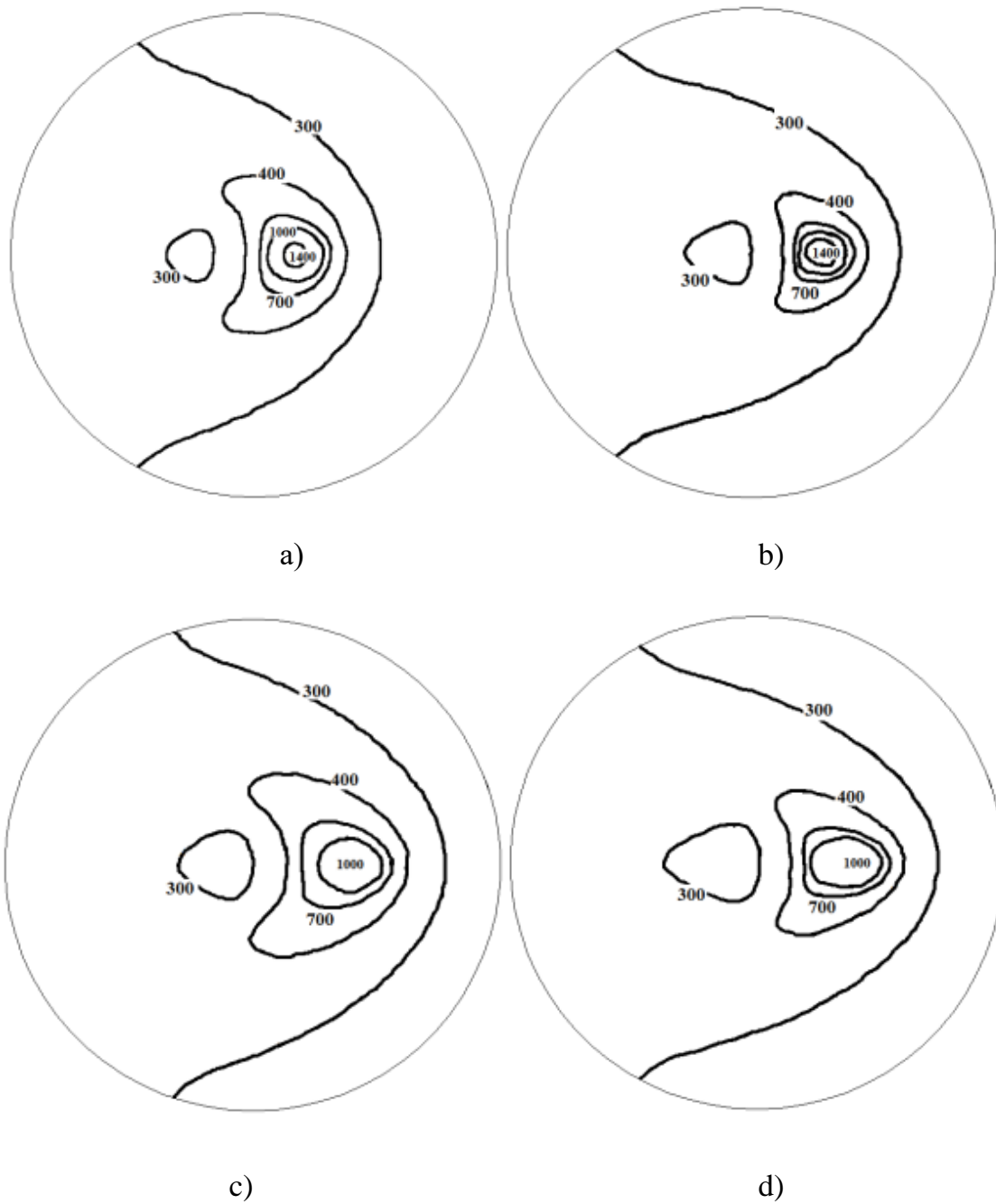
Figure 4.52 – Distribution of temperature fields (K) on the surface of a sapphire wafer when exposed to laser radiation with a wavelength of 10.6 μm considering the anisotropic nature of thermal properties
a) is the cut (0001) or C-plane, beam cross-section is circular;
b) is the cut $(1\bar{1}02)$ or R-plane, beam cross-section is circular;
c) is the cut (0001) or C-plane, crescent-shaped beam;
d) is the cut $(1\bar{1}02)$ or R-plane, crescent-shaped beam.
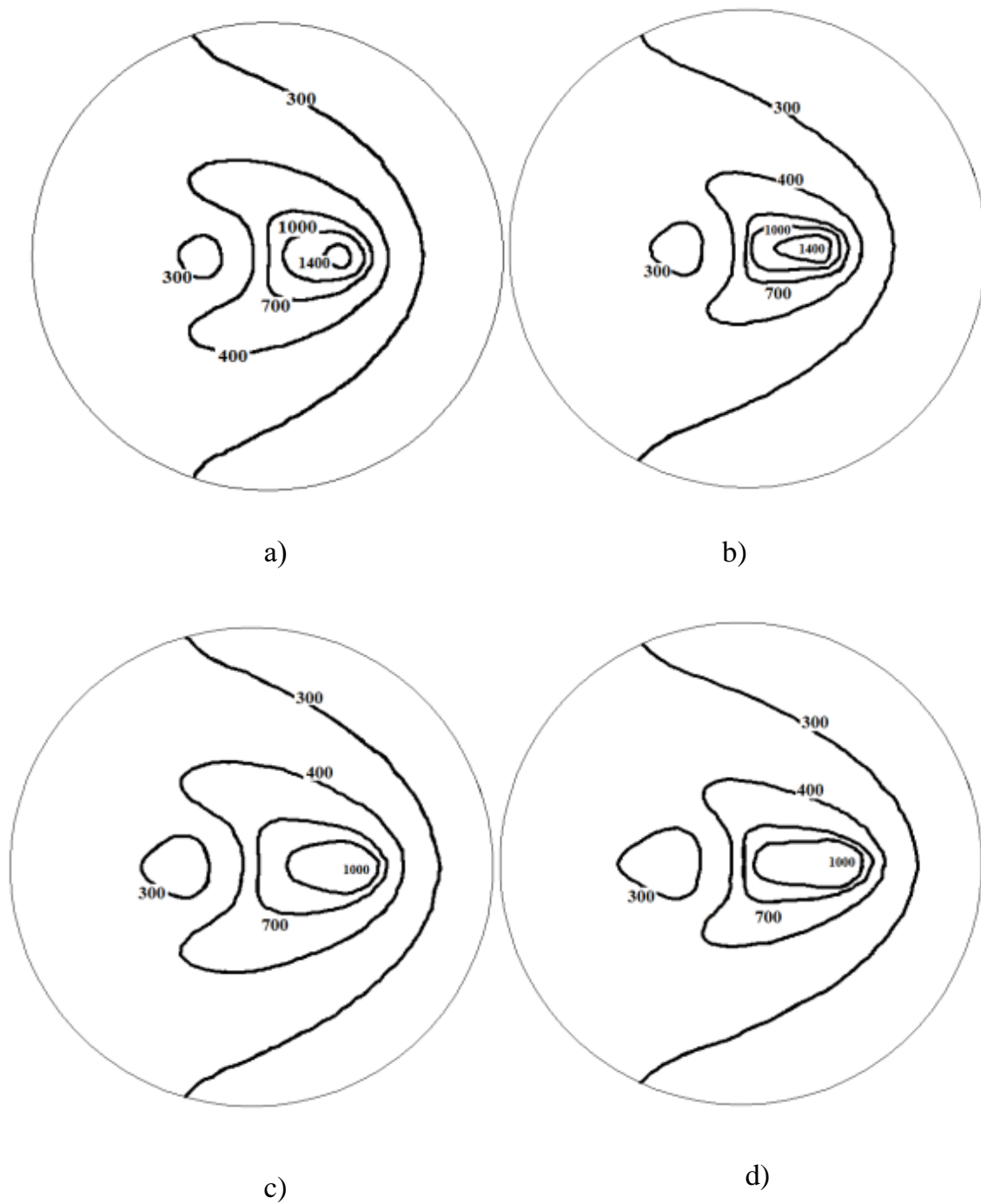
Figure 4.53 – Distribution of temperature fields (K) on the surface of a sapphire wafer under simultaneous exposure to laser radiation at wavelengths of 10.6 μm and 5 μm considering anisotropy of thermal properties

a) is the cut (0001) or C-plane, beam cross-section is circular;

b) is the cut ($1\bar{1}02$) or R-plane, beam cross-section is circular;

c) is the cut (0001) or C-plane, crescent-shaped beam;

d) is the cut ($1\bar{1}02$) or R-plane, crescent-shaped beam.

Subsequently, the thermal energy resulting from heat conduction distributes throughout the volume of the wafer. At the point of refrigerant supply, the surface is rapidly cooled, resulting in a temperature reduction nearly to the initial values. Nevertheless, when employing crescent-shaped beams, the maximum temperature values are inferior to those observed with circular beams.

The examination of the data presented in Table 4.6 reveals that employing crescent-shaped beams yields comparable maximum tensile stress values in the refrigerant exposure area, akin to those observed with circular beams. Concurrently, the highest temperature values within the sample are diminished. For instance, during the single-beam thermal cleaving of 0.2 mm thick wafers under selected modes, the maximum temperature for mode I with crescent-shaped beams is reduced by 55–212°C compared to circular beams, contingent upon the wafer thickness and the specific type of controlled laser thermal cleaving used. The separation of thin wafers results in a greater temperature difference. In mode II, the temperature variation ranges from 65 to 432°C. It is important to highlight that, at constant power densities, the cross-sectional area of the crescent-shaped beam is 15% smaller than that of the beam with a circular cross-section. Consequently, the power required from the radiation source to achieve the same maximum tensile stresses in the refrigerant supply area is reduced.

Adjusting the parameters of crescent-shaped laser beams allows for an enhancement in tensile stresses within the processing area, in contrast to thermal cleaving with circular beams, all while maintaining the maximum temperatures in the sample. This results in improved stability regarding crack nucleation.

CHAPTER 5. LASER THERMAL CLEAVING OF BRITTLE NON-METALLIC MATERIALS ALONG CLOSED CURVILINEAR TRAJECTORIES

5.1. Increasing the efficiency of laser thermal cleaving along closed curvilinear trajectories

When manufacturing complex-shaped items from brittle nonmetallic materials, circumstances arise that need cutting along closed curvilinear contours, as exemplified in the blanking operation for automotive mirrors. The feasibility of employing CLT for this objective was examined in references [34, 38].

The analysis of the works [2, 31, 35] on this issue, together with our own research [68, 94], indicates that the extensive application of CLT is hindered by certain limitations that result in diminished machining accuracy and surface quality of the final products. Let us highlight the core issues and examine the recommended methods to address them.

Initially, it is important to note that in established laser thermal cleaving devices, the design features result in a displacement of the refrigerant exposure area relative to the laser action trajectory when cutting along a curvilinear contour, particularly with small radii of curvature. This results in significant deviations of the resultant microcrack from the cutting line. A layout of the setup was developed to address this limitation, featuring a five-axis control system (Figure 2.6). The implementation of a five-axis control system enables the elimination of deviations in the center of the refrigerant exposure area from the laser beam trajectory during processing, thanks to the independent movement capability of the refrigerant nozzle [68]. The implementation of the outlined technical solution is essential, yet it alone does not guarantee a reduction in the deviations of the splitting microcrack from the processing line. This occurs because cutting along a curvilinear contour disrupts the symmetry of the thermoelastic stress distribution, a feature typically associated with straight-line cutting, for various additional reasons.

The influence of heated areas within the material along the curvilinear contour can lead to a deviation of the crack from the intended processing line [31]. Nonetheless, a more substantial reason involves the application of laser beams with an elliptical cross-section, positioned with the larger axis aligned tangentially to the trajectory of curvilinear motion. Utilizing laser beams with this specific cross-sectional shape [31] facilitates optimal conditions for the generation of thermoelastic stresses during straight-line thermal cleaving, in contrast to beams with a circular cross-section. When beams with an elliptical cross-section are orientated tangentially to the processing

line for curvilinear cutting, the edges of the beam do not align with the cutting line, resulting in asymmetrical heating of the material. Due to asymmetrical heating, the crack deviates from both the designated processing line and the direction that is perpendicular to the material surface.

The result of these factors is a reduction in machining accuracy and a decline in edge quality following the final cleaving of laser microcracks during the production of the final product defined by a closed curvilinear contour.

It was previously suggested in [50, 111] to use beams with a crescent-shaped contour to heat the processed material while cutting along a curvilinear contour. The application of these beams in curvilinear contour cutting can notably diminish the earlier discussed disruption of the symmetrical distribution of thermoelastic stresses concerning the processing line. Nonetheless, as already noted in the review, a significant drawback of this technique lies in the technical challenges associated with its implementation, which necessitates a considerable increase in the complexity of the optical systems employed in the relevant devices.

This work proposes the use of additional bulk heating of the material through laser radiation to eliminate undesirable deviations from the direction perpendicular to the surface. For instance, silicate glasses and alumina ceramics can be treated with radiation at a wavelength of $\lambda=1.06$ μm. In this scenario, it is recommended, based on experimental data, to shift the area of supplementary heating away from the cutting line (Figure 5.1).

In Figure 5.1, position 1 is associated with the laser beam at a wavelength of 10.6 μm, position 2 corresponds to the refrigerant exposure area, and position 3 relates to the laser beam cross-section at a wavelength of 1.06 μm.
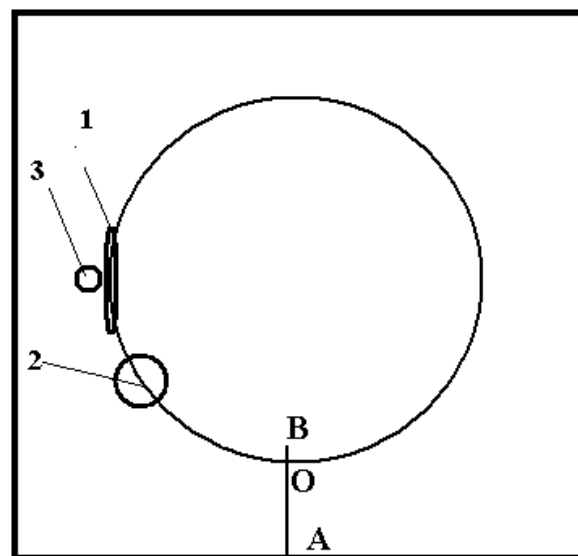

Figure 5.1 – Mutual arrangement of the impact areas of laser beams and a refrigerant

170

The segment AB represents the line of the pre-cut on the material surface, orientated perpendicular to the tangent of the cutting line. The point O indicates both the starting and terminating positions of the contour processing.

The numerical simulation of this process was conducted to clarify the peculiarities of double-beam thermal cleaving of brittle nonmetallic materials along closed curvilinear trajectories.

The outcomes of the simulation are illustrated in Figures 5.2–5.7. The calculations were performed considering the properties of silicate glass outlined in Section 2.1 for a wafer with geometric dimensions of 50×50×4 mm.

The radius of the circle along which the centers of the elliptical section of the beam and the refrigerant exposure area were moved was considered to be 17.5 mm. The linear cutting speed was set at 15 mm/s. Furthermore, the selected values for the laser beam parameters were as follows: the major axis of the elliptical section $A = 14 \cdot 10^{-3}$ m, the minor axis $B = 2 \cdot 10^{-3}$ m for the beam with a radiation wavelength $\lambda = 10.6$ μm and a radiation power $P = 30$ W; the radius of the YAG-laser radiation spot $R = 1 \cdot 10^{-3}$ m and its radiation power $P_0 = 40$ W.

Calculations of the thermoelastic field were conducted for four distinct options regarding curvilinear contour processing:

– single-beam scheme of controlled thermal cleaving;

– double-beam scheme using a CO_2 laser beam with an elliptical cross-section alongside a YAG laser beam with a circular cross-section;

– double-beam scheme featuring the YAG laser beam shifted by 1 mm in the radial direction towards the geometric center of the contour;

– double-beam scheme with the YAG laser beam shifted by 1 mm in the radial direction away from the geometric center of the contour.

It is important to observe that, within the chosen operating modes, the maximum temperature values across all four options remained below the glass transition temperature of silicate glass.

Figures 5.2 and 5.3 demonstrate the spatial distribution of temperature and stresses r that act perpendicular to the tangent of the processing line in a glass wafer during the single-beam cutting process along a circular trajectory. When CLT is used for curvilinear cutting, it generates a spatial arrangement of tensile and compressive stresses in the work material, analogous to that observed in straight-line cutting.

When examining the characteristics of cutting along a curvilinear trajectory, it is essential to consider that the distribution of compressive stresses within the sample volume, similar to straight-line cutting, influences the shape and depth of microcrack development. The initiation and propagation of these microcracks occur in the region of tensile stresses created in the area where the refrigerant is supplied.
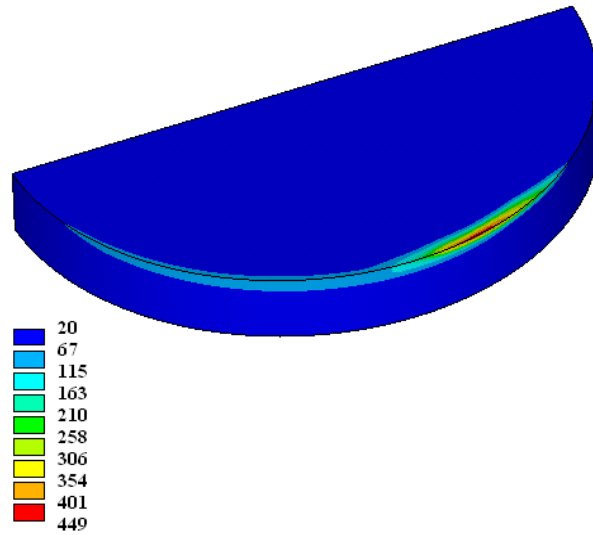
Figure 5.2 – Temperature distribution in the sample affected by a laser beam
and a refrigerant moving along the circular cutting contour, °C
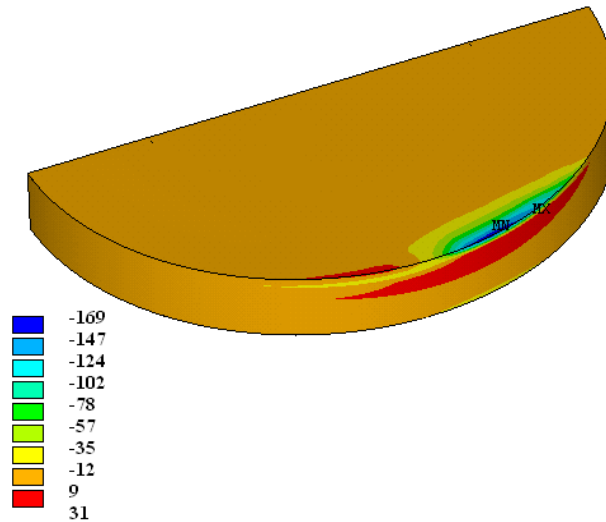
Figure 5.3 – Distribution of stresses σ_r in the sample affected by a laser beam
and a refrigerant, moving along the circular cutting contour, MPa

Figure 5.4 shows the dependencies of stresses σ_r that act perpendicular
to the tangent of the cutting line at various depths in relation to the radial
coordinate at CLT. Single-beam processing exhibits an asymmetric distri-
bution of stresses σ_r in relation to the cutting line. The explanation for this
lies in the previously discussed asymmetric heating of the material in rela-
tion to the separation line, resulting from the application of a laser beam with
an elliptical cross-section, which is aligned along the tangent to the curvilin-
ear contour of the processing. Upon analyzing the presented stress depend-
encies σ_r, it can be concluded that the implementation of this technological
mode necessitates a deviation of the splitting microcrack from the vertical
direction, as evidenced by the experimental observations.
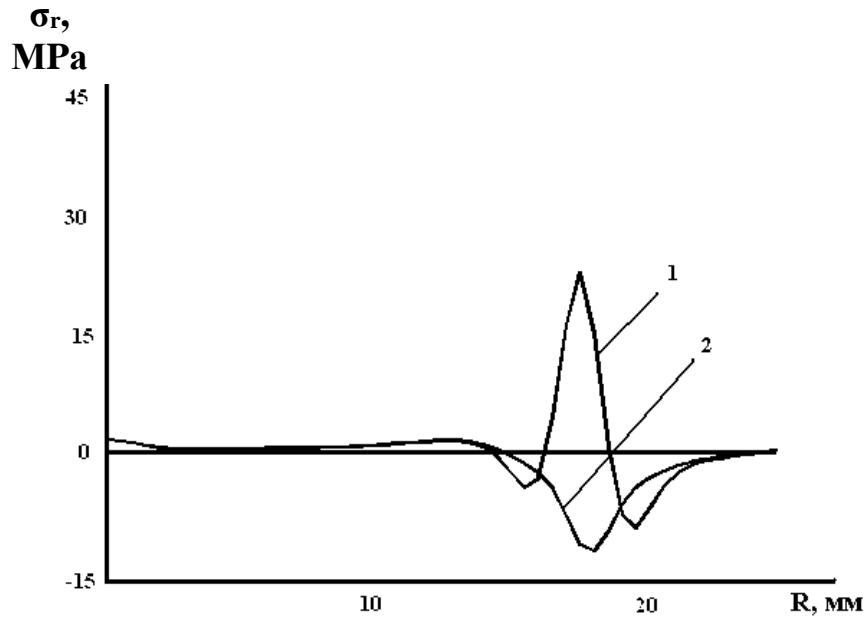
Figure 5.4 – Stress σ_r as a function of radial coordinate
Single-beam scheme of controlled thermal cleaving using an elliptical CO_2 laser beam:
$1 - Z = 0$ mm, $2 - Z = 0.25$ mm

Figures 5.5 and 5.6 show analogous stress dependencies $\sigma_r(r)$, typical for double-beam processing. This occurs when the trajectories of the CO_2 laser beam and the YAG laser beam are aligned, as shown in Figure 5.5. In contrast, Figure 5.6 depicts the scenario where the center of the YAG laser beam section is shifted radially by 1 mm from the edge to the center of the processing contour.
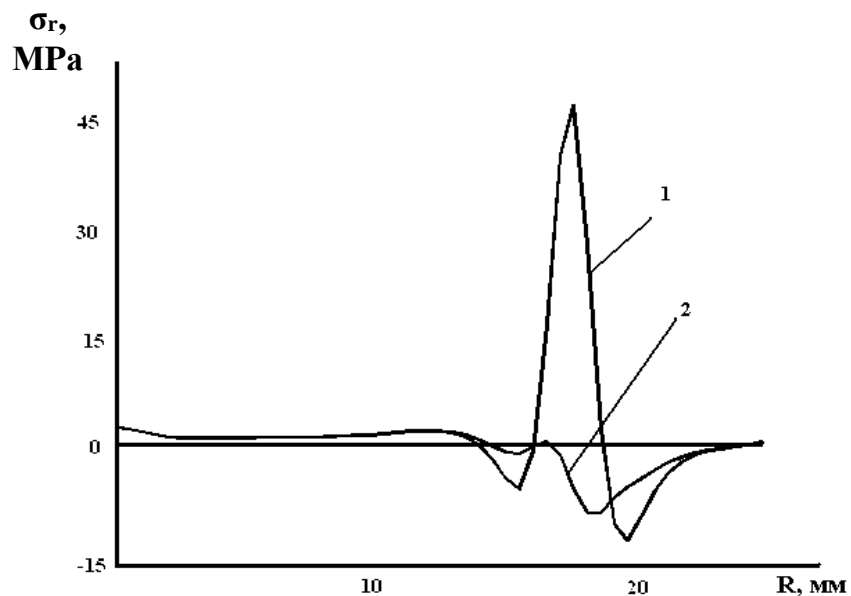

Figure 5.5 – Stress σ_r as a function of radial coordinate
Double-beam processing scheme using an elliptical cross-section of a CO_2 laser beam
and a circular YAG laser beam: $1 - Z = 0$ mm, $2 - Z = 0.25$ mm

173

Upon analysis, it becomes evident that the selected beam arrangement options lead to a significant enhancement in the maximum tensile stress values, increasing from 22 MPa in the single-beam processing scheme to 47 MPa and 33 MPa, respectively, with the implementation of the second and third processing schemes. Nonetheless, the arrangement of laser beams leads to an increased asymmetry in the distribution of the stress field, a phenomenon that becomes particularly evident when employing the scheme with the YAG laser beam shifted radially from the geometric center of the contour.

Figure 5.6 – Stress σ_r as a function of radial coordinate
Double-beam processing scheme involving a 1 mm radial shift of the center of the YAG laser beam cross-section to the contour center: 1– Z = 0 mm, 2 – Z = 0.25 mm

Figure 5.7 illustrates the dependencies of stresses $\sigma_r(r)$ that act perpendicular to the line of circular microcrack formation during the double-beam processing, with a shift of the YAG laser beam from the center of the contour. Upon analyzing these dependencies, it can be concluded that this beam arrangement effectively minimizes deviations of the microcrack from the vertical direction, as this particular scheme yielded the most favorable outcomes in the experiment.

Through the analysis of the distribution of thermoelastic fields, it was concluded that additional exposure to laser radiation at a wavelength of 1.06 μm can lead to significant alterations in the spatial location of the compressive stress zone. This approach facilitates the establishment of conditions conducive to the formation of a spatial configuration of compressive stresses, effectively compensating for their asymmetry.

Thus, with additional exposure to laser radiation at a wavelength corresponding to the volume absorption by the material, it is possible to eliminate the deviation of the deposited microcrack relative to the plane that is perpendicular to the surface of the material.

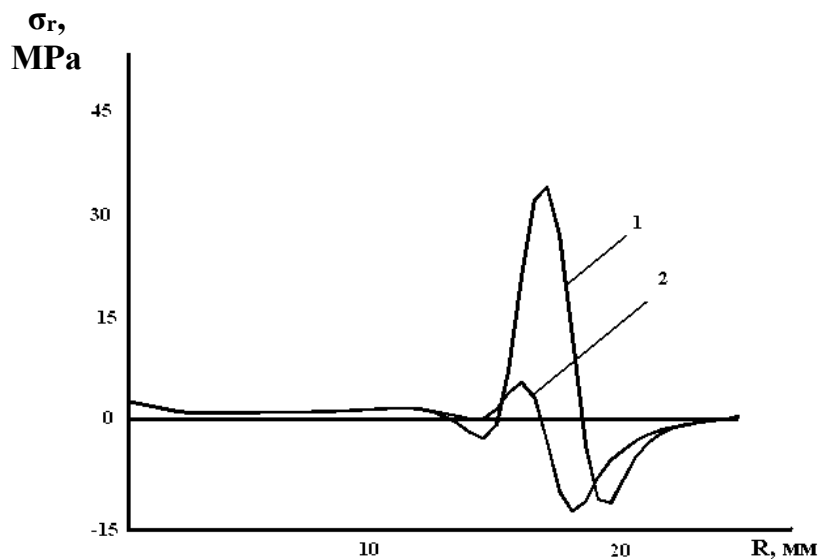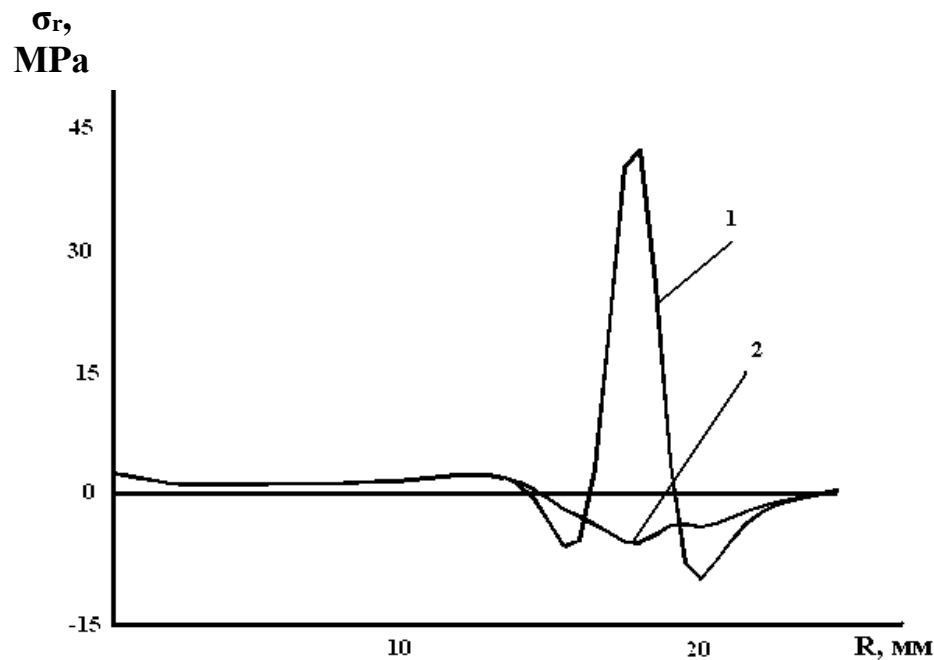Figure 5.7 – Voltage σ_r as a function of radial coordinate
Double-beam processing scheme involving a 1 mm radial shift of the center of the
YAG laser beam cross-section from the contour center:
$1 - Z = 0$ mm, $2 - Z = 0.25$ mm.

Another issue encountered when cutting along a closed curvilinear contour is the deviation of the cutting line from the intended trajectory at the point of closure. The propagation of a microcrack in this area is notably affected by its own "tail," where significant stresses are concentrated both at the apex of the tail and at the apex of the microcrack itself.

To address this issue, it was necessary to initiate a curvilinear closed microcrack from a rectilinear microcrack that had been previously established in the radial direction. In this scenario, there is no formation of an additional zone of significant stresses at the apex of the "tail" of the curvilinear crack at the point where the laser contour undergoes closure.

Considerable challenges emerge during the final cleaving of laser microcracks when producing the finished product, particularly when the contour forms a closed curve. The conducted investigation revealed that for effective final splitting of a circular microcrack, it is beneficial to apply short-term heating to a glass plane-parallel wafer using a circular heat source from the side opposite to the surface being processed by the laser.

175

To clarify the unique aspects of the final thermal cleavage procedure of a circular microcrack created in a glass plane-parallel wafer through laser thermal cleaving, calculations were conducted on the thermoelastic fields generated by a circular heat source within the material.

Figure 5.8 presents the outcomes of the temperature field calculations, while Figure 5.9 illustrates the results of the radial stress calculations σ_r which act perpendicular to the pre-deposited circular microcrack. Figure 5.8 demonstrates that, under the specified calculation parameters, the maximum temperature does not attain the glass transition temperature, which is essential for achieving brittle final cleavage of the sample.

Figure 5.8 – Temperature as a function of radial coordinate
1 is on the surface being heated; 2 is in the middle of the wafer;
3 is on the surface with a microcrack

Upon examining the dependencies of stresses σ_r at varying depths perpendicular to the pre-deposited circular microcrack, in relation to the radial coordinate, it becomes evident that on the heated surface within the influence of the circular heat source, there are considerable compressive stresses, approximately 150 MPa in magnitude. On the opposite surface, there exists an area characterized by compressive stresses, with a value approximately measuring 50 MPa.

In this situation, a zone of tensile stresses emerges within the material's inner layers, the value of which is adequate to promote the propagation of the existing microcrack. Consequently, the use of a circular heat source enables the establishment of the necessary distribution of thermoelastic fields within the material, facilitating the eventual progression of a circular microcrack introduced via the CLT method [68].
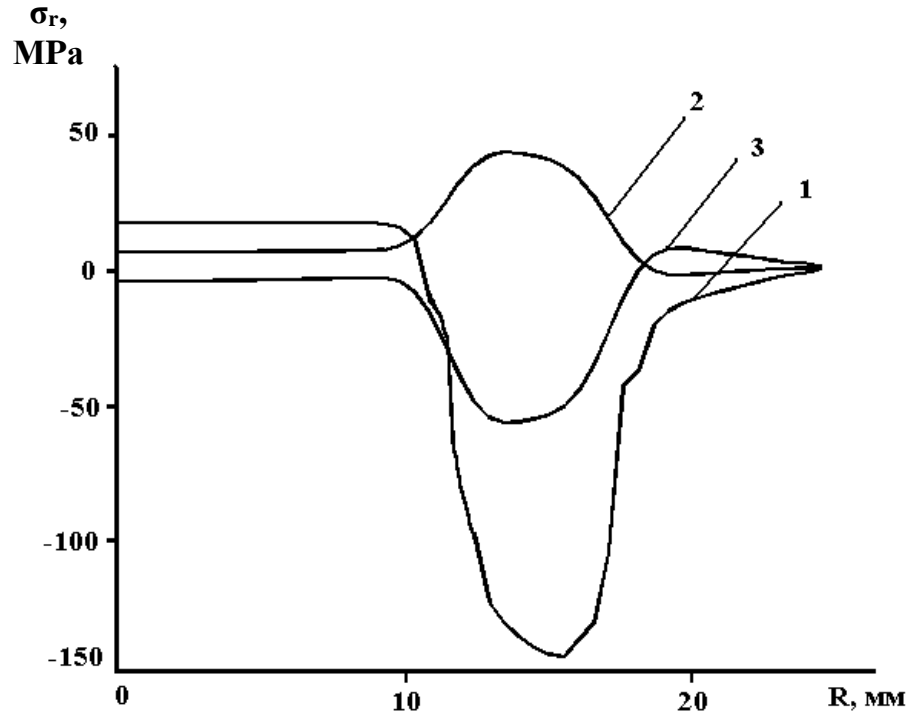
176

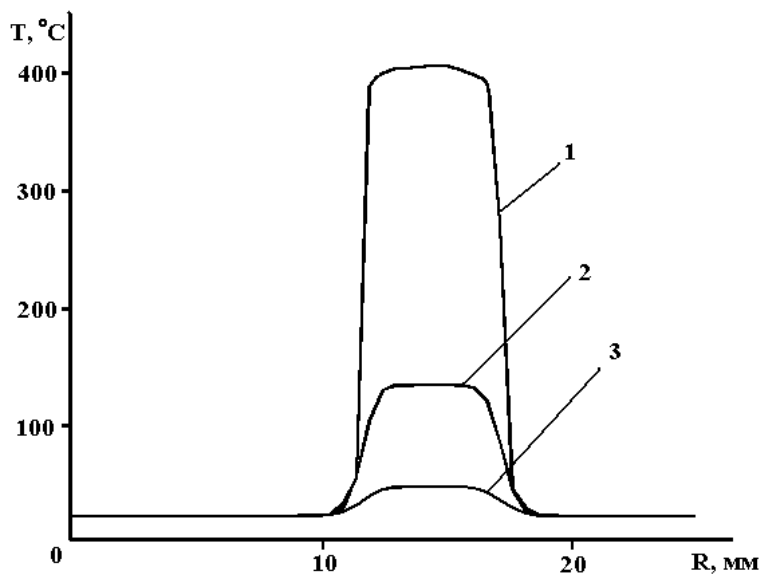Figure 5.9 – Stress σ_r as a function of radial coordinate
1 is on the surface being heated; 2 is in the middle of the wafer;
3 is on the surface with a microcrack

The proposed measures aimed at enhancing the quality of finished products are implemented in the experiment as detailed below [68]. A sheet of glass, serving as the source material, is positioned upon a coordinate table. The table is repositioned, and an initial cut is executed on the material's surface, orientated perpendicular to the initial segment of the cutting line (it is recommended that this initial cut be in the form of a microcrack caused by laser radiation). The surface of the material is subjected to heating along the cutting line through the application of laser radiation, specifically at a wavelength of 10.6 microns.

Simultaneously, the local cooling of the heating region is achieved through the introduction of a refrigerant. Furthermore, owing to the innovative design of the developed setup and the implementation of a five-coordinate control system, any deviations of the refrigerant exposure area from the laser radiation exposure line during processing are effectively mitigated. Concurrently, the material undergoes exposure to laser radiation at a wavelength of 10.6 μm, alongside additional exposure to laser radiation at a wavelength of 1.06 μm.

The additional heating of the material is performed with a shift from the center of the contour of processing.

The application of a laser beam, shifted from the cutting line and characterized by a wavelength that aligns with the bulk absorption of the material

177

being processed, results in the establishment of a spatial configuration of stress fields. This configuration serves to counterbalance the asymmetry induced by the elliptical cross-section of the laser beam, which is orientated tangentially to the curvilinear contour.

During the final phase of microcrack propagation, the cutting line experiences closure at point O (Figure 5.1). Here, the impact of its own "tail" on the progression of the deposited microcrack diminishes, as the apex of the microcrack in the chosen processing scheme aligns with the previously deposited cut AB. In this scenario, there is no formation of an additional zone of significant stresses at the closure point of the laser contour. This leads to a notable decrease in the deviation of the developing microcrack from the laser impact line at the processing contour's closure point.

Additionally, for the ultimate separation of the material along the contour, the surface of the material is heated from the side that is opposite to the area impacted by the laser beams using a heat source, the configuration of which coincides with the shape of the contour. In such a case, thermoelastic stresses develop within the material, with their distribution and magnitude being conducive to the eventual formation of through-the-thickness splitting microcracks.

Experimental studies were conducted following the aforementioned sequence of actions. During the experiments, circular microcracks with a radius $R = 15 \div 25$ mm were observed in glass samples of M3 – M5 grades, which had a thickness of $2 \div 4$ mm (Figure 5.10).
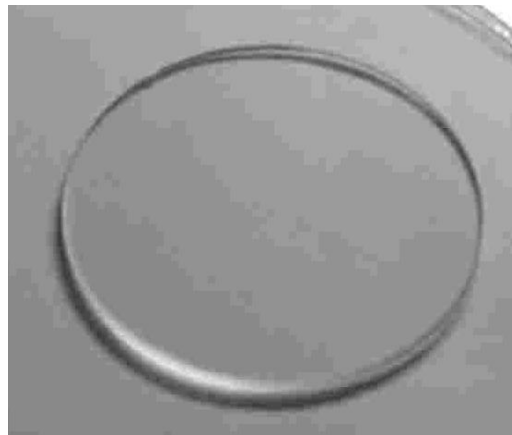
Figure 5.10 – Glass sample obtained via curvilinear thermal cleaving

The ILGN-802 laser, exhibiting a radiation power of up to 60 W and a wavelength of $\lambda = 10.6$ μm, alongside the YAG laser LTN-103 with a power up to 100 W, were employed in this study. During the process of glass separation, laser radiation with $\lambda = 10.6$ μm was focused through a spherocylindrical lens, producing beams defined by an elliptical cross-section, with

the major axis measuring A = (8 ÷ 14) mm and the minor axis measuring B = (0.5 ÷ 2) mm. Radiation with λ = 1.06 μm was focused through a spherical lens, producing beams with a circular cross-section, with a radius r = (0.5 ÷ 1) mm. The shift of the beam at λ =1.06 μm from the contour was measured to be (0.1 ÷ 1.5) mm, while the linear cutting speed of the samples was 15 ÷ 30 mm/sec. Steel rings, subjected to temperatures 400 ÷ 500 °C, served as a source of heat for short-term heating applications.

The findings from the experimental studies indicate that the proposed solutions enhance both the efficiency and quality of separating brittle nonmetallic materials along closed curvilinear contours.

5.2. Examination of laser separation techniques for brittle nonmetallic tubular-shaped materials

A significant form of laser thermal cleaving along closed curvilinear trajectories involves the separation of brittle nonmetallic tubular materials. The initial findings on the laser cutting of glass tubes through thermocleaving are presented in references [7, 29], with subsequent advancements detailed in references [10, 34]. Reference [7] indicates that the laser cutting of glass tubes through laser thermal cleaving offers notable benefits over conventional techniques, primarily highlighting the superior quality of the resulting end-face surfaces.

Reference [7] highlights two fundamentally different approaches to implementing the process of laser thermal cleaving.

The first approach entails creating a radially converging laser beam, resulting in the development of a circular heat source along the contour. Upon the realization of this method, the separation of materials occurs almost instantaneously. The main drawback of this technology lies in its low reliability and low repeatability during the process, which is typical of a single exposure to a heat source. Furthermore, the practical implementation of this technology is hindered by the complex nature of the optical system employed for beam formation. Nonetheless, in various scenarios, implementing this technology is justifiable (such as in the separation of glass tubes during the continuous drawing process [7]).

The fundamental idea of the second approach lies in the application of multiple laser impacts on the material throughout the processing line. This is accomplished by either rotating the tube in relation to the laser beam or the other way around (for example, the movement of the laser beam on the surface of the tube can be provided by a system of rotating mirrors that create a light guide [7]).

However, in most existing studies, the rotation of tubes in relation to the laser beam is employed because this method offers a more straightforward technical implementation.

During the examination of this technology, several modifications were developed that incorporate mechanical fracture and cooling alongside laser heating, used in various combinations and sequences.

In reference [211], a method is proposed to enhance the efficiency of laser thermal cleaving of glass tubes. This involves redirecting the laser radiation that is reflected from the tube into the processing zone using a strategically positioned mirror. In [186], a method is proposed to enhance the cutting efficiency of glass tubes, characterized by the simultaneous laser heating of multiple rotating tubes.

The majority of recognized methods for processing glass products through laser thermal cleaving do not elevate the temperature in the laser's influence area beyond the glass transition temperature of the specific grade of glass. In the first chapter, examples of the implementation of thermal cleaving technology for plane-parallel samples were presented, where surpassing the glass transition temperature in the processing zone is permitted. A comparable technology has been created for the thermal cleaving of tubular-shaped glass products [105, 106]. The core principle involves elevating the temperature of the sample in the separation zone during the initial processing stage to levels exceeding the softening temperature, yet remaining at or below the evaporation temperature. In subsequent processing, the temperature is reduced to a level below the glass transition temperature. This thermal effect leads to the formation of a fine mesh of longitudinal and transverse cracks in the glass along the separation line. Moreover, with an increase in rotation speed, the maximum temperature values decline to levels below the glass transition temperature. A crack that extends through the thickness is created along the line of separation. The primary drawback of this technology lies in the inadequately high quality of the resulting endfaces, attributed to the formation of a microcrack network during the initial processing stage.

Upon examining the outcomes of the previously referenced studies alongside our own experiments – specifically, the investigations into laser thermocleavage processes conducted on the prototype setup developed by the authors [87] – we can identify several processing patterns that yield practically acceptable results.

The first pattern employs the multiple heating of the tube surface due to its rotation relative to a stationary laser beam.

The second pattern demonstrates the implementation of the CLT in tube processing. Simultaneous laser heating and cooling are conducted along the separation line for several tube revolutions.

The third pattern relies on the integration of preheating the separation contour using laser radiation over several tube revolutions, followed by the treatment of the cutting line through simultaneous application of laser radiation and a refrigerant.

The separation of brittle nonmetallic tubular-shaped materials in the aforementioned processing options is carried out using CO_2 laser radiation at a wavelength of 10.6 μm. The favorable outcomes observed in the fourth chapter and the first section of this chapter regarding the application of double-beam technology for the separation of plane-parallel samples through thermal cleaving laid the groundwork for investigating the impact of supplementary exposure to laser radiation at a wavelength of 1.06 μm on the process of laser thermal cleaving of tubular-shaped products.

A variety of publications detail methods for engineer computations of laser thermocleaving modes specifically for brittle nonmetallic tubular-shaped materials [7, 26]. The analytical solutions derived in these studies may prove beneficial for engineer computations and for clarifying the relationships among the parameters that affect the thermal cleaving process of tubular-shaped products.

Nonetheless, the solutions presented, along with those derived for plane-parallel samples, are established based on the linear differential equation of heat conduction, where the thermophysical coefficients remain independent of temperature. Simultaneously, the solutions to the problems regarding the determination of the components of the stress tensor are derived in either one-dimensional or two-dimensional formulations.

This section presents a comparative analysis of the unique characteristics of the laser thermal cleaving process when implementing various processing schemes, specifically focusing on single-beam and double-beam methods [60, 73, 94]. The computational investigation concentrated on examining the distribution of temperature fields and temperature stress fields, using standard processing modes of S52 glass tubes with an outer diameter of 14 mm. The thermoelastic fields were calculated via the finite element method, as detailed in other sections of the monograph, with the implementation carried out in ANSYS software.

The properties of glass provided in Table 2.1 were used for the calculations. The thermophysical properties of glass are greatly influenced by temperature. Given that these dependencies are significant (during the laser thermal cleaving of tubular-shaped glass products, the temperature varies considerably), the calculations were performed with these factors considered.

The parameters of the laser beam used in the calculations were as follows: the major axis of the elliptical cross-section was $A = 6 \cdot 10^{-3}$ m, and the minor axis was $B = 1 \cdot 10^{-3}$ m, corresponding to a radiation wavelength of $\lambda = 10.6$ μm and a radiation power of $P = 15$ W. Additionally, the radius of the YAG laser radiation spot with a radiation power of $P_0 = 40$ W was measured to be $R = 1 \cdot 10^{-3}$ m. The calculations were conducted for a tube with an outer radius of 7 mm, an inner radius of 6 mm, and a length of 20 mm. The tube's rotation frequency concerning the laser beams was considered to be 45 revolutions per minute. The cooling of the tube surface was considered to be facilitated by a heat transfer coefficient of 8000 W/(m²·K) due to the influence of the refrigerant [152]. The simulation of tube cutting was conducted for the single-beam processing using a CO_2 laser (Figure 5.11, a) and for the double-beam processing, which integrates the effects of CO_2 and YAG lasers (Figure 5.11, b).
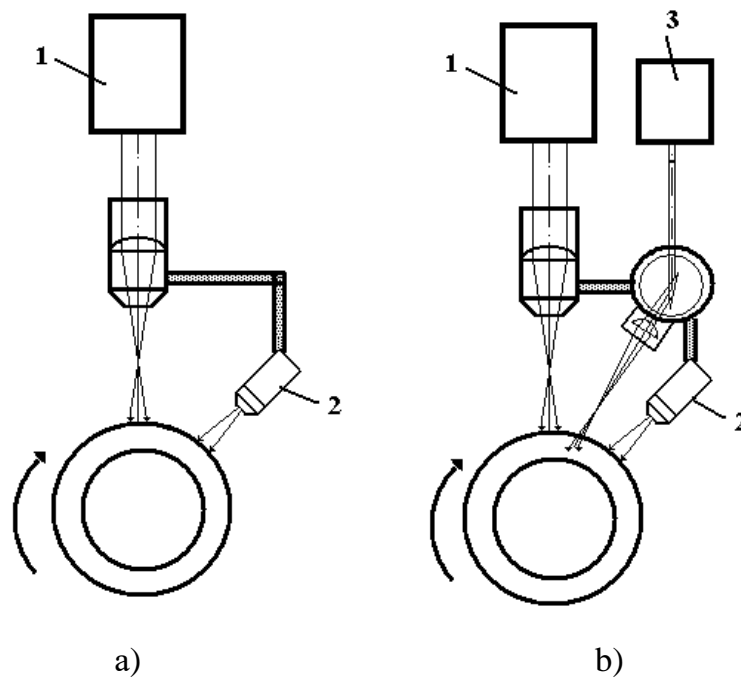
Figure 5.11 – Options for laser thermal cleaving of glass tubes
a) single-beam; b) double-beam;
1 is the CO_2 laser; 2 is the refrigerant supply nozzle; 3 is the YAG laser

Calculations of the temperature and stresses acting parallel to the tube axis (along the Z-axis) as a function of the revolution number were conducted for both processing options; three distinct schemes of the time sequence of laser radiation and refrigerant exposure on the workpiece were employed (Figures 5.12–5.15).

The first scheme involves subjecting the tube to laser heating over several revolutions.

In simulating the processing based on the second scheme, it is important to consider that over several revolutions, a portion of the tube material is subjected to heating from laser radiation, while simultaneously, the tube surface is cooled at a distance from the area being heated by the laser (Figure 5.11).

In the third simulation scheme, it is posited that the tube enters the laser irradiation zone; subsequently, after the tube completes several revolutions around its axis, its surface is subjected to the refrigerant. Concurrently, the tube undergoes additional revolutions while being simultaneously exposed to both laser irradiation and the refrigerant, thereby establishing the third scheme as a sequential integration of the first two.

Figure 5.12 – Computed temperature dependencies at fixed points
relative to the revolution number during single-beam processing
a) processing scheme 1;
b) processing scheme 2; c) processing scheme 3

1 is on the outer surface of the tube; 2 is in the middle of the tube wall;
3 is on the inner surface of the tube

Comparing the calculated temperature dependencies at fixed points presented in Figures 5.12–5.13 (1 – on the outer surface of the tube; 2 – in the middle of the tube wall; 3 – on the inner surface of the tube), it can be concluded that supplementary exposure to laser radiation with a wavelength of 1.06 μm does not result in notable alterations in the characteristics of these dependencies. A slight increase in maximum temperature values can be observed when employing each of the double-beam processing schemes in comparison to the corresponding single-beam processing schemes. This effect, as anticipated, is most evident in the layers of the material that are farther from the surface.

Figure 5.13 – Computed temperature dependencies at fixed points
relative to the revolution number during double-beam processing
a) processing scheme 1;
b) processing scheme 2; c) processing scheme 3
1 is on the outer surface of the tube; 2 is in the middle of the tube wall;
3 is on the inner surface of the tube

Analyzing Figures 5.12 a and 5.13 a, it becomes evident that during the process of multiple laser heating of the tube material, which rotates around its axis in relation to a stationary laser beam (or beams, in the case of double-

beam processing), the temperature at each point on its external surface experiences a sharp periodic increase due to laser radiation, followed by a gradual decrease attributed to the relatively low thermal conductivity of glass. Concurrently, there is a noted rise in the maximum temperature of the glass.

When using the second scheme (Figure 5.12, b), which is essentially a controlled laser thermal cleaving for processing tubular-shaped bodies, there occurs repeated rapid local heating of the work surface. It alternates with rapid cooling caused by the influence of the refrigerant. The maximum glass temperature shows virtually no increase. Thus, each revolution is characterized by almost identical temperature changes at the tube points.

The dependencies of temperature on the revolution number, characteristic of the third processing scheme, at the first stage exhibit features akin to those previously discussed regarding the first scheme: the temperature of the surface points experiences periodic sharp increases followed by smooth decreases. Concurrently, there is an increase in the maximum temperature of the sample.

During the second stage of processing, the temperature behavior of the tube surface points in relation to the number of the revolution mirrors the observations made with the second scheme: the temperature at the surface points experiences periodic sharp increases followed by sharp decreases, while the maximum temperature remains unchanged. The temperature variation outlined previously when employing the third scheme results from the sequential integration of the initial two processing schemes.

Comparing the computed dependencies of the stresses acting in the axial direction of the tube relative to the revolution number (Figures 5.14–5.15), it can be concluded that the use of single-beam and double-beam separation, along with supplementary exposure to laser radiation ($\lambda = 1.06\ \mu m$), maintains the primary characteristics of axial stress variations at fixed points in the processed material over time.

At the same time, the additional effect of YAG laser radiation causes a significant increase in both tensile and compressive stresses, which leads to a notable increase in the probability of initiation and sustained propagation of a splitting microcrack.

Another common pattern of dependencies identified through numerical simulation reveals that stresses of identical sign develop on both the outer and inner surfaces of the glass tube. Simultaneously, the stresses on the outer boundary of the tube significantly exceed those on its inner surface, while in the material layers near the center of the tube wall, stresses of an opposite sign are generated.
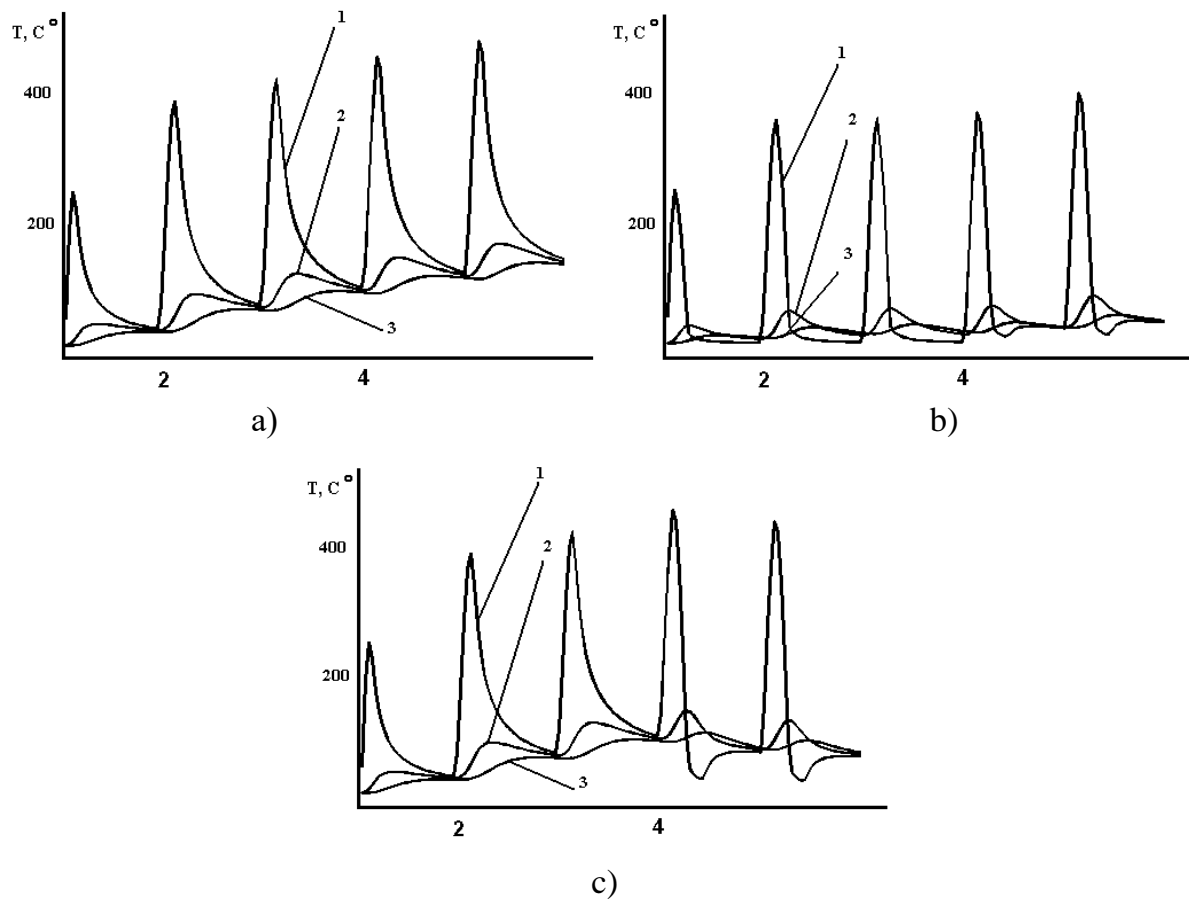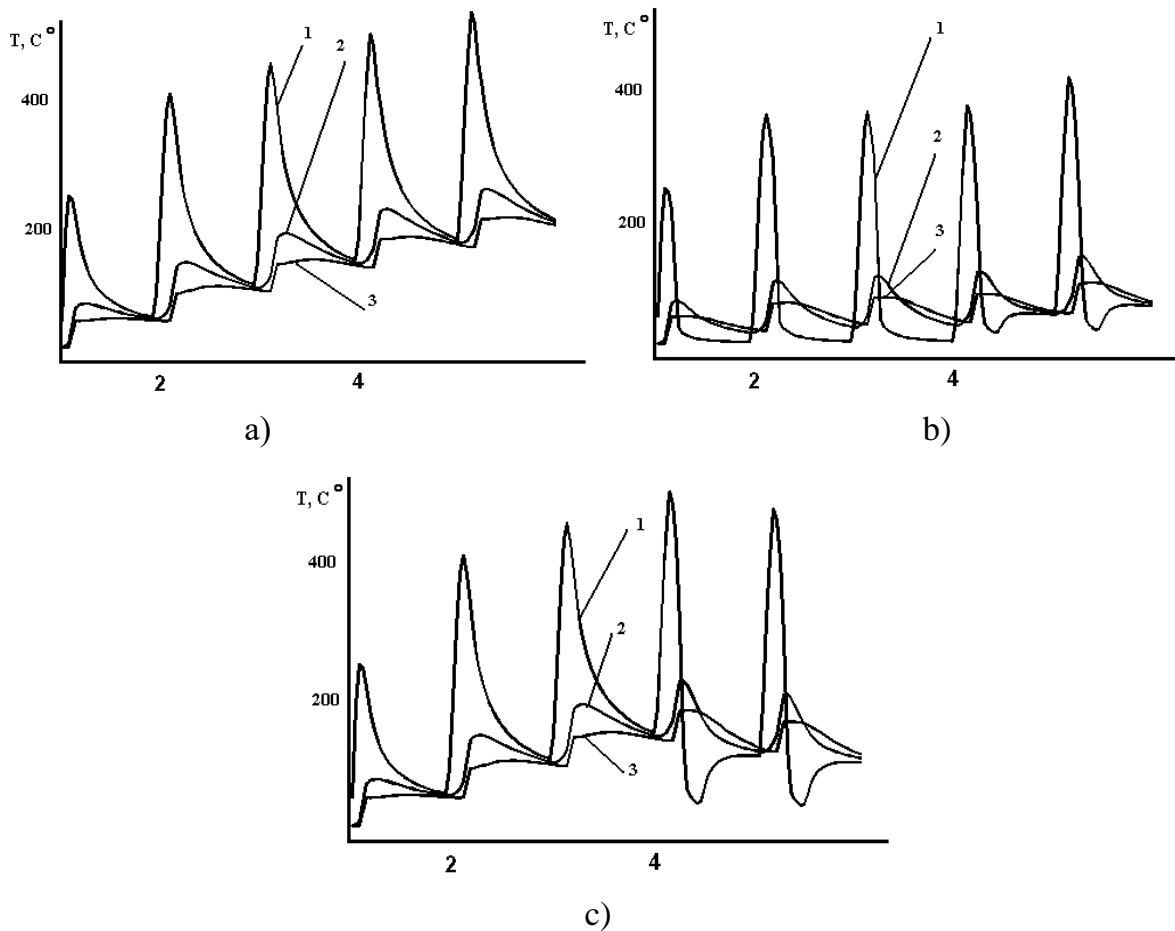
Figure 5.14 – Computed dependencies of stresses σz at fixed points
relative to the revolution number during single-beam processing
a) processing scheme 1;
b) processing scheme 2; c) processing scheme 3
1 is on the outer surface of the tube; 2 is in the middle of the tube wall;
3 is on the inner surface of the tube

When processing according to the first scheme (with multiple laser heating of the material), there is a sequential alternation of axial tensile and compressive stresses at the points of the tube surface, accompanied by a gradual increase in tensile stresses. This change of stresses results in a through-the-thickness tube separation. However, the quality of this separation frequently falls short of optimal standards.

When the second processing scheme is used, tensile stresses sufficient to initiate a splitting crack manifest on the tube surface almost immediately after the first revolution. Further, in the absence of significant changes, the tensile axial stresses that periodically occur in the area affected by laser radiation are substituted by compressive stresses generated in the region influenced by the refrigerant. This scheme guarantees the development of a non-directional splitting crack, with the characteristics of its formation being

186

largely consistent with those observed during the controlled laser thermal cleaving of plane-parallel samples. The end-face surfaces produced through this method demonstrate outstanding quality. This technology has a drawback in that it requires mechanical final cleaving to obtain the end product.
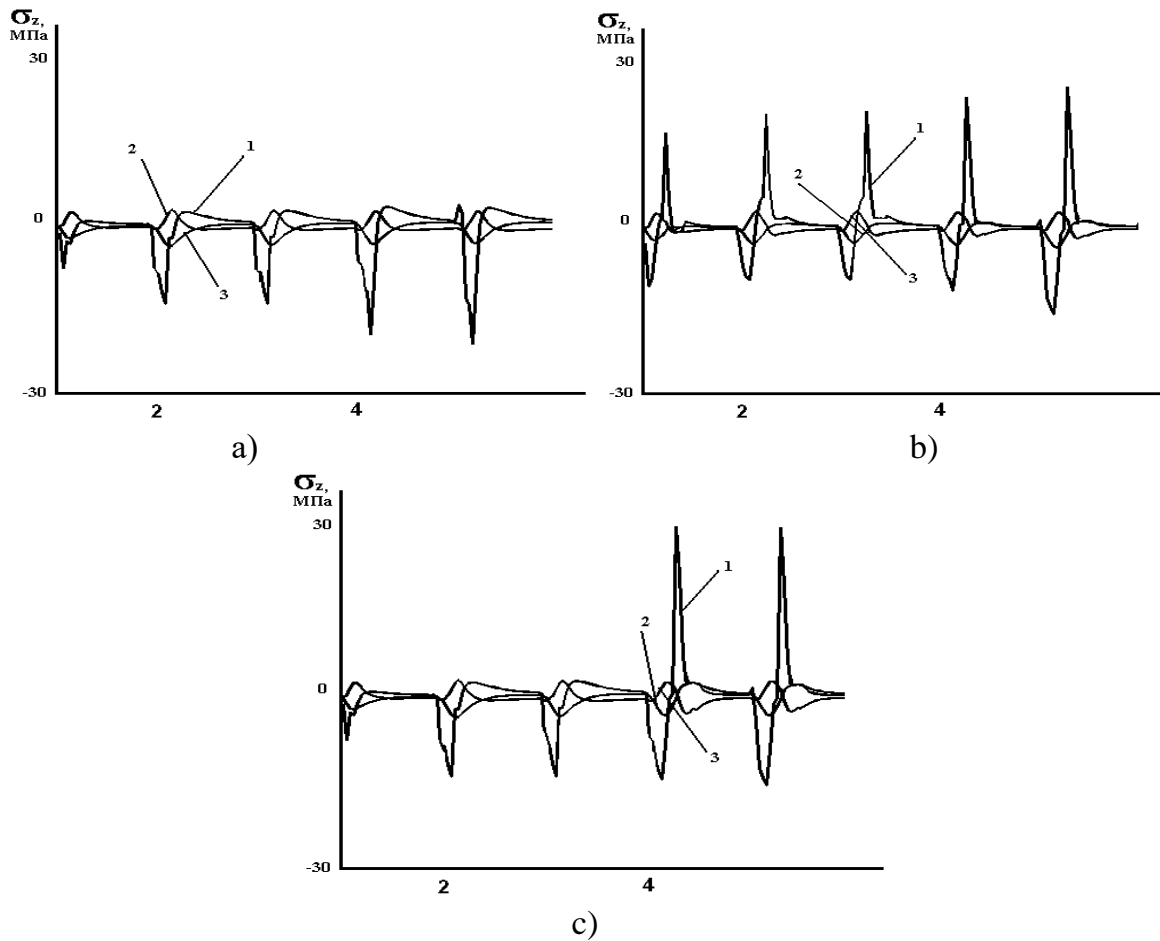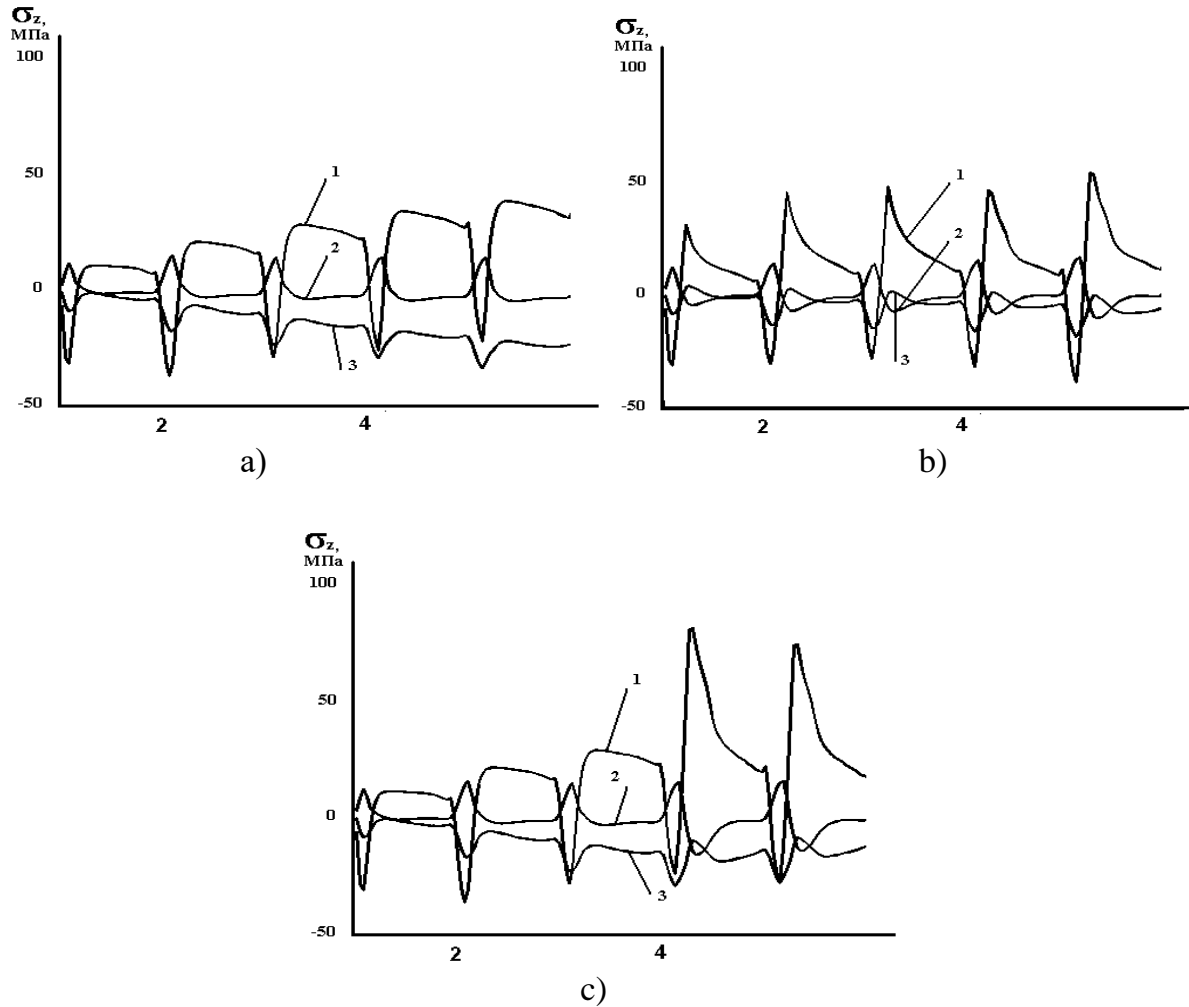

Figure 5.15 – Computed dependencies of stresses σ_Z at fixed points
relative to the revolution number during double-beam processing
a) processing scheme 1;
b) processing scheme 2; c) processing scheme 3
1 is on the outer surface of the tube; 2 is in the middle of the tube wall;
3 is on the inner surface of the tube

Using the third scheme, which sequentially combines the first two along with temperature dependencies, reveals that the relationships of axial stresses concerning the revolution number at the first stage align in nature with those derived from the first processing scheme. Meanwhile, at the second stage, they correspond with the dependencies obtained from the second scheme. The implementation of the third scheme guarantees the generation of a through-the-thickness crack while maintaining a high quality of

the resulting separation surfaces. In practical terms, the most efficient use of double-beam processing involves a method where preliminary laser heating of the work material occurs over several revolutions, combined with simultaneous application of laser radiation and a refrigerant along the material's contour, leading to the development of a splitting crack.

5.3. Simulation of the process for separating multilayer inhomogeneous glass structures along curvilinear contours

Multilayer glass (triplex) is used in the manufacturing of fences, decorative elements, robust glass structures, double-glazed units, armored glass, and automotive glazing elements. In certain instances, it is necessary to separate completed triplex sheets and perform edge trimming, which includes curvilinear trajectories.

In industrial settings, the process of cutting triplex laminated glass typically involves making cuts from both sides, subsequently leading to the breaking of the material. Following that, specialized infrared heating elements uniformly warm the entire cutting line. Throughout this procedure, the glue film undergoes a transformation in its properties, facilitating the separation of the two components of the triplex. Waterjet cutting finds application as well.

In [212], it is demonstrated that laser cleaving can be employed for triplex separation. This method involves sequential local heating and cooling along the separation line, leading to the formation of a nonthrough crack in the refrigerant exposure area, which follows the laser beam along the processing line. The ultimate development of the crack extending through the entire thickness of the glass wafer to the PVB film is accomplished via mechanical, thermal, or ultrasonic final cleaving methods. Defect-free edges are created, allowing for the elimination of additional processing operations on the separated surface, such as grinding and polishing. Increased exposure in the separation zone using infrared heating elements to soften the film and achieve final separation of the triplex results in defect-free edges, thereby minimizing the risk of side cracks in the separation area.

The use of the laser cleaving technique for separation along curvilinear trajectories presents several challenges. This encompasses potential deviations of the created crack profile from the cutting line and challenges in its initiation at a given location on the material surface [67, 86].

The studies [198–201, 213–215] explore the creation of nonthrough channels in brittle nonmetallic materials, including silicate glasses and crystals, using pulsed optical breakdown of the surface through micro-, pico-,

and femtosecond lasers. This allows for the formation of channels ranging from 100 to 500 microns in diameter.

The research conducted in [216] established the potential for using such channels to initiate a splitting crack during the double-beam controlled laser thermal cleaving of a triplex along rectilinear trajectories.

Therefore, it appears logical to simulate the process of laser cleaving in multilayer heterogeneous glass structures by employing a series of channels that are pre-deposited along the processing contour. This approach aims to initiate a splitting crack and serve as guides for its propagation along curvilinear trajectories.

According to Figure 5.16, a series of through-the-thickness holes obtained through pulsed optical breakdown of the surface using micro-, pico-, and femtosecond lasers is arranged along the processing line. A circular cross-section laser beam 1 and refrigerant 2 move along the processing line.
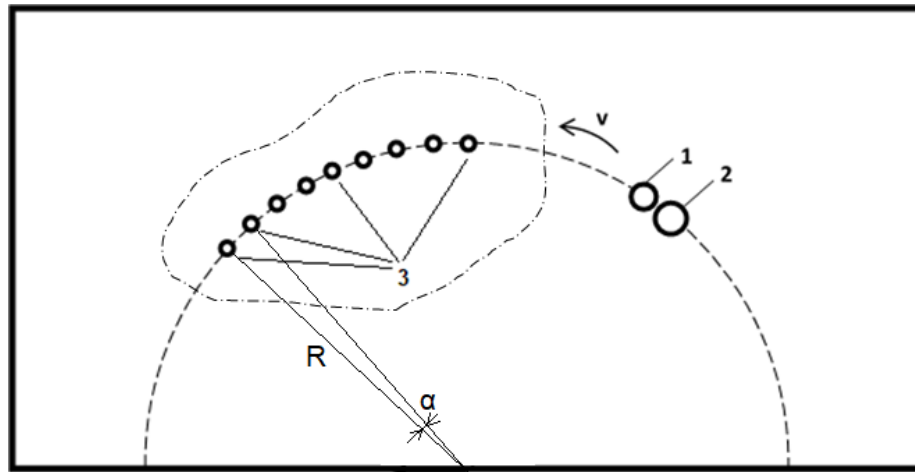
Figure 5.16 – Combined laser thermal cleaving along curvilinear trajectories

The sample for simulation consisted of two wafers of silicate float-glass, each with a thickness of 3 mm, bonded with a PVB film of 0.38 mm thickness. The trajectory radius of the laser beam and refrigerant was set at R = 4 cm. For modelling purposes, the radii of the through-the-thickness channels were chosen as 150, 225, and 300 μm, with angular sectors between the channels of 1.5, 3, and 4.5 degrees. The characteristics of glass and PVB film are detailed in references [217–223].

The CO_2 laser beam, which has its energy absorbed in a thin surface layer of the material, is represented as a surface heat source characterized by a power density of $0.8 \cdot 10^6$ W/m^2, with a circular cross-section having a radius of 2 mm. Symmetrical formations of laser beams and refrigerant impact areas are observed on either side of the triplex.

The refrigerant was supplied to the surface as a finely dispersed air-water mixture with a diameter of 6 mm. In this way, the CO_2 laser beam and the refrigerant on the surface of the wafer were positioned directly behind each other along the processing line.

The material processing speed v, as indicated in the schemes presented in Figure 5.16, was selected to be 10 mm/s. It is essential to ensure that the temperature of the material remains below the glass transition temperature during the implementation of the laser cleaving process for silicate glasses. The highest calculated temperature value in the processing zone remains below the glass transition temperature, recorded at 680 K.

Figure 5.17a shows the calculated distribution of thermoelastic stresses, directed perpendicular to the processing line, on the surface of the material in the zone of laser beam and refrigerant impact at a fixed moment of time when laser cleaving is realized in the case of absence of through-the-thickness channels applied along the processing line. Figure 5.17b shows a graph of the distribution of these stresses along the processing line. The calculations were performed using the finite element method implemented in the Ansys engineering simulation software [223].

a)   b)
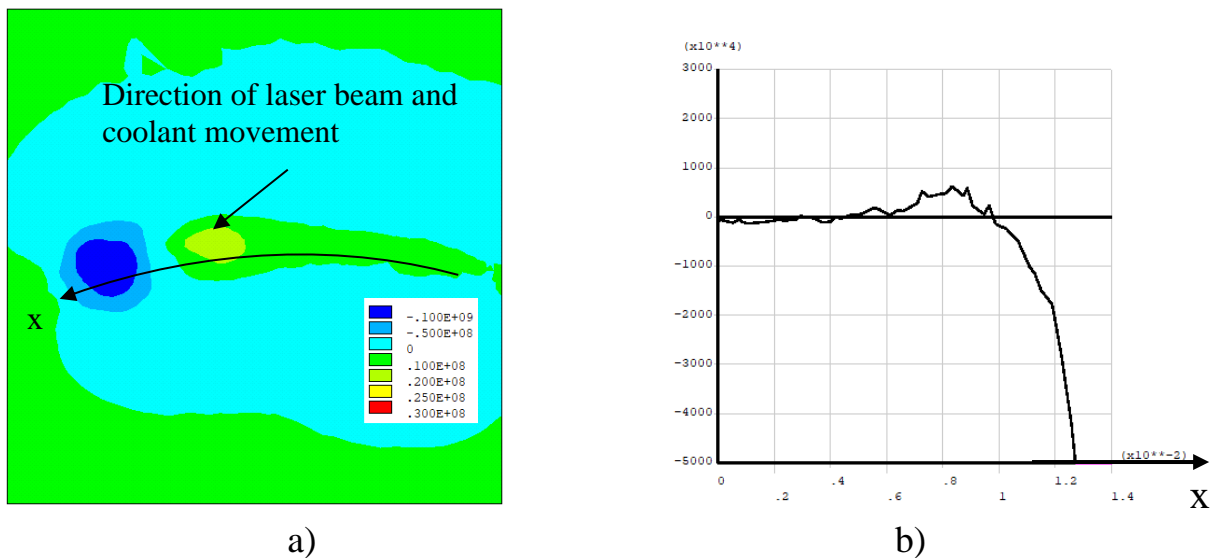
Figure 5.17 – Computed distribution and dependency graph of thermoelastic stresses σ_R, Pa: a) on the material surface; b) along the processing line

The obtained distribution is characteristic of the process of controlled laser thermal cleaving, which combines sequential laser heating of the material and subsequent cooling of its surface. In this case, a zone of significant tensile stresses is formed in the processed material in the zone of refrigerant supply, where the material is cooled sharply. The maximum of these stresses

is displaced relative to the line of CO_2 laser and refrigerant influence (a characteristic asymmetry in stress distribution along the processing line is observed). The stress value along the processing line, as can be seen from the graph in Figure 5.17b, is significantly lower than the maximum stress value in the processing zone equal to 16.3 MPa. As a consequence, crack nucleation and propagation will occur with a displacement from the processing line.

Figure 5.18 illustrates the computed distribution of thermoelastic stresses when through-the-thickness channels are present, with their centers aligned along the processing line. This is for a sector angle of $\alpha=3°$ and different radii of the channels.

a)   b)   c)
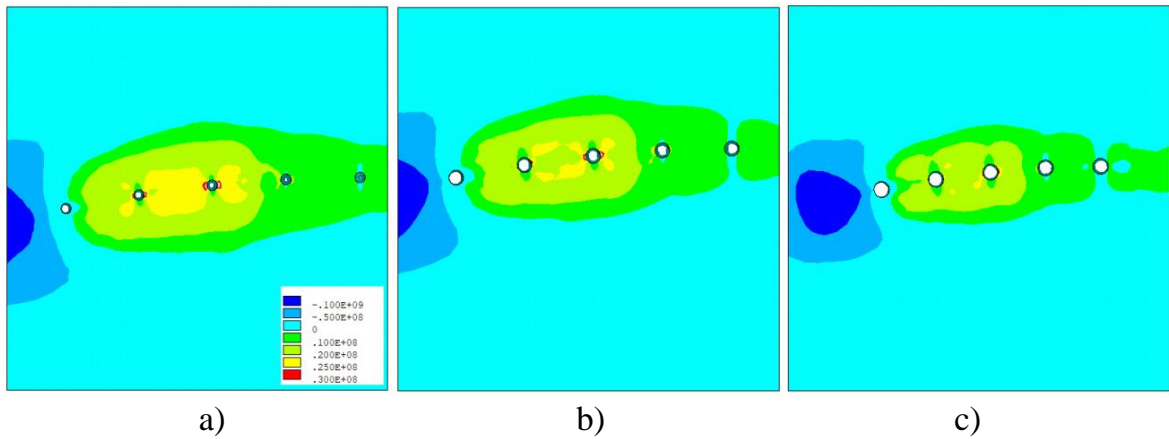
Figure 5.18 – Computed distribution of thermoelastic stresses σ_R, Pa, for $\alpha=3°$
and radius of through-the-thickness channels: 150 μm; 225 μm; 300 μm

Figure 5.19 is a computed dependency graph of similar stresses along the processing line.

a)   b)   c)
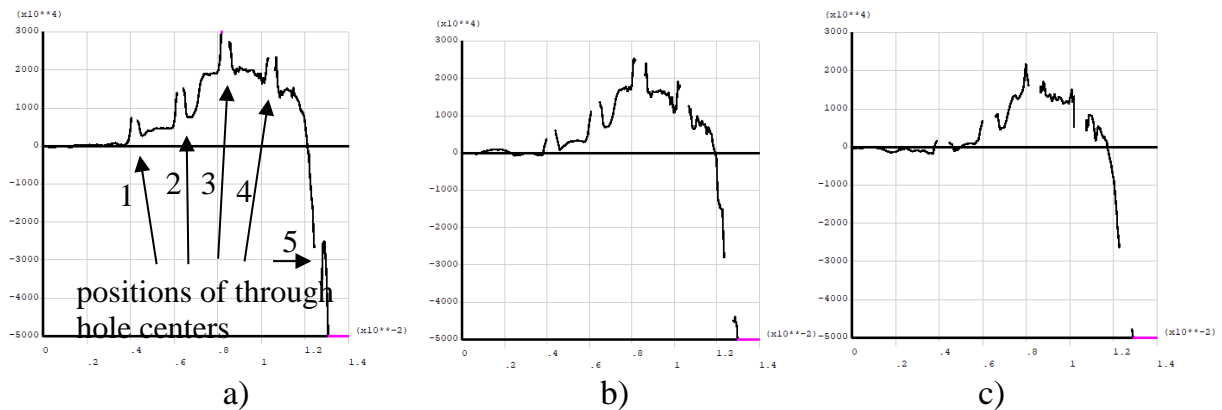
Figure 5.19 – Dependency graph of thermoelastic stresses σ_R, Pa
on the material surface along the processing line for $\alpha=3°$
for the radius of through-the-thickness channels:
a) 150 microns; b) 225 microns; c) 300 microns

191

The calculation results shown in Figures 5.18–5.19 indicate that the presence of through-the-thickness channels effectively removes the asymmetry in the distribution of thermoelastic stresses concerning the processing line. The highest tensile stresses are concentrated along the processing line adjacent to the channels, with these values significantly exceeding those observed in the absence of channels. This scenario fosters conditions beneficial for the stable nucleation of a splitting crack (Table 5.1). It is important to observe that within the channels related to refrigerant supply, a region of tensile stresses is established, which influences the progression of a splitting crack along the processing line. The maxima of tensile stresses, orientated perpendicular to the processing line, occur at the end-faces of the channels. Decreasing the radius of channels results in a heightened maximum tensile stress within the channel areas, as well as an overall rise in stresses in the regions between the holes. This establishes the circumstances for the initiation of cracks from the deposited holes and their progression along the processing line to the subsequent hole, indicating the propagation of cracks from one channel to another.

Table 5.1 – Calculated values of maximum tensile stresses σ_R, MPa in the area of through-the-thickness channels during the process of double-beam laser thermal cleaving of triplex

| Angle of the sector, °	1.5			3			4.5		
Radius of the through-the-thickness channel R, μm	150	225	300	150	225	300	150	225	300
Stress value, MPa	43.6	27.2	20.6	45.7	37.4	30.2	43.5	32.8	30.3

The analysis of stress distribution for different values of the sector angle between the centers of through-the-thickness channels (see Figure 5.20) leads to the conclusion that their value at the end-faces of holes, as well as in the processing area between them, is higher for the sector angle equal to 3°.

Thus, there exists a specific rational value for the distance between the hole centers that enables the greatest stability of the nucleation and development of the splitting crack. This distance is determined by the radius of curvature of the trajectory and the processing parameters, and it can be determined through simulating each technological mode of separation.

The numerical simulation conducted on the combined laser cleaving scheme along curvilinear trajectories reveals that within the region of refrigerant exposure along the line passing through the centers of adjacent holes, an area of significant tensile stresses orientated transversely to the processing line develops on the material surface. The crack originating from the hole propagates along this line. Concurrently, the value of tensile stresses in

areas subjected to refrigerant exposure, particularly in the presence of channels, is markedly elevated compared to scenarios devoid of such channels. This phenomenon is influenced by the diameter of the holes, the distance between them, and processing parameters. Thus, a series of deposited channels throughout the processing line facilitates the control of both the initiation and progression of cracks along curvilinear trajectories within the processing line.

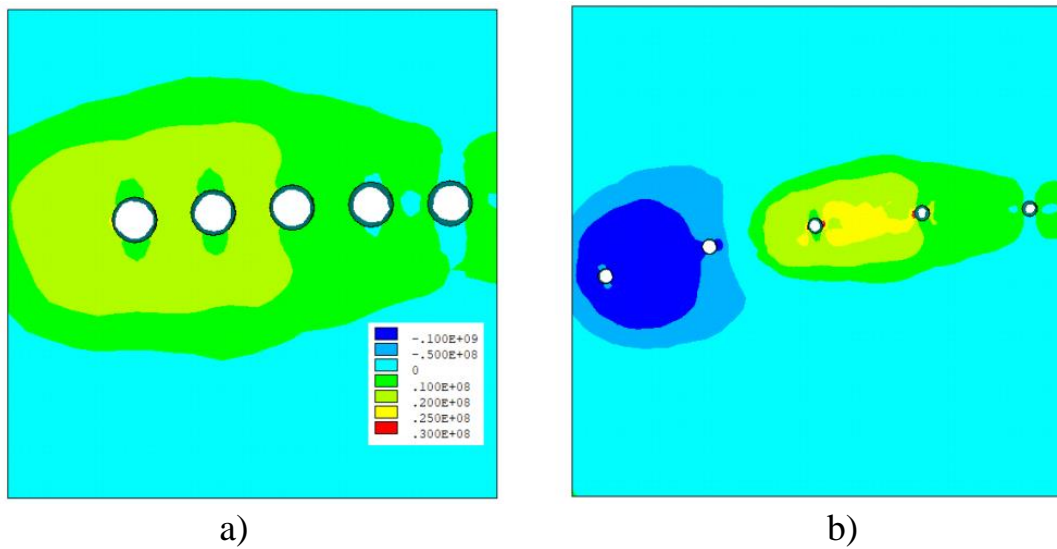a)   b)

Figure 5.20 – Computed distribution of thermoelastic stresses σR, Pa for the angle of the sector between channel centers 3° for the radius of through-the-thickness channels: a) for an angle of α=1.5° and a channel radius of 300 μm; b) for an angle of α=4.5° and a channel radius of 225 μm

CONCLUSION

This monograph presents the findings derived from extensive research conducted by the authors on the process of controlled laser thermal cleaving of brittle nonmetallic materials. The authors' chosen approach of employing numerical simulation through the finite element method, in conjunction with experimental investigations, allowed for the identification of technological parameter values that guarantee qualitative product separation. This methodology enabled the modernization and development of several innovative and highly effective schemes for the separation of brittle nonmetallic materials using laser thermal cleaving techniques.

The efficacy of the practical implementation of the newly proposed laser thermal cleaving schemes, as outlined in the monograph, lies in enhancing the quality of produced goods, diminishing the labor intensity associated with their creation, broadening the spectrum of products manufactured, conserving labor and energy resources, elevating the environmental standards of production, and fostering a more refined labor culture.

The findings outlined in the monograph may be of interest to enterprises within the electronic industry, as well as other organizations in the Republic of Belarus and internationally, that engage in laser technologies for material processing. The research results presented in the monograph are integrated into the educational framework of the Faculty of Physics and Information Technologies at Francisk Skorina Gomel State University for the training of engineering students.

The authors envision continued advancement in the pursuit of optimal technological methods for processing, particularly through the combined application of numerical simulation and metamodels, which are distinguished by their exceptional computational efficiency.

Examples of using such models in engineering calculations are provided in [225–227]. One of the objectives of metamodeling is to determine approximate values of output parameters without the need for exhaustive calculations. Artificial neural networks are among the methods employed in the modelling of laser cleaving of glass, as demonstrated in [228]. Artificial neural networks are widely employed in a variety of scientific and technological disciplines due to their capacity to identify nonlinear dependencies in large data sets [229, 230].

Another aim of metamodeling is to address optimization problems. Examples of solving these problems through genetic algorithms can be found in [231, 232]. The application of genetic algorithms involves the search for solutions through the inheritance and enhancement of useful properties within a set of objects when simulating their evolutionary process, as demonstrated in [233, 234–236].

The authors are presently engaged in a study focused on optimizing the technological parameters of laser processing to improve the efficiency of material separation, using neural network models alongside those developed through nonparametric regression methods. The findings have been published in academic journals and presented at various conferences. Several state programs focused on this subject are currently in progress [237–240]. The authors hold a firm conviction that the outcomes of research in this field will be manifested in the forthcoming monograph.

REFERENCES

1. Laser technology in 7 books: manual for universities / A. G. Grigoryants, A. A. Sokolov; ed. by A. G. Grigoryants. – Moscow: Higher school [Vysshaya shkola], 1988. – Book. 4: Laser processing of non-metallic materials. – 191 p.

2. Kondratenko, V. S. Laser-controlled thermal cleaving of brittle materials: a series of lectures / V. S. Kondratenko. – Moscow: MSUIECS, 2004. – 88 p.

3. Grigoryants, A. G. Basics of Laser Material Processing / A. G. Grigoryants. – Moscow: Mashinostroenie, 1989. – 304 p.

4. Rykalin, N. N. Laser processing of materials / N. N. Rykalin, A. A. Uglov, A. N. Kokora. – Moscow: Mashinostroenie, 1975. – 296 p.

5. Duley, W. Laser Processing and Analysis of Materials: transl. from English. / W. Duley. – Moscow: Mir, 1986. – 504 p.

6. Laser and electron-beam material processing: handbook / N. N. Rykalin [et al.]. – Moscow: Mashinostroenie, 1985. – 496 p.

7. Machulka, G. A. Laser processing of glass. – Moscow: Sov. radio, 1979. – 136 p.

8. Kondratenko, V. S. Investigation and advancement of the laser-controlled thermocleavage technique for glass cutting: PhD thesis in Engineering : 05.17.11 / V. S. Kondratenko. – Moscow, 1983. – 179 p.

9. Shalupaev, S. V. Thermoelastic fields formed in solids using light and sound flows: PhD thesis in Physics and Mathematics: 01.04.05 / S. V. Shalupaev. – Minsk 1987. – 157 p.

10. Shershnev, E. B. Development and implementation of innovative effective processes in the production of glassware using laser technology: PhD thesis in Engineering : 05.17.11 / E. B. Shershnev. – Moscow, 1990. – 145 p.

11. Malov, I. E. Development of the technology for controlled thermal cleaving of sheet glass using the radiation of a solid-state laser: PhD thesis in Engineering: 05.17.11 / I. E. Malov. – Moscow, 2000. – 18 p.

12. Orlov, A. S. Development of theoretical frameworks, technological processes, and equipment for thermal cutting of brittle non-metallic materials illustrated through thin-walled cylindrical glass products: extended abstract of thesis work … D.Sc. in engineering : 05.03.06 / A. S. Orlov. – Rostov-on-Don, 2005. – 40 p.

13. Ivanov, I. A. Development and study of the method for separating transparent brittle dielectric materials via laser radiation on copper vapor: extended abstract of thesis work …PhD in engineering : 05.03.01 / I. A. Ivanov. – Moscow, 2006. – 20 p.

14. Chernykh, S. P. Development of technology for post-growth treatment of devices using wide-gap semiconductor materials: extended abstract of thesis work …PhD in engineering: 05.11.14 / S. P. Chernykh. – Moscow, 2007. – 20 p.

15. Nikityuk, Yu. V. Physical regularities of laser thermal cleaving of silicate glasses and alumina ceramics: PhD thesis in Physics and Mathematics: 01.04.21 / Yu. V. Nikityuk. – Gomel, 2009. – 166 p.

16. Gindin, P. D. Development of innovative technologies and equipment using the technique of laser controlled thermal cleaving for machining components of instrument making, micro- and optoelectronics: extended abstract of thesis work … D.Sc. in engineering: 05.11.14 / P. D. Gindin; MSUIECS. – Moscow, 2009. – 43 p.

17. Naumov, A. S. Development of the technology for separating instrumental wafers into crystals: extended abstract of thesis work …PhD in engineering: 05.11.14 / A. S. Naumov. – Moscow, 2009. – 19 p.

18. Trubienko, O. V. Research and development of technology for blunting of sharp edges on products via laser controlled thermal cleaving: extended abstract of thesis work …PhD in engineering: 05.11.14 / O. V. Trubienko. – Moscow, 2009. – 23 p.

19. Nelina, S. N. Development and study of the technology for producing monocrystalline sapphire substrates intended for electronic components: extended abstract of thesis work …PhD in engineering : 05.27.01 / S. N. Nelina. – Taganrog, 2010. – 24 p.

20. Borisovsky, V. E. Advancement of theoretical frameworks and the creation of a set of technologies and equipment for the laser treatment of quartz glass: extended abstract of thesis work … D.Sc. in engineering: 05.11.14 / V. E. Borisovsky; MSUIECS. – Moscow, 2011. – 36 p.

21. Sorokin, A. V. Development of technological process of laser parallel thermocleaving of brittle materials: extended abstract of thesis work …PhD in engineering : 05.11.14 / A. V. Sorokin. – Moscow, 2011. – 20 p.

22. Chirkov, A. V. Development of an automated subsystem aimed at optimising the selection of efficient laser processing modes for products made from brittle nonmetallic materials: extended abstract of thesis work …PhD in engineering : 05.13.06 / A. V. Chirkov. – Moscow, 2011. – 26 p.

23. Khlyzov, V. A. Development of the control system and automation of the technological process for laser controlled thermocleavage on industrial units : extended abstract of thesis work …PhD in engineering: 05.11.14 / V. A. Khlyzov. Moscow, 2012. – 20 p.

24. Lumley, R. M. Controlled separation of brittle materials used a laser / R. M. Lumley // J. Of the Amer. Cer. Soc. – 1968. – Vol. 49, No. 9. – pp. 850 – 854.

25. Initiation of a controlled fracture: pat. № 3610871 US, IPC H01L 21/28 / R. M. Lumley; assignee Western Electric Company Incorporated.; – applied 19.02.70; published 05.10.71. / [Electronic resource] Mode of access: http://patft.uspto.gov. – Date of access: 19.05.2007

26. Thermal cleaving of glass tubes by laser radiation / Machulka G. A. [et al.] // Electronic industry. – 1976. – Issue 1(49). – pp. 59 – 63.

27. Kondratenko V. S., Serdyukov A. N. Heating of materials using a moving laser source // Abstracts of the 1982 All-Union Seminar on laser technology in instrument making. – Moscow, 1983. – pp. 83.

28. Kondratenko, V. S., Serdyukov, A. N. Calculation of the temperature fields during laser controlled thermal cleaving // Electron Technique. Part 11. Laser technology and optoelectronics. 1984. – Issue 5(31). – pp. 62.

29. Kondratenko, V. S., Serdyukov, A. N., Shalupaev, S. V. Laser heating of materials during thermal cleaving considering heat transfer // Electron Technique. Part 11. Laser technology and optoelectronics. – 1987, – No. 1(41). – pp. 7.

30. Bokut' B. V., Kondratenko, V. S., Myshkovets V. N., Serdyukov, A. N., Shalupaev, S. V. Thermoelastic fields in solids during their processing by laser beams of special geometry. – Minsk: Preprint B. I. Stepanov Institute of Physics of the National Academy of Sciences of Belarus. – 1987. – 59 p

31. Method of cutting non-metallic materials: pat. 2024441 RF, IPC 5 C03B33/02 / V. S. Kondratenko; assignee V. S. Kondratenko; applied 04.02.92; published 12.15.94 / [Electronic resource]. – 2007. – Access mode: www.fips.ru – Date of access: 19.05.2007.

32. Controlled thermal cleaving of glass using laser radiation / V. S. Kondratenko [et al.] // Electronic Industry. – 1978. – No. 9. – pp. 65–68.

33. Solinov, V. F. Influence of the refrigerant on the process of laser-controlled thermal cleaving of glass / V. F. Solinov, V. S. Kondratenko, V. M. Braude // Technics, Economics, Information. Ser. Production technology. – 1983. – Issue 2. – pp. 12–17.

34. Kondratenko, V. S. Thermal cleaving of glass tubes when exposed to laser irradiation / V. S. Kondratenko, A. S. Tanaseichuk, E. B. Shershnev // Electronic technology. – Part II. Laser technology and optoelectronics. – 1986. – No. 4. – pp. 30 – 37.

35. Kondratenko, V. S. Peculiarities of the process of laser controlled thermal cleaving of sheet glass along the curvilinear contour / V. S. Kondratenko, A. S. Tanaseichuk, E. B. Shershnev // Electronic technology. Part 11. Laser technology and optoelectronics. – 1986. – No. 4(40). – pp. 46 – 49.

36. Kondratenko, V. S. New efficient methods for laser processing of glass sheets / V. S. Kondratenko, A. S. Tanaseichuk, E. B. Shershnev // Electronic technology. Part 11. Laser technology and optoelectronics. – 1986. – No. 4(40). – pp. 38 – 45.

37. Laser thermal cleaving of quartz glass / V. S. Kondratenko [et al.] // Electronic industry. Part. 11. Laser technology and optoelectronics. – 1987. – No. 4(44). – pp. 25 – 28.

38. Strength of glass products using different methods of laser edge treatment / V. S. Kondratenko [et al.] // Electronic industry. – 1988. – No. 1. – pp. 30 – 31.

39. Kondratenko, V. S. Time parameters of the process during surface thermal cleaving when exposed to CO_2 laser radiation / V. S. Kondratenko [et al.] // Materials, technologies, tools. – 2002.– No. 2. – pp. 82 – 85.

40. V. S. Kondratenko. Laser-controlled thermal cleaving of glass in the production of electronic products // Electronic industry. – 1988. – No. 1. – pp. 28 – 29.

41. Crack control device in the process of laser cleaving of glass / V. S. Kondratenko [et al.] // Instruments. – 2005. – No. 6 (60) – pp. 9 – 10.

42. Method of blunting sharp edges of products: pat. 2163226 RF, IPC 5 C03B33/02 / V. S. Kondratenko; assignee V. S. Kondratenko. – No.2000116613/03; applied 06.28. 00; published 02.20.01 // Official Bulletin "Inventions, Utility Models" [Electronic resource]. – 2007. – Access mode: www.fips.ru. – Date of access: 19.05.2007.

43. Method of cutting brittle non-metallic materials: pat. 2206525 RF, IPC 5 C03B33/02 / V. S. Kondratenko; assignee V. S. Kondratenko. – No.2001120746/03; applied 07.25.01; published 06.20.03 // Official Bulletin "Inventions, Utility Models" / [Electronic resource]. – 2007. – Access mode: www.fips.ru. – Date of access: 19.05.2007.

44. Method of cutting brittle non-metallic materials: pat. 2206526 RF, IPC 5 C03B33/02 / V. S. Kondratenko; assignee V. S. Kondratenko. – No.2001120747/03; applied 07.25.01; published 06.20.03 // Official Bulletin "Inventions, Utility Models" / [Electronic resource]. – 2007. – Access mode: www.fips.ru – Date of access: 19.05.2007.

45. Method of cutting brittle non-metallic materials: pat. 2206527 RF, IPC 5 C03B33/02 / V. S. Kondratenko; assignee V. S. Kondratenko. –

No.2001122793/03; applied 08.15.01; published 06.20.03 // Official Bulletin "Inventions, Utility Models" / [Electronic resource]. – 2007. – Access mode: www.fips.ru – Date of access: 19.05.2007.

46. Method of cutting brittle non-metallic materials: pat. 2206528 RF, IPC 5 C03B33/02 / V. S. Kondratenko; assignee V. S. Kondratenko. – No.2001122794/03; applied 08.15.01; published 06.20.03 // Official Bulletin "Inventions, Utility Models" / [Electronic resource]. – 2007. – Access mode: www.fips.ru – Date of access: 19.05.2007.

47. Method of cutting brittle non-metallic materials: pat. 2224648 RF, IPC 5 C03B33/02 / V. S. Kondratenko; assignee V. S. Kondratenko. – No.2002123517/03; applied 09.03.02; published 02.27.04 // Official Bulletin "Inventions, Utility Models" / [Electronic resource]. – 2007. – Access mode: www.fips.ru – Date of access: 19.05.2007.

48. Method of cutting brittle non-metallic materials: pat. 2237622 RF, IPC 5 C03B33/02 / V. S. Kondratenko; assignee V. S. Kondratenko. – No.2002114927/03; applied 06.07.02; published 10.10.04 // Official Bulletin "Inventions, Utility Models" / [Electronic resource]. – 2007. – Access mode: www.fips.ru – Date of access: 19.05.2007.

49. Method of cutting brittle non-metallic materials: pat. 2238918 Russian Federation, IPC 5 C03B33/02 / V. S. Kondratenko; assignee V. S. Kondratenko. – No.2002114928/03; applied 06.07.02; published 10.27.04 // Official Bulletin "Inventions, Utility Models" / [Electronic resource]. – 2007. – Access mode: www.fips.ru – Date of access: 19.05.2007.

50. Method of cutting non-metallic materials and device for its implementation: International patent application PCT/RU94/00276, international publication WO 096/20062, IPC B23K 26/00B; assignee V. S. Kondratenko; applied 23.12.2004; published 04.07.96

51. Method of splitting non-metallic materials: pat. 5609284 USA, IPC B23K 1500; B26F 316 / V. S. Kondratenko; assignee Fonon Technology Limited. – applied 30.09.94; published 11.03.97 // [Electronic resource]. – Access mode: http://patft.uspto.gov. – Date of access: 19.05.2007

52. Method of cutting brittle non-metallic materials: pat. 2333163 RF, IPC C03B33/09 / V. S. Kondratenko; assignee V. S. Kondratenko. – No.2007125597/03; applied 09.07.07; published 10.09.08 // Official Bulletin "Inventions, Utility Models" / [Electronic resource]. – 2008. – Access mode: www.fips.ru – Date of access: 27.03.2009.

53. Analysis of the features of laser thermal cleaving of quartz glass / V. A. Emelyanov [et al.] // Electronic Engineering. Section: Laser Technology and Optoelectronics. – 1991. – Issue 3(59). – pp. 90 – 92.

54. Dynamics of generating temperature stress fields during laser-controlled thermal cleaving / V. A. Emelyanov [et al.] // Laser news. – 1995. – No.4. – pp. 14 – 17.

55. Peculiarities of surface cracking during glass cutting using neodymium laser radiation / V. S. Kamenkov [et al.] // Physics and Chemistry of Materials Treatment. – 1996. – No.3. – pp. 51 – 55.

56. Yu. V. Khlopkov. Laser cutting of glass for light filters for TVs and PCs // Steklo i Keramika (Glass and Ceramics). – 1994. – No.7. – pp. 33 – 34.

57. Laser cutting of ceramic materials with metallized surface / E. B. Shershnev, A. V. Maksimenko, V. N. Myshkovets, Yu. V. Nikityuk // Journal of Optical Technology. – 2001. – Vol. 68, No. 10. – pp. 41 – 44.

58. Laser thermal cleaving of dielectric materials / S. V. Shalupaev, E. B. Shershnev, A. N. Serdyukov, Yu. V. Nikityuk // Ceramics. Polish ceramic bulletin. – 2001. – Vol. 65. – pp. 75 – 83.

59. Shalupaev, S. V. Laser separation of glass in a plane parallel to the surface / S. V. Shalupaev, E. B. Shershnev, Yu. V. Nikityuk // Proceedings of F. Skorina Gomel State University. – 2001. – No. 6 (9). – pp. 114 – 117.

60. Shalupaev, S. V. Silica gel glasses after laser radiation / S. V. Shalupaev, A. V. Semchenko, Yu. V. Nikityuk // Material Science. – 2003. – Vol. 21, No. 4. – P. 495 – 501

61. Processing of ceramic and glass tubular-shaped products via laser thermal cleaving / S. V. Shalupaev, E. B. Shershnev, V. N. Myshkovets, A. V. Maksimenko, Yu. V. Nikityuk // Ceramics. Polish ceramic bulletin. – 2003. – Vol. 79. – pp.115 – 120.

62. Analysis of thermoelastic fields formed during laser thermal cleaving of ceramic-metal structures / S. V. Shalupaev, V. N. Myshkovets, A. V. Maksimenko, Yu. V. Nikityuk, G. A. Baevich, V. V. Grischenko // Metalloobrabotka. – 2005. – No. 2(26) – pp. 33 – 36.

63. Precision laser processing of brittle non-metallic materials / S. V. Shalupaev, E. B. Shershnev, Yu. V. Nikityuk, A. A. Sereda // Proceedings of F. Skorina Gomel State University. – 2005. – No. 3 (30). – pp. 87 – 92.

64. Laser processing of quartz glasses synthesized via sol-gel method / S. V. Shalupaev, V. V. Gaishun, A. V. Semchenko, Yu. V. Nikityuk // Materials. Technologies. Tools. – 2005. – No. 2. – pp. 70 – 73.

65. Investigation of the process of laser thermal cleaving of thick ceramic wafers / S. V. Shalupaev, E. B. Shershnev, Yu. V. Nikityuk, A. A. Sereda // Vestnik of Polotsk State University. Part B. – 2005. – No. 6. – pp. 140 – 143.

66. Laser dual-beam method of processing of high-strength ceramic materials / S. V. Shalupaev, M. Alexeyuk, E. B. Shershnev, Yu. V. Nikityuk, A. A. Sereda // Ceramics. Polish ceramic bulletin – 2005. – Vol. 89. – pp. 44 – 49.

67. Double-beam laser thermal cleaving of brittle non-metallic materials / S. V. Shalupaev, E. B. Shershnev, Yu. V. Nikityuk, A. A. Sereda // Journal of Optical Technology. – 2005. – Vol. 73, No. 5. – pp. 62 – 66.

68. Laser thermal cleavage of brittle nonmetallic materials along closed curvilinear contours/ S. V. Shalupaev, Yu. V. Nikityuk, A. A. Sereda // Journal of Optical Technology. – 2008. – Vol. 75, No. 2. – pp. 11 – 15.

69. Shalupaev, S. V. Combined laser thermal cleaving / S. V. Shalupaev, E. B. Shershnev, Yu. V. Nikityuk // Laser physics and spectroscopy: Proceedings of the IV Intern. conf. on laser physics and spectroscopy, Grodno, October 4 – 8, 1999 / NASB, MOE RB, BRFFR, Yanka Kupala State University of Grodno; edited by V. K. Kononenko [et al.]. – Grodno, 1999. – P.2.– pp. 177 – 179.

70. Technological complex for laser processing of materials / S. V. Shalupaev, A. T. Malashchenko, Yu. V. Nikityuk, I. M. Kamornikov // Theoretical and technological bases of hardening and restoration of machine-building products: a collection of scientific papers / Euphrosyne Polotskaya state university of Polotsk; edited by S. A. Astapchik [et al.]. – Novopolotsk, 2001. – pp.726 – 728.

71. Shalupaev, S. V. Laser double-beam processing of materials in the production of electronic products / S. V. Shalupaev, E. B. Shershnev, Yu. V. Nikityuk // INTERMATIC-2004: Proceedings of the International Scientific and Practical Conf. "Fundamental Problems of Radio-Electronic Instrument Engineering", Moscow, September 7–10, 2004 / MIREA – Russian Technological University; editorial staff: Yu. V. Gulyaev [et al.]. – Moscow 2004. – P.1. – pp. 133 – 135.

72. Laser thermal cleaving of brittle non-metallic materials along closed curvilinear trajectories / S. V. Shalupaev, E. B. Shershnev, Yu. V. Nikityuk, A. A. Sereda // Interaction of Radiation with Solid Body: Proceedings of the 6th Intern. conf., Minsk, May 26–28, 2005 / Belarusian State University, NASB, MOE RB, BRFFR, Belarusian Physical Society; edited by V. M. Anishchik [et al.]. – Minsk, 2005. – pp. 436 – 438.

73. Peculiarities of the laser thermal cleaving process under the additional effect of hot air-flow / S. V. Shalupaev, Yu. V. Nikityuk, A. A. Sereda, A. S. Pobiyakha // Interaction of Radiation with Solid Body: Proceedings of the 7th International Conference, Minsk, September 26–28, 2007/ Belarusian State University, NASB, MOE RB, BRFFR, Belarusian Physical Society; edited by V. M. Anishchik [et al]. – Minsk, 2007. – pp. 68 – 70.

74. Double-beam laser thermal cleaving of brittle nonmetallic tubular-shaped materials / S. V. Shalupaev, Yu. V. Nikityuk, I. M. Kamornikov, A. A. Sereda, A. S. Pobiyakha // VII International Scientific Conference "Laser Physics and Optical Technologies": a collection of scientific papers in 3 volumes, Minsk, June 17–19, 2008 / NAS of Belarus, B. I. Stepanov Institute of Physics, NASB, BRFFR, RFBR, Belarusian Physical Society; edited by N. S. Kazak [et al.]. – Minsk, 2008. – Vol. 2. – pp. 227 – 230.

75. Nikityuk, Yu. V. Analysis of thermoelastic processes for asymmetric laser heating / Yu. V. Nikityuk // VI Erugin Readings: abstracts of reports of the International Mathematical Conf., Gomel, May 20 – 21, 1999: in 2 parts. / F. Skorina Gomel State University, BRFFR. – Gomel, 1999. – P. 2. – pp. 51 – 52.

76. Nikityuk, Yu. V. Combined laser thermal cleaving / Yu. V. Nikityuk, I. M. Kamornikov // Intern. conf. of young scientists and specialists "Optics-99": abstracts, St. Petersburg, Russia, October 19 – 21, 1999 / D. S. Rozhdestvensky Optical Society. – ITMO University. – St. Petersburg, 1999. – pp. 160 – 161.

77. Nikityuk, Yu. V. Thermoelastic fields in the process of controlled laser thermal cleaving / Yu. V. Nikityuk, A. V. Nikityuk // Physics of Condensed Media; abstracts of VII Republican scientific conference of undergraduate and postgraduate students., Grodno, May 5 – 7, 1999 / Yanka Kupala State University of Grodno. MOE RB: edited by V. A. Liopo. – Grodno, 1999. – pp. 175 – 177.

78. Two-beam method of separation of ceramic materials with metallized surface / S. V. Shalupaev, A. V. Maksimenko, V. V. Sviridova, Yu. V. Nikityuk // New competitive and progressive technologies, machines and mechanisms in the conditions of the modern market: materials of the international scientific-technical conference, Mogilev, May 18 – 19, 2000 / MOE RB, NAS of Belarus, Belarusian-Russian University: editorial staff: I. S. Sazonov [et al.]. – Mogilev, 1999. – pp. 177.

79. Nikityuk, Yu. V. Temperature fields arising as a result of the impact on the material of a laser beam moving along a curvilinear trajectory / Yu. V. Nikityuk, I. M. Kamornikov, A. N. Kupo // International Youth Scientific Conference "XXVI Gagarin Readings": abstracts, Moscow, 2000 / Ministry of Education of the Russian Federation, MATI, Russian State Technological University. – Moscow, 2000. – pp. 294 – 295.

80. Nikitjuk, Y. V. Laser glass thermosplitting in mutually orthogonal planes / Y. V. Nikitjuk // International Conference «Problems of Interaction of Radiation with Matter»: book of Abstracts, Gomel, 30 oct. – 1 nov. 2001 / BFFR, F. Skorina Gomel State University: editors I. V. Semchenko [et. al.]. – Gomel, – 2001. – pp. 57.

81. Shalupaev, S. V. Double-beam laser processing of brittle nonmetallic materials. / S. V. Shalupaev, E. B. Shershnev, Yu. V. Nikityuk // Quantum Electronics: Proceedings of the V International Scientific and Technical Conference, Minsk, November 22 – 25, 2004 / Belarusian State University, NAS of Belarus, BRFFR: edited by I. S. Manak [et al.]. – Minsk, 2004. – pp. 148.

82. Shalupaev, S. V. Determination of the trajectory of the splitting crack development during laser asymmetric thermal cleaving using the finite element analysis method/ S. V. Shalupaev, Yu. V. Nikityuk, A. E. Shershnev // Topical Issues of Strength: Proceedings of XLIII International Conference, Vitebsk, 27 sep. – 5 oct. 2004 / Vitebsk State Technological University, Research Institute of Mathematics and Mechanics SPbSU. – Vitebsk, 2004. – pp. 246.

83. Shalupaev, S. V. Complex laser processing of quartz products / S. V. Shalupaev, Yu. V. Nikityuk, A. E. Shershnev // Materials, equipment and resource-saving technologies: proceedings of the international scientific and technical conference, Mogilev, April 21–22, 2005: in 2 parts / MOE RB, MOE RF, NAS of Belarus, Belarusian-Russian University; editorial staff: I. S. Sazonov [et al.]. – Mogilev, 2005. – P. 1. – pp. 193 – 194.

84. Setup for laser thermal cleaving of brittle non-metallic materials: pat. 683 Republic of Belarus, IPC C 03B 33/02 / S. V. Shalupaev, E. B. Shershnev, Yu. V. Nikitiuk; assignee F. Skorina Gomel State University. – No. u 20010292; applied 10.12.01; published 30.09.02 // Afitsyyny bulletin / Nat. tsentr intelektual. ulasnastsi. – 2002. – No. 3. – pp. 224 – 225.

85. Laser cutting unit for brittle non-metallic materials: pat. 1979 Republic of Belarus, IPC C 03B 33/02 / S. V. Shalupaev, E. B. Shershnev, Yu. V. Nikitiuk, I. M. Kamornikov, I. L. Poltoran; assignee F. Skorina Gomel State University. – No. u 20040527; applied 19.11.04; published 30.06.05 // Afitsyyny bulletin / Nat. tsentr intelektual. ulasnastsi. – 2005. – No. 2. – pp. 277.

86. Laser cutting unit for brittle non-metallic materials: pat. 2164 Republic of Belarus, IPC C 03B 33/02 / S. V. Shalupaev, E. B. Shershnev, Yu. V. Nikitiuk, A. A. Sereda, A. M. Evtukhov; assignee F. Skorina Gomel State University. – No. u 20050085; applied 02.21.05; published 09.30.05 // Afitsyyny bulletin / Nat. tsentr intelektual. ulasnastsi. – 2005. – No. 3. – pp. 64.

87. Laser cutting unit for brittle non-metallic materials: pat. 2274 Republic of Belarus, IPC C 03B 33/02 / S. V. Shalupaev, E. B. Shershnev, Yu. V. Nikityuk, A. A. Sereda; assignee F. Skorina Gomel State University. – No. u 20050188; applied 04.04.05; published 12.30.05 // Afitsyyny bulletin / Nat. tsentr intelektual. ulasnastsi. – 2005. – No. 4. – pp. 43.

88. Laser cutting unit for brittle non-metallic materials: pat. 2283 Republic of Belarus, IPC C 03B 33/02 / S. V. Shalupaev, E. B. Shershnev, Yu. V. Nikitiuk, A. M. Evtukhov; assignee F. Skorina Gomel State University – No. u 20050225; applied 04.18.05; published 12.30.05 // Afitsyyny bulletin / Nat. tsentr intelektual. ulasnastsi. – 2005. – No. 4. – pp. 44.

89. Method of separating brittle nonmetallic materials under the action of thermoelastic stresses: pat. 10167 Republic of Belarus, IPC C 03B 33/00/ S. V. Shalupaev, E. B. Shershnev, Yu. V. Nikityuk, A. A. Sereda; assignee F. Skorina Gomel State University – No. a 20051034; applied 27.10. 05; published 30.12.07 // Afitsyyny bulletin / Nat. tsentr intelektual. ulasnastsi. – 2007. – No. 6. – pp. 87.

90. Method of separating brittle nonmetallic materials under the action of thermoelastic stresses: pat. 2342333, Russian Federation, IPC C 03B 33/00 / S. V. Shalupaev, E. B. Shershnev, Yu. V. Nikityuk, A. A. Sereda; assignee F. Skorina Gomel State University – No. 2006113101; applied 18.04.06; published 27.12.08 // Bulletin No.36.

91. Method of separating brittle nonmetallic materials under the action of thermoelastic stresses: pat. 10022 Republic of Belarus, IPC C 03B 33/00 / S. V. Shalupaev, E. B. Shershnev, Yu. V. Nikityuk, A. A. Sereda; assignee F. Skorina Gomel State University – No. a 20050697; applied 11.07.05; published 30.12.07 // Afitsyyny bulletin / Nat. tsentr intelektual. ulasnastsi. – 2007. – No. 6. – pp. 86 – 87.

92. Method of separation of brittle nonmetallic materials under the action of thermoelastic stresses: pat 2320549, Russian Federation, IPC C 03B 33/00 / S. V. Shalupaev, E. B. Shershnev, Yu. V. Nikityuk, A. A. Sereda; assignee F. Skorina Gomel State University – No. 2006112521; applied 14.04.06; published 27.03.08 // Bulletin No.9.

93. Method of separating brittle non-metallic materials: pat. 11830 Republic of Belarus, IPC C 03B 33/00 / S. V. Shalupaev, Yu. V. Nikityuk, A. A. Sereda; assignee F. Skorina Gomel State University – No. a 20070599; applied 21.05.07. // Afitsyyny bulletin / Nat. tsentr intelektual. ulasnastsi. – 2009. – No. 2 – pp. 72

94. Shalupaev, S. V. Thermoelastic fields formed in brittle non-metallic materials during laser thermal cleaving / S. V. Shalupaev, Yu. V. Nikityuk. – Gomel: F. Skorina Gomel State University 2007. – 44 p. – (Preprint / MOE RB, F. Skorina Gomel State University; No. 4).

95. To design and produce a technological complex for laser processing of materials and to master its production: report on research and development (concluded) / F. Skorina Gomel State University; supervising director

205

S. V. Shalupaev. (S. V. Shalupaev, Yu. V. Nikityuk, I. M. Kamornikov, E. B. Shershnev) – Gomel, 2004. – 37 p. – No. SR 2002508.

96. Enhancement of efficiency in the controlled laser thermal cleaving process for dielectric materials / V. K. Sysoev [et al.] // Journal of Optical Technology [Opticheskii Zhurnal]. – 2004. – Vol. 71, No. 2. – pp. 65 – 69.

97. Controlled Hybrid Light-Laser Hybrid Thermal Cleaving of Glasses / V. K. Sysoev [et al.] // Technical Physics Letters. – 2007. – Vol. 33, issue 1. – pp. 54 – 59.

98. G. V. Shepelev, I. N. Shiganov, I. E. Malov. Cutting sheet glass with the beam of a solid-state laser // Technology of Mechanical Engineering. – 2000. – No. 5. – pp. 23 – 26.

99. Malov, I. E. Development of the technology for controlled thermal cleaving of sheet glass using radiation of a solid-state laser: PhD thesis in Engineering: 05.03.07 / I. E. Malov; Bauman Moscow State Technical University. – Moscow, 2000. – 185 p.

100. V. Solinov, A. Sirota, V. Chadin. Laser cutting of glass // Construction materials, equipment, technologies of the XXI century. – 2004. – No.5. – pp. 50 – 52.

101. Method of cutting plates of brittle materials: pat. 000544. Eurasian Patent Office, IPC C 03B 33/00 / A. S. Sirota, V. F. Solinov, E. F. Solinov, V. M. Tovmasyan, V. S. Chadin; assignee LAZTEX LTD. – No.199900040; applied 10.13.98; published 10.28.99 / [Electronic resource]. – 2007. – Access mode: www.eapo.org – Date of access: 19.05.2007.

102. Method of laser processing of glass: pat. 002296 Eurasian Patent Office, IPC C 03B 33/00, B 23K 26/00 A. K. Aliev, A. S. Sirota, V. F. Solinov, E. F. Solinov, V. S. Chadin; assignee LAZTEX LTD. – No.20000026; applied 05.17.00; published 02.28.02. / [Electronic resource]. – 2007. – Access mode: www.eapo.org – Date of access: 19.05.2007.

103. Method of cutting glass: pat. 004322 Eurasian Patent Office, IPC C 03B 33/00 A. K. Aliev, A. S. Sirota, V. F. Solinov, E. F. Solinov, V. S. Chadin; assignee LAZTEX LTD. – №200100614; applied 2001.03.05; published 2002.10.31 / [Electronic resource]. – 2007. – Access mode: www.eapo.org – Date of access: 19.05.2007.

104. Method of cutting glass: pat. 004167 Eurasian Patent Office, IPC C 03B 33/09 A. K. Aliev, A. S. Sirota, V. F. Solinov, E. F. Solinov, V. S. Chadin; assignee LAZTEX LTD. – No. 2001000008; applied 2001.03.01; published 2004.02.26 / [Electronic resource]. – 2007. – Access mode: www.eapo.org – Date of access: 19.05.2007.

105. Orlov, I. A. Laser cutting of tubular glass products using the thermal cleaving method: extended abstract of thesis work … PhD in engineering: 05.03.07 / I. A. Orlov; Bauman Moscow Technical University. – Moscow, 1992. – 16 p.

106. Cutting method for hollow glass products: pat. 2015118 RF, IPC 5 C 03B 33/00 / I. A. Orlov, V. S. Chadin; assignee I. A. Orlov, V. S. Chadin. – No. 4942111/33; applied 1991.06.17; published 1994.06.30. // Official Bulletin "Inventions, Utility Models" / [Electronic resource]. – 2008. – Access mode: www.fips.ru – Date of access: 27.03.2009.

107. Method of laser cutting of tubular glass blanks: pat. 1721995 USSR, IPC C 03B 33/08 / I. I. Dutka, V. S. Kovalenko, G. L. Matviyishin; assignee Lviv Erotron Design Bureau. – No. 4700601/33; applied 1989.06.20; published 1996.02.27. // Official Bulletin "Inventions, Utility Models" / [Electronic resource]. – 2008. – Access mode: www.fips.ru – Date of access: 27.03.2009.

108. Method and apparatus for cutting through a flat workpiece made of brittle material, especially glass: pat. 5984159 USA, IPC C 03B 33/09 / H. Ostendarp, C. Hermanns, D. Hauer, J. Stein, G. Geissler, R. Steinfartz, B. Hoetzel, A. Blunck; assignee Schott Glas. – NO. 09/060185; applied 04. 14. 98; published 10. 16. 99 / [Electronic resource]. – Access mode: http://patft.uspto.gov. – Date of access: 19.05.2007.

109. Method and device for cutting flat work pieces of a brittle material: pat. 6635848 USA, IPC C 03B 33/09 / D. Hauer, B. Hoetzel, assignee Schott Glas. – 10/130522; applied 09. 20. 02; published 10. 21. 03. / [Electronic resource]. – Access mode: http://patft.uspto.gov. – Date of access: 19.05.2007.

110. Method and device for the separation of flat workpieces made from a brittle material: pat. 6811069 USA, IPC C 03B 33/09 / D. Hauer, B. Hoetzel, assignee Schott Glas. – 10/149781; applied 06. 13. 02; published 11. 02. 04. / [Electronic resource]. – Access mode: http://patft.uspto.gov. – Date of access: 19.05.2007.

111. Method and device for cutting flat work pieces made of a brittle material: pat. 7014082 USA, IPC C 03B 33/09 / D. Hauer, B. Hoetzel, assignee Schott AG. – № 10/941338; applied 09. 15. 04; published 03. 21. 06. / [Electronic resource]. – Access mode: http://patft.uspto.gov. – Date of access: 19.05.2007.

112. Method and apparatus for separating non-metallic substrates utilizing a laser initiated scribe: pat. 6211488 USA, IPC B23K 26/073 / B. Hoekstra, L. Glebov, O. Efimov; assignee Accudyne Display and Semiconductor Systems Inc. – No. 09/240057; applied 01. 29. 99; published 04.

03. 01. / [Electronic resource]. – Access mode: http://patft.uspto.gov. – Date of access: 19.05.2007.

113. Method and apparatus for separating non-metallic materials: pat. 6660963 USA, IPC B23K 26/073 / B. Hoekstra, R. Flannigan, D. Wegerif; assignee Applied Photonics Inc. – 10/196658; applied 07.16.2002; published 09. 12. 03. // [Electronic resource]. – Access mode: http://patft.uspto.gov. – Date of access: 19.05.2007.

114. Method and apparatus for separating non-metallic materials: pat. 6489588 USA, IPC B23K 26/14 / B. Hoekstra, R. Flannigan, D. Wegerif; assignee Applied Photonics Inc. – No. 09/718453; applied 11. 22.00; published 12. 03. 02. / [Electronic resource]. – Access mode: http://patft.uspto.gov. – Date of access: 19.05.2007.

115. Tsai, C. Laser cutting of thick ceramic substrates by controlled fracture technique / C. Tsai, H. Chen // Journal of materials processing technology. – 2003. – Vol. 136. – pp. 166 – 173.

116. Tsai, C. Apply an on-line crack detection technique for laser cutting by controlled fracture / C. Tsai, C. Liou // The international journal of advanced manufacturing technology. – 2001. – Vol. 18. – pp. 724 – 730.

117. Tsai, C. Application of iterative path revision technique for laser cutting with controlled fracture / C. Tsai, H. Chen // Optics and lasers in engineering. – 2004. – Vol. 41. – pp. 189 – 204.

118. Tsai, C. The laser shaping of ceramic by a fracture machining technique, / C. Tsai, H. Chen // The international journal of advanced manufacturing technology. – 2004. – Vol. 23. – pp. 342 – 349.

119. Tsai, C. Laser milling of cavity in ceramic substrate by fracture-machining element technique / C. Tsai, H. Chen // Journal of materials processing technology. – 2003. – Vol. 136. – pp. 158 – 165.

120. Tsai, C. Machining a smooth surface of ceramic material by laser fracture machining technique / C. Tsai, C. Ou // Journal of Materials Processing Technology. – 2004. – Vol. 156. – pp. 1797 – 1804.

121. Method of cutting sheet glass: application 93028964 RF, IPC 6 C 03B 33/02 / V. P. Strekalov. V. S. Kondratenko, V. I. Gundyak; assignee JSC "Kristall". – No. 93028964; applied 06.01.93; published 06720.95. / [Electronic resource]. – 2007. – Access mode: www.fips.ru – Date of access: 19.05.2007.

122. Jenoptik laser technologies official website [Electronic resource]. – Access mode: http://www.lasertechnologies-jenoptik.com – Date of access: 19.05.2007.

123. Ptg industries official website [Electronic resource]. – Access mode: http://www.ptgindustries.com – Date of access: 19.05.2007.

124. Fonon Technology official website [Electronic resource]. – Access mode: http://www.fonon.com – Date of access: 19.05.2007.

125. JSC "MZ "Sapphir" official website [Electronic resource]. – 2007. – Access mode: http://www.ropnet.ru/sapphir/ltob.htm – Date of access: 19.05.2007.

126. Votss Ltd official website [Electronic resource]. – 2007. – Access mode: http://votss.rbcmail.ru/.htm. – Date of access: 19.05.2007.

127. NANOLAB official website [Electronic resource]. – 2007. – Access mode: http://www.laser – tech.ru. – Date of access: 19.05.2007.

128. Laser equipment setup "Kvant-20" for glass cutting / B. A. Parfenov [et al.] // Electron Technique. Ser. II. Laser technology and optoelectronics. – 1979. – Issue 1 (7). – pp. 11 – 15.

129. M. B. Stigin, A. N. Chudinov. Laser processing of glass by picosecond pulses // Quantum Electronics. – 1994. – No. 8. – pp. 787 – 790.

130. S. M. Barinov, V. Ya. Shevchenko. Strength of technical ceramics. – Moscow: Nauka, 1996. – 159 p.

131. Method and apparatus for breaking brittle materials: pat. 582772 USA, B23K 26/073 / J. Ariglio, H. Menegus; assignee Corning Incorporated. – No. 08/810480; applied 03. 03. 97; published 10. 27. 98. / [Electronic resource] Access mode: http://patft.uspto.gov. – Date of access: 19.05.2007.

132. Method for breaking a glass sheet: pat. 5776220 USA, IPC B23K 26/073 R. Allaire, H. Menegus, B. Raeder, H. Stevens; assignee Corning Incorporated. – No. 08/573471; applied 12. 15. 95; published 07. 07. 98. / [Electronic resource] Access mode: http://patft.uspto.gov. – Date of access: 19.05.2007.

133. Severing of glass or vitrocrystalline bodies: pat. 3935419 USA, C03B 33/00 / E. Lambert, J. Lambert, B. Longueville; assignee Glaverbel-Mecaniver S.A. – No. 05/405,597; applied 10. 11. 73; published 01. 27. 76. / [Electronic resource] Access mode: http://patft.uspto.gov. – Date of access: 19.05.2007.

134. Increase of laser cutting efficiency of dielectric materials with metallized surface / B. V. Bokut' [et al.] // Electron Technique. Ser.7. Technology, production organization and equipment. – 1988. – Issue 4 (149). – pp. 3 – 5.

135. Combined laser-scribing and laser-breaking for shaping of brittle substrates: pat. 6744009 USA, B23K 26/14 / J. Xuan, C. Shih; assignee Seagate Technology LLC. – No. 10/227751; applied 08. 27. 02; published 09. 01. 04. / [Electronic resource] Access mode: http://patft.uspto.gov. – Date of access: 19.05.2007.

136. Segerlind, L. Application of the finite element method. – Moscow: Mir, 1979. – 392 p.

137. Gallagher, R. Finite element method: fundamentals. – Moscow: Mir, 1984. – 215 p.

138. O. K. Zenkevich, The Finite Element Method in Engineering [Russian translation]. – Moscow: Mir, 1975. – 541p.

139. Shabrov N. N. The finite element method in the calculation of heat engines parts. – Leningrad: Mashinostroenie, 1983. – 212 p.

140. S. P. Kundas, T. A. Kashko. Computer modeling of technological systems: study guide in 2 parts. – Minsk: BSUIR, 2004. – P.1. – 168 p.

141. A. B. Kaplun, E. M. Morozov, M. A. Olferyeva. ANSYS in the hands of an engineer: a practical guide. – Moscow: Editorial URSS, 2003. – 272 p.

142. Chigarev A. V. ANSYS for engineers: reference manual / A. V. Chigarev, A. S. Kravchuk, A. F. Smalyuk. – Moscow: Mashinostroenie, 2004. – 512 p.

143. List of software tools certified by the Council for Certification of Software Tools of Gosatomnadzor of Russia (1999 – 2003) // Gosatomnadzor Bulletin of Russia . – 2003. – No. 1. – pp. 70 – 76.

144. V. I. Yugov, N. G. Rasskazchikov, D. V. Demin. Laser technologies in the production of products from glass, glass fibers, glass fabrics and materials on their basis // Production technologies and product quality: Proceedings of the 4th International Scientific-Technical Conference, Vladimir, September 25 – 27, 2001. – Moscow: Nov. tekhnol., – 2001. – pp. 120 – 124.

145. Introduction to ANSYS: strength and thermal analysis: textbook / A. S. Shalumov [et al.]. – Kovrov: KSTA, 2002. – 52 p.

146. O. C. Zienkiewicz, K. Morgan. Finite elements and approximation. – Moscow: Mir, 1986. – 318 p.

147. V. P. Dyakonov, I. V. Abramenkova, A. A. Penkov. Fundamentals of mathematics and mathematical modeling // New information technologies: study guide. – Smolensk: SSPU, 2003. – Part 3. – 192 p.

148. S. B. Sapozhnikov, A. O. Scherbakova. Moisture influence on the stress state of the fiber-matrix interface of reinforced plastic // Izvestiya Chelyabinskogo Nauchnogo Tsentra. – 2001. – issue 3. – pp. 43–48.

149. Crawford, J. Evaluating mesh density / J. Crawford // ANSYS Solutions. – 1999. – Vol. 1, No. 2. – pp. 12 –16.

150. H. S. Carslaw, J. C. Jaeger. Conduction of teat in solids. – Moscow: Nauka, 1964. – 487 p.

151. Kartashov E. M. Analiticheskie metody v teploprovodnosti tverdykh tel [Analytical methods in thermal conduction of solids]. –Moscow: Vysshaya shkola, 1985, – 480 p. (In Russian).

152. Kovalenko, A. D. Fundamentals of thermoelasticity / A. D. Kovalenko. – Kiev: Naukova Dumka, 1970. – 307 p

153. G. P. Karzov, B. Z. Margolin, V. A. Shevtsova. Physical and mechanical modeling of fracture processes. – St. Petersburg: Politechnika, 1993. – 391 p.

154. Selected nonlinear problems of fracture mechanics. V. A. Levin, E. M. Morozov, Y. G. Matvienko. – Moscow: Fizmatlit, 2004. – 408 pc.

155. Parton, V. Z. Fracture mechanics: from Theory to Practice. – Moscow: Nauka, 1990. – 240 p.

156. P. A. Ivashchenko, Y. A. Kalinin, B. N. Morozov. Measurement of laser parameters. – Moscow : Izdatelstvo standartov, 1982. – 168 p.

157. Sarzhevsky, A. M. Optics. In two parts. – Minsk: Izd-vo "Universitetskoe", 1986. – Vol. 2. – 317 p.

158. V. S. Aleynikov, V. I. Masychev. Optimization of technological processes for glass thermal treatment in Electrovacuum Product Manufacturing via Volumetric Heating with CO Laser Radiation – Electronic Engineering. Series 7. Technology, production organization and equipment. – Moscow: Central Research Institute "Electronics", 1990. – Issue 13(1553). – 45 p.

159. Technology of building and technical glass and slag glass-ceramics: Textbook for technical schools / V. V. Polliak [et al]. – Moscow: Stroyizdat, 1983. – 432 p.

160. V. S. Gorshkov, V. G. Savelyev, N. F. Fedorov. Physical chemistry of silicates and other refractory compounds: University Textbook. – Moscow: Vyssh. shk., 1988. – 400 p.

161. Boguslavsky I. A. High-strength tempered glass. Moscow: Stroyizdat, 1969. – 208 p.

162. Tretyakov, Yu. D. Ceramics in the Past, Present and Future // Soros Education Journal. – 1998. – No. 6. – pp. 53 – 59.

163. Balkevich, V. L. Technical ceramics : Study guide for higher educational institutions/ V. L. Balkevich. – Moscow: Stroyizdat, 1984. – 256p.

164. Kolenko, E. A. Process engineering of laboratory experiment. Reference book. – St. Peterburg: Politehnika, 1994. – 751 p.

165. Glass / Apen A. A. [et al.]; general editor N. M. Pavlushkina. – Moscow : Stroyizdat, 1973. – 487 p.

166. New ceramics / P. P. Budnikov [et al.]; ed. by P. P. Budnikov. – Moscow : Izd-vo literatury po stroitel'stvu, 1969. – pp. 124 – 150.

167. Yu. A. Kontsevoi, Yu. M. Litvinov, E. A. Fattkhov. Plasticity and strength of semiconductor materials and structures. – Moscow : Radio and communication [Radio i svyaz'], 1982. – 240 p.

168. Ceramics and its junctions with metals in engineering / V. A. Presnov [et al.]. – Moscow: Atomizdat, 1969. – 232 p.

169. Bartenev, G. M., Prochnost' i mekhanizm razrusheniya polimerov [Strength and Fracture Mechanism of Polymers], Moscow: Khimiya, 1984. – 280 p.

170. I. M. Melnichenko, E. N. Poddenezhny. Sol-gel technology – a breakthrough into the XXI century // Technology, Economics, Organization. – 1997. – No. 2. – pp. 32 – 35.

171. E. N. Poddenezhnyi, A. A. Boiko Zol'-gel'sintez opticheskogo kvartsevogo stekla. – Gomel: PO Sukhoi Gomel State Technical University, 2002. – 210 p.

172. Shahani, A. R. Simulation of glass cutting with an impinging hot air jet / A. R. Shahani, M. Seyyedian // International Journal of Solids and Structures. – 2004. – Vol. 41. – pp. 1313 – 1329.

173. ANSYS in the hands of an engineer: Fracture mechanics / E. M. Morozov, A. Yu. Muizemnek, A. S. Shadsky. – Moscow: LENAND, 2008. – 456 p.

174. Shalupaev, S. V. Analysis of laser thermosplitting processes within the framework of the linear fracture mechanics / S. V. Shalupaev, M. Aleksiejuk, Y. V. Nikitjuk, A. A. Sereda // CERAMICS. POLISH CERAMIC BULLETIN. – 2008. – Vol.101. – pp. 275–284.

175. Naumov A. S. Ph.D. thesis "Development of technology for the separation of instrument plates on crystals" in Engineering Science. – Moscow, MGUPI, 2007

176. Konstantinova, A., Grechushnikov, B., Bokut, B., Valashko, E. Optical Properties of Crystals. – Minsk: Nauka i Tehnika, 1995. – 302 p.

177. E. S. Falkevich, E. O. Pulner, I. F. Chervonnyi, et al., Technology of semiconductor silicium. – Moscow: Metallurgiya, 1992. – 408 p. (in Russian)

178. Koritskiy Y. V., Pasynkova V. V., Tareeva B. M. Reference book on electrotechnical materials. – Leningrad: Energoatomizdat, 1988. – 728 p.

179. Lackner, T. Determination of axisymmetric elastic constants in anisotropic silicon for a thyristor tablet / T. Lackner // Journal of electronic materials. – 1989. – Vol. 18. – pp. 19 – 24.

180. Acoustic crystals / A. A. Blistanov [et al.] ; edited by M. P. Shaskolskaya. – Moscow: Nauka, 1982. – 632 c.

181. Heyliger P., Ledbetter H., Kim S. Elastic constants of natural quartz // J. Acoust. Soc. Am. – 2003. – Vol. 114. – pp. 644–650.

182. Gluckman, L. I. Piezoelectric quartz resonators. – Moscow: Radio and communication [Radio i svyaz'], 1981. – 232 p.

183. A. G. Smagin, M. I. Yaroslavskiy. Piezoelectricity of Quartz and Quartz-Crystal Resonators. – Moscow : Energiya, 1970. – 488 p. (in Russian)

184. Kestler, W., Jung, W., Bryant, J. On the selection of quartz resonators // Osnovy skhemotekhniki. – 2001. – No. 5. – pp. 19.

185. Gluckman, L. I. Piezoelectric quartz resonators : 3rd Edition, Revised and Supplemented – Moscow : Radio and communication [Radio i svyaz'], 1981. – 232 p.

186. Method for cutting glass tubes: patent 857025 USSR, IPC B23K 26/073 5 C03B33/06 / V. S. Kondratenko, A. S. Tanaseichuk; assignee enterprise mailbox number P-6229; applied 1979.12.19; published 1981.08.23 / [Electronic resource]. – 2007. – Access mode: www.fips.ru – Date of access: 19.05.2007.

187. Physical Foundations of Laser Processing of Diamonds: A Textbook for Universities / A. I. Shkadov; edited by A. M. Bocharov. – Smolensk, 1997. Book 3. – 288 p.

188. Shalupaev, S. V. Dependence of the diamond laser processing efficiency on crystallographic directions / S. V. Shalupaev, E. B. Shershnev, Y. V. Nikitjuk, V. V. Sviridova // SPIE. – 2001. – Vol. 4358. – pp. 329 – 333.

189. E. B. Shershnev, Yu. V. Nikityuk, A. E. Shershnev / Modeling of laser processing of diamond crystals // Proceedings of F. Skorina Gomel State University. – 2011. – No. 6 (69). – pp. 164 –168.

190. A. M. Krivtsov, O. S. Loboda, S. S. Khakalo. Comparison of micromodels describing the elastic properties of diamond //A Journal of Russian Academy of Sciences. Mechanics of Solids, 2012. – No. 5.– pp. 44–52.

191. V. N. Belomestnykh, E. G. Soboleva. Unconventional approach to determining anisotropic Poisson's ratios in cubic crystals [Electronic resource] // Letters on materials. – 2012. – Vol. 2, No 1. – pp. 13–16.

192. I. P. Sukharev. Experimental Methods of Deformation and Strength Research. – Moscow: Mashinostroenie. – 1987. – 212p.

193. Watsar S. D., Bharule A. Stress analysis of finite plate with special shaped cutout // International Journal of Scientific Engineering and Research. – 2015. – Vol. 3. – No. 4. – pp. 145–150.

194. Pravin R. Gawande1, Ajay Bharule. An investigation on cracked plate for stress intensity factor for selected configurations under different loading modes // International Journal of Scientific Engineering and Research. –2014. – Vol. 3(05). – pp. 154–161.

195. Yamada K. et al. Photoelastic observation of stress distributions in laser cleaving of glass substrates // Precision Engineering. – 2017. – Vol. 47. – pp. 333–343.

196. Iwatsuki S. et al. Examination of internal stress by photoelasticity in laser cleaving of glass // Precision Engineering. – 2020. – Vol. 64. – pp. 122–128.

197. E. B. Shershnev, Yu. V. Nikityuk, S. I. Sokolov, A. E. Shershnev Increasing the efficiency of laser controlled thermal cleaving of silicate glasses // Scientific Seminar on Optics and Theoretical Physics, dedicated to the 70th anniversary of the birth of A. N. Serdyukov, ed. by A. V. Roga-chev [et al], 2014, pp. 251–253.

198. The effect of CO_2 laser radiation trapping into a narrow channel during metal processing through combined laser radiation / A. V. Fedin [et al] // Bulletin of the Russian Academy of Sciences: Physics. – 1999. – 63, No. 10. – pp. 2053–2058.

199. S. A. Kakorin, V. L. Komolov, M. N. Libenson Features of pho-toexcitation and temperature distribution in a semiconductor subjected to dual-frequency counter influence // Technical Physics Letters. – 1982. – Vol. 8, issue 9. – pp. 513 – 517.

200. V. L. Komolov, M. N. Libenson, G. D. Shandybina Heating and laser destruction of semiconductors // Izvestiya AS USSR, Physical Series. – 1985. – Vol.46, No. 6. – pp. 1103 – 1110.

201. Optical breakdown of gallium arsenide under pulsed two-frequency impact / A. M. Bonch-Bruevich [et al] // Technical Physics Letters. – 1982. – Vol. 8, Issue 8. – pp. 507 – 510.

202. A. Ya. Nashel'skii. Technology of semiconductor materials. – Moscow: Metallurgia, 1987. – 336 p.

203. Laser separation of metal-ceramic multilayer structures / S. V. Shalupaev [et al.] // Ceramics. Polish ceramic bulletin. – 2001. – Vol. 65. – pp. 69 – 74.

204. Yamada M. Secondary harmonic generator having waveguides for a laser beam : pat. 4973117 USA. – 1990.

205. Cai Y. et al. Laser cutting silicon-glass double layer wafer with laser induced thermal-crack propagation // Optics and Lasers in Engineer-ing. – 2016. – Vol. 82. – pp. 173-185.

206. Sinev L. S. Mechanical stresses estimation in silicon and glass bonded at elevated temperature, Science and Education of the Bauman MSTU, 2014, No. 12, pp. 951–965. DOI: 10.7463/1214.0745310. (in Russian)

207. GOST 13659-68 Colorless optical glass. Physico-chemical prop-erties. Parameters. – 01.01.1980. – Moscow, 1968. – 28 p.

208. Sapphire [Electronic resource] / Tydex official website. – Access mode: http://www.tydexoptics.com/pdf/ru/Sapphire.pdf. – Date of access: 10.07.2018.

209. Leucosapphire (Al2O3). Optics from sapphire: lenses, protective windows, micro optics from leucosapphire [Electronic resource] / ALKOR Technologies official website. – Access mode: http://www.alkor.net/al-korru/Sapphire1.html. – Date of access: 10.07.2018.

210. The effect of anisotropy on the deformation and fracture of sapphire wafers subjected to thermal shocks / T. Vodenitcharova [et al.] // Journal of Materials Processing Technology. – 2007. – Vol. 194. – pp. 52–62.

211. Method of laser cutting of tubular glass blanks: Pat. 1721995 USSR, IPC B23K 26/073 C 03B 33/08 / Dutka I. I., Kovalenko V. S., Matviyishin G. L.; assignee Lviv Design Bureau "Erotron"; applied 1989.06.20; published 1996.02.27 / [Electronic resource]. – 2007. – Access mode: www.fips.ru – Date of access: 19.05.2007.

212. S. V. Shalupaev Development of technology of thermal cleaving of anisotropic and multilayer inhomogeneous structures via laser beams of specific geometry : research report / F. Skorina Gomel State University. – Gomel, 2021. – 69 p. – No. GR 20161487

213. Gagarin, A. P. Investigation of the large-scale effect of laser radiation on metals and glasses: extended abstract of thesis work … Dr. Sci. in Physics and Mathematics: 05.27.03. – Moscow, 1999. – 40 p.

214. V. V. Kononenko, V. P. Pashinin, M. S. Komlenok, V. I. Konov Modification of quartz glass by laser pulses of femtosecond duration // Computer Optics. – Vol. 33, No.3. – 2009. – pp. 254–259.

215. Sergeev, M. S. Investigation of the large-scale impact of laser radiation on metals and glass: Ph.D. thesis in Engineering Science: 01.04.05. – St. Petersburg, 2016. – 131 p.

216. Shalupaev, S. V., Nikityuk Yu. V., Sereda A. A. Laser thermal cleaving of multilayer heterogeneous glass structures // Proceedings of the Anniversary Scientific and Practical Conference commemorating the 90th anniversary of Francisk Skorina Gomel State University (Gomel, November 19–20, 2020) : in 3 parts / Ch. ed. S. A. Khakhomov. – Gomel : Francisk Skorina Gomel State University, 2020. pp. 191 – 194.

217. AGS. Technical Data Sheet – Planibel [Electronic resource] / AGS Glass UK Ltd official website. – Access mode: https://www.agc-yourglass.com/. – Date of access: 10.03.2021.

218. CAMILLA FORS. MECHANICAL PROPERTIES OF INTERLAYERS IN LAMINATED GLASS – Experimental and Numerical Evaluation (Master's Dissertation) [Electronic resource] / Lund University official website. FACULTY OF ENGINEERING. – Access mode: http://www.byggmek.lth.se. – Date of access: 20.03.2021.

219. PROPERTIES OF SODA-LIME SILICA FLOAT GLASS [Electronic resource] / Technical Bulletin. NSG group. – Access mode:

https://www.pilkington.com/resources/ats129propertiesofglass20130114.pdf. – Date of access: 10.04.2021.

220. GOST 9438-97. Adhesive polyvinyl butyral film. Specifications. 01.07.2002 – Minsk: Belarus. state institute of standardization and certification, 2003. – 29 p.

221. Properties of SGP and PVB [Electronic resource] / DuPont official website. – Access mode: https://www.dupont.com/building.html. – Date of access: 10.04.2021.

222. Saflex® Clear PVB interlayer [Electronic resource] / Saflex official website. – Access mode: https://www.saflex.com/products. – Date of access: 10.04.2021.

223. Kikoin, I. K. Tables of Physical Quantities // Ch. ed. Kikoin, I. K. – Moscow: Atomizdat, 1976. – 1008 p.

224. Ansys [Electronic resource] / Ansys, Inc. official website. – Access mode: https://ansys.com. – Date of access: 14.02.2021.

225. Agalakov Yu. G., Bernstein A. V. Data dimensionality reduction in simulation modeling tasks // Information technologies and computer systems. – 2012. – No. 3. – pp. 3–17.

226. Koziel S., Leifsson L. Surrogate-based modeling and optimization. Applications in engineering. New York: Springer, 2013. – 412 p. https://doi.org/10.1007/978-1-4614-7551-4

227. Jiang P., Zhou Q., Shao X. Surrogate model-based engineering design and optimization. Singapore: Springer, 2020. – 240 p. https://doi.org/10.1007/978-981-15-0731-1

228. Kadri M. B., Nisar S., Khan S. Z., Khan W. A. Comparison of ANN and finite element model for the prediction of thermal stresses in diode laser cutting of float glass // Optik – International Journal for Light and Electron Optics. – 2015. – Vol. 126, No. 19. – pp. 1959–1964. http://doi.org/10.1016%2Fj.ijleo.2015.05.033

229. V. A. Golovko, V. V. Krasnoproshin. Neural Network. Technologies of Data Processing [Neirosetevye tekhnologii obrabotki dannykh], Minsk: BSU, 2017. – 263 p. (In Russ.)

230. Chollet F. Deep Learning with Python. N.Y.: Manning, 2018. – 400 p.

231. Bessmeltsev, V. P., Bulushev, E. D. Optimization of laser micromachining regimes // Autometriya. – 2014. – Vol. 50, No. 6. – pp. 3–21.

232. Parandoush P., Hossain A. A review of modeling and simulation of laser beam machining // International Journal of Machine Tools and Manufacture. – 2014. – V. 85. – P. 135 – 145. https://doi.org/10.1016/j.ijmachtools.2014.05.008

233. Emelyanov V. V., Kureichik V. V., Kureichik V. M. Teoriya i praktika evolyutsionnogo modelirovaniya [Theory and practice of evolutionary modeling]. Teoriya i praktika evolyutsionnogo modelirovaniya [Theory and practice of evolutionary modeling]. Moscow, Fizmatlit Publ., 2003, 432 p. (In Russ.).

234. Krasnovskaya S. V., Naprasnikov V. V. Review of optimization algorithms possibilities when modeling the compression-condensation units via the finite element methodв // Proceedings of the National Academy of Sciences of Belarus. Physical-technical series [Vestsi Natsyyanal'nai akademii navuk Belarusi. Seryya fizika-tekhnichnykh navuk]. – 2016. – No. 2. – pp. 92 – 98. (In Russ.).

235. Fonsecay C., Flemingz P. Genetic algorithms for multiobjective optimization: Formulation discussion and generalization // In Proceedings of the 5th International Conference on Genetic Algorithms. CA, USA. San Francisco: Morgan Kaufmann Publishers Inc.,1993. – pp. 416–423.

236. Nikitjuk Y. V., Serdyukov A. N., Aushev I. Y. Determination of the parameters of two-beam laser splitting of silicate glasses using regression and neural network models // Journal of the Belarusian State University. Physics. – 2022. – Vol. 1 – pp. 35–43. https://doi.org/ 10.33581/2520-2243-2022-1-35-43

237. Yuri V. Nikityuk, Anatoly N. Serdyukov, Igor Yu. Aushev Determination of the parameters of two-beam laser splitting of silicate glasses using regression and neural network models. Journal of the Belarusian State University. Physics. 2022; 1:00–00. https://doi.org/10.33581/2520-2243-2022-1-00-00

238. Yuri V. Nikityuk, Anatoly N. Serdyukov, Igor Yu. Aushev Optimization of laser cleaving parameters of quartz glass // Problems of Physics, Mathematics and Technology. – 2021. – No. 4 (49). – pp. 21 – 28. – DOI: https://doi.org/10.54341/20778708_2021_4_49_21 (impact factor RSCI - 0.322)

239. Yuri Nikitjuk, Andrey Sereda, Anatoly Serdyukov, Sergey Shalupaev, and Igor Aushev Parametric optimization of silicate-glass-based asymmetric two-beam laser splitting // Journal of Optical Technology. 2023. – Vol. 90, No. 6, pp. 296–301. https://doi.org/10.1364/JOT.90.000296

240. Determination of the Parameters of Controlled Laser Thermal Cleavage of Crystalline Silicon Using Regression and Neural Network Models. NIKITJUK, SERDYUKOV, Crystallography Reports. – 2023. – Vol. 68, No. 7. – pp. 195–200. © Pleiades Publishing, Inc., 2023 https://link.springer.com/article/10.1134/S1063774523600679

Scientific publication

Nikityuk Yuri Valerievich,
Sereda Andrei Alexandrovich,
Serdyukov Anatoly Nikolaevich

LASER CLEAVING OF BRITTLE NON-METALLIC MATERIALS

In the author's edition